Structural Modification of Stationary Rotor Systems for Dynamic Performance

Thesis submitted in accordance with the requirements of the University of Liverpool and National Tsing Hua University for the degree of Doctor in Philosophy

by

Sunghan Tsai

August 2019

To my family and my fiancée

Abstract

The applications of rotor systems are common in our daily life and industry. Aero engines and power generating equipment are good examples of rotor systems. Due to the recent increasing interest in higher energy efficiency and higher power density, the structural dynamic performance of such a rotor system is becoming more important. A poor structural dynamic design can cause large vibration responses, low power efficiencies, bad user experiences, or possibly a complete failure of the system. For these reasons, the dynamic properties need to be thoroughly considered, designed, and sometimes modified. However, there are cases in which the system of interest is too complex to be accurately modelled, thus making accurate simulations difficult or infeasible. For this problem, the receptance-based inverse structural modification method can potentially be a good solution.

In this thesis, a receptance-based inverse structural modification method is studied to improve a rotor system's dynamic performance. Such a method has a number of merits compared to other methods in the area of structural modification, which include (a) the procedure of the analysis is straightforward in the sense that the modifications to be made are determined by the desired dynamical properties, (b) it does not require the system matrices (**M**, **C**, and **K**) or the modal data to carry out the analysis, (c) the tedious trial-and-error approach can be avoided, (d) experimental data can be directly used in the method, and (e) various dynamic properties can be assigned. As a result, the method continually receives research interest although the idea was proposed slightly more than a decade ago. The relevant work in this area of research is reviewed and the challenges are identified regarding its theoretical developments and practical applications. Some of the challenges are taken as the objectives of this study.

First, the receptance-based method is further extended and the assignment problem is cast as an optimization problem to assign various dynamical properties using more than one form of modifications and accommodate structural modifications at more than one location. Several forms of modifications previously reported in the

literature can be simultaneously included in the extended method. The applicability of the method is demonstrated by a number of simulations and experiments. It is applied to a laboratory geared rotor-bearing system to achieve natural frequency and antiresonant frequency assignments solely using experimental receptances. Additionally, it is shown by experiments that the locations of the given modifications can be determined without a numerical model so that the highest first bending natural frequency of a rotor system can be achieved.

A big unsolved challenge in implementing the receptance-based structural modification method in practice is the lack of high-quality measurement of rotational (in bending) or torsional receptances. A receptance-based indirect measurement technique using a T-block attachment is proposed to address this issue. The numerical model of the system of concern is not required. The proposed technique can take account of the information from a number of excitations and responses, and provides the flexibility in their choices of location. The proposed technique has shown better performance over the torsional receptance estimation technique in the literature and is extended to estimate high-quality rotational receptances. The estimated receptances can now be used in various applications such as modal analysis, model updating, and structural modification.

Moreover, the frequency assignment via coupling of subsystems is studied. The subsystems considered are rotor systems which can be rather complex. The theory is developed based on Receptance Coupling technique and formulated as an optimization problem, and only the receptances at the connection ends of the subsystems of interest are required. Both bending natural frequencies and torsional natural frequencies can be assigned using a modifiable joint with multiple DoFs, respectively or simultaneously. The technique is demonstrated by a few simulations and is possible to be implemented in practice through the proposed rotational/torsional receptance estimation technique.

Acknowledgements

First and foremost, I would like to express my sincere appreciation to my UoL-supervisor Professor Huajiang Ouyang. It has been an honour to be his Ph.D. student. Over the course of the study, I continuously received his valuable guidance and rigorous feedback that have helped me overcome many difficulties in my research. His passion in the research was motivational and has encouraged me to be more productive and to achieve more. I want to thank him for establishing such an excellent example as a successful researcher and professor. I would also like to thank my NTHU-supervisor Professor Jen-Yuan Chang for offering me this opportunity to this joint Ph.D. programme. I deeply appreciate his substantial assistance and the financial support over these years.

I gratefully acknowledge the support provided by the UoL-NTHU Dual Ph.D. Programme. The program covered the tuition fees in both institutes and provided a monthly stipend so that I do not have to worry much about my living expense and can focus more on the research.

Moreover, I would like to thank my colleagues, academic staff, and technicians in the Dynamics and Control Group at University of Liverpool and in the PME department at NTHU for their assistance and supports. This Ph.D. research is made possible because of their help and contributions. I also want to thank my friends I made at University of Liverpool for being caring and friendly. I really enjoyed the company, and my stay in the UK was made delightful mainly because of you.

Last but not least, I want to give special thanks to my family and my fiancée for their love and encouragement. The faith my family members have in me and their unselfish supports have been the greatest motivation for me. To my beloved fiancée, Yi-An, thank you for always being there for me and keeping me going. The love, supports, and understandings you have during these years are so much appreciated. Thank you.

Sung-Han Tsai

June 2019

Content

List of figures

List of tables

Nomenclature

Symbol	Description
$\mathbf{M}$	Mass matrix
$\mathbf{C}$	Damping matrix
$\mathbf{K}$	Stiffness matrix
$\mathbf{G}$	Gyroscopic matrix
$\mathbf{Z}$	Dynamic stiffness matrix
$\mathbf{I}$	Identity matrix
$\mathbf{H}(s)$	Receptance matrix
$\widehat{\mathbf{H}}(s)$	Modified receptance matrix
$\widetilde{\mathbf{H}}(s)$	Subsidiary receptance matrix
$h_{ij}(s)$	The ij^{th} entry of receptance matrix
$\hat{h}_{ij}(s)$	The ij^{th} term of modified receptance matrix
$\tilde{h}_{ij}(s)$	The ij^{th} term of subsidiary receptance matrix
$\Delta\mathbf{Z}(s)$	Dynamic stiffness modification matrix
ξ	Damping ratio
s	Laplace variable
λ	Eigenvalue
$\mathbf{v}$	Eigenvector
$\mathbf{V}$	Eigenvector matrix
ω	Frequency in rad/sec
$b_r(s)$	Rank-one modification at r^{th} coordinate
$\mathbf{f}$	Vector of forces
$\mathbf{q}$	Vector of displacement responses
$\mathbf{u}$	Vector of (complex) amplitudes
$\mathbf{e}_r$	Unit vector at coordinate r
Ω	Spin speed
I_p	Polar moment of inertia
I_d	Diametral moment of inertia
$\mathbf{C}_{\text{s}}$	Damping matrix of the stator
$\mathbf{C}_{\text{cir}}$	Internal damping matrix of the rotating part
$\mathbf{K}_{\text{cir}}$	Circulatory stiffness matrix
$\mathbf{z}$	State vector
$\mathbf{y}$	Output vector
μ	Closed-loop eigenvalue
$\mathbf{w}$	Close-loop eigenvector

$\mathbf{B}$	Control distribution matrix
$\mathbf{b}$	Single-input control distribution vector
$\mathbf{G}$	Displacement feedback control gain matrix
$\mathbf{g}$	Displacement feedback control gain vector
$\mathbf{P}$	Velocity feedback control gain matrix
$\mathbf{p}$	Velocity feedback control gain vector
$\mathbf{x}$	Vector of design variables
$\mathbf{x}_0$	Vector of initial estimates of design variables
α_r	r^{th} weighting coefficient
β	Trade-off coefficient

1. Introduction

In this chapter, the history of rotating machines is briefly summarized and the current trends in rotating machine developments are described. Due to the increasing power density in a rotating machine, the dynamic properties of such a machine and any associated structure have become increasingly important. Structural Modification has been an effective way to ensure the dynamic performance, whose principal idea is to improve a structure's dynamical behaviour by modifying the structure and provide a guideline for the modifications required in order to bring about the desired dynamic properties. The outline of this thesis is presented at the end of this chapter as well as the original contributions of this thesis.

1.1. Background

The study and the development of rotating systems have been an important field for scientists and engineers owing to the fact that they are widely used in our daily life and in various industries. Several important historical events relating to the development of rotating systems have happened in the past two centuries and have shaped the world we see today. Beginning with the First Industrial Revolution in 1760's when the first 10 horsepower steam engines were invented and then were widely used in farming and weaving. In 1840 the advancements in machine tool industry and production and manufacturing technology led to the Second Industrial Revolution due to the two most important technologies at the time: the invention of internal combustion engines and AC motors. Their power density was high enough to be used in many manufacturing or transportation systems. Almost a hundred years later, there were significant improvements in turbines, aircraft, and vehicles, not only due to World War 2 (1939 to 1945) but also because of the increasing needs from developed and developing countries. The above-mentioned technologies, no matter whether the energy source is from fuel or electricity, they all transmit energy through rotational mechanisms. Designers and engineers definitely need a certain level of

theoretical knowledge about the dynamic behaviour of the machines, which is usually referred to as rotordynamics, so that the machines can work efficiently and run smoothly.

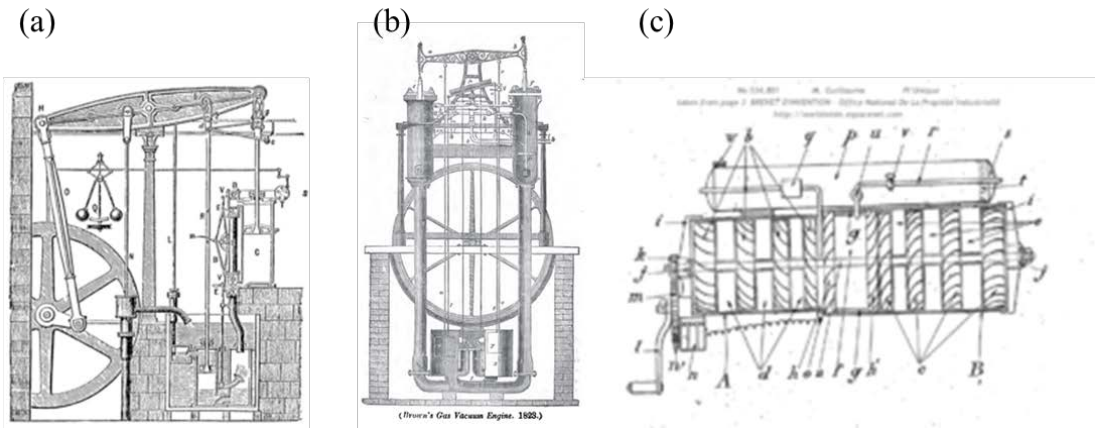

Figure 1. 1. (a) Steam engine designed by Boulton and Watt in 1784 [1]. (b) Early internal combustion engine by Samuel Brown in 1823 [2]. (c) First patented gas turbine for aircraft by Maxime Guillaume in 1921 [3].

Nowadays, the energy consumption of machines and energy efficiency starts to draw people's attention owing to the raising awareness of environmental protection and the global energy crisis. Taking electrical motors as an example, many electrical motor companies have been focusing on downsizing current electrical motors or integration of motor components (such as driver, inverter, gear, or impeller) to reduce unnecessary material cost or waste; however, in order to maintain the same power output, the rotating speed of the rotor must have to be increased. In general, machines are becoming more advanced and complex than before. Some machines are required to operate at very high speed and also remain stable under severe conditions. On the whole, recent rotating machines tend to be more precise, more efficient, and more powerful; moreover, low maintenance frequency is always preferred. Some of the ongoing and promising technologies are, for instance, (1) Active magnetic bearings, (2) Active fluid-film dampers, (3) Flywheel energy storage systems, and (4) Off-site condition monitoring systems. Brief descriptions of these technologies will be given as follows:

(1) Active magnetic bearing uses magnetic forces to provide non-contact support to rotors; therefore, friction forces and mechanical wear can be almost removed. Through decades of efforts, active magnetic bearings are increasingly implemented in several machines such as compressors, pumps, generators, and machine tools. In fact, there are still considerable unsolved challenges and limitations waiting to be addressed such as their maximum load capacity, information processing techniques/ control algorithms, and so on [4].

(2) Semi-active or active squeeze film dampers support the rotor by a thin layer of pressurized fluid between the bearing surfaces and have shown several advantages over conventional ball bearings and journal bearings, especially in suppressing unbalanced vibration. Through a special design, stiffness and damping of the device can be controlled independently and precisely, which can reduce the vibration response amplitude when the rotating speed passes through critical speeds and enhance the robustness and flexibilities of the rotor system [5].

(3) Flywheel energy storage systems provide a measure to store energy without any chemical reaction, i.e. no batteries. The total energy a device can store depends on the speed, mechanical properties of the rotating mechanism, and the operating environment. The flywheel inside the frame tends to rotate at a very high speed (20,000 to over 50,000 rpm). This system usually operates in a vacuum enclosure and use magnetic bearings as supports to mitigate the air drag and mechanical friction; therefore, this increases the energy efficiency and largely reduces the maintenance effort [6].

(4) Off-site condition monitoring systems are getting more attention than before since the developments and the increasing needs of wind turbines in pursuit of clean energy supply and energy conservation [7]. Due to the noise and size of wind turbines, they are usually located in the rural area or offshore where the maintenance of machines can become difficult, and the cost could be high. An off-site condition monitoring system can reflect the current condition of the machine and provide early warnings or diagnoses of the machine, which reduces the frequency of manual

maintenances and the cost. The idea of Internet of Things (IoT) also boosts the study in this area.

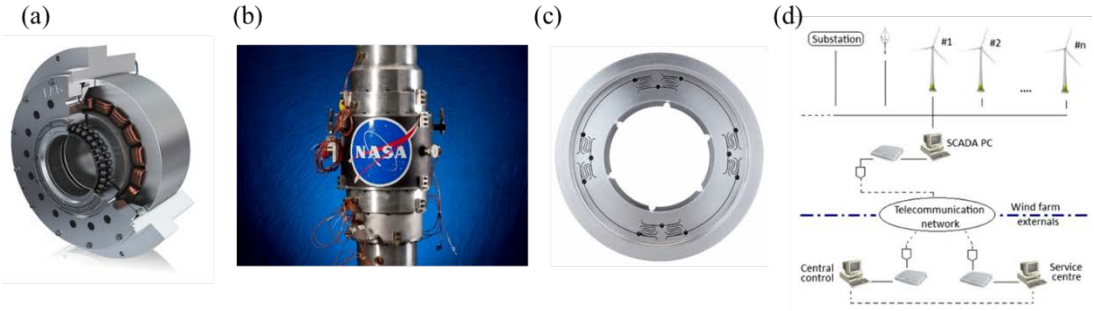

Figure 1. 2. (a) Active magnetic bearing designed and manufactured by Schaeffler. (b) An energy storage system developed by NASA. (c) Integral squeeze film damper by Waukesha. (d) Simplified diagram of a wind farm monitoring control and data acquisition system [7].

1.2. Motivation

Due to the current tendencies, the power density of a machine significantly escalates and its mechanical structure is becoming more complex. For example, the shaft in the flywheel energy storage system is rotating so fast that one of the primary limits of the system is the tensile strength of the material of the rotor. The drivetrain in cars and the shaft in turbines have to transmit a great amount of torque than before. Without a proper consideration of mechanical or structural dynamic design, unsatisfied machine dynamic response or even serious mechanical failures could happen, which are shown in Fig. 1.3

When a rotating machine is not stable or has some problems during operation, it is economical and more convenient to modify the original structure rather than to redesign the whole machine; therefore, several questions such as “How to modify the structure?”, “What is the best way to modify it?”, and “How to design or control the dynamic behaviour of the structure?” arise. Moreover, the improvement of response is getting more and more attention as a result of growing demand of precise machining and advanced manufacturing in nanometer scale in which vibration could have a critical effect on the outcome. The solution to those questions is usually referred to as

a research field called Structural Modification. Structural Modification focuses on improving or changing certain dynamic properties of a structure by modifying its structural properties. This idea has been implemented in many products' prototype development stage and will continue to play an essential part in designing better machines or commercial products. It is believed that improving current structural modification techniques would be beneficial to not only the products' performance but also the engineering R&D activities.

(a) (b)

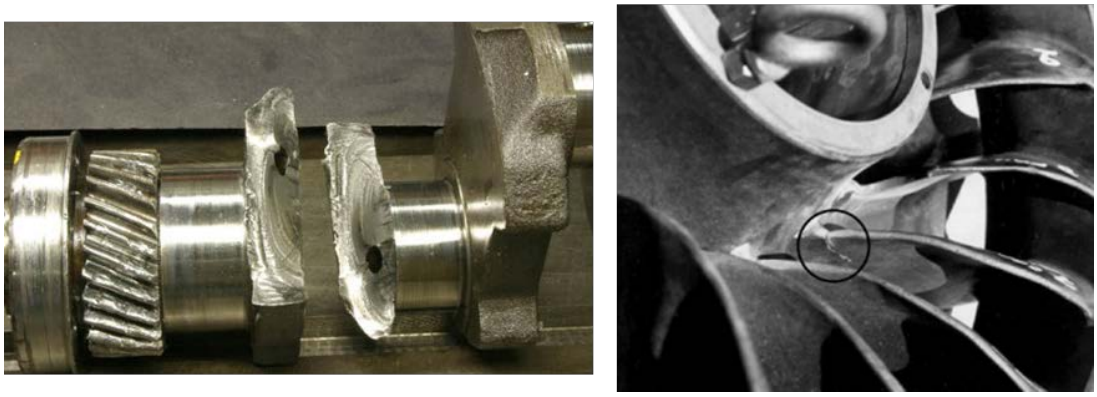

Figure 1. 3. (a) Fatigue failure in crankshaft due to excessive torsional vibration [8]. (b) Blade cracking caused by vibration induced fatigue [9].

1.3. The scope of this research

The aim of this PhD project is to address some current issues in the research of receptance-based inverse structural modification with an emphasis on the applications on rotor systems. The receptance-based inverse structural modification techniques can be implemented on a stationary rotor system so that the modified system can possess desired dynamic properties such as natural frequencies, antiresonant frequencies, nodes, modal displacements, ratios of receptances, etc. It should be mentioned that the rotor systems under consideration are stationary as it is still very difficult to accurately measure receptances from a rotating structure and that an important merit of receptance method will be taken away if measured receptances are not accurate enough. Although the study focuses on rotor systems in the stationary status, the dynamical property improvement made in the stationary status can have influences on

the system in rotation to an extent. For instance, from the Campbell diagram the frequencies of the forward whirl modes and the backward whirl modes can be adjusted by shifting the original frequencies at zero rotational speed. The mode shapes of the rotating system would not deviate much from those of the associated stationary system when the rotational speed is low.

The rest of the thesis is organized as follows:

Chapter 2 first presents a brief review on Forward Structural Modification, which is the early approach that deals with structural modification problems. Next, a comprehensive literature review on the topic of inverse structural modification and receptance-based inverse structural modification is given. Both the theoretical development and the practical implementation are covered. The theoretical development includes several different modelling approaches and structural modification strategies. Since the receptance-based inverse structural modification is of our primary interest, from a practical point of view, the measurement or estimation of receptance function are the main topic to be covered. A number of open problems in this research field are then identified through the existing literature, and the objectives of this thesis is to address some of the open problems.

As this thesis focuses on the applications on rotor systems, Chapter 3 presents the fundamental finite element modelling for rotordynamic analysis. The selection of analysis reference frame is important for rotordynamic analysis in order to obtain time-independent equations of motion. The modelling of a few common components, such as shaft, bearing, disc, and gear, are given with derivations or references. Then, the eigenvalue analysis of the rotordynamic model is presented and followed by a case study. A number of interesting phenomena about rotordynamics is discussed. The model presented in this chapter is adopted throughout the thesis and thus is deemed necessary to take a chapter to describe.

Chapter 4 focuses on the fundamental theory of the receptance-based inverse structural modification method and its development. The method can be divided into two groups; one is structural modification by passive elements, and the other is active control via sensors and actuators. For passive control, two basic forms of modifications, rank-one modification and spring-mass oscillator, are introduced. Their

properties and limitations in assigning dynamical properties are discussed. For active control, the theories of using SISO and MIMO control strategies for structural modification are presented. Their advantages and drawbacks compared with passive control approaches can be seen in this chapter. In the end, the partial pole assignment problem is demonstrated using MIMO control.

Chapter 5 extends the equations for the passive receptance-based inverse structural modification method, and the structural modification problem is cast as an optimization problem. The extended equation can accommodate more than one form of modifications and is capable of assigning various dynamical properties based on only receptances. The proposed technique is tested on a numerical model and a laboratory geared rotor-bearing test rig. Both sets of structural modification results are successful and accurate. In addition, the work provides some practical and experimental insights which help relieve the lack of experimental implementations in this area of research. Lastly, the technique is used to determine the optimum locations of the modifications for the rotor system to achieve the highest bending natural frequency. Note that no theoretical model or simulation are required for the technique to work.

Chapter 6 addresses the issue pertaining to the measurements of torsional receptances. Torsional receptance has been difficult to measure or estimate. The theory of the proposed technique is based on Receptance Coupling techniques, and the torsional receptance is estimated through attaching a T-block to the structure of interest. Only a few receptances of the T-block and some of the assembled structure are required for the estimation. The proposed technique is applied to a laboratory rotor system, and high-quality receptance functions are indirectly measured.

Chapter 7 studies the frequency assignment problem of coupling of subsystems. It deals with the issue of which the available modifications are too complex to be modelled as simple modification units, such as point masses, grounded springs, spring-mass oscillators, etc. Under the context, the proposed technique is derived based on Receptance Coupling technique and only requires receptances at the connection ends of each subsystem. Several numerical simulations are used to demonstrate the applicability of the method. Besides, the measurement method proposed in Chapter 6

is extended to the estimation of rotational receptances (in bending). Numerical simulations show that rotational receptances can be obtained with high quality and accuracy.

In Chapter 8, the main conclusions are summarized and some recommendations for future research are given.

In Appendix A, the procedure of the eigensensitivity model updating technique is included. Appendix B gives the derivation relating to the coordinate transformation used in the equations in Chapter 6.

1.4. Original contributions

The original contributions that have been made in this PhD project are mainly presented in Chapters 5 to 7. They can be concisely summarized in the following list:

Chapter 5

1. Extend the receptance-based inverse method to assign various dynamical properties (natural frequency, antiresonant frequency, eigenstructure, node, and receptance) using more than one form of modifications and accommodate the modifications at more than one location.
2. Give experimental and practical insights to the implementation of receptance-based inverse structural modification on a laboratory geared rotor-bearing system.
3. Successfully implement natural frequency and antiresonant frequency assignments on a laboratory geared rotor-bearing system based on measured receptances.
4. Determine the optimal location for given modifications based on measured receptance functions to achieve the highest first bending natural frequency.

Chapter 6

5. Propose a receptance-based method for torsional receptance measurement which outperforms the existing method reported in the literature.
6. Successfully obtained high-quality torsional FRFs on a laboratory two-disc rotor-bearing rig without using the numerical model of the rig.

7. Incorporate the rotational accelerometer and study the locations for excitations and responses to achieve better estimation accuracy.

Chapter 7

8. Achieve frequency assignment through coupling of subsystems. Only the receptances at the interface of the subsystems are required.
9. Extend the method proposed in Chapter 6 to rotational receptance measurements (in bending). High-quality rotational receptances can be obtained.
10. Numerically achieve the bending and torsional natural frequency assignment of a coupled rotor system simultaneously.

2. Literature review

The purpose of this section is to cover related literature and the state-of-the-art structural modification on the assignments of dynamic properties. This research topic can be broadly discussed from two aspects, one is the theoretical development and the other is the practical implementation. The practical implementations of structural modification would vary on a case-by-case basis due to the theoretical assumptions made in the techniques and the structure of concern. Therefore, it is worth reporting how researchers implement the technique in a real situation so as to gain practical insights and know the limitations of the techniques.

For the theoretical side, there are two complementary approaches to address structural modification problems: one is direct/forward structural modification approach and the other is inverse structural modification approach. The forward structural modification aims to predict the exact change to the structure's dynamic properties when known modifications are made at a given location while the inverse modification determines what modifications should be made so that the modified structure can have the prescribed dynamic characteristics. The latter is more useful and time-efficient in many practical conditions, which has encouraged many researchers to study this area in recent decades; consequently, in this chapter much more effort is made in reviewing the literature pertaining to the latter whilst a brief introduction on forward structural modification is presented first.

Through this literature review, some open problems in this research area are identified. These open problems provide motivations for researchers who are interested in this topic and wish to make novel contributions.

2.1. Forward structural modification

Early studies of forward structural modification, which is also known as re-analysis, were reviewed and summarized by Baldwin and Hutton [10]. They classified the techniques into three groups based on the assumptions of the form of modifications: techniques based on small modifications, techniques based on localized modifications,

and techniques based on modal approximation. Several approaches such as Rayleigh quotient, sensitivity analysis, and perturbation approach were used to address forward structural modification problems without a complete reanalysis of the whole structure. Rayleigh quotient may appear to be the first technique within these approaches. The eigenvalue problem of a general, conservative, vibrating system can be described by

$$\mathbf{K}\mathbf{v}_i = \lambda_i \mathbf{M}\mathbf{v}_i \tag{2.1}$$

where **K** and **M** are stiffness and mass matrices of the system and both consist of real entries, λ_i and $\mathbf{v}_i$ are the eigenvalue and the corresponding eigenvector of the i^{th} mode. The Rayleigh quotient allows the eigenvalue λ_i to be calculated if the eigenvector $\mathbf{v}_i$ is known. The eigenvalue of a modified system can be determined by [10]

$$\lambda_i + \Delta\lambda_i = \frac{\tilde{\mathbf{v}}_i{}^{\mathrm{T}}(\mathbf{K} + \Delta\mathbf{K})\tilde{\mathbf{v}}_i}{\tilde{\mathbf{v}}_i{}^{\mathrm{T}}(\mathbf{M} + \Delta\mathbf{M})\tilde{\mathbf{v}}_i} \tag{2.2}$$

where $\tilde{\mathbf{v}}_i$ is the i^{th} modified eigenvector. The Rayleigh quotient is inherently insensitive to small error in eigenvector guessing and has a minimal value in the vicinity of the eigenvector. In other words, the modified eigenvalue can be estimated for any arbitrary eigenvector as long as it is not far away from the exact modal eigenvector. As a result, with the help of sensitivity analysis on eigenvectors or eigenvalues, which focus on the rate of change or derivatives of eigenpair with respect to design variables [11-14], a good approximation of the modified eigenpair can be obtained.

The general structural modification by localized modification (point mass or point stiffness) was developed by Weissenburger [15]. What makes it different from sensitivity analysis or perturbation approach is that it can cope with large modifications locally. The work was later extended to viscously damped linear systems by Pomazal and Snyde [16]. Ram and Blech studied the effect of simultaneously changing stiffness and mass of an undamped vibratory system [17], who concluded that: connecting a vibratory system to a grounded mass-spring oscillator results in the increase of all the natural frequencies below the natural

frequency of the oscillator and the decrease of all the natural frequencies above the natural frequency of the oscillator as shown in Fig. 2.1. This applies to lumped systems as well as continuous systems.

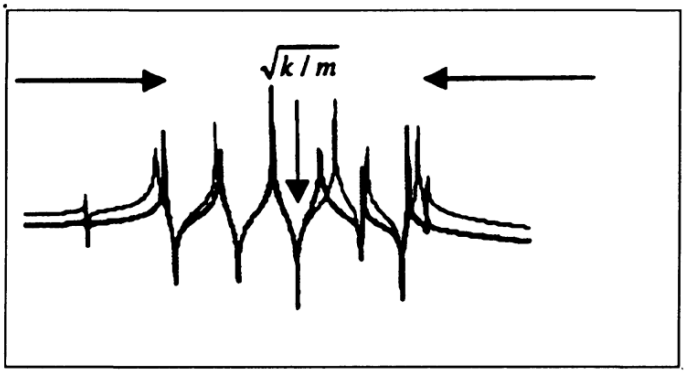

Figure 2. 1. Shifts of natural frequencies due to the addition of a grounded single degree of freedom oscillator [18].

Another two useful observations for point structural modification at the free end (not a nodal point for modes) of a cantilever beam are summarized here: (1). A simple mass modification decreases all the resonances, and every resonance is shifted leftwards, towards the closest antiresonance. When the mass modification reaches infinity, resonances will cancel out with antiresonances. (2). When a grounded spring is attached at the free end, every resonance moves towards each antiresonance at the right while all antiresonances are fixed. These observations are shown in Fig. 2.2 and 2.3 below.

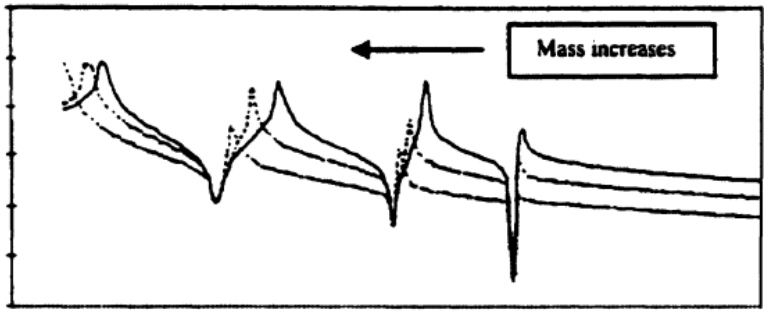

Figure 2. 2. Tendency of a point FRF of a cantilever beam due to point mass modification at the free end [18].

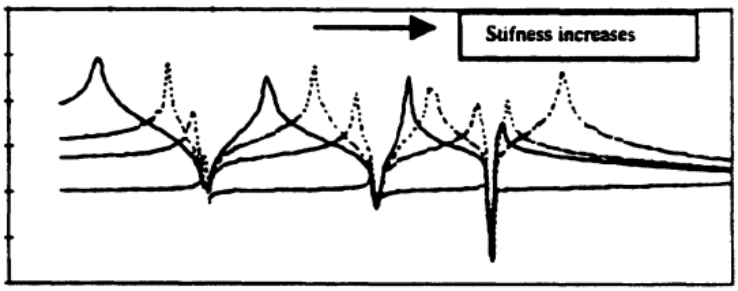

Figure 2. 3. Tendency of a point FRF of a cantilever beam due to a grounded spring modification at the free end [18].

2.2. Inverse structural modification

Theoretically, both forward and inverse structural modification approaches can yield accurate results if the dynamical characteristics of the structure are accurately known. However, inverse structural modification has been a more active research field in the last decades as it provides a more intuitive and time-efficient way to design or modify a structure. There are generally three types of models to describe a structure's dynamic behaviour, which are

- Spatial model: It is also called physical model, which refers to mass, stiffness, and damping matrices of a system.
- Modal model: It represents the eigenstructure of a system, which includes natural frequency, damping ratio, and mode shape (modal constant).
- Response model: It can be directly obtained from conducting experimental modal analysis (EMA) on a system, and is usually represented by Frequency Response Functions (FRFs).

These three models are interchangeable without producing any error only if any one of three models is correctly and completely known (see Fig. 2.4). Depending on the model adopted, the inverse structural modification techniques can be different. In practice, a spatial model can be built using a Finite Element (FE) model and updated through model updating techniques. Farahani, Aryan, and Bahai [19, 20] proposed methods that used system matrices along with sensitivity analysis. Nonetheless, the accuracy of the outcome could decrease when the model, boundary condition, or joint

modelling is complex [21]. The increase in computational time is also an issue when the number of degrees of freedom (DoFs) in a model is large.

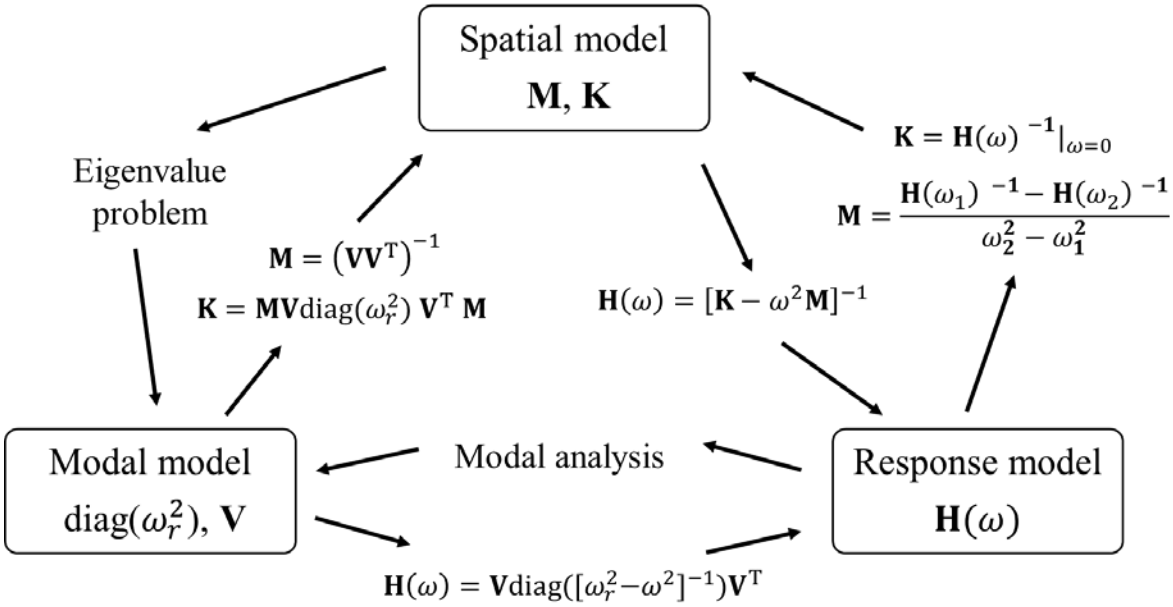

Figure 2. 4. Relationship among the three models. (ω_r is the frequency of the r^{th} pole and $\mathbf{V}$ is the mass-normalized mode shape matrix)

A modal model can be derived from experimental data through modal identification techniques such as complex exponential method (CE), least-squares complex exponential method (LSCE) [22], rational fraction polynomial method, polyreference least-squares complex frequency-domain method (p-LSCF) [23], etc. A complete set of modal data could result in an exact solution for inverse structural modification problem; however, it is extremely difficult to identify most of a modal data set from an experimental point of view, thus leading to the so-called "Truncation Error" due to the use of incomplete modal data. Many early studies [24-26] were focused on minimizing or circumventing the effect in order to achieve sufficiently accurate solutions. Bucher and Braun [25] used only a partial set of eigensolutions (left and right eigenvectors) extracted from measured FRFs to calculate the exact solutions for eigenvalue and eigenvector assignments and developed a procedure to circumvent truncation error. Left and right eigenvectors are related and orthogonal with each other. Left eigenvectors can be physically interpreted as a term proportional to the inertial force to a vibration mode, however, the extraction process is inherently ill-conditioned [27]. Braun and Ram [26] determined the optimal approximate solution

for natural frequency assignments in a Rayleigh-Ritz sense. Since the solution is not unique, they then solved underdetermined least-square problems with inequality constraints to determine physically feasible solutions.

Techniques based on a response model, on the other hand, tackle truncation error and are able to circumvent modelling inaccuracy. However, the results heavily depend on the quality of FRFs as they are usually directly implemented; in other words, from an experimental point of view, every step in modal testing, for instance, the equipment in use, signal processing, and testing expertise, is crucial. On balance, addressing inverse structural modification problem using FRFs has wider applications and offers several advantages, which encourages its development in recent years. Among many techniques, receptance method has received considerable attention since it doesn't require a theoretical model to find the solution, that is to say, one can deal with a complex structure even though a realistic finite element model is very difficult to construct and thus is usually unavailable. Receptance method can be used to assign several dynamic characteristics including natural frequency, antiresonant frequency, node location, mode shape, or frequency response level, and it can be further divided into two groups based on their implementations: one is structural modification by passive elements (such as masses, springs, or beams), and the other is active vibration control using sensors and actuators.

2.2.1. Receptance method

Passive control

Passive structural modification offers several advantages over active control. For example, the modified system is guaranteed to be stable, it does not require additional sensors, actuators or power suppliers, and it is possible to deliver large modifications to the system [28]. Among early studies, Tsuei and Yee [29] proposed a method for inverse structural modification based on the FRFs of an undamped vibrating system. The method could determine the required mass or stiffness modification value to give

a system an assigned natural frequency with only a few computations; it is worth mentioning that not every frequency is achievable. Later on, the same idea was extended to assign a damped natural frequency of a damped structure by the same authors [30] in which they rearranged the equation of motion of a damped system into a first-order state space form and applied an iteration process to find a solution. Both studies considered changing only the mass matrix or stiffness matrix separately. A method of simultaneous mass and stiffness modification on lumped systems was presented in a book by Maia *et al.* [31] in which a coefficient matrix and predetermined mass/stiffness ratios were introduced in the modification matrices instead of their absolute values. Methods for assigning an antiresonant frequency for a spring-mass system were also covered in this book. Moreover, Maia *et al.* stated that it is possible to fix one natural frequency and shift another, thus optimizing the response with a frequency range of concern.

The most basic form of modification, rank-one modification, for pole (natural frequency) or zero (antiresonant frequency) assignment has been well studied and summarized in a review paper by Mottershead [32] in which the total number of DoFs of the system remains the same after modifications. Exact numerical solutions are available for rank-one modifications, which include point mass modification, grounded spring modification, or springs connected between two coordinates, if a solution exists. It is also possible to fix antiresonant frequencies while shifting natural frequencies since the zeros of a cross-receptance or a point receptance are not affected by the modification made at one of the coordinates of the receptance concerned. Cakar [33] extended the rank-one modification to keep some natural frequencies unchanged by an addition of a grounded spring after one or more mass modifications.

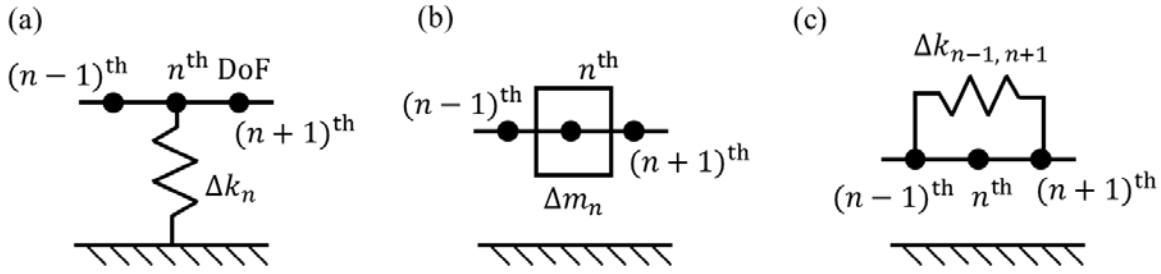

Figure 2. 5. Schematic of the forms for rank-one modifications: (a) grounded spring (b) point mass (c) spring connecting two coordinates

Mottershead and Lallement [34] studied pole-zero cancellation to form a vibration node. It is demonstrated by shifting a pole to a zero by adding a spring connecting two coordinates. The paper also proved that it is impossible to produce a pole-zero cancellation through a rank-one modification at the same coordinate, which can also be observed from Fig. 2.1 to 2.3. Mottershead *et al.* [35] later presented a procedure to achieve node assignment by applying rank-one modifications at coordinates other than the node location.

One of the merits of receptance method is that it only requires a few receptances (or FRFs) on the coordinates to be modified. When conducting natural frequency assignment, it is straightforward to determine the necessary receptances. However, this is not the case for antiresonant frequency assignment since antiresonant frequencies are local properties and must be solved from the adjugate/subsidiary system. Other than that, the subsidiary frequency response functions do not have a clear physical interpretation. This issue was studied and resolved by Mottershead [36], and the relationship between the subsidiary FRFs and FRFs was established. It can be shown that a subsidiary FRF can be expressed in terms of a few FRFs of the original system, thereby making it possible to conduct antiresonant frequency assignment only using experimental data.

Kyprianou *et al.* [37] showed that up to two natural frequencies could be assigned through an addition of a single DoF spring-mass oscillator. It was also shown that the effect of attaching an oscillator can be included in the system dynamic stiffness matrix without expanding its original total number of DoFs. Zhu *et al.* [38] proposed a similar procedure to assign receptances at particular frequencies by using one or more simple spring-mass oscillators. This provided an alternative way to reduce the vibration response of a system. Kyprianou *et al.* [28] managed to assign the natural frequencies and antiresonant frequencies of a continuous frame structure shown in Fig. 2.5 in which the leg on the right was taken as the modification to the Γ-shaped frame structure. The modification involved a 3×3 receptance matrix that covers two translational DoFs and, more importantly, one rotational DoF at the connection. The modification is represented by a constrained Euler-Bernoulli beam, and its geometric

properties (t, b, and d) are obtained by solving a set of simultaneous polynomial equations that matches the assignment requirement. This study showed that the methodology based on receptance method still works even if the assigned frequency and mode shape are much different from the original ones.

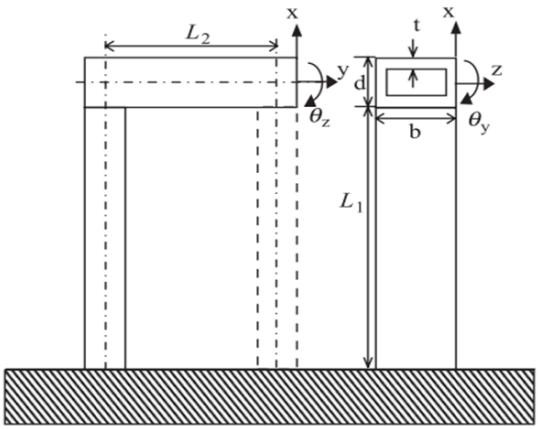

Figure 2. 6. Schematic diagram of the frame structure [28].

A different approach was made by Richiedei *et al.* [39] and Ouyang *et al.* [40] in which the inverse problem was transformed into a multi-variable optimization problem. Both eigenvalues and corresponding eigenvectors could be assigned through minimizing an objective function, and the required mass and stiffness modifications could be computed simultaneously; additionally, for the specific case in which the function is proved to be convex, the solution is guaranteed to be a global minimum and is not affected by initial guess. In fact, convex optimization problem has been studied for decades, and available algorithms are reliable and efficient. A Tikhonov regularization term [41] for penalizing large modifications and inequality constraints on the design variables were directly introduced to the optimization process, which weights the solutions according to practical assessments. These studies motivated the work of Liu *et al.* [42] about eigenstructure assignment (frequency and mode shape) through placing multiple spring-mass oscillators. Liu *et al.* [43] later assigned torsional natural frequencies and modal displacements of a 12-DoF spring-mass shaft system in the optimization sense, in this case only torsional receptances are required.

Besides using mass, spring, or oscillators as modifications, modifying a structure through coupling another complex structure is possible; however, only few works have

been done on this regard. Ram [44] determined the receptance of a coupled system, which is formed by linking subsystems via a simple connector such as a spring, a dashpot, or a mass, based on the receptances of the individual subsystems. Birchfield *et al.* [45] extended Ram's work to include more elements into the connectors between subsystems. The results from these works can be directly applied to pole assignment in such a scenario. However, in reality, the coupling between any two structures can be complex and hence possibly cannot be approximated by those simple connectors mentioned in Ram or Birchfield's works. The theoretical background behind their work is essentially based on receptance coupling technique, which has been applied to identify a machinery's performance for many years. For instance, the point receptance of the free-end of a cutting tool on a milling machine spindle [46-48] can be identified using measured and analytical receptances. The results are useful for the prediction of the machine's stability under different operating manufacturing cutting speeds and depth of cuts. Joint properties [49, 50] can also be identified through this technique.

Active control

Although active control seems to become increasingly popular and have a wide variety of applications in recent years, it should not be considered to be the only and better solution than passive control. In most cases, a bad design will remain bad no matter how sophisticated the applied active control method is. An active control solution should only be sought after the structure has been passively improved. It is also worth noting that active control only works well in a bandwidth (limited frequency range) designed by the adopted control system.

The first receptance-based-only active control method can be traced back to the paper done by Ram and Mottershead [51] in 2007. This method, based on the Sherman–Morrison formula of a rank-one modification in the frequency domain, was a state feedback (position and velocity feedback) control method and can be used for the assignment of poles and zeros. One of the advantages is that only receptances at certain locations are needed to calculate the gains, in other words, an observer is not

necessarily required. They stated that the pole assignment is possible whenever the system is controllable. The method was demonstrated by Papatheou *et al.* [52] in a laboratory aerofoil rig setup for suppression of flutter using a V-stack piezoelectric actuator. A receptance-based output feedback method was proposed by Mottershead *et al.* [53], which is readily applicable to multiple-input-multiple-output (MIMO) systems. The method was successfully implemented on a T-shaped plate for assignments of poles, zeros, or both using measured receptances.

The time delay between the measurement of the states and the actuation of the actuators in a state feedback control was considered by Ram *et al.* [54]. It was shown that a time delay does not affect the pole assignment equation; the pole assignment is possible when the open-loop system (without delay) is controllable. However, the characteristic equation with time delay inevitably includes a transcendental function, inducing an infinite number of roots (secondary eigenvalues). It is not guaranteed that all desired poles are assigned to the primary eigenvalues, hence the system can possibly still remain unstable. The posteriori stability check can be done by calculating the close-loop eigenvalues, using classical control techniques such as systems margins or Nyquist plot, or Padé approximations [55]. Another stability test using Small-Gain Theorem [56] was proposed by Santos *et al.* [57].

Mottershead *et al.* [58] proposed a method for assigning pole sensitivities based on receptance method using single-input state feedback control. The sensitivities of poles are shown to be given by a linear combination of the control gains. Assigning the sensitivities of poles can be desirable when considering the robustness of dynamical performance. Later, Tehrani *et al.* [59] achieved robust pole placement by minimizing the sensitivities of poles to measurement noise in receptances.

Ouyang [60] demonstrated the pole assignment of asymmetric second-order dynamical systems on a friction-induced self-excited problem using state feedback control. Poles with positive real parts are shifted to poles with negative ones. It was found that any two of the three control gains, active mass, active damping, and active stiffness, but active mass and active stiffness, can assign complex poles to an asymmetric system for any distributions of actuators. Ouyang [61] incorporated passive structural modifications into active feedback control to prevent having high

control gains. It was demonstrated by stabilizing an unstable asymmetric system represented by a friction-induced vibration model. The time-delay in such a model was considered by Singh and Ouyang [62]. They found that, for the same desired poles, the control gains and the energy required by the actuators generally decreases when the time delay in the state feedback loop increases. In addition to assigning stable poles to an unstable friction-induced asymmetric system, Liang *et al.* [63] considered assigning their corresponding sensitivities so as to achieve better robustness against uncertain contact parameters such as friction coefficient, contact damping, and contact stiffness.

Tehrani *et al.* [64] extended the receptance-based active control to a class of single DoF nonlinear systems, Duffing oscillator. The first-order open-loop FRF was used instead of the original receptances of a linear dynamical system. Pole assignment was achieved by iteratively updating the control gains, the closed-loop displacement amplitude, and the open-loop receptance to take account of the dependency on the displacement amplitude introduced by the nonlinearity. Singh and Ling [65] applied receptance method on viscoelastic systems to circumvent the modelling errors and difficulties in the attempt to accurately model the dynamic behaviour of viscoelastic systems. Numerical examples of pole and zero assignments of a structure composed of viscoelastic elements were given to demonstrate the effeteness of using receptances. From the literature review about active control employing receptance method, it can be found that receptance method can be well applied to linear systems but nonlinear systems due to the dynamic complexity.

2.3. Rotational FRF measurement

There are several reasons accounting for lack of experiments and applications of receptance method reported from the past literature. From an experimental point of view, the first challenge to appear would be the measurement of receptances, especially for receptances associated with rotational DoFs. Until now, there hasn’t been a successful way to “directly” measure rotational receptances. This spatial incompleteness of rotational DoFs information has a direct adverse influence on the

results of structural modification when rotational DoFs are heavily involved in the structure's response [66]. As a matter of fact, 15/21 of the entries in a 6×6 receptance matrix of 6 DoFs involve rotational DoF in the input or the output. Therefore, in this subsection, the focus is shifted to how to "indirectly" obtain good quality rotational FRFs. It should be mentioned that torsional FRF can be seen as a special case of rotational FRF around the axis of rotation for a machine and will also be discussed here.

Before going into indirect measurements, the difficulties and the development of direct measurements are discussed first. The difficulties in directly obtaining rotational FRFs can be broadly grouped into two aspects: (1) the measurement of rotational (or torsional) response and (2) the excitation and the measurement of a moment (or a torque). The former is relatively easy as there are various sensors available for measuring angular displacement, angular velocity, angular acceleration, or current signal [67]. Janssens and Britte [68] summarized and compared several kinds of sensors for measuring angular quantities. In summary, coder-based sensors such as magnetic pickups, optical encoders [69], or magnetic encoders are used for torsional displacement measurement; laser Doppler vibrometer [70, 71] can directly measure the angular velocity, and the angular acceleration can be measured by sets of two linear accelerometers, or angular accelerometers [72]. Except for non-contact sensors, additional devices such as slip rings or telemetry systems are required to transmit the signal, which inevitably increases the cost and introduce additional noise.

On the other hand, there has not been an ideal solution for the excitation and the measurement of a moment/torque. To date, a few studies have reported their attempts to solve the problem. Champoux *et al.* [73] intuitively used two synchronized impact hammers to generate moments on a steel plate; additionally, conventional twin shaker configurations, in which two shakers are driven out of phase, were studied [74-76]. Sihler [77] proposed that a three-phase electrical motor or generator could be used as a torsional exciter for large rotary machines to produce continuous torque with adjustable frequency and amplitude. For small rotary machines, Drew and Stone [78] investigated and evaluated the applicability of a 1.7-kW AC servo-drive system. They suggested that the torsional damping and stiffness characteristics of the servo-drive

system with respect to motor speed had to be determined experimentally to model the drive accurately, but the damping and stiffness characteristics might not be very consistent when using different techniques. Instead of using electromagnetic exciters, Cho *et al.* [79] utilized magnetostrictive patch transducers (MPT), which were mainly used for nondestructive ultrasonic testing [80], to generate torsional impulses through changing the external magnetic field. Two permanent magnets were installed in the MPT to boost the actuation power, and the same transducer was also used as a sensor to measure the torsional response. Although in theory it is possible to obtain rotational FRFs through the exciters and sensors mentioned above (direct measurement), the accuracy, quality, and the coherence of the FRFs are likely to be poor in practice. In other words, the application of the experimental FRFs could be quite limited. They could be used to roughly identify the torsional natural frequencies and the mode shapes but cannot be applied to structural modification, substructure coupling, or model updating where accurate FRFs are required.

Since it is not likely to obtain high-quality and accurate rotational or torsional FRFs directly, indirect measurement methods have to be sought, and which can be broadly classified into three categories: FRF/Modal expansion [81], finite-difference technique, and block attachment. The basic idea of FRF expansion is to use a number of measured FRFs to estimate the FRFs at the unmeasured locations. Ewins [82] demonstrated that theoretically one can derive a point FRF (at location k) through the measurement of another point FRF (at location j) and a cross FRF (between locations k and j), but the process could be restricted in practice due to modal incompleteness (residual problem) and spatial incompleteness. Avitabile and O'Callahan [83] implemented System Equivalent Reduction Expansion Process (SEREP) to expand the measured modal vectors to rotational DoFs and proposed two additional frequency-based approaches to compensate the truncation effect for both translational and rotational DoFs. Drozg *et al.* [84] demonstrated that a response model (full DoF FRF matrix) can be obtained using modal expansion, which is based on at least one full column in the FRF matrix, and Lagrange Multiplier Frequency Based Substructuring (LM FBS) method. Recently, a FRF expansion strategy for nonlinear structures was proposed by Wang *et al.* [85].

The Finite-difference technique, which was first introduced by Sattinger [86], is essentially based on the spatial derivative of translational responses measured at discrete data points to obtain the rotational quantities. According to the locations of the measurements and the excitations, different approximations of the derivative including backward difference, central difference, or forward difference could be made. Duarte and Ewins [87] compared the results estimated from different orders of differentiation approximation and considered the compensation of the residual term when modal parameters were used. It was also pointed out in several papers [88, 89] that the spacing between data points would affect the quality of the results and the positions of antiresonances of rotational FRFs in practice. Gibbons *et al.* [65] showed that the finite-difference technique could be unstable when spacing is too large or too small and thus proposed a procedure that could be used to experimentally obtain an optimal spacing. Schmitz [90] tried to measure the torsional response of a twist drill tool-holder-spindle-machine assembly and applied Receptance Coupling Substructure Analysis (RCSA) [91] to decouple the additional adapter structure and the twist drill; however, the results were not satisfactory due to the complexity of the twist drill model and the coupling between the bending and the torsional responses. Yang *et al.* [92] improved Schmitz's work by modelling the geometry of the cutter in great detail, including distributed damped-elastic contact condition between the tool holder and the cutter, and removing the adapter's mass effect.

For block attachment, the general purpose of attaching a structure is that a moment/torque can be generated by a force acting at a distance away from the location of interest to be measured. Several configurations of attachments were proposed as shown in Fig. 2.7, which could take the forms of a T-shape, an I-shape, an L-shape, or an X-shape. Sanderson and Fredo [75] and Sanderson [76] studied the rigid configurations of the T-shape and the I-shape and considered two types of bias errors (the rotational inertia of the configurations and the rotational velocity) in the measurement in which two shakers were used to produce a moment. The use of a rigid L-shaped structure was studied by Cheng and Qu [93] with a similar approach. They primarily focused on excluding the mass or rotational inertia introduced by the attachment to reflect the rotational receptance. Montalvao *et al.* [94] applied a

receptance coupling technique to estimate rotational receptance without generating a moment, but the results have a limited frequency band and the problem could be ill-conditioned as it is sensitive to changes in data.

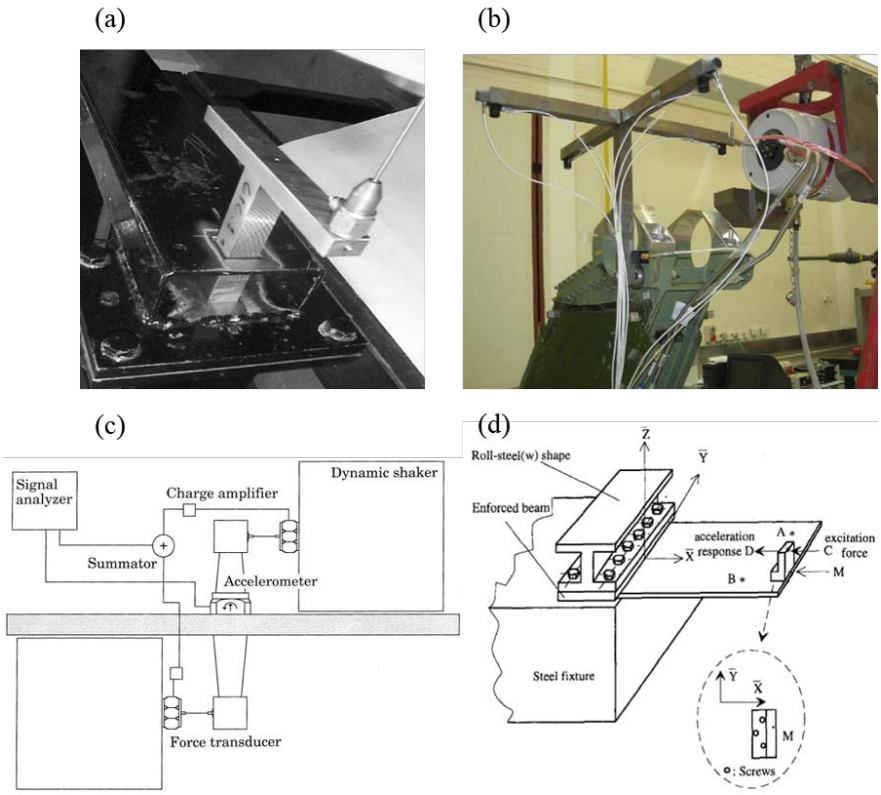

Figure 2. 7. Forms of block attachments for rotational FRF estimations. (a) T-shape [66], (b) X-shape [95], (c) I-shape [76], and (d) L-shape [96].

Mottershead *et al.* [66] considered the elasticity of the attachment when estimating rotational FRFs. They applied a T-block as a modification to the parent structure and proposed a multi-input, multi-output estimator for estimating (two transverse linear and one rotation) in-plane receptances. The estimation made use of the forces and linear displacements measured on the T-block and included mass and the stiffness matrixes of the T-block model, thereby improving the conditioning of the problems. This work was later extended by Mottershead *et al.* [95] to determine a full 6x6 matrix of receptances using an X-block. The work presented by Lv *et al.* [97] might be the first attempt to estimate the torsional receptance of a shafting structure. The estimation process can be broken down into two steps: (1) estimation at the joint of the T-block when the T-block and the shafting structure are assembled, and then (2)

estimation at the connection location of the shafting structure and the T-block. It was shown that the bending natural frequencies of the whole structure would appear in the estimated torsional receptance if noise was present. In the experiment part, the T-block was replaced by a straight beam and only the first step of the estimation was carried out. In general, the techniques, which are based on using a block attachment, often use the information from the assembled structure and from the block attachment. It is worth mentioning that this idea is closely related to Transfer Path Analysis (TPA). A comprehensive review on TPA was presented by Seijs *et al.* [98], which should shed light on the theoretical background of the idea behind using a block attachment and its applications.

2.4. Open problems

Through the literature review, some open problems in this research field can be identified. They can be broadly divided into problems associated with difficulties in theory and those connected to issues about practical implementations. Those open problems are briefly summarized in Table 2.1 below, some of which are further discussed in the following content.

Table 2. 1. Identified open problems in receptance-based structural modification.

Theory	Practical implementation
• Partial eigenstructure assignment. • Modification through additions of complex subsystems. • Optimization problems: search for a global minimum solution, integer programming, etc. • Optimal location for modification • Nonlinear structural modification and nonlinear vibration control.	• Measurement/ estimation of rotational or torsional receptances. • How to obtain sufficiently “accurate” receptances either in simulation or experiment. • Realization of accurate modifications, e.g. stiffness modification.

Lack of experimental implementations

First, as pointed out earlier, most of the studies so far have focused on the theoretical development and validation with numerical models while few investigations have reported on the practical implementations of the methods. In addition to [28] and [40], Zarraga *et al.* [99] demonstrated the successful shift of the natural frequency of a doublet mode of a simplified brake-clutch structure so as to suppress squeal noise due to friction. Mottershead *et al.* [95] studied the modification of a helicopter tail cone in the form of a heavy block mass, using the receptances measured with the aid of an additional X-shaped attachment and its (small) finite element model. Caracciolo *et al.* [100] improved the dynamic behaviour of vibratory linear feeders based on a systematic approach through inverse structural modifications. A laboratory vibratory linear feeder was manufactured according to the optimization of the simplified spring-mass model to verify the design method.

Partial assignment

The concept of assigning part of the dynamic properties while keeping the others unchanged has recently received increasing attention. Partial eigenvalue assignment and partial eigenstructure assignment are the two most common problem of interest. Partial eigenvalue assignment aims to overcome the frequency spill-over, a phenomenon in which unassigned natural frequencies are also shifted after the assignment of a subset of natural frequencies. This phenomenon could result in an unfavourable situation in which an unassigned frequency is relocated to an unwanted value. On the other hand, partial eigenstructure assignment aims at assigning certain eigenpairs while keeping all the other eigenpairs unchanged [101].

The partial assignment problem can be dealt with through passive structural modification (Ouyang and Zhang [102], Belotti *et al.* [103], Gurgoze and Inceoglu [104]), active feedback control (Ghandchi *et al.* [105], Bai *et al.* [106], Datta *et al.* [101]), or an active–passive hybrid approach [107]. Compared with active control

approach, passive approach for partial assignment is reliable and cost-effective, but theoretically more demanding due to the limited effects of the mass and stiffness modification in preventing spill-over [108]. Richiedei and Trevisani [107] proposed a method using both passive and active control to achieve partial eigenstructure assignment. It is reasonable to believe that incorporating both approaches would allow more freedom in such assignment problem. On the other hand, it has been shown that including receptances could improve the computation efficiency and reduce modelling errors. For example, Ram *et al.* [109] presented a hybrid method that combined system matrices and receptances for partial pole assignment. The inevitable time delay between measurements and actuation was also taken into account. Ghandchi Tehrani *et al.* [105] developed a receptance-based method for single- and multiple-input state feedback partial pole assignment. Ram and Mottershead [110] proposed a method that is applicable to both single-input and multiple-input-multiple-output vibration control for partial pole assignment using only measured receptances, but time delay was not considered in this paper. Bai and Wan [111] demonstrated the effectiveness of integrating receptances and system matrices in a partial pole assignment problem through several numerical examples, which required solving only a small linear system and a few undesired eigenpairs. Singh and Brown [112] implemented an active control method based on receptances to achieve partial pole assignment on an aerofoil wing model for flutter suppression. Tehrani and Ouyang [113] presented a partial pole assignment method for asymmetric systems using single-input state feedback. The poles are grouped into assigned poles and unassigned (unchanged) ones, and the control gains were sought by solving the corresponding equations for both assigned and unassigned poles. Ariyatanapol *et al.* [114] also studied the partial pole assignment for asymmetric systems but with time-delay, which potentially can be applied to friction-induced vibration problems or rotating machines in practical conditions.

High-quality indirect torsional/rotational FRF estimation

From the literature review in Section 2.3, it can be noticed that so far only very few methods for indirect torsional measurement have been reported compared with those for indirect rotational (in bending) measurement. Lv *et al.*'s work [97] might be the only study that primarily focuses on torsional receptance measurement. The proposed methods are sensitive to measurement noise and have a limited frequency range, which indicates that there is room for further improvement. Being able to obtain high-quality torsional or rotational FRFs can be beneficial to many engineering applications, for instance, they can be used for torsional structural modification purpose [43], model updating, parameter identification [115], suppression of chatter [116], or the improvement of performance in metalworking machines (drilling machines [117] and milling machines [118]).

Modification through coupling of subsystems

In both reality and theory, the forms of modifications for a structure are often limited to rank-one modifications or single-DoF oscillators. However, often structures need to be connected together. For a dynamic property assignment in such a condition, the original structure is modified by an addition of one or more structures. The additional structures can be more complex than a single mass, a grounded spring, or a single-DoF oscillator. In addition to the aforementioned works [44] and [45], Belotti and Richiedei [119] achieved pole and mode shape assignment through adding auxiliary systems. The problem is treated as an optimization problem and the topology of the auxiliary systems must be predetermined (can be designed arbitrarily). In their example, the original system was modified by a multiple-predetermined spring-mass auxiliary systems, and their values (mass and stiffness) were to be found using Homotopy optimization [120, 121], which is adopted to boost the convergence towards a global minimum in a non-convex optimization problem.

Optimization method

Casting an inverse structural modification problem as an optimization problem has proven to be more efficient and flexible than traditional methods and later given rise to several interesting prospects in this research field. For example, in nearly all of the structural modification literature the value of the modification is assumed to be continuous; however, it might not be appropriate in practical situations in which getting the precise value of weight, stiffness, or requirement is infeasible or expensive. For example, if the calculation shows a precise mass modification of 621g has to be formed by a number of rigid masses weighing 250g each as the only available modifications, how many rigid masses should be added so that the modified structure has the new frequency closer to the desired assignment? Rounding off the optimal values to the nearest available discrete values sometimes could be the solution to the problem, but the problem can get complicated when the number of variables increases. Furthermore, rounding off the solution can possibly violate the design constraints or lead to an outcome that is far away from expectations. A branch in optimization problems called Integer Programming [122], which is able to take integer values for design variables, could be the solution to the aforementioned issue. Ouyang *et al.* [123] proposed an approach that cast the eigenstructure assignment problem as the minimization of a mixed-integer function which included both continuous and discrete design variables. Owing to the convexity of the continuous relaxation, the mixed-integer function was solved by means of a partial enumeration of a reduced set of feasible solutions. Up to now, there have not been many papers addressing this problem under the context of structural dynamic optimization, which can be an open topic for structural modification researchers.

How to efficiently search for a global minimum of a non-convex problem or to boost the chance of getting it in a structural modification context is another problem waiting to be addressed. Although a number of algorithms [124, 125] have been proposed in global optimization, their applications on structural modification are still unknown. This can be a very tricky question as it requires strong engineering and

mathematical background knowledge. One of the possible applications would be the search for the smallest modifications when there are multiple solutions to an assignment problem.

3. Finite Element modelling for rotordynamic analysis

In this chapter, the fundamental knowledge for conducting rotordynamic analysis using Finite Element Method (FEM) is provided. Some important dynamic characteristics for rotating machines, which make them different from static structures, are discussed. Depending on different FE models in use, the dynamic characteristics that can be observed can be different owing to the modelling assumptions made in the models. The modelling of a few common components in a rotating machine is also introduced, which is later followed by a case study of a geared rotor-bearing system. The numerical model is constructed using MATLAB. The purpose of this chapter is not to provide an in-depth or detailed study on FE modelling techniques but to give a compact guideline for analysing rotor dynamic problems using FEA. Two comprehensive books, “Dynamics of Rotating Machines” by Friswell *et al.* [126] and “Dynamics of Rotating Systems” by Genta [127], are the major sources of references of this chapter.

3.1. FE models

A number of simplified models have been proposed in the past for rotordynamic analysis such as a single-DoF model (spring-mass), the Rankine model (2 DoF), and Jeffcott Rotor. However, they are only able to represent simple rotors and become impractical in obtaining accurate information of complex rotating machines. Because of that, the most prevalent models for rotordynamic analysis nowadays are based on the FEM in which the rotor is usually modelled as beam elements such as the alleged 1-dimensional (1-D) model [128] and the $1\frac{1}{2}$-dimensional ($1\frac{1}{2}$–D) model. There is also a 2-dimensional model approach using 2-D axisymmetric harmonic elements (see [129] and Nastran Rotordynamics User’s Guide) and a 3-dimensional (3-D) model approach that is based on the 3-D models generated by CAD.

The 3-D model approach is convenient as the model can be automatically meshed by commercial CAE software and is able to produce more accurate results when the geometries of the rotating system cannot be well modelled using beam elements or the housings and foundations are flexible and coupled to the rotor. On the downside, the model may easily comprise tens of thousands of DoFs, making it computationally expensive. Reduction techniques are thus often required to reduce the order and the computational cost; additionally, this approach imposes certain difficulties as the axial symmetricity of the rotor is not clearly defined by the mesh. Depending on the symmetricity in the rotor and the stator models, an appropriate reference frame can be selected so as to obtain time-independent equations of motion. The preferred reference frame for different conditions is summarized in Table 3.1 where isotropic stator means that the elastic and damping forces of the stator do not change with the angle of rotation in the plane perpendicular to the rotation axis. It is important to note that when both the stator and the rotor are not axially symmetric, no reference frame in which the equations of motion has constant coefficients exists. Such a system is in general governed by differential equations with periodic coefficients [127]. It is nontrivial to solve such equations and no closed-form solution can be obtained. Because of the difficulties, in the Rotordynamic Analysis Guide by ANSYS it clearly states that all rotating parts must be axisymmetric.

Apart from the cases of axially symmetric and non-axially symmetric rotors, there is a case of cyclic symmetric rotor, for example, wind turbines and bladed turbine disks. While traditional vibration analysis focuses on cyclic symmetric rotors with no bearings or housings, recent trend on the rotating machine design has motivated the study of the entire rotor-bearing-housing system [130]; for instance, strongly coupled vibration between the blades and the tower has been reported and plays an important role in the dynamics of the wind turbine. The analysis for a rotating cyclic symmetric rotor is very different from a static one. Although such a structure can be described in a rotating reference frame, it is still desirable to obtain the response in a stationary reference frame (ground-based response) for two reasons according to [131] by Shen and Kim. First, in practical applications sensors often are not directly mounted on the rotating parts and thus ground-based responses are measured. Second, the dynamic

characteristics shown in ground-based responses are commonly shared by any rotors with arbitrary geometry. Kim and Shen [132] proposed a procedure to obtain the ground-based response of a rotating cyclic symmetric rotor that considered gyroscopic and centrifugal softening effects. It was also demonstrated that the asymmetry in a rotor can cause secondary resonances in addition to the forward and backward whirls as a result of higher harmonics from the mode shapes, and these secondary resonances can only be observed in a stationary reference frame.

Table 3. 1. Analysis reference frame.

Preferred reference frame		Axially symmetric rotor?	
		Yes	No
Isotropic stator?	Yes	Stationary/ Rotating	Rotating
	No	Stationary	None

Although 3-D modelling is the trend for rotordynamic analysis for sophisticated rotating machines, there hasn't been a suitable solution to inherently take the dynamic effects (on element level) associated with the rotating parts into account, such as rotating damping, gyroscopic effect, centrifugal stiffening, and centrifugal softening [127]. For a general-purpose rotating machine, 1-D model could be sufficient to capture the overall dynamics especially when low-frequency modes are of primary concern. In this chapter, the classical 1-D model is presented to provide a compact guideline for rotordynamic analysis.

3.1.1. Coordinate system

The axial symmetricity of a rotor is automatically imposed when beam elements are used to model the rotor in 1-D and $1\frac{1}{2}$–D models; therefore, a stationary reference frame O_{xyz}, which is shown in Fig. 3.1 (a), is used for this study. All the axes and the directions of rotation follow the right-hand rule. The beam element described here has two nodes per element and each node has six DoFs. The nodal displacements for the

beam element are shown in Fig. 3.1 (b), which can be arranged into a displacement vector **q** given by

$$\mathbf{q} = [u_1, v_1, \phi_1, \theta_1, w_1, \psi_1, u_2, v_2, \phi_2, \theta_2, w_2, \psi_2]^{\mathrm{T}} \tag{3.1}$$

The defined displacements reflect the fact that a rotor can vibrate mainly in the directions of three perpendicular axes and around them. Axial vibration takes place in line with the axis of the rotor, and the sources for axial vibration can be coupling/shaft misalignments, helical gears, resonance of some parts in the axial direction, and coupling dynamics. Torsional vibration can often be seen in many power transmission systems due to the natural behaviour of gears, motors, generators, flywheels, couplings, etc. Any discontinuous or time-varying power generation, slightly unstable transmission, or even friction (stick-slip) can excite torsional vibration to some degree. Lateral vibration, also called bending vibration or flexural vibration, is the most common type of vibration among machines and has been extensively studied by researchers and engineers. It is usually caused by mass unbalance, external lateral forces (vibration from other machines, interaction between structures, etc.), and the resonances of the rotor itself. Excessive bending vibration could result in bearing wear, fatigue, low power efficiency, poor user experience, or even failure.

In general, the torsional displacements (ψ_1 and ψ_2) and the axial displacements (w_1 and w_2) are assumed to be uncoupled with each other as well as the other DoFs. In other words, their effects could be considered separately for the sake of simplicity, but in some situations they may produce a significant effect on the lateral behaviour. For instance, in a geared rotor-bearing system, the torsional motion is coupled with bending due to the gear mesh profile and its working mechanism, and the axial force can result in a stiffening or a softening effect when the beam is under tensile force or compressive force.

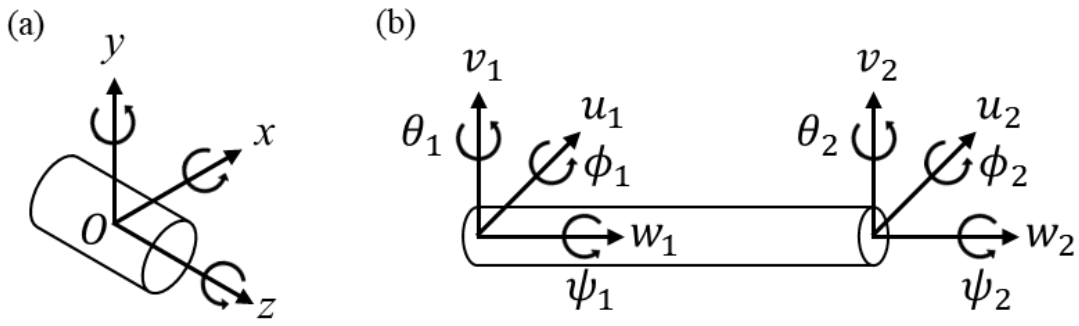

Figure 3. 1. Coordinate systems used for rotors. (a) Right-handed stationary reference frame. (b) Local nodal displacements.

3.1.2. Equations of motion

In a 1-D model, the general form of equations of motion for a model with rotating components in a stationary reference frame is given by

$$\mathbf{M}\ddot{\mathbf{q}}(t) + (\mathbf{C}_{\mathrm{s}} + \mathbf{C}_{\mathrm{cir}} + \Omega\mathbf{G})\dot{\mathbf{q}}(t) + (\mathbf{K} + \Omega\mathbf{K}_{\mathrm{cir}})\mathbf{q}(t) = \mathbf{f}(t) \qquad (3.2)$$

where $\mathbf{q}(t)$ and $\mathbf{f}(t)$ are the vector of DoFs and that of external forces, and Ω is the rotational speed. For a better presentation of the matrix property and the meaning of each term in Eq. (3.2), consult Table 3.2 below. What make Eq. (3.2) different from the equations of motion of a static structure are the speed-dependent terms such as gyroscopic and circulatory matrices, which are linked with the gyroscopic couples and the internal damping of the rotor, respectively. Rotor internal damping is a complicated phenomenon and can come from many sources, for example, material damping, friction in joints and couplings (considered to be the main source), and shrink fits. It is known that rotor internal damping can cause self-induced instability when operating in supercritical speed, i.e. speed above the first critical speed. It was not well considered in past practical situations until recently as common rotating machines were often operating below their first critical speeds and such instability can be supressed by adding external dampers, redesigning rotor fits, or modifying bearings. As machine's performance/weight efficiency is increasing, rotor internal damping has become a more noticeable problem. As a result, it can be argued that the 1-D model

might not be adequate to model rotor internal damping or carry out instability analysis [133].

Table 3. 2. Properties of matrices

Notation	Name	Matrix property	Meaning
$\mathbf{M}$	Mass matrix	symmetric	Discretized or lumped mass of the model
$\mathbf{C}_s$	Damping matrix	symmetric	Damping of the stators
$\mathbf{K}$	Stiffness matrix	symmetric	Discretized or lumped stiffness of the model
$\mathbf{G}$	Gyroscopic matrix	skew-symmetric	Gyroscopic couples, which arise because of the conservation of angular momentum
$\mathbf{C}_{\mathrm{cir}}$	Damping matrix	Symmetric (if proportional damped)	Internal damping of the rotating parts
$\mathbf{K}_{\mathrm{cir}}$	Circulatory matrix	skew-symmetric (if proportional damped)	Internal damping of the rotating parts

If internal damping is neglected, gyroscopic effect would be the only factor to account for the influence of rotation. When Ω approaches zero, the analysis is no different from that of a static structure. Gyroscopic effect represents the relationship between the precession velocity (an angular velocity) and the change in the angular moment (so-called gyroscopic moment). For instance, assuming that a rotor is spinning and having a large angular moment about the *z*-axis (see Fig. 3.1), if a moment about the *x*-axis is applied, the rotor has precession velocity about the *y*-axis; by the same token, if the rotor is forced to precess about the *y*-axis, gyroscopic moment about the *x*-axis must exist to maintain equilibrium. This relationship can be expressed by the formulas

$$M_x = I_p \Omega \omega_y \tag{3.3}$$

and

$$M_y = -I_p \Omega \omega_x \tag{3.4}$$

where I_p is the polar moment of inertia of the rotor. M and ω are the gyroscopic moment and the precession velocity.

Although a 1-D model is adopted in this study, it is still worth briefly introducing another beam-element-based model, the so-called $1\frac{1}{2}$–D model. In a 1-D model, the discs, blades, or bladed disc, which are common structures protruding in the radial direction of a shaft, are considered rigid bodies whilst the $1\frac{1}{2}$–D model aims to overcome this limitation and takes the flexibility and the associated dynamic influences of them into consideration. The effects of the protruding parts to the shaft can be dominant, particularly for structures with relatively long and thin protruding parts such as wind turbines and propellers. As suggested by Genta and Silvagni [134], the basic equations of motion of an undamped $1\frac{1}{2}$–D model in a stationary reference frame can be given by

$$\mathbf{M}\ddot{\mathbf{q}}(t) + \Omega\mathbf{G}\dot{\mathbf{q}}(t) + (\mathbf{K} + \Omega^2(\mathbf{K}_\mathrm{s} - \mathbf{M}_\mathrm{n}))\mathbf{q}(t) = \mathbf{f}(t) \qquad (3.5)$$

where $\mathbf{G}$ is the gyroscopic matrix and $\mathbf{K}_\mathrm{s}$ is the centrifugal stiffening matrix (also often called geometric matrix), which would appear once the flexibility of discs or blades is considered. The other geometric terms, such as those caused by thermal stressing and are independent from Ω, could be implicitly included in $\mathbf{K}$ [127]. $\mathbf{K}_\mathrm{s}$ has a stiffening effect owing to the tensile stress caused by rotation, thus increasing the resonant frequencies as the rotation speed increases; on the other hand, $\mathbf{M}_\mathrm{n}$, the centrifugal softening matrix, tends to counteract the stiffening effect as a result of the centrifugal force acting on the structure. Genta and Silvagni [134] also stated that the centrifugal softening effect is not as strong as the stiffening effect; as a result, the term $(\mathbf{K}_\mathrm{s} - \mathbf{M}_\mathrm{n})$ would produce a net stiffening effect.

The element matrices of rotating thin discs and those of a rotating array of blades were developed in [135] and [136] by Genta and Tonoli, respectively. The discs and the array of blades were modelled as annular elements in which the displacements along the angle were approximated by a truncated Fourier series. The transition elements were also presented to ensure the compatibility of the displacement fields at the shaft-disc, shaft-disc-array of blades, or the disc-array of blades interfaces. A generalization of the elements proposed in [135] and [136] was presented by Genta *et*

al. [137], flexible discs and blades were modelled as annular elements with the displacement field approximated by trigonometrical expansion along the tangential direction and by polynomial shape functions along the radial direction. It should be highlighted that the array of blades were assumed to be axisymmetric; therefore, the number of blades must be equal or greater than 3 in order for the array to be dynamically equivalent to an axial-symmetric structure [136].

3.2. Modelling of common components

The finite element modelling of a few components in a rotating machine, including shaft, bearing, disc and gear, is summarized in this section. The system comprised of those components is often referred to as a geared rotor-bearing system, which has a wide variety of practical applications.

Shaft

In the early studies of rotordynamics, the rotor was modelled as a massless shaft or a rigid shaft. As such a simplistic model is inadequate for modern rotating systems, FE beam element has taken over for general rotordynamic analysis. Since 1-D modelling approach is adopted in this study, the shaft or the rotor is therefore modelled as Timoshenko beam elements to include shear and rotary inertia effects. The derivation of a Timoshenko beam element can be found in many textbooks and thus is not repeated here. In this study, the so-called 3D Timoshenko beam element presented in Wu's book [138] is used. The 3D Timoshenko element consists of two sets of in-plane DoFs which are orthogonal, for instance, the *x*-*z* plane and *y*-*z* plane in Fig. 3.1. The DoFs in the torsional direction can be easily added to the mass and stiffness matrices when torsion is independent of bending, thus leading to 6 DoFs in total at one node.

Bearing

Rotating machines require a set of bearings to support them during rotation. There are many different types of bearings and the most prevalent types in a rotating system include rolling-element bearing, plain bearing, fluid bearing, and magnetic bearing. These bearings, which have distinctive working principals, are designed to cover different operation requirements and have a great effect on the dynamic behaviour of the rotor and the associated system.

As briefly introduced in Section 1.1, the magnetic bearing uses magnetic field to lift the rotor and has been intensively studied in recent years since there is nearly zero friction between the rotor and the stator; thus, the service life can be widely extended and the energy loss can be greatly reduced. It is increasingly used in flywheel energy storage systems, compressors, pumps, and electric motors. Fluid bearings, such as hydrodynamic journal bearings, hydrostatic journal bearings, and air bearings, consist of a thin layer of pressurized liquid or gas to support the load. Those with fluid lubrication are generally called journal bearing and widely used in large rotating machines for their rather high load-capacity. Plain bearings are, in terms of the structure, the simplest type of bearings that consists no rolling elements or external lubricant supply. One common example is self-lubricating bearing, which is essentially a bushing or a sleeve in terms of its geometry. Traditional self-lubricating bearings are sintered metal components with high porosity in which the void spaces are impregnated with lubricant oil. The oil is release when pressure or heat is applied. Nowadays, such a bearing made from composite material or high-performance plastic is available, which can provide high load-capacity, wear-resistant, chemical resistance, and require low maintenance effort.

The aforementioned bearings all have their niche applications, but for general-purpose applications rolling-element bearing is still the most widely used bearing. Because of that, the modelling of a rolling-element bearing is of great importance and has been studied by many researchers for decades. Although such a bearing only consists of four key components (inner race, outer race, balls or rollers, and cage), the

kinematic and the modelling are not as clear as it may seem, due to several phenomena such as the nonlinear speed-dependent displacement-load relationship, the complex tribo-mechanical behaviour, centrifugal loads, gyroscopic moment, deformation of rings, etc. Eventually, in a rotating machine, the rolling bearing model has to be coupled with the rotor model to reflect the dynamic behaviour of the whole system. For a 1-D model, a bearing is conventionally represented by a grounded spring and a grounded damper. It should be noted that, in essence, the spring and the damper represent the overall characteristic of the bearing and the housing combined, not the bearing alone. This model is easily integrated and thus is adopted in this study. If the resulting effect of the bearing is seen as a restoring force and there is no coupling between transverse and rotational motion, the model can be expressed explicitly as

$$\{\mathbf{f}_\mathrm{b}\} = -\begin{bmatrix} k_{uu} & k_{uv} & 0 & 0 \\ k_{vu} & k_{vv} & 0 & 0 \\ 0 & 0 & k_{\phi\phi} & k_{\phi\theta} \\ 0 & 0 & k_{\theta\phi} & k_{\theta\theta} \end{bmatrix} \begin{Bmatrix} u \\ v \\ \phi \\ \theta \end{Bmatrix} - \begin{bmatrix} c_{uu} & c_{uv} & 0 & 0 \\ c_{vu} & c_{vv} & 0 & 0 \\ 0 & 0 & c_{\phi\phi} & c_{\phi\theta} \\ 0 & 0 & c_{\theta\phi} & c_{\theta\theta} \end{bmatrix} \begin{Bmatrix} \dot{u} \\ \dot{v} \\ \dot{\phi} \\ \dot{\theta} \end{Bmatrix} \tag{3.6}$$

where the force in the axial direction is neglected. Apparently, it needs to be assumed that the bearing-housing component is linear for Eq. (3.6) to be valid. A quick estimation for the bearing radial stiffness was presented by Gargiulo [139]. Lim and Singh [140] gave an estimation of the bearing stiffness for a “full” 5x5 stiffness matrix covering DoFs of $u, v, \phi, \theta,$ and w. On the other hand, the damping coefficients are often neglected due to its complexity. It is worth mentioning that there are a few other models besides Eq. (3.6) such as quasi-static bearing model and dynamic bearing model, which can be found in the comprehensive review done by Cao *et al.* [141].

Disc

Simple circular structures such as flywheels, shaft collars, shaft sleeves, wheels, and lock nuts could be modelled as disc elements. Here, it is assumed that the discs are rigid, in other words, they mainly contribute kinetic energy to the vibrating system instead of strain energy, and rotate about the centre if they are axisymmetric. The total kinetic energy includes transitional kinetic energy and rotational kinetic energy; in

general, the rotation kinetic energy is easier to analyse in the frame that rotates with the disc while the translational kinetic energy can be obtained in a stationary reference frame.

To describe the orientation of the frame that is fixed with the disc with respect to a stationary reference frame, three Euler angles are introduced. Euler angles, in general, represent any manner describing the rotation of a rigid body in a three dimensional space through three consecutive transformations of coordinates about a specific set of axes [142]. Thus, the total kinetic energy can be expressed by

$$\mathrm{T} = \frac{1}{2}m(\dot{u}^2 + \dot{v}^2) + \frac{1}{2}I_d\left({\omega_{x_3}}^2 + {\omega_{y_3}}^2\right) + \frac{1}{2}I_p{\omega_{z_3}}^2 \tag{3.7}$$

where m is the mass of the disc; I_d and I_p are the diametral moment of inertia and the polar moment of inertia of the disc; ω_{x_3}, ω_{y_3}, and ω_{z_3} are the instantaneous angular velocities about the three axes of the frame that rotates with the disc (disc-referenced frame), i.e. a frame that is transformed three times from the stationary frame. The number in the subscript denotes the number of transformations made. If the transformations are applied in the following order: θ about the x-axis of the stationary frame, ϕ about the new y-axis (y_1), ψ about the new z-axis (z_2), the individual transformation matrices are

$$\begin{Bmatrix} x_1 \\ y_1 \\ z_1 \end{Bmatrix} = \begin{bmatrix} 1 & 0 & 0 \\ 0 & \cos\theta & \sin\theta \\ 0 & -\sin\theta & \cos\theta \end{bmatrix} \begin{Bmatrix} x \\ y \\ z \end{Bmatrix}$$

$$\begin{Bmatrix} x_2 \\ y_2 \\ z_2 \end{Bmatrix} = \begin{bmatrix} \cos\phi & 0 & -\sin\phi \\ 0 & 1 & 0 \\ \sin\phi & 0 & \cos\phi \end{bmatrix} \begin{Bmatrix} x_1 \\ y_1 \\ z_1 \end{Bmatrix} \tag{3.8}$$

$$\begin{Bmatrix} x_3 \\ x_3 \\ z_3 \end{Bmatrix} = \begin{bmatrix} \cos\psi & \sin\psi & 0 \\ -\sin\psi & \cos\psi & 0 \\ 0 & 0 & 1 \end{bmatrix} \begin{Bmatrix} x_2 \\ y_2 \\ z_2 \end{Bmatrix}$$

These rotation matrices are orthogonal matrices, so the inverse of the matrix is equal to its transpose. It is true that the time derivative of the Euler angles is directly equal to the rotation rate of the disc-referenced frame only if the Euler angles are extremely small. Thus, it is important to determine the effects on the rotation rate when

small changes are made in each Euler angle. The corresponding change of rotation rate can be expressed as $\vec{\boldsymbol{\omega}} = \dot{\psi}\vec{\mathbf{z}_3} + \dot{\phi}\vec{\mathbf{y}_2} + \dot{\theta}\vec{\mathbf{x}_1}$, which can be rewritten in matrix form as

$$\begin{aligned}\vec{\boldsymbol{\omega}} = &\begin{Bmatrix}0\\0\\\dot{\psi}\end{Bmatrix} + \begin{bmatrix}\cos\psi & \sin\psi & 0\\ -\sin\psi & \cos\psi & 0\\ 0 & 0 & 1\end{bmatrix}\begin{Bmatrix}0\\\dot{\phi}\\0\end{Bmatrix}\\ &+ \begin{bmatrix}\cos\psi & \sin\psi & 0\\ -\sin\psi & \cos\psi & 0\\ 0 & 0 & 1\end{bmatrix}\begin{bmatrix}\cos\phi & 0 & -\sin\phi\\ 0 & 1 & 0\\ \sin\phi & 0 & \cos\phi\end{bmatrix}\begin{Bmatrix}\dot{\theta}\\0\\0\end{Bmatrix}\end{aligned} \tag{3.9}$$

where $\boldsymbol{\omega}$ can be seen as the instantaneous angular velocity about the disc-referenced frame. Multiplying out Eq. (3.9) gives

$$\vec{\boldsymbol{\omega}} = \begin{Bmatrix}\omega_{x_3}\\\omega_{y_3}\\\omega_{z_3}\end{Bmatrix} = \begin{Bmatrix}\dot{\theta}\cos\psi\cos\phi + \dot{\phi}\sin\psi\\ -\dot{\theta}\sin\psi\cos\phi + \dot{\phi}\cos\psi\\ \dot{\theta}\sin\phi + \dot{\psi}\end{Bmatrix} \tag{3.10}$$

Substituting Eq. (3.10) to Eq. (3.7) results in

$$\begin{aligned}\mathrm{T} = &\frac{1}{2}m(\dot{u}^2 + \dot{v}^2) + \frac{1}{2}I_d\left(\dot{\phi}^2 + \dot{\theta}^2\cos^2\phi\right)\\ &+ \frac{1}{2}I_p\left(\dot{\psi}^2 + 2\dot{\psi}\dot{\theta}\sin\phi + \dot{\theta}^2\sin^2\phi\right)\end{aligned} \tag{3.11}$$

Assuming that the Euler angles θ and ϕ are small and neglecting higher-order terms leads to

$$\mathrm{T} = \frac{1}{2}m(\dot{u}^2 + \dot{v}^2) + \frac{1}{2}I_d\left(\dot{\phi}^2 + \dot{\theta}^2\right) + \frac{1}{2}I_p\left(\dot{\psi}^2 + 2\dot{\psi}\dot{\theta}\phi\right) \tag{3.12}$$

Since the total kinetic energy is obtained, the element matrices can be easily found by applying Lagrange's equations. If the local coordinates are arranged in a vector $[u, v, \theta, \phi, \psi]^{\mathrm{T}}$, the resulting equations are

$$\begin{bmatrix}m & 0 & 0 & 0 & 0\\ 0 & m & 0 & 0 & 0\\ 0 & 0 & I_d & 0 & 0\\ 0 & 0 & 0 & I_d & 0\\ 0 & 0 & 0 & 0 & I_p\end{bmatrix}\begin{Bmatrix}\ddot{u}\\\ddot{v}\\\ddot{\theta}\\\ddot{\phi}\\\ddot{\psi}\end{Bmatrix} + \dot{\psi}\begin{bmatrix}0 & 0 & 0 & 0 & 0\\ 0 & 0 & 0 & 0 & 0\\ 0 & 0 & 0 & I_p & 0\\ 0 & 0 & -I_p & 0 & 0\\ 0 & 0 & 0 & 0 & 0\end{bmatrix}\begin{Bmatrix}\dot{u}\\\dot{v}\\\dot{\theta}\\\dot{\phi}\\\dot{\psi}\end{Bmatrix} \tag{3.13}$$

which are the mass matrix and the gyroscopic matrix of the disc, and $\dot{\psi}$ is essentially the rotational speed (Ω) of the disc. It should be noted that the the angular velocities made about each Euler angle that are used in the derivation above do not explicitly agree with the coordinate system defined in Section 3.1.1; however, under the small angle assumption, the Euler angles could be assumed to coincide with the axes in the stationary referenced frame, thus making Eq. (3.13) compatible with the coordinate adopted.

Gear

Gears are widely used in many mechanical systems. When used in a rotor system, gears are prone to coupling the torsional and bending DoFs. This coupled dynamic characteristics lead to critical speeds and natural modes that can be much different from those of the original uncoupled model. Traditionally, there are two main approaches to study the dynamic behaviour, which are the finite element method and transfer matrix method. For the finite element method, a model of a gear pair is considered and shown in Fig. 3.2. The following procedure is based on a work by Rao *et al.* [143].

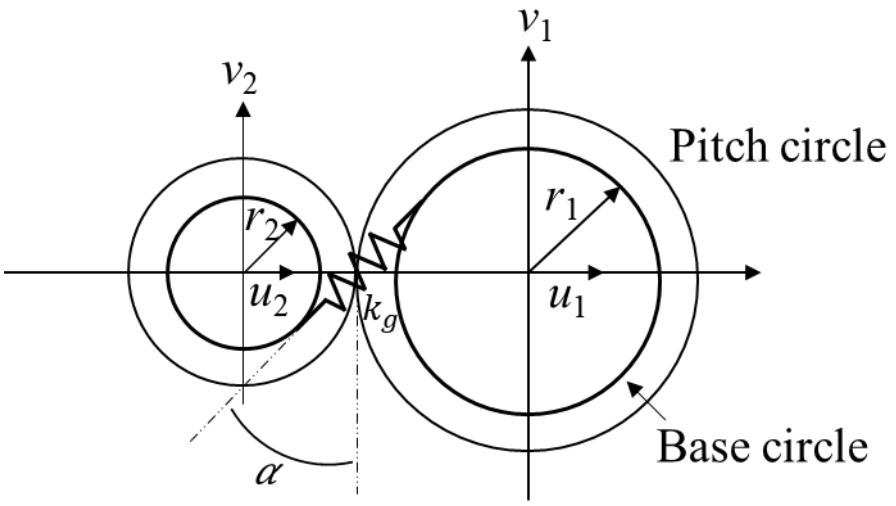

Figure 3. 2. Arrangement of the gear model

Based on the definitions of the gear geometry and the equivalent gear stiffness along the pressure line in Fig. 3.2, the force at the gear mesh produced by the relative displacement between the two gears can be expressed as

$$\begin{aligned} \mathrm{F_g} &= k_\mathrm{g}[(u_1 - u_2)\sin\alpha + (v_1 - v_2)\cos\alpha - (r_1\psi_1 + r_2\psi_2)] \\ &= k_\mathrm{g}\mathbf{n_g}^\mathrm{T}\mathbf{q_g} \end{aligned} \tag{3.14}$$

where $\mathbf{n_g}^\mathrm{T}\mathbf{q_g}$ represents the relative displacement and they are

$$\mathbf{n_g} = [\sin\alpha, \cos\alpha, 0, 0, -r_1, -\sin\alpha, -\cos\alpha, 0, 0, -r_2]^\mathrm{T} \tag{3.15}$$

and

$$\mathbf{q_g} = [u_1, v_1, \phi_1, \theta_1, \psi_1, u_2, v_2, \phi_2, \theta_2, \psi_2]^\mathrm{T} \tag{3.16}$$

Since this gear model only contributes strain energy to the system, the strain energy should be first formulated in order to obtain the corresponding stiffness matrix, which is

$$\mathrm{U_g} = \frac{1}{2}k_\mathrm{g}\left(\mathbf{n_g}^\mathrm{T}\mathbf{q_g}\right)^\mathrm{T}\left(\mathbf{n_g}^\mathrm{T}\mathbf{q_g}\right) = \frac{1}{2}k_\mathrm{g}\mathbf{q_g}^\mathrm{T}\mathbf{K_g}\mathbf{q_g} \tag{3.17}$$

Thus, the stiffness matrix can be represented as

$$\begin{aligned} \mathbf{K_g} &= k_\mathrm{g}\mathbf{n_g}\mathbf{n_g}^\mathrm{T} \\ &= k_\mathrm{g}\begin{bmatrix} \mathrm{S}^2 & \mathrm{SC} & 0 & 0 & -\mathrm{S}r_1 & -\mathrm{S}^2 & -\mathrm{SC} & 0 & 0 & -\mathrm{S}r_2 \\ SC & \mathrm{C}^2 & 0 & 0 & -\mathrm{C}r_1 & -\mathrm{SC} & -\mathrm{C}^2 & 0 & 0 & -\mathrm{C}r_2 \\ 0 & 0 & 0 & 0 & 0 & 0 & 0 & 0 & 0 & 0 \\ 0 & 0 & 0 & 0 & 0 & 0 & 0 & 0 & 0 & 0 \\ -\mathrm{S}r_1 & -\mathrm{C}r_1 & 0 & 0 & {r_1}^2 & \mathrm{S}r_1 & \mathrm{C}r_1 & 0 & 0 & r_1r_2 \\ -\mathrm{S}^2 & -\mathrm{SC} & 0 & 0 & \mathrm{S}r_1 & \mathrm{S}^2 & \mathrm{SC} & 0 & 0 & \mathrm{S}r_2 \\ -\mathrm{SC} & -\mathrm{C}^2 & 0 & 0 & \mathrm{C}r_1 & \mathrm{SC} & \mathrm{C}^2 & 0 & 0 & \mathrm{C}r_2 \\ 0 & 0 & 0 & 0 & 0 & 0 & 0 & 0 & 0 & 0 \\ 0 & 0 & 0 & 0 & 0 & 0 & 0 & 0 & 0 & 0 \\ -\mathrm{S}r_2 & -\mathrm{C}r_2 & 0 & 0 & r_1r_2 & \mathrm{S}r_2 & \mathrm{C}r_2 & 0 & 0 & {r_2}^2 \end{bmatrix} \end{aligned} \tag{3.18}$$

where $\mathrm{S} = \sin\alpha$ and $\mathrm{C} = \cos\alpha$. α is the gear's contact angle shown in Fig. 3.2.

3.3. Eigenvalue problem

The equation of motion describing the free vibration of a rotating system can be obtained by letting $\mathbf{f}(t) = 0$. Finding the natural frequencies or the mode shapes of the system is equivalent to finding the eigensolutions of such an equation:

$$\mathbf{M}\ddot{\mathbf{q}}(t) + (\mathbf{C}_{\mathrm{s}} + \mathbf{C}_{\mathrm{cir}} + \Omega\mathbf{G})\dot{\mathbf{q}}(t) + (\mathbf{K} + \Omega\mathbf{K}_{\mathrm{cir}})\mathbf{q}(t) = 0 \qquad (3.19)$$

As no assumption has been made on the form of the damping and the presence of the gyroscopic matrix, Eq. (3.19) may not be able to be decoupled into *n* second-order uncoupled equations. Therefore, the classical approach to solve Eq. (3.19) in a general context is to transform it into a first-order state-space using a new coordinate vector $\mathbf{z}(t) = \begin{Bmatrix}\mathbf{q}(t)\\ \dot{\mathbf{q}}(t)\end{Bmatrix}$. Eq. (3.19) can then be rewritten as

$$\begin{bmatrix}\mathbf{I} & \mathbf{0}\\ \mathbf{0} & \mathbf{M}\end{bmatrix}\dot{\mathbf{z}}(t) + \begin{bmatrix}\mathbf{0} & -\mathbf{I}\\ (\mathbf{K} + \Omega\mathbf{K}_{\mathrm{cir}}) & (\mathbf{C}_{\mathrm{s}} + \mathbf{C}_{\mathrm{cir}} + \Omega\mathbf{G})\end{bmatrix}\mathbf{z}(t) = 0 \qquad (3.20)$$

One shall assume $\mathbf{M} > 0$; thus, Eq. (3.2) can be expressed in the form of

$$\dot{\mathbf{z}}(t) + \mathbf{A}\mathbf{z}(t) = 0 \qquad (3.21)$$

where

$$\mathbf{A} = \begin{bmatrix}\mathbf{0} & -\mathbf{I}\\ \mathbf{M}^{-1}(\mathbf{K} + \Omega\mathbf{K}_{\mathrm{cir}}) & \mathbf{M}^{-1}(\mathbf{C}_{\mathrm{s}} + \mathbf{C}_{\mathrm{cir}} + \Omega\mathbf{G})\end{bmatrix} \qquad (3.22)$$

is a $2n \times 2n$ real non-symmetric matrix. By assuming that a solution has the form of $\mathbf{z}(t) = \mathbf{z}\mathrm{e}^{st}$, Eq. (3.21) becomes

$$-\mathbf{A}\mathbf{z} = s\mathbf{z} \qquad (3.23)$$

which is now in a form of a standard eigenvalue problem and has $2n$ eigenvalues and $2n$ right/left eigenvectors. The QZ algorithm, which is also called the generalized Schur decomposition, can be implemented to calculate all the eigenpairs [144].

Since **A** is real, the eigenvalues would occur in complex conjugate pairs. The response of the system, which is real, can be obtained by the sum of the solutions $\mathbf{z}(t) = \sum_{r=1}^{2n} \alpha_r \mathbf{z}_r e^{s_r t}$ in which α_r are complex constants depending on the initial

conditions and $r = 1,2,3,\ldots,2n$; thus, the eigenvectors must also occur in complex conjugate pairs. Each $\mathbf{z}_r$ now contains a vector of displacements and a vector of velocities, both of size $n \times 1$. From the point of view of linear algebra, any two right eigenvectors of square matrix $\mathbf{A}$ are linearly independent and right eigenvectors are biorthogonal to left eigenvectors if the corresponding eigenvalues are distinct.

It is worthwhile to mention some characteristics of the complex eigenvectors since they can no longer be interpreted as real eigenvectors whose elements of a mode are totally in-phase or out-of-phase (for undamped or proportionally damped systems). For complex eigenvectors, in other words, the coordinates in a system do not reach their maximum amplitudes at the same time due to the different phase angles introduced in the imaginary parts of the eigenvectors. The mode shape now appears to be a traveling wave, and the locations of nodes are not fixed. A useful method to visualize the response of a complex mode shape is to draw an Argand diagram which represents the magnitudes, phases, and associated oscillations in a complex plane.

As a matter of fact, damping increases the complexity in a system's eigensolutions and is difficult to model or be quantified in practical situations. The solution of an undamped system is a fair approximation to that of the damped system as long as the damping effect is small. If the damping terms in Eq. (3.19) are neglected, Eq. (3.19) results in a conservative gyroscopic system which can be represented as

$$\mathbf{M}\ddot{\mathbf{q}}(t) + \Omega\mathbf{G}\dot{\mathbf{q}}(t) + \mathbf{K}\mathbf{q}(t) = 0 \tag{3.24}$$

It can be seen that converting to the state-space form, e.g. Eq. (3.20), loses many matrices' advantageous properties such as symmetry and sparsity, which may lead to higher memory storage and a slight increase in computational time. The following paragraphs describe a method proposed by Meirovitch [145] to solve the undamped gyroscopic equation utilizing the good properties of the matrices. Following the state-space approach, the linearization of Eq. (3.24) can be expressed as

$$\begin{bmatrix} \mathbf{K} & \mathbf{0} \\ \mathbf{0} & \mathbf{M} \end{bmatrix} \dot{\mathbf{z}}(t) + \begin{bmatrix} \mathbf{0} & \mathbf{K} \\ -\mathbf{K} & \Omega\mathbf{G} \end{bmatrix} \mathbf{z}(t) = 0 \text{ with } \mathbf{z}(t) = \begin{Bmatrix} \mathbf{q}(t) \\ \dot{\mathbf{q}}(t) \end{Bmatrix} \tag{3.25}$$

It should be noted that a linearization is not unique, and the linearization, which maintains the most structural properties of the matrices, should be chosen. For instance, if both **M** and **K** in Eq. (3.25) are positive definite, the two $2n \times 2n$ matrices are real non-singular matrices, and one is symmetric and the other is skew-symmetric. Assuming a solution is in the form of $\mathbf{z}(t) = \mathbf{z}\mathrm{e}^{st}$, one can obtain the following eigenvalue problem

$$(s\mathbf{A} + \mathbf{B})\mathbf{z} = \mathbf{0} \tag{3.26}$$

where

$$\mathbf{A} = \begin{bmatrix} \mathbf{K} & \mathbf{0} \\ \mathbf{0} & \mathbf{M} \end{bmatrix} \text{ and } \mathbf{B} = \begin{bmatrix} \mathbf{0} & \mathbf{K} \\ -\mathbf{K} & \Omega\mathbf{G} \end{bmatrix} \tag{3.27}$$

It is well known that the eigenvalues of an undamped gyroscopic system are pure imaginary complex conjugates whilst the eigenvectors also occur in complex conjugate pairs. Meirovitch considered a pair of eigensolution $(\mathrm{i}\omega_r, \mathbf{r}_r + \mathrm{i}\mathbf{m}_r)$ and substituted it back to Eq. (3.26), which results in

$$\mathrm{i}\omega_r\mathbf{A}\,\mathbf{r}_r - \omega_r\mathbf{A}\mathbf{m}_r + \mathbf{B}\mathbf{r}_r + \mathrm{i}\mathbf{B}\mathbf{m}_r = 0 \tag{3.28}$$

Separating the real and the imaginary parts gives

$$\mathbf{B}\mathbf{r}_r = \omega_r\mathbf{A}\mathbf{m}_r \text{ and } \mathbf{B}\mathbf{m}_r = -\omega_r\mathbf{A}\,\mathbf{r}_r \tag{3.29}$$

Substituting $\mathbf{z}_r$ in the latter from the first and $\mathbf{y}_r$ in the first from the latter, for example,

$$\mathbf{m}_r = (1/\omega_r)\mathbf{A}^{-1}\mathbf{B}\mathbf{r}_r \tag{3.30}$$

Eq. (3.29) then becomes

$$\mathbf{E}\mathbf{r}_r = {\omega_r}^2\mathbf{A}\mathbf{r}_r \text{ and } \mathbf{E}\mathbf{m}_r = {\omega_r}^2\mathbf{A}\mathbf{m}_r \quad r = 1, 2, \ldots, n \tag{3.31}$$

where

$$\mathbf{E} = \mathbf{B}^{\mathrm{T}}\mathbf{A}^{-1}\mathbf{B} \tag{3.32}$$

is a real symmetric positive definite matrix. Hence, the original eigenvalue problem of order $2n$ has been reduced to two eigenvalue problems of order $2n$ with real symmetric matrices. They can then be solved efficiently using a number of algorithms.

Each of the equations in Eq. (3.31) has n pairs of repeated eigenvalues that are real positive values and n pairs of $2n$-dimentional eigenvectors. Both real part $\mathbf{r}_r$ and imaginary part $\mathbf{m}_r$ satisfy the same eigenvalue problem and are related by Eq. (3.30).

Nonetheless, for numerical computation, Eq. (3.32) could be prone to having round-off errors if the matrix to be inversed is badly scaled, that is to say, matrix **A** should be carefully chosen (must be non-singular) or the eigenvalues might not appear in pairs as a result. In other words, this method cannot be applied to generally damped structures and free rotors. Moreover, it was later shown by Meirovitch [146] that vectors $\mathbf{r}_r$ and $\mathbf{m}_r$ are linearly independent because the system is positive definite; therefore, the response of an undamped gyroscopic system could be derived through closed-form functions based on expansion theorem. The free response $\mathbf{z}(t)$ in Eq. (3.25) can be computed from

$$\mathbf{z}(t) = \sum_{r=1}^{n} c_{1r}(\mathbf{r}_r + \mathrm{i}\mathbf{m}_r)\mathrm{e}^{\mathrm{i}\omega_r t} + c_{2r}(\mathbf{r}_r - \mathrm{i}\mathbf{m}_r)\mathrm{e}^{-\mathrm{i}\omega_r t} \qquad (3.33)$$

where c_{1r} and c_{2r} are real coefficients depending on the initial displacement and velocity.

3.4. A case study

Consider a geared rotor-bearing system shown in Fig. 3.3. In this case study, the main interest is to study the dynamical properties of such a system within 0 and 6000 rpm and highlight some important features in rotordynamic analysis.

The system depicted in Fig. 3.3 consists of two parallel shafts that are connected through a pair of identical gears. The shafts have the following material properties: Young's modulus of 205 GPa, Poisson ratio of 0.33, and mass density of 7850 $\mathrm{kg/m^3}$. The shafts have diameters of 1.7 cm and total lengths of 30 cm and 80 cm, respectively. They are modelled using 13 Timoshenko beam elements and therefore have 15 nodes in total. The lengths of the beam elements are shown in Fig. 3.3. Three identical rigid discs are keyed to the shafts at node 2, 10, and 12. Each disc has weight of 4.1404 kg,

diametral moment of inertia of 0.0061 kgm^2, and polar moment of inertia of 0.0116 kgm^2. Likewise, the inertia influence of the gears are represented by two rigid discs of which each weight is 1.024 kg, the diametral moment of inertia is 4.675×10^{-4} kgm^2, and the polar moment of inertia is 7.58×10^{-4} kgm^2. The gear contact angle and the gear contact stiffness are set to 22.5 degree and 10^4 N/m. Bearings are assumed to have a stiffness of 9×10^6 N/m in the *x* direction and 10^7 N/m in the *y* direction, and a damping of 10^4 Ns/m in each direction. There is no cross-coupling in bearings. The internal damping of the rotor is neglected.

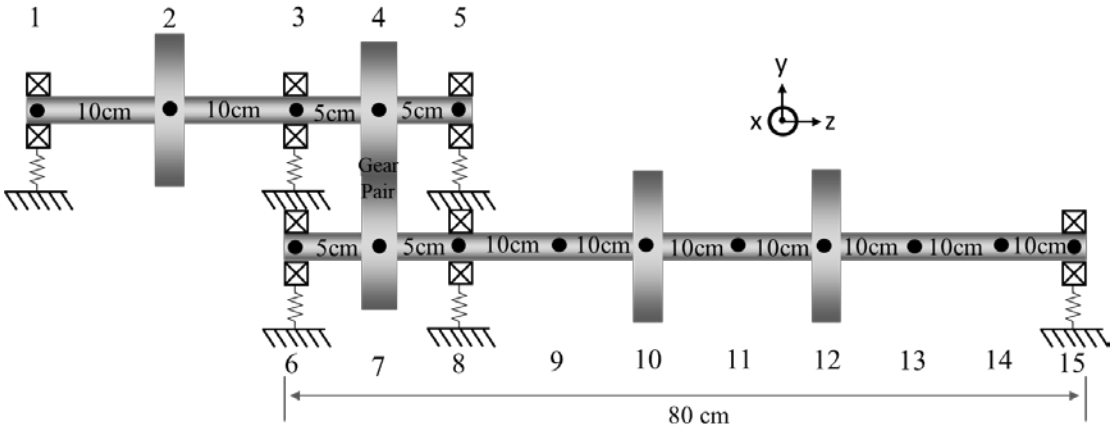

Figure 3. 3. The layout of the geared roto-bearing system.

Discussion:

Since the system is damped and has a rigid body mode in the torsional direction, the eigenvalue problem has to be solved in the state-space form. Due to the presence of the gyroscopic term, the equation of motion needs to be updated and solved at each spin speed of interest. Table 3.3 shows the first few eigenvalues of the system at 0 rpm and 6000 rpm, respectively. It is conventionally assumed that the eigenvalues are of the form $-\xi\omega_\text{n} \pm \omega_\text{n}\sqrt{1-\xi^2}$ where ξ is the damping ratio, ω_n is the natural frequency, and $\omega_\text{n}\sqrt{1-\xi^2} = \omega_\text{d}$ is the damped natural frequency. The corresponding natural frequencies and the damping ratios for the eigenvalues are also presented in Table 3.3.

It is believed that the bending natural frequencies would occur in pairs and each pair of natural frequencies do not necessarily share the same value whilst the torsional

natural frequencies are distinct. This is because the bearing stiffness in the *x* and *y* directions are not identical and the beam element is composed of two uncoupled sets of DoFs in the *x*-*z* plane and in the *y*-*z* plane. Therefore, it can be easily concluded that, in Table 3.3, the first root is a torsional natural frequencies at 7 Hz and the rest are two sets of bending natural frequencies at about 28 Hz and 97 Hz. As no damping is present on the torsional DoF, the damping ratio of the torsional mode is close to zero.

It is well known that the bending natural frequencies split because of gyroscopic effect as the rotational speed increases. In a set of two split frequencies, one is referred to as the forward whirl (FW) mode and the other is referred to as the backward whirl (BW) mode. A FW mode means the orbit of the rotor rotates in the same direction as the spin direction whilst a BW mode rotates in the opposite direction. In the stationary reference frame, the gyroscopic moment tends to increase the stiffness of the FW mode, thus increasing the natural frequency. On the contrary, the stiffness of the BW mode is weaken. As a result, FW modes in general occur at a higher frequency than BW modes but this is not guaranteed. As can been seen in Table 3.3, the frequency difference in each pair of the bending modes at 6000 rpm is greater than that at 0 rpm.

Table 3. 3. The eigenvalues of the system at two different spin speeds.

Speed	Roots	ω_n(Hz)	ω_d(Hz)	ξ
0	0 ± 43.99i	7.0	7.0	2.3×10^{-5}
	-1.96 ± 177.50i	28.252	28.250	0.011
	-1.65 ± 178.46i	28.404	28.403	0.0092
	-16.86 ± 611.67i	97.388	97.351	0.028
	-14.76 ± 613.26i	97.632	97.603	0.024
6000	0 ± 43.99i	7.0	7.0	2.3×10^{-5}
	-1.59 ± 171.40i	27.280	27.279	0.0093
	-2.01 ± 184.12i	29.305	29.304	0.0109
	-14.15 ± 572.89i	91.206	91.178	0.0247
	-16.36 ± 643.02i	102.373	102.340	0.0254

The orbits of the first four bending modes at 6000 rpm at the node number 10 (disc location) are plotted in Fig. 3.4. By following the right hand rule, one can

determine whether a mode is a FW mode or a BW mode. It should be mentioned that in some cases a system could simultaneously possess both FW and BW at different locations along the rotor. Additionally, in this case, the orbits are in fact elliptical rather than circular due to the anisotropic bearings.

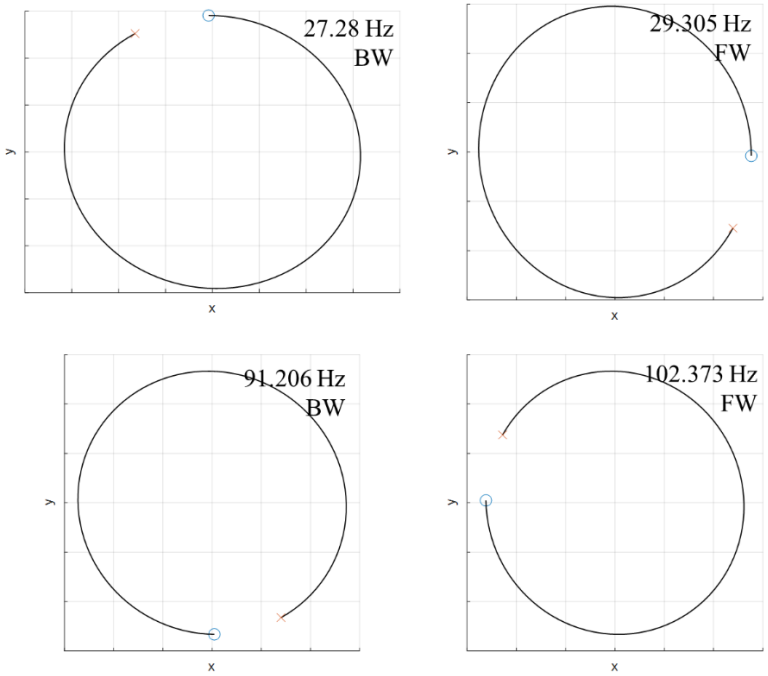

Figure 3. 4. The orbits of the bending modes, viewed from the positive *z*-axis, at node number 10 at 6000 rpm. The circle denotes the start of the orbit and the cross denotes the end.

It can be shown that although the two shafting systems are connected through a skew spring, which represents the gear contact, the longer one still has a greater influence than the shorter one in the system's overall dynamic properties as the natural frequencies of the geared rotor-bearing system are rather close to that of the longer shafting system alone. This suggests that the current gear model is not able to provide strong coupling between the two shafting systems. For this reason, it is representative to plot the mode shapes only from the longer shaft of the geared rotor-bearing system. Fig. 3.5 includes the four bending mode shapes at 6000 rpm. It can be noticed that the rotor exhibits similar mode shapes of a classical pinned-pinned beam.

In addition to bending modes, the first torsional mode about the axial direction is plotted in Fig. 3.6. It is clear that the angle of twist varies linearly between any two

adjacent masses (gears or discs) that have relatively larger polar moment of inertia than the shafts.

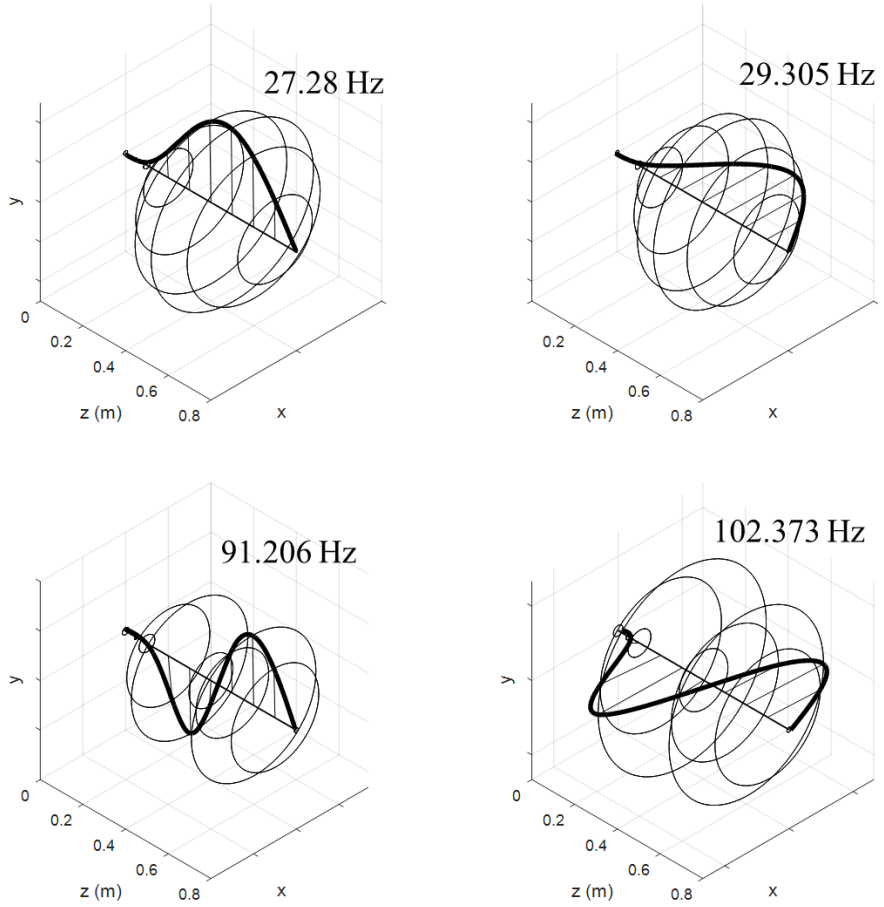

Figure 3. 5. Mode shapes of the bending modes at 6000 rpm.

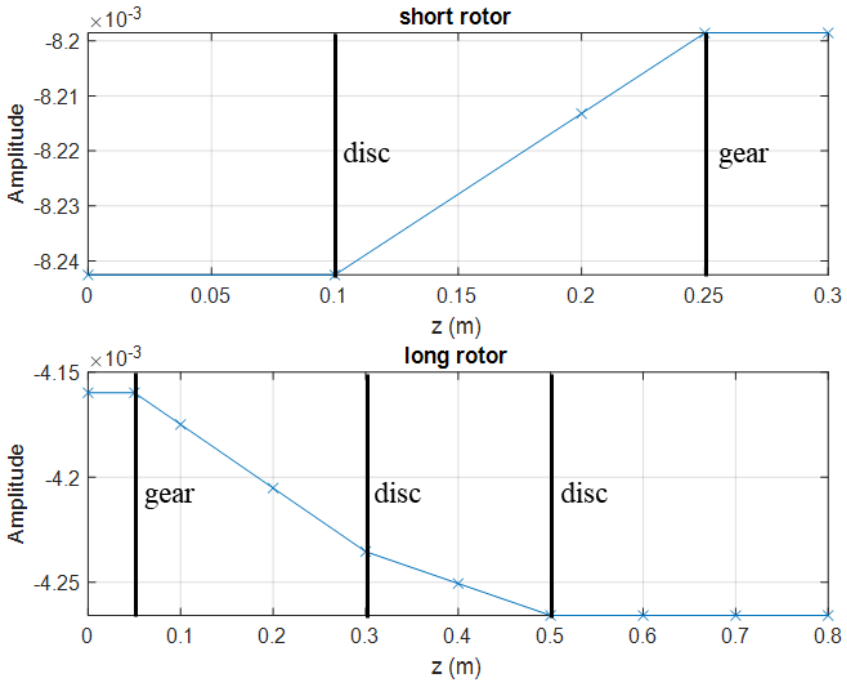

Figure 3. 6. Mode shape of the first torsional mode.

As the natural frequency is influenced by the rotational speed, a Campbell diagram, which shows the natural frequencies of the system with respect to spin speeds, can be obtained as shown in Fig. 3.7. It is often useful to include some reference lines in the same diagram that shows frequencies at the spin speed (1x), at twice the spin speed (2x), at half the spin speed (0.5x), or at other harmonics and subharmonics of the spin speed, as in Fig. 3.7. These frequencies are featured by various excitations that are commonly found in a rotating machine such as unbalance, misalignment, loose assembly, oil whirl, etc.

From the Campbell diagram, the critical speeds can be easily identified. Simply stated, the critical speed is a rotational speed that matches the natural frequency of a rotating object. As a result, the system's response significantly increases when operating at or close to the critical speeds. Through the definition, it is clear that the intersections of the natural frequencies and the 1x reference line are the critical speeds of primary interest. To avoid big vibration response, most of the rotating machines' operating speeds are either below the first critical speed or between any two sequential critical speeds.

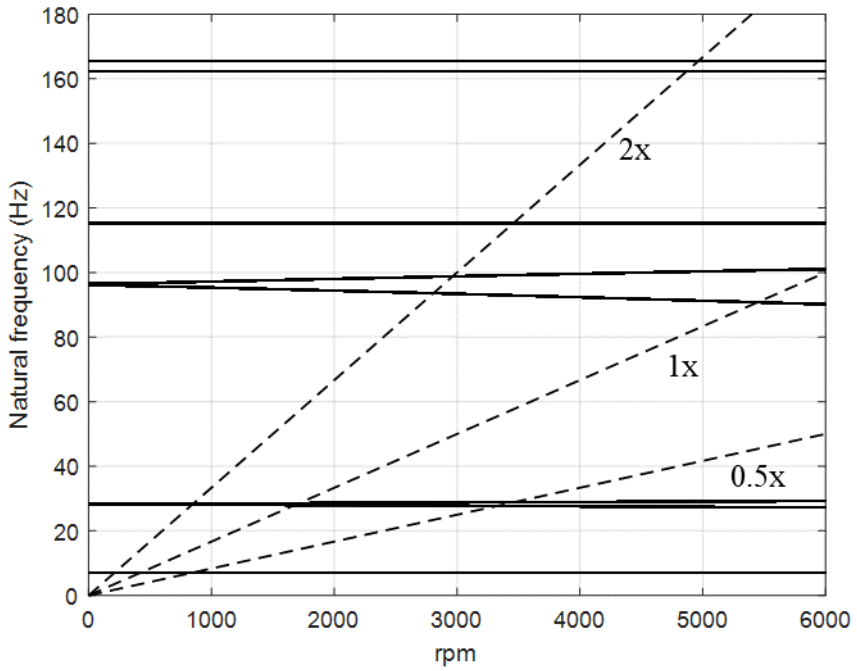

Figure 3. 7. The Campbell diagram of the geared rotor-bearing system.

It has been assumed that the discs are rigid throughout the case study, and this assumption is in fact true for the majority of the cases; however, it is still important to check if the assumption holds especially when the rotational speed is high or the disc is thin. The commercial FEA software Abaqus is employed to study the flexibility of the disc used in this case study. In the simulation, the rotordynamic load is defined using the syntax ROTDYNF, and it should be defined along with a nonlinear static step in order to take the centrifugal load effects and load stiffness terms into account. It should be mentioned that currently the rotordynamic load (ROTDYNF) is not supported in the Abaqus CAE interface and thus has to be explicitly applied in the .inp file and solved by the Abaqus solver through the Command window. Moreover, as discussed in Section 3.1, Abaqus manual also suggests that ROTDYNF can only be applied to axisymmetric structures in a stationary reference frame. After the rotordynamic load is applied, Complex Eigenvalue Extraction is used to obtain the natural frequencies and the mode shapes. As a result, the Campbell diagram of the disc can be obtained as shown in Fig. 3.8.

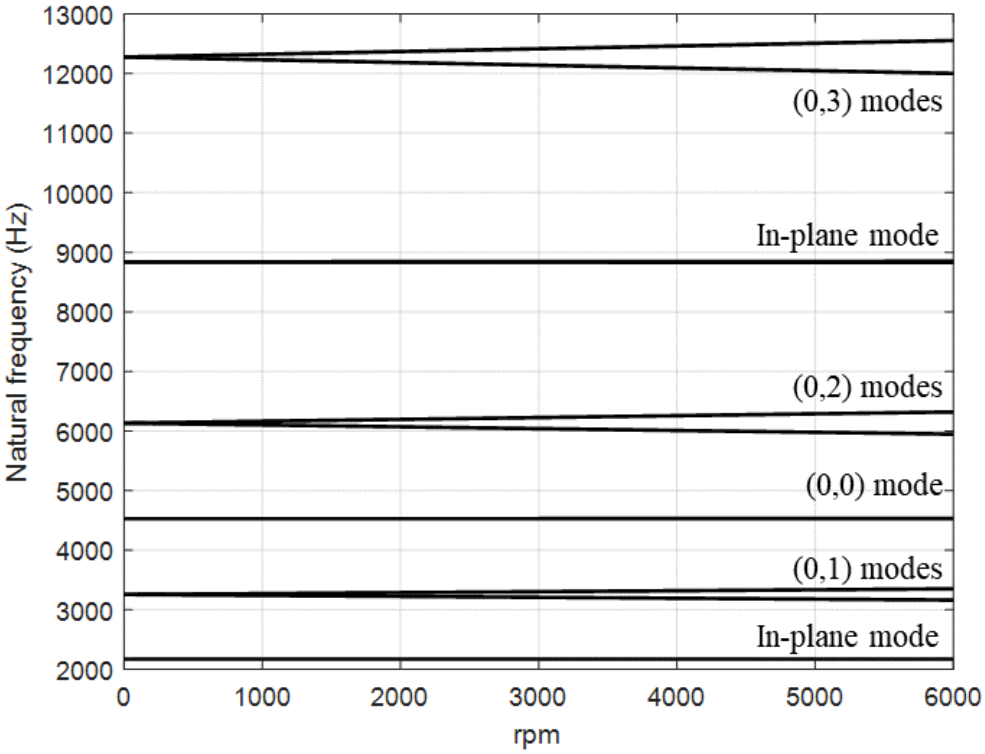

Figure 3. 8. Campbell diagram of the flexible disc.

It is clear that a flexible disc also experiences the change of some natural frequencies as the spinning speed changes. For a disc-like structure, it is common to denote the modes in the way as (NC, ND) where NC is the number of nodal circles and ND stands for the number of nodal diameters. When a disc is stationary, it is well known that modes with $\mathrm{ND} = 0$ have distinct eigenvalues and mode shapes, whereas any mode with $\mathrm{ND} \neq 0$ possesses two linearly independent sine- and cosine-oriented modes that share a same natural frequency. For instance, the first few mode shapes of the flexible disc (clamped-free) are shown in Fig. 3.9. When the disc starts spinning, the natural frequencies of modes with $\mathrm{ND} \neq 0$ split as the spin speed increases, which can be seen in Fig. 3.8. The mode with higher natural frequency is referred to as a forward mode whilst the one with lower natural frequency is called a backward mode.

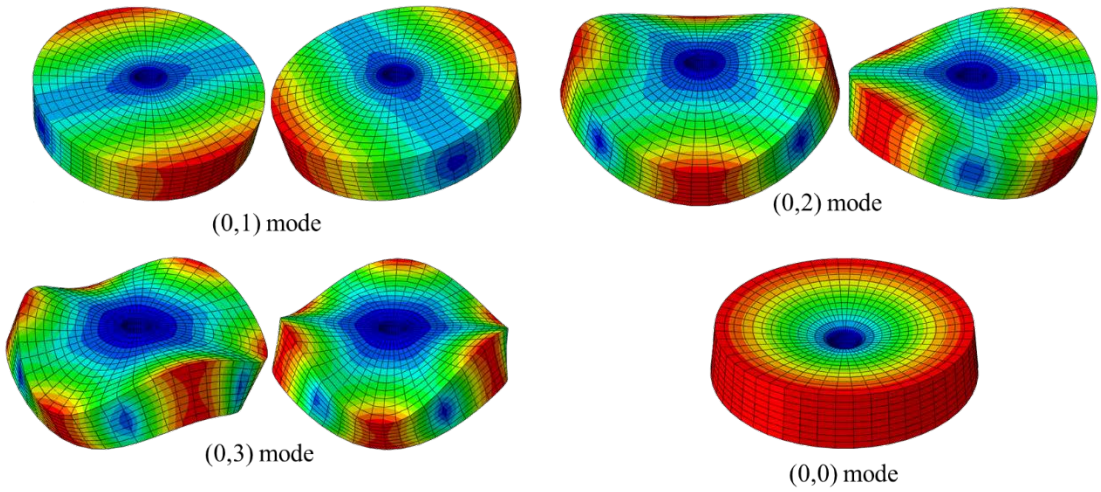

Figure 3. 9. A few out-of-plane modes of the flexible disc.

From Fig 3.8, it is also clear that the lowest natural frequency, which is about 2171 Hz, is much higher than the frequency range of concern in the geared rotor-bearing system. Although the natural frequencies of the backward modes decreases as the spinning increases, the disc is not likely to be excited within 0-6000 rpm in the system. As a result, assuming that the disks are rigid throughout the analysis of the geared rotor-bearing system is thus reasonable.

4. Receptance-based inverse structural modification methods

The merits of using receptances for inverse structural modification problems have been discussed in Section 2.2. In this chapter, the aim is to cover the theoretical developments of using receptances in such an inverse problem. The definition of receptance and its difference from dynamic stiffness matrix are first presented, and followed by the theoretical developments of receptance-based methods for passive control. Lastly, some receptance-based methods for active control are presented.

4.1. Receptance and dynamic stiffness matrix

The general equation of motion of a viscously-damped multi-DoF system can be expressed as

$$\mathbf{M}\ddot{\mathbf{q}}(t) + \mathbf{C}\dot{\mathbf{q}}(t) + \mathbf{K}\mathbf{q}(t) = \mathbf{f}(t) \tag{4.1}$$

where **M**, **C**, **K** are real $n \times n$ mass, damping, and stiffness matrices. In general, **M** is positive definite and **K** is semi-positive definite. $\mathbf{q}(t)$ represents the displacements of the DoFs in the system and $\mathbf{f}(t)$ is the vector containing the external forces. If the steady-state response is the primary interest and $\mathbf{f}(t) = \mathbf{f}\mathrm{e}^{st}$, the response can take the form of $\mathbf{q}(t) = \mathbf{u}\mathrm{e}^{st}$. Substituting this into Eq. (4.1) leads to

$$[s^2\mathbf{M} + s\mathbf{C} + \mathbf{K}]\mathbf{u} = \mathbf{f} \tag{4.2}$$

The matrix $[s^2\mathbf{M} + s\mathbf{C} + \mathbf{K}] \in \mathbb{C}^{n\times n}$ is referred to as the dynamic stiffness matrix and denoted as **Z**(*s*)**.** The dynamic stiffness matrix can be seen as an analogue of the stiffness in Hooke's law when *s* is equal to zero. With any *s*, each element in Eq. (4.2) can be written as

$$f_i = \sum_{j=1}^{n} z_{i,j}u_j \tag{4.3}$$

where $z_{i,j}$ is the $(i^{th}$ row, j^{th} column) element in the dynamic stiffness matrix. It can be seen that, from Eq. (4.3), a $z_{i,j}$ can only be exactly determined when the displacements at DoF other than *j* are zero, i.e. $z_{i,j} = f_i/u_j$. However, the constraint to make all displacements but DoF *j* zero is extremely hard to achieve in practice. That is to say, it is not straightforward to construct or study the force-displacement relationship using the dynamic stiffness matrix, the stiffness matrix elements are to be measured. To describe such a relationship in a more convenient form, Eq. (4.2) can be pre-multiplied by the inverse of the dynamic stiffness matrix, which leads to

$$\mathbf{u} = \mathbf{H}\mathbf{f} \tag{4.4}$$

in which $\mathbf{H}(s) = [s^2\mathbf{M} + s\mathbf{C} + \mathbf{K}]^{-1}$ is known as the receptance matrix or the frequency response function matrix. In contrast to Eq. (4.3), the displacement at DoF *i* is given by

$$u_i = \sum_{j=1}^{n} h_{i,j} f_j \tag{4.5}$$

This provides a rather convenient means to describe the force-displacement relationship. It only requires a receptance function $h_{i,j}$ to determine the displacement at DoF *i* due to the excitation at DoF *j*, in other words, $h_{i,j}$ represents the response at i^{th} DoF caused by a unit load applied at j^{th} DoF at various excitation frequencies. By the same token, $h_{i,j}$ can be obtained through experimental modal analysis in practice. The receptance matrix is in theory symmetric, and thereby the reciprocal relation $h_{i,j} = h_{j,i}$ holds; nonetheless, the measured receptance matrix is prone to being non-symmetric due to the inevitable measurement noise, measurement errors, and non-smooth nonlinearities [40].

In addition to being the transfer function between input and output or the inverse of the dynamic stiffness matrix, receptance matrix can also be expressed in terms of eigenvalues (s_r) and eigenvectors $(\mathbf{v}_r)$ of the quadratic eigenvalue problem of Eq. (4.1) or the ratio of two polynomials as shown in Eqs. (4.6) and (4.7), respectively.

$$\mathbf{H}(s) = \sum_{r=1}^{n} \left(\frac{\mathbf{v}_r \mathbf{v}_r^{\mathrm{T}}}{s - s_r} + \frac{\mathbf{v}_r^* \mathbf{v}_r^{*\mathrm{T}}}{s - s_r^*} \right) \text{ where } s = \mathrm{i}\omega \tag{4.6}$$

$$h(s) = \frac{\mathrm{N}(s)}{\mathrm{D}(s)} = \sum_{i=0}^{m} a_i s^i \Big/ \sum_{j=0}^{n} b_j s^j \tag{4.7}$$

4.2. Receptance method for passive control

In this section, the theoretical developments of using receptances to formulate the inverse structural modification problem are presented. The formulations of the classical forms of modification including rank-one modification and single-DoF spring-mass oscillator are introduced. It should be stated that the following contents regarding the formulas of rank-one modification in this section are mainly based on [32].

4.2.1. Rank-one modification

The dynamic stiffness matrix of a rank-one modification at r^{th} DoF can be expressed in the form of $b_r(s) = s^2 \Delta m_r + s \Delta c_r + \Delta k_r$. Combining $b_r(s)$ with the system's equation of motion, Eq. (4.2), and rearranging the equation to the form of Eq. (4.4) give

$$\mathbf{u} = [s^2 \mathbf{M} + s\mathbf{C} + \mathbf{K} + \mathbf{e}_r b_r(s) \mathbf{e}_r^{\mathrm{T}}]^{-1} \mathbf{f} \tag{4.8}$$

where vector $\mathbf{e}_r$ has a unity element at r^{th} DoF and zero elements everywhere else. According to Sherman–Morrison formula, the receptance matrix of the modified system ($\widehat{\mathbf{H}}$) can be derived from Eq. (4.8), which is

$$\widehat{\mathbf{H}}(s) = \mathbf{H}(s) - \frac{b_r(s) \mathbf{H}(s) \mathbf{e}_r \mathbf{e}_r^{\mathrm{T}} \mathbf{H}(s)}{1 + b_r(s) \mathbf{e}_r^{\mathrm{T}} \mathbf{H}(s) \mathbf{e}_r} \tag{4.9}$$

One can use another set of mapping vector to find the (i^{th}, j^{th}) element in $\widehat{\mathbf{H}}(s)$, for instance, $\mathbf{e}_i^{\mathrm{T}} \widehat{\mathbf{H}}(s) \mathbf{e}_j$, which results in

$$\hat{h}_{ij}(s) = \frac{h_{ij}(s) + h_{ij}(s)b_r(s)h_{rr}(s) - b_r(s)h_{ir}(s)h_{rj}(s)}{1 + b_r(s)h_{rr}(s)} \tag{4.10}$$

The poles of the modified system occur when the denominator of Eq. (4.10) equals to zero. In the same way, the zeros of the receptance $\hat{h}_{ij}(s)$ can be found by setting the numerator to zero. Eq. (4.10) can be simplified into the following cases based on the DoFs of interest:

(a) A point receptance of the modified system, i.e. $i = j \neq r$.

$$\hat{h}_{ii}(s) = \frac{h_{ii}(s) + b_r(s)\big(h_{ii}(s)h_{rr}(s) - h_{ir}(s)h_{ri}(s)\big)}{1 + b_r(s)h_{rr}(s)} \tag{4.11}$$

(b) A point receptance of the modified system with a rank-one modification at the same coordinate, i.e. $i = j = r$.

$$\hat{h}_{rr}(s) = \frac{h_{rr}(s)}{1 + b_r(s)h_{rr}(s)} \tag{4.12}$$

(c) A cross receptance with a rank-one modification at one of the cross receptance coordinates, i.e. $r = j$.

$$\hat{h}_{ir}(s) = \frac{h_{ir}(s)}{1 + b_r(s)h_{rr}(s)} \tag{4.13}$$

It can be seen that the denominator doesn't change in any of the cases. This agrees with the fact that a pole is a global parameter, which doesn't change with the locations of observation. The assignment of pole can be simply formulated as

$$b_r(s_\mathrm{d}) = \frac{-1}{h_{rr}(s_\mathrm{d})} \tag{4.14}$$

which allows the required parameters of the modification to be determined so as to assign a pole at a desired value s_d. In practice, it is more feasible to carry out mass or stiffness modifications whilst it is quite difficult or even not possible to realize pure damping modifications. For pure mass or stiffness modifications, Eq. (4.14) can be expressed as

$$\Delta m_r = \frac{-1}{s^2 h_{rr}(s_\mathrm{d})} \quad \text{and} \quad \Delta k_r = \frac{-1}{h_{rr}(s_\mathrm{d})} \tag{4.15}$$

Zarraga *et al.* [99] simply made use of Eq. (4.15) and successfully suppressed the squeal noise of the brake-clutch device.

From Eqs. (4.11) - (4.13), it can be found that zeros in a receptance can only be assigned when the modification is not applied at the coordinates associated with the receptance. The modification required to assign a zero of a cross receptance $\hat{h}_{ij}(s)$ can be determined by

$$b_r(s) = \frac{-h_{ij}(s)}{h_{ij}(s)h_{rr}(s) - h_{ir}(s)h_{rj}(s)} \quad \text{where } r \neq i, j \tag{4.16}$$

and the corresponding formula for a point receptance $\hat{h}_{ii}(s)$ is

$$b_r(s) = \frac{-h_{ii}(s)}{h_{ii}(s)h_{rr}(s) - h_{ir}(s)h_{ri}(s)} \quad \text{where } r \neq i \tag{4.17}$$

which require only four and three receptances (if the reciprocal relation holds), respectively, to calculate the required modification.

Other than a point-mass or a grounded-spring modification, the modification of a spring connecting two coordinates can be considered in the same way. The receptance matrix of the modified system can be expressed as

$$\hat{\mathbf{H}}(s) = \mathbf{H}(s) - \frac{\Delta k_{r_1 r_2}(s)\mathbf{H}(s)\left(\mathbf{e}_{r_1} - \mathbf{e}_{r_2}\right)\left(\mathbf{e}_{r_1} - \mathbf{e}_{r_2}\right)^{\mathrm{T}}\mathbf{H}(s)}{1 + \Delta k_{r_1 r_2}(s)\left(\mathbf{e}_{r_1} - \mathbf{e}_{r_2}\right)^{\mathrm{T}}\mathbf{H}(s)\left(\mathbf{e}_{r_1} - \mathbf{e}_{r_2}\right)} \tag{4.18}$$

where a spring $\Delta k_{r_1 r_2}(s)$ is added between the $r_1{}^{\text{th}}$ and $r_2{}^{\text{th}}$ coordinates. Similar to Eq. (4.10), a particular receptance can be written explicitly from Eq. (4.18) as

$$\hat{h}_{ij}(s) = h_{ij}(s) - \frac{\Delta k_{r_1 r_2}(s)\left(h_{ir_1}(s) - h_{ir_2}(s)\right)\left(h_{r_1 j}(s) - h_{r_2 j}(s)\right)}{1 + \Delta k_{r_1 r_2}(s)\left(h_{r_1 r_1}(s) - h_{r_1 r_2}(s) - h_{r_2 r_1}(s) + h_{r_2 r_2}(s)\right)} \tag{4.19}$$

Since more coordinates are involved in this type of modification, the number of required receptances must increase.

It can be noticed that the amplitude of a receptance can also be adjusted through rank-one modifications. For this purpose, it is convenient to rewrite Eq. (4.10) in terms of the ratio of the modified receptance and the original receptance, which is

$$b_r = \frac{\gamma h_{ij}(s) - h_{ij}(s)}{h_{rr}(s)h_{ij}(s) - h_{ir}(s)h_{rj}(s) - \gamma h_{ij}(s)h_{rr}(s)} \tag{4.20}$$

where $\gamma = \hat{h}_{ij}(s)/h_{ij}(s)$.

The assignment of a vibration node by a rank-one modification was studied by Mottershead and Lallement [34]. Their work provided an insight into how a vibration node is formed but receptances were not employed in the discussion. They stated that a vibration node will result from a pole-zero cancellation in which the necessary and sufficient conditions for the cancellation are met and the zeros are distinct. The necessary and the sufficient conditions are shown as follows

Sufficient condition: The zero of the point receptance $h_{ii}(s)$ to be canceled must also be a zero of the cross receptance $h_{ij}(s)$ where $j = 1, \cdots, n, (j \neq i)$.

Necessary condition: The pole and the zero to be cancelled have the same value.

The problem of pole-zero cancellation for repeated poles or zeros was later studied by Mottershead *et al.* [147], and the use of receptance in such a problem was proposed by Mottershead *et al.* [35]. The formulations for node assignments using a rank-one modification are explained as follows. The eigenvalue problem of a modified system due to a rank-one modification at the r^{th} coordinate can be written as

$$[s^2\mathbf{M} + s\mathbf{C} + \mathbf{K} + \mathbf{e}_r b_r(s)\mathbf{e}_r^{\mathrm{T}}]\mathbf{u} = \mathbf{0} \tag{4.21}$$

Premultiplying Eq. (4.21) by the receptance matrix of the original system gives

$$[\mathbf{I} + \mathbf{H}(s)\mathbf{e}_r b_r(s)\mathbf{e}_r^{\mathrm{T}}]\mathbf{u} = \mathbf{0} \tag{4.22}$$

The i^{th} and the r^{th} equations in Eq. (4.22) are

$$u_i + b_r(s)h_{ir}(s)u_r = 0 \quad \text{and} \quad \big(1 + b_r(s)h_{rr}(s)\big)u_r = 0 \tag{4.23}$$

If one wants to create a node at the i^{th} coordinate, i.e. $u_i = 0$, this results in

$$b_r(s)h_{ir}(s)u_r = 0 \tag{4.24}$$

As $u_r \neq 0$, the node must occur at the frequency of a zero in $h_{ir}(s)$. To satisfy the sufficient condition, the zero must as well appear in $h_{ii}(s)$. When the desired frequency is found, for example, s_{d}, the modification can be determined from Eq. (4.23) as

$$b_r(s_{\text{d}}) = \frac{-1}{h_{rr}(s_{\text{d}})} \tag{4.25}$$

It can be seen that this equation is the same as Eq. (4.11). The idea is that the zero of a modified receptance does not change if the modification is made at the same coordinate, that is to say, making a rank-one modification at the r^{th} coordinate does not change the zeros in $h_{ir}(s)$ but influence the poles of the system. Once the pole is shifted to frequency of the zero in $h_{ir}(s)$, a node is formed at that frequency if the sufficient condition is met.

Apart from the above-mentioned assignment problems, one may be interested to know whether the assignment of the eigenstructure, natural frequency and mode shape, using a rank-one modification is possible. Assuming that the desired eigenpair is $\big(s_{\text{d}}, \mathbf{u}^{\text{d}}\big)$, then the equations in Eq. (4.22) can be expressed as

$$u^{\text{d}}{}_i = -b_r(s_{\text{d}})h_{ir}(s_{\text{d}})u^{\text{d}}{}_r \quad \text{where} \quad i = 1,2,3,\dots,n \tag{4.26}$$

It is clear that there are more equations than the number of variables in $b_r(s_{\text{d}})$. In other words, it is desirable to find a solution that minimizes

$$\sum_{i=1}^{n}\big(u^{\text{d}}{}_i + b_r(s_{\text{d}})h_{ir}(s_{\text{d}})u^{\text{d}}{}_r\big)^2 \tag{4.27}$$

However, the required modification for Eq. (4.27) is almost always insufficient to provide satisfactory results since the number of DoFs of the system is much larger than the number of design variables. Fortunately, for eigenstructure assignments,

potentially not all the nodal displacements are required to be specified, and incorporating more design variables can greatly relieve the restrictions. This leads to the modifications of multiple DoFs and poses new problems. A more detailed discussion on this issue will be presented in Chapter 5.

Example 4.2.1

A 5-DoFs system borrowed from [40] is considered for the demonstration of a structural modification problem with a rank-one modification. The schematic of the 5-DoFs system is shown in Fig. 4.1, and the corresponding values of the system parameters are listed in Table 4.1. The natural frequencies of the system are 22.28, 32.61, 42.92, 52.71, and 64.57 Hz. Determine the parameters for the rank-one modification of the case in which a node is assigned at x_2 due to a rank-one modification at x_4.

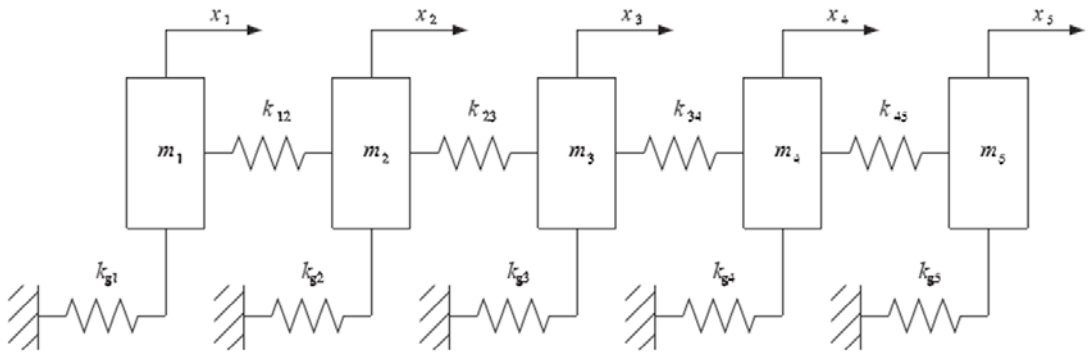

Figure 4. 1. Schematic of the 5-DoFs system.

Table 4. 1. System parameters.

k_{12} [N/m]	k_{23} [N/m]	k_{34} [N/m]	k_{45} [N/m]	k_{g} [N/m]
7.36×10^4	6.82×10^4	7.35×10^4	8.21×10^4	9.89×10^4
m_1 [kg]	m_2 [kg]	m_3 [kg]	m_4 [kg]	m_5 [kg]
1.73	5.12	8.21	2.61	1.34

To assign a node at x_2 using a rank-one modification at x_4, the node must occur at the frequency of a zero in both $h_{24}(s)$ and $h_{22}(s)$. The zero can be analytically

determined by solving the individual subsidiary systems. Alternately, from the FRFs of the two receptances shown in Fig. 4.2, it can also be found that the two receptance functions both have a zero at frequency around 50 Hz; thus, in this case s_d is set to 3.1577×10^2i. Assuming damping modification is excluded, the resulting equation for the problem is

$$(-9.9711 \times 10^4)\Delta m_4 + \Delta k_4 = 1.3864 \times 10^5 \qquad (4.28)$$

which is an underdetermined problem and has more than one solution. All the possible solutions are in a line in the space constructed by $\Delta k \; and \; \Delta m$ as shown in Fig. 4.3. One can determine the most suitable solution based on some constraints of the modifications, for example, negative stiffness or mass modification may be rather expensive or infeasible so the solutions in the first quadrant are usually more desirable.

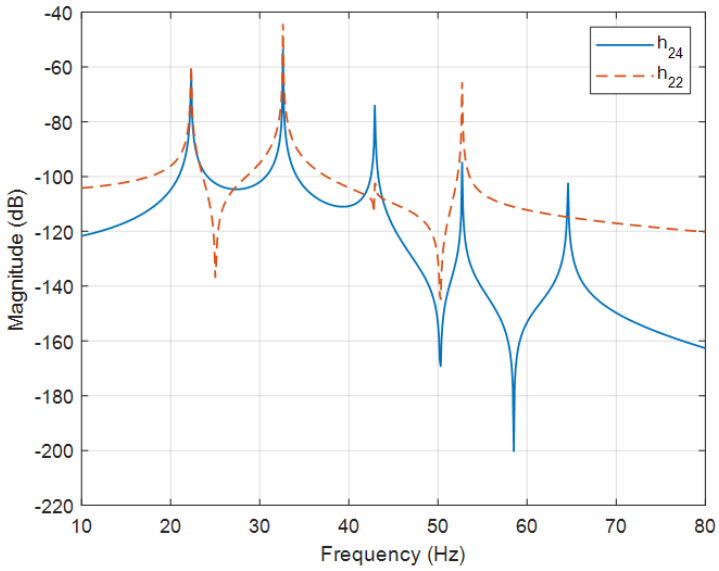

Figure 4. 2. Receptance functions of the original system.

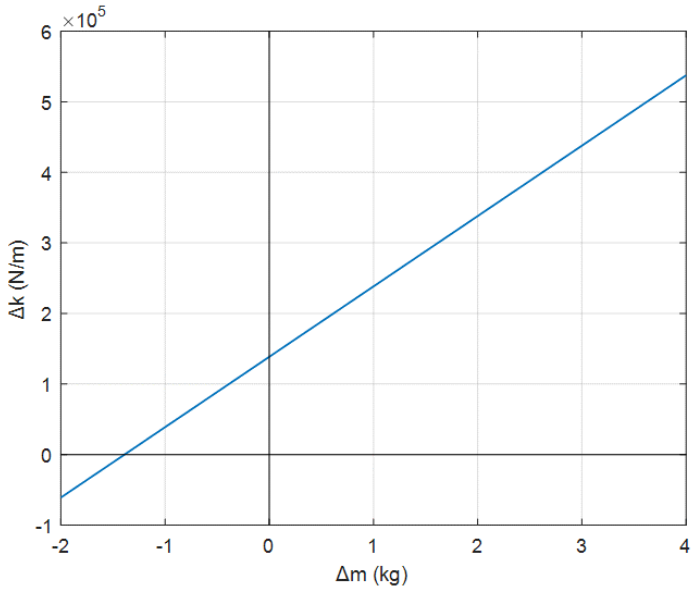

Figure 4. 3. All the feasible solutions.

If the solution of $\Delta m_4 = 1.5$ and $\Delta k_4 = 2.8821 \times 10^5$ is picked, the resulting natural frequencies are 23.32, 33.06, 50.26, 52.71, and 65.45 Hz. The zeros of $h_{24}(s)$ are 50.26 and 58.49 Hz. The receptance functions of the modified system are shown in Fig 4.4. It can be seen that a zero and the third pole of the system are cancelled with each other at the frequency of 50.26 Hz and thus the cross receptance only shows four peaks.

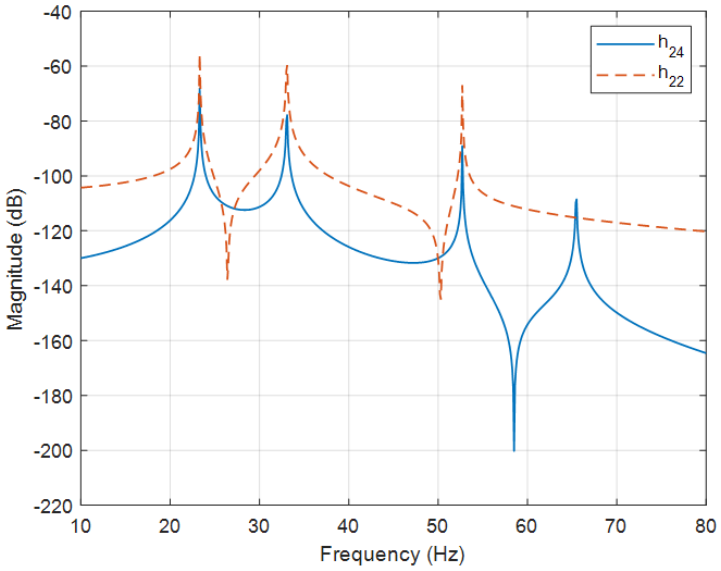

Figure 4. 4. Receptance functions of the modified system.

The mode shapes of the third mode before and after the modification are plotted together in Fig. 4.5. It is clear that the nodal displacement at x_2 is nearly zero after the modification, leading to a node at the coordinate.

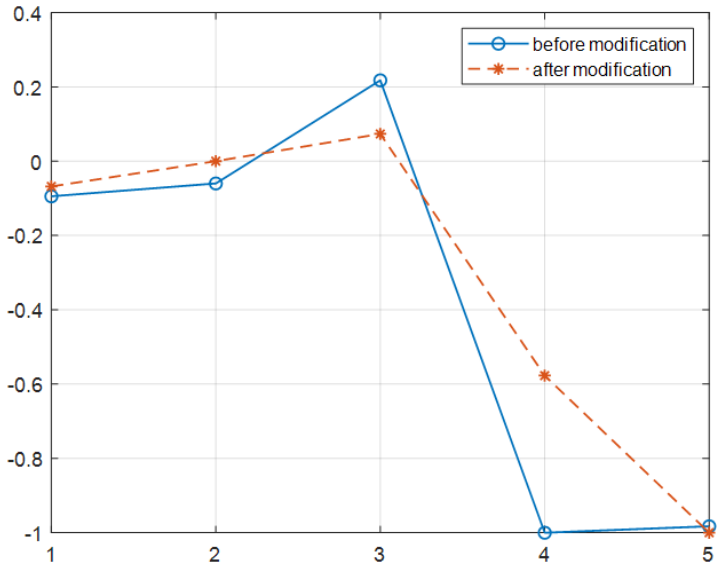

Figure 4. 5. Mode shapes before and after the modification.

4.2.2. Spring-mass oscillator

The spring-mass oscillator, which is illustrated in Fig. 4.6, is another popular form of modification that is easy to implement. This type of modification is especially useful when the existing masses and stiffness are not available for modifications. The theoretical background of using such a modification in the receptance-based inverse structural modification problem is presented in this section.

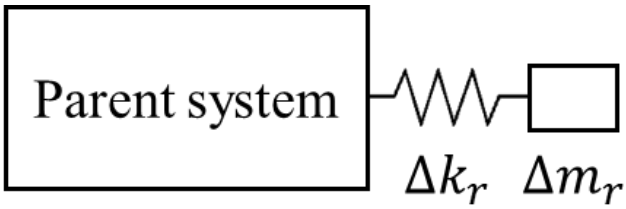

Figure 4. 6. A spring-mass oscillator attached at the r^{th} coordinate of the parent system.

The receptance-based method for the modification of spring-mass oscillator was considered by Kyprianou *et al.* [37]. Although the spring-mass oscillator adds an extra DoF to the original system, it can be shown that the size of the system matrices can be maintained and the influence of the spring-mass oscillator in the form of dynamic stiffness matrix is equivalent to

$$b_r(s) = \frac{s^2 \Delta m_r \Delta k_r}{\Delta k_r + s^2 \Delta m_r} \tag{4.29}$$

The equations of motion of the modified system in which a spring-mass oscillator is attached to the r^{th} DoF can be written as

$$(\mathbf{I} + \mathbf{H}(s) e_r b_r(s) e_r{}^{\mathrm{T}})\mathbf{u} = \mathbf{H}(s)\mathbf{f} \tag{4.30}$$

Expanding the equation gives

$$\mathbf{u} + \mathbf{h}_r(s) b_r(s) u_r = \mathbf{H}(s)\mathbf{f} \tag{4.31}$$

where $\mathbf{h}_r(s)$ is the r^{th} column of the receptance matrix and u_r is the r^{th} element in $\mathbf{u}$. Substituting Eq. (4.29) into Eq. (4.31) and extracting the r^{th} row give

$$u_r = \left(1 + \frac{s^2 \Delta m_r \Delta k_r h_{rr}(s)}{\Delta k_r + s^2 \Delta m_r}\right)^{-1} \mathbf{h}_r(s)^{\mathrm{T}} \mathbf{f} \tag{4.32}$$

which can produce the r^{th} modal displacement of the modified system. Each receptance function can be explicitly written as

$$\hat{h}_{ri}(s) = \frac{(\Delta k_r + s^2 \Delta m_r) h_{ri}(s)}{\Delta k_r + s^2 \Delta m_r + s^2 \Delta m_r \Delta k_r h_{rr}(s)} \quad \text{where } i = 1,2,\dots,n \tag{4.33}$$

An interesting way to see this equation is that, if the parent structure is fixed in space, i.e. the receptance of the parent structure is zero, Eq. (4.33) simply implies the receptance function of a single DoF system.

From the structural modification point of view, it is clear that the receptance can be easily assigned by specifying the ratio of the receptances. The characteristic equation for pole assignment can be found from the denominator, which is

$$\frac{{s_\mathrm{d}}^2 \Delta m_r \Delta k_r}{\Delta k_r + {s_\mathrm{d}}^2 \Delta m_r} h_{rr}(s_\mathrm{d}) + 1 = 0 \tag{4.34}$$

Up to two natural frequencies can be assigned using a single spring-mass oscillator. Similarly, the characteristic equation for zero assignment is simply

$$(\Delta k_r + {s_\mathrm{d}}^2 \Delta m_r) h_{ri}(s_\mathrm{d}) = 0 \tag{4.35}$$

It can be seen that Eq. (4.35) is independent of $h_{ri}(s_\mathrm{d})$, which suggests that a spring-mass oscillator does not affect the original zeros but create a new one in all the cross receptances and point receptance relating to the r^{th} coordinate at

$$s_\mathrm{d} = \sqrt{\frac{\Delta k_r}{\Delta m_r}}\,\mathrm{i} \tag{4.36}$$

Therefore, the influence of adding a spring-mass oscillator is dual, it concurrently achieves a pole assignment and creates a zero. It is interesting to note that when the assigned natural frequency is at a zero of $h_{rr}(s_\mathrm{d})$, the solution to the characteristic equation for pole assignment, Eq. (4.34), is exactly the same as that for zero assignment, Eq. (4.36). This leads to a pole-zero cancellation at the r^{th} DoF and creates a node at the desired frequency as a result. If this zero is shared by other receptance function(s) $h_{ri}(s_\mathrm{d})$, depending on the number of receptance functions, one or more nodes can be created at the same time. In contrast, nodes will not be generated by assigning a zero at a pole of the parent system as it fails to meet the sufficient condition described in section 4.2.1. Instead, the pole of the parent system will be eliminated and replaced by two new poles at two different frequencies.

It is important to evaluate the nodal displacement of the spring-mass oscillator to prevent it from having large oscillations. This can be done through inspecting the equation of motion of a free-free spring-mass oscillator (see Fig. 4.7), which is

$$(s^2 \Delta m_r + \Delta k_r) u_{n+1} - \Delta k_r u_r = f \tag{4.37}$$

Assuming that there is no external force at the oscillator, the equation can be written as

$$\frac{u_{n+1}}{u_r} = \frac{\Delta k_r}{(s^2 \Delta m_r + \Delta k_r)} \tag{4.38}$$

which gives the ratio of the nodal displacements at the oscillator and at the modification coordinate. For an undamped system, the ratio of the nodal displacements can be plotted against the normalized frequency ω/ω_n (where $\omega_n = \sqrt{\Delta k_r/\Delta m_r}$), which is shown in Fig. 4.8. It can be seen that the nodal displacement of the oscillator is greater than or equal to that at the modification coordinate before the natural frequency of the oscillator, and that, in theory, the ratio goes to infinite at ω_n as, corresponding to Eq. (4.35), a zero is created on the receptance functions relating to the modification coordinate. For this reason, in practical applications, a damper is included in the spring-mass oscillator to decrease the vibration response.

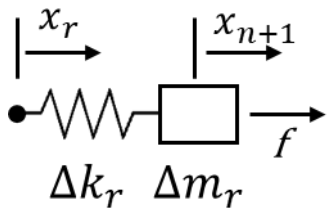

Figure 4. 7. Free-body diagram of a spring-mass oscillator.

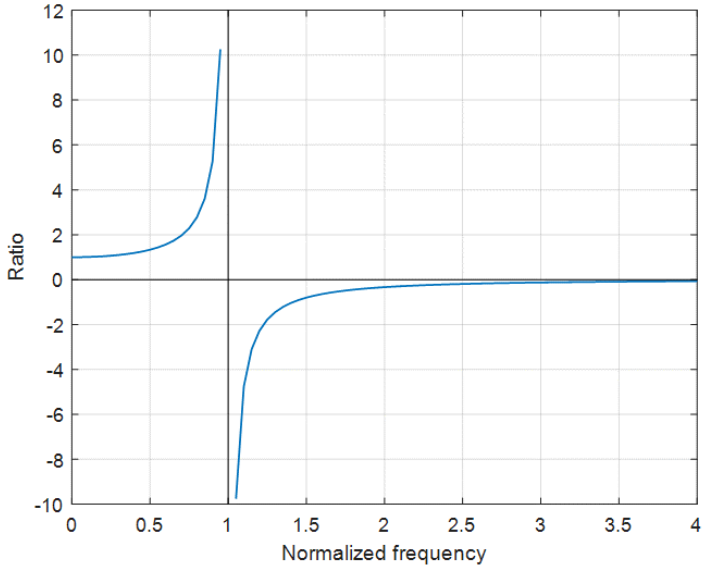

Figure 4. 8. The ratio of the nodal displacements with respect to the normalized frequency.

Example 4.2.2

The same 5-DoFs system in example 4.2.1 is considered to demonstrate the structural modification using a spring-mass oscillator. The following cases are discussed:

(a) Determine how many nodes can be assigned using a spring-mass oscillator applied at m_4.

(b) Assign a zero at the third natural frequency of the original system and compare the receptance functions before and after the modification.

Solution for problem (a)

As mentioned above, node assignments can be achieved by assigning poles at the frequencies of zeros using spring-mass oscillators. The number of nodes that can be assigned at a frequency is determined by the number of receptance functions that have the antiresonance at the frequency in question. From the receptance functions plotted in Fig. 4.9, it can be seen that, for instance, two nodes at the 4th and the 5th DoFs can be assigned at around 25 Hz, or a node at the 3rd DoF can be assigned at about 31 Hz.

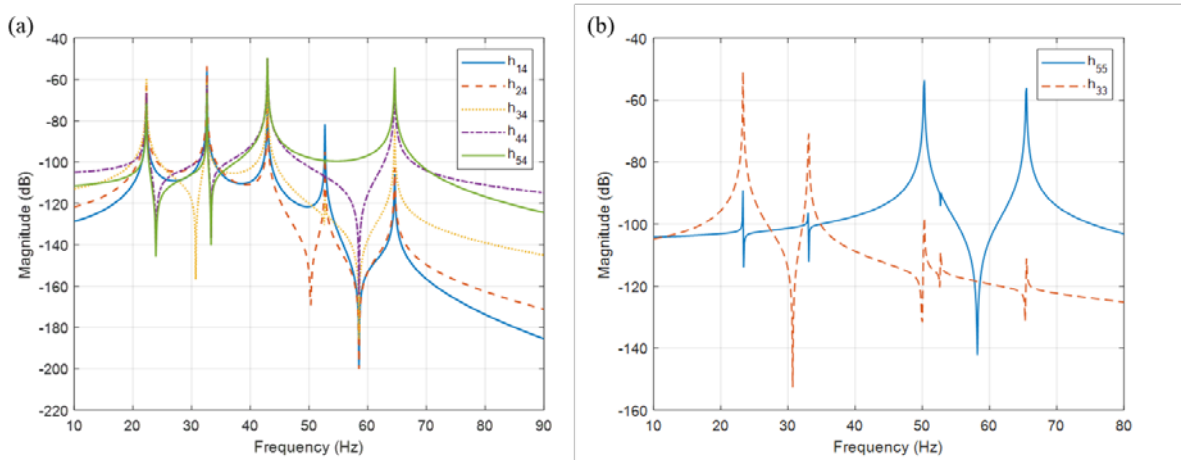

Figure 4. 9. (a) All the receptance functions related to the 4th coordinate. (b) Receptance functions that show zeros of interest.

To demonstrate a node assignment, two nodes are assigned at the 4th and the 5th DoF at their first zero (23.923 Hz). The characteristic equation becomes a linear equation with two unknowns. If a solution, $\Delta m_4 = 1.5$ and $\Delta k_4 = 3.3891 \times 10^4$, is

applied, the same receptance functions in Fig. 4.9 after the modification and the corresponding mode shape are summarized in Fig. 4.10 and Fig. 4.11, respectively.

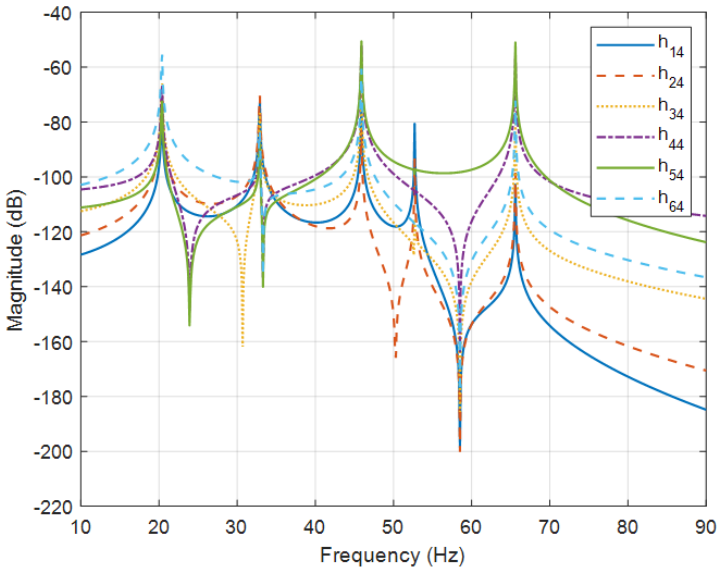

Figure 4. 10. All the receptance functions pertaining to the 4th coordinate after a pole-assignment.

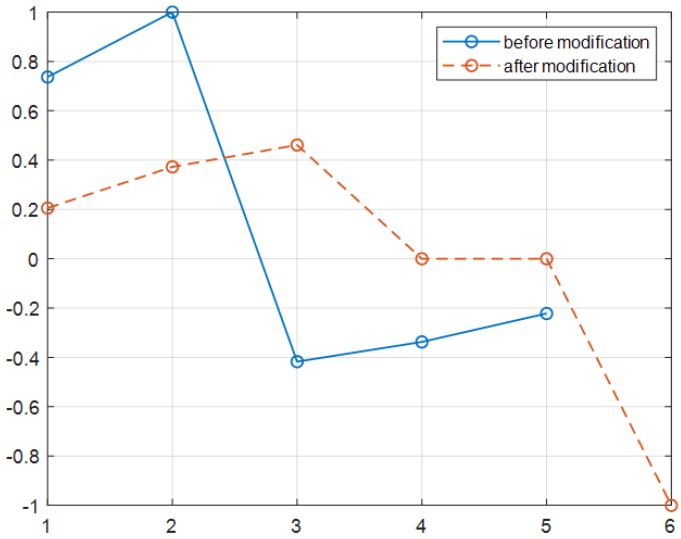

Figure 4. 11. The mode shapes of the second mode before and after the modification.

The achieved natural frequencies are 20.36, 23.92, 32.87, 45.88, 52.71, and 65.58 Hz in which the second natural frequency coincides with the specified zero, thus showing only 5 peaks in the FRFs. Consequently, two nodes are assigned at the 4th and the 5th DoFs as shown in Fig 4.11.

Solution for problem (b)

A zero can be assigned at the third natural frequency (42.92 Hz) using Eq. (4.36). The corresponding characteristic equation is also a linear equation with two unknowns. If a solution, $\Delta m_4 = 1.5$ and $\Delta k_4 = 1.0909 \times 10^5$ is selected, the resulting receptance functions are plotted in Fig. 4.12. It is clear that the response around 42.92 Hz is greatly decreased and that there are some frequencies, e.g. around 34 and 52 Hz, of which the response is increased.

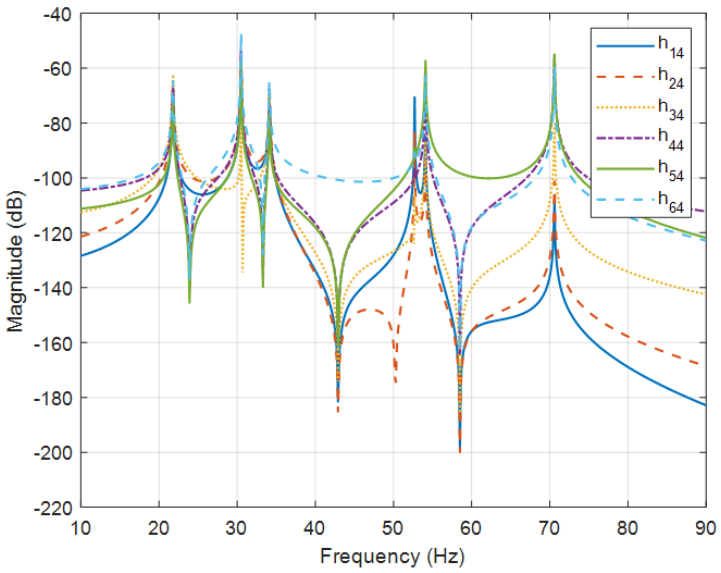

Figure 4. 12. The receptance functions pertaining to the 4th coordinate after a zero-assignment.

4.3. Receptance method for active control

The literature regarding receptance-based active control is previously reviewed in section 2.2.1. In this section the theory for the related methods is presented, and the difference between active control and passive control is discussed. The application of the method is also demonstrated by a few numerical examples.

In many studies, the problems of pole assignment are based on using system matrices **M**, **C**, **K**, for example, it is well-known that all the poles (either real or complex conjugate pairs) of a linear system can be assigned arbitrarily by carefully

designed feedback gains if the system is controllable (full state feedback). This can be achieved by transforming the second-order system into a first-order state-space form and applying one of the techniques, such as linear quadratic regulator, to find the proper feedback gains [148]. However, it is often preferable to work with the second-order system directly instead of recasting it into a state-space form as it destroys all the exploitable properties of the system matrices such as symmetry, definiteness, sparsity, and bandedness. In addition, it is natural to just assign the problematic poles to the desired locations while keeping the rest unchanged. This type of problem is referred to as partial pole assignment problem.

Datta *el al.* [149] addressed the partial pole assignment problem of a symmetric definite pencil by state-feedback control. Three orthogonality relations for the open loop system were investigated and one of which was used to derive the explicit solution to the partial pole assignment problem. A similar problem with multiple input feedback control was studied by Datta and Sarkissian [150], and a summary of relevant studies before 2001 was presented by the same authors [151] including partial eigenstructure assignment problems.

An alternative approach that makes use of receptances was first introduced by Mottershead and Ram [51] in 2006. It avoids the possible modelling errors of the system matrices, especially in modelling the damping matrix, and is not computationally expensive compared with using FE models. Since then, the receptance-based technique and its extension has been an active area of research. The fundamental theoretical background is presented and followed by a few numerical examples.

The equations of motion of a linear system with single-input feedback control can be formulated as

$$\mathbf{M}\ddot{\mathbf{q}}(t) + \mathbf{C}\dot{\mathbf{q}}(t) + \mathbf{K}\mathbf{q}(t) = \mathbf{b}u(t) + \mathbf{f}(t) \tag{4.39}$$

where $\mathbf{q}, \mathbf{b}, \mathbf{f} \in \mathbb{R}^{nx1}$. $\mathbf{b}$ defines the locations of the actuators whilst $u(t)$ is the single-input control function that can be expressed in terms of the displacements and the velocities of the DoFs in the system when state feedback control is considered. That is

$$u(t) = \mathbf{p}^{\mathrm{T}}\dot{\mathbf{q}}(t) + \mathbf{g}^{\mathrm{T}}\mathbf{q}(t) \tag{4.40}$$

where $\mathbf{p}, \mathbf{g} \in \mathbb{R}^{nx1}$ are constant vectors implying the locations of the sensors. Combining Eqs. (4.39) and (4.40) gives

$$\mathbf{M}\ddot{\mathbf{q}}(t) + (\mathbf{C} - \mathbf{b}\mathbf{p}^{\mathrm{T}})\dot{\mathbf{q}}(t) + (\mathbf{K} - \mathbf{b}\mathbf{g}^{\mathrm{T}})\mathbf{q}(t) = \mathbf{f}(t) \tag{4.41}$$

It is clear that implementing displacement and velocity feedback control has the effect of modifying the stiffness and damping matrices. In passive structural modification the modifications are required to be symmetric to be physically feasible while active control allows non-symmetric modifications as Eq. (4.41) suggests. Non-symmetric modifications result in higher flexibility in a pole assignment problem but may make the system unstable. Transferring Eq. (4.41) into Laplace domain gives

$$[\mathbf{M}s^2 + \mathbf{C}s + \mathbf{K} - \mathbf{b}(\mathbf{g} + s\mathbf{p})^{\mathrm{T}}]\mathbf{q}(s) = \mathbf{f}(s) \tag{4.42}$$

which shows that the close-loop dynamic stiffness is modified by the rank-1 matrix $\mathbf{b}(\mathbf{g} + s\mathbf{p})^{\mathrm{T}}$. By applying the Sherman–Morrison formula to Eq. (4.42), the receptance matrix of the modified system can be written as

$$\widehat{\mathbf{H}}(s) = \mathbf{H}(s) + \frac{\mathbf{H}(s)\mathbf{b}(\mathbf{g} + s\mathbf{p})^{\mathrm{T}}\mathbf{H}(s)}{1 - (\mathbf{g} + s\mathbf{p})^{\mathrm{T}}\mathbf{H}(s)\mathbf{b}} \tag{4.43}$$

By the same token, the problem of pole and zero assignment is associated with the denominator and the numerator of Eq. (4.43), respectively.

Pole-assignment problem

Assuming that $\mathbf{H}(s) \in \mathbb{C}^{n\times n}$ and $\mathbf{b}$ are known and that the desired eigenvalues $[s_1 \quad s_1 \quad \cdots \quad s_{2n}]^{\mathrm{T}}$ are decided, the characteristic equation $(\mathbf{g} + s_k\mathbf{p})^{\mathrm{T}}\mathbf{H}(s_k)\mathbf{b} = 1$, for k = 1, 2, …, 2n, is to be solved to obtain the control gains $\mathbf{g}$ and $\mathbf{p}$. Denoting $\mathbf{r}_k = \mathbf{H}(s_k)\mathbf{b}$, the characteristic equation can be rearranged in a matrix form [51] as

$$\begin{bmatrix} \mathbf{r}_1{}^{\mathrm{T}} & s_1\mathbf{r}_1{}^{\mathrm{T}} \\ \mathbf{r}_2{}^{\mathrm{T}} & s_2\mathbf{r}_2{}^{\mathrm{T}} \\ \vdots & \vdots \\ \mathbf{r}_{2n}{}^{\mathrm{T}} & s_{2n}\mathbf{r}_{2n}{}^{\mathrm{T}} \end{bmatrix} \begin{Bmatrix} \mathbf{g} \\ \mathbf{p} \end{Bmatrix} = \begin{Bmatrix} 1 \\ 1 \\ \vdots \\ 1 \end{Bmatrix} \tag{4.44}$$

Then, the control gains can be determined by inversion of the matrix

$$\mathbf{G} = \begin{bmatrix} \mathbf{r}_1{}^{\mathrm{T}} & s_1\mathbf{r}_1{}^{\mathrm{T}} \\ \mathbf{r}_2{}^{\mathrm{T}} & s_2\mathbf{r}_2{}^{\mathrm{T}} \\ \vdots & \vdots \\ \mathbf{r}_{2n}{}^{\mathrm{T}} & s_{2n}\mathbf{r}_{2n}{}^{\mathrm{T}} \end{bmatrix} \tag{4.45}$$

Two theorems pertaining to the property of **G** and the solution of Eq. (4.44) were given in [51] with proofs. For the sake of convenience, the theorems are restated here without proofs.

Theorem 1: **G** is invertible if the system is controllable and s_k for $k = 1, 2, \ldots, 2n$ are distinct.

Theorem 2: If **G** is invertible and the set $[s_1 \quad s_1 \quad \cdots \quad s_{2n}]^{\mathrm{T}}$ is closed under conjugation, then **g** and **p** are real.

It is interesting to note that it is not necessary to place a sensor or an actuator at every DoF of the system. In theory, all the poles can be assigned using a single actuator and the minimum number of sensors required is determined by the number of pairs of complex conjugate poles. For instance, there should be at least 3 sensors at different coordinates to assign 3 pairs of complex conjugate poles. If there are more or fewer sensors, the gains can be sought in the least-squares sense.

Zero-assignment problem

The characteristic equation of the zeros of a receptance function can be given by

$$\mathbf{e}_i{}^{\mathrm{T}}\Big(\mathbf{H}(s_k)[1 - (\mathbf{g} + s_k\mathbf{p})^{\mathrm{T}}\mathbf{H}(s_k)\mathbf{b}] + \mathbf{H}(s_k)\mathbf{b}(\mathbf{g} + s_k\mathbf{p})^{\mathrm{T}}\mathbf{H}(s_k)\Big)\mathbf{e}_j = 0 \tag{4.46}$$

for $k = 1, 2, \ldots, l$ and $l \leq 2(n-1)$. Rearranging Eq. (4.46) gives

$$\begin{aligned} -h_{ij}(s_k)[\mathbf{g}^{\mathrm{T}}\mathbf{H}(s_k)\mathbf{b} + s_k\mathbf{p}^{\mathrm{T}}\mathbf{H}(s_k)\mathbf{b}] \\ + \mathbf{e}_i{}^{\mathrm{T}}\mathbf{H}(s_k)\mathbf{b}\big[\mathbf{g}^{\mathrm{T}}\mathbf{H}(s_k)\mathbf{e}_j + s_k\mathbf{p}^{\mathrm{T}}\mathbf{H}(s_k)\mathbf{e}_j\big] \\ = -h_{ij}(s_k) \end{aligned} \tag{4.47}$$

or

$$\begin{aligned}\left(-h_{ij}(s_k)\mathbf{b}^{\mathrm{T}}\mathbf{H}(s_k)^{\mathrm{T}} + \mathbf{e}_i{}^{\mathrm{T}}\mathbf{H}(s_k)\mathbf{b}\mathbf{e}_j{}^{\mathrm{T}}\mathbf{H}(s_k)^{\mathrm{T}}\right)\mathbf{g} \\ + s_k\left(-h_{ij}(s_k)\mathbf{b}^{\mathrm{T}}\mathbf{H}(s_k)^{\mathrm{T}}\right. \\ \left. + \mathbf{e}_i{}^{\mathrm{T}}\mathbf{H}(s_k)\mathbf{b}\mathbf{e}_j{}^{\mathrm{T}}\mathbf{H}(s_k)^{\mathrm{T}}\right)\mathbf{p} = -h_{ij}(s_k)\end{aligned} \tag{4.48}$$

Eq. (4.48) can be written in a matrix form by letting $\mathbf{t}_k{}^{\mathrm{T}} = -h_{ij}(s_k)\mathbf{b}^{\mathrm{T}}\mathbf{H}(s_k)^{\mathrm{T}} + \mathbf{e}_i{}^{\mathrm{T}}\mathbf{H}(s_k)\mathbf{b}\mathbf{e}_j{}^{\mathrm{T}}\mathbf{H}(s_k)^{\mathrm{T}}$, which is

$$\begin{bmatrix}\mathbf{t}_1{}^{\mathrm{T}} & s_1\mathbf{t}_1{}^{\mathrm{T}} \\ \mathbf{t}_2{}^{\mathrm{T}} & s_2\mathbf{t}_2{}^{\mathrm{T}} \\ \vdots & \vdots \\ \mathbf{t}_l{}^{\mathrm{T}} & s_l\mathbf{t}_l{}^{\mathrm{T}}\end{bmatrix}\begin{Bmatrix}\mathbf{g} \\ \mathbf{p}\end{Bmatrix} = \begin{Bmatrix}-h_{ij}(s_1) \\ -h_{ij}(s_2) \\ \vdots \\ -h_{ij}(s_l)\end{Bmatrix} \tag{4.49}$$

Similar to Eq. (4.44), this equation allows the determination of gains **g** and **p**, which are required to be real to be realizable as they have direct influence over the system's stiffness and damping matrix. For that reason, the following theorem regarding the real solution was derived.

Theorem 3: If $i = j$ and the set $[s_1 \quad s_2 \quad \dots \quad s_l]^{\mathrm{T}}$ is closed under conjugation, then **g** and **p** can be chosen as real vectors.

Assignment of poles and zeros

Combining the results from the previous two assignment problems and denoting the desired poles and zeros as $[s_1 \quad s_2 \quad \dots \quad s_r]^{\mathrm{T}}$ and $[\mu_1 \quad \mu_2 \quad \dots \quad \mu_l]^{\mathrm{T}}$ respectively lead to

$$\begin{bmatrix}\mathbf{r}_1{}^{\mathrm{T}} & s_1\mathbf{r}_1{}^{\mathrm{T}} \\ \mathbf{r}_2{}^{\mathrm{T}} & s_2\mathbf{r}_2{}^{\mathrm{T}} \\ \vdots & \vdots \\ \mathbf{r}_r{}^{\mathrm{T}} & s_r\mathbf{r}_r{}^{\mathrm{T}} \\ \mathbf{t}_1{}^{\mathrm{T}} & \mu_1\mathbf{t}_1{}^{\mathrm{T}} \\ \mathbf{t}_2{}^{\mathrm{T}} & \mu_2\mathbf{t}_2{}^{\mathrm{T}} \\ \vdots & \vdots \\ \mathbf{t}_l{}^{\mathrm{T}} & \mu_l\mathbf{t}_l{}^{\mathrm{T}}\end{bmatrix}\begin{Bmatrix}\mathbf{g} \\ \mathbf{p}\end{Bmatrix} = \begin{Bmatrix}1 \\ 1 \\ \vdots \\ 1 \\ -h_{ij}(\mu_1) \\ -h_{ij}(\mu_2) \\ \vdots \\ -h_{ij}(\mu_l)\end{Bmatrix} \tag{4.50}$$

where $r + l \leq 2n$.

Controllability and observability

The controllability and observability are two important properties of a control system. Controllability is associated with the ability to control all the states of a system of a certain actuator configuration whilst observability measures the ability to estimate the states of a system with a particular sensor configuration. It is true that all the poles of a closed-loop system can be assigned arbitrarily in the complex plane if the system is controllable and observable. As a matter of fact, the pole-zero cancellation is achieved by making use of the controllability or the observability of the system.

The classical definitions of the two properties are described in state-space form rather than in physical coordinates. The state-space form of a linear time-invariant system can be expressed as

$$\dot{\mathbf{z}}(t) = \mathbf{A}\mathbf{z}(t) + \mathbf{D}\mathbf{u}(t) \tag{4.51}$$

$$\mathbf{y}(t) = \mathbf{C}\mathbf{z}(t) \tag{4.52}$$

where $\mathbf{z}(t) = \begin{Bmatrix}\mathbf{q}(t)\\ \dot{\mathbf{q}}(t)\end{Bmatrix}$ is the $2n \times 1$ state vector, $\mathbf{u}(t)$ is an $r \times 1$ input vector, $\mathbf{y}(t)$ is a $p \times 1$ output vector, and

$$\mathbf{A} = \begin{bmatrix}\mathbf{0} & \mathbf{I}\\ -\mathbf{M}^{-1}\mathbf{K} & -\mathbf{M}^{-1}\mathbf{C}\end{bmatrix}_{2n\times 2n}, \qquad \mathbf{D} = \begin{bmatrix}\mathbf{0}\\ \mathbf{M}^{-1}\mathbf{B}\end{bmatrix}_{2n\times r} \tag{4.53}$$

and $\mathbf{C}$ is a $p \times 2n$ output coefficient matrix. Recall that $\mathbf{B} \in \mathbb{R}^{n\times \boldsymbol{r}}$ is the input coefficient matrix that implies the coordinates of the actuators. $\mathbf{u}(t)$ may be written as $\mathbf{u}(t) = [\mathbf{G}^{\mathrm{T}} \quad \mathbf{P}^{\mathrm{T}}]\mathbf{z}(t)$ in a MIMO state-feedback control.

Following the description in Inman's book [152], the state, $\mathbf{z}(t)$, is said to be controllable at $t = t_0$ if there exists a piecewise continuous bounded input $\mathbf{u}(t)$ that causes the state vector to move to any final value $\mathbf{z}(t_f)$ in a finite time $t_f > t_0$. A system is said to be completely controllable if each state $\mathbf{z}(t_0)$ is controllable. Controllability can be examined by the rank deficiency of the controllability matrix, which can be defined by

$$[\mathbf{D} \quad \mathbf{AD} \quad \mathbf{A}^2\mathbf{D} \quad \cdots \quad \mathbf{A}^{2n-1}\mathbf{D}]_{2n\times 2nr} \tag{4.54}$$

A system is completely controllable if and only if Eq. (4.54) has rank 2*n*.

Inman [152] stated that the system is completely observable if, for each initial state $\mathbf{z}(t_0)$, there exists a finite time $t_f > t_0$ such that the information of $\mathbf{u}(t), \mathbf{A}, \mathbf{D}, \mathbf{C},$ and $\mathbf{y}(t)$ is sufficient to determine $\mathbf{z}(t_0)$ for any (unbounded) input $\mathbf{u}(t)$. In other words, observability refers to the determination of the current state from future output [148]. Observability can be tested through the rank deficiency of the observability matrix, which is

$$\begin{bmatrix} \mathbf{C} \\ \mathbf{CA} \\ \vdots \\ \mathbf{CA}^{2n-1} \end{bmatrix}_{2np \times 2n} \tag{4.55}$$

The system is completely observable if and only if Eq. (4.54) has rank 2*n*.

One may argue that transforming a second-order differential equation to its state-space form destroys the desired properties of the matrices and loses the physical meanings. Hamdan and Nayfeh [153] proposed a method that quantitatively measures a system's the modal controllability and observability under its second-order form. For an *n*-DoFs MIMO control system

$$\mathbf{M}\ddot{\mathbf{q}}(t) + \mathbf{C}\dot{\mathbf{q}}(t) + \mathbf{K}\mathbf{q}(t) = \mathbf{B}\mathbf{u}(t), \qquad \mathbf{y}(t) = \mathbf{R}^{\mathrm{T}}\mathbf{q}(t) + \mathbf{T}^{\mathrm{T}}\dot{\mathbf{q}}(t) \tag{4.56}$$

they showed that (1) the i^{th} mode is completely controllable from the j^{th} input if and only if

$$\operatorname{rank}\left[s_i{}^2\mathbf{M} + s_i\mathbf{C} + \mathbf{K} \quad \vdots \quad \mathbf{b}_j\right] = n \tag{4.57}$$

and (2) the $^{i\text{th}}$ mode is completely observable in the k^{th} output if and only if

$$\operatorname{rank}\begin{bmatrix} \mathbf{r}_k{}^{\mathrm{T}} + s_i\mathbf{t}_k{}^{\mathrm{T}} \\ s_i{}^2\mathbf{M} + s_i\mathbf{C} + \mathbf{K} \end{bmatrix} = n \tag{4.58}$$

where $\mathbf{r}_k$ and $\mathbf{t}_k$ are the k^{th} columns of **R** and **T**, respectively. The modal controllability and observability can also be tested using the system's left and right eigenvectors, respectively. Base on the tests using eigenvectors, they proposed to use

(1) The cosine of the angle between $\mathbf{b}_j$ and the left eigenvector $\mathbf{l}_i$ as a measure of controllability of the i^{th} mode from the j^{th} input. This can be shown by

$$\cos\theta_{ij} = \frac{\left|\mathbf{l}_i{}^{\mathrm{T}}\mathbf{b}_j\right|}{\left\|\mathbf{b}_j\right\|\left\|\mathbf{l}_i\right\|} \tag{4.59}$$

(2) The cosine of the angle between $\mathbf{r}_k + s_i\mathbf{t}_k$ and the right eigenvector $\mathbf{v}_i$ as a measure of observability of the i^{th} mode from the k^{th} output. This can be shown by

$$\cos\phi_{ki} = \frac{\left|\mathbf{v}_i{}^{\mathrm{T}}\left(\mathbf{r}_k{}^{\mathrm{T}} + s_i\mathbf{t}_k{}^{\mathrm{T}}\right)\right|}{\left\|\mathbf{r}_k{}^{\mathrm{T}} + s_i\mathbf{t}_k{}^{\mathrm{T}}\right\|\left\|\mathbf{v}_i\right\|} \tag{4.60}$$

The higher the magnitude of the measure is, the easier it is to control or observe the eigenvalues.

Example 4.3.1

Consider the 5-DoFs undamped system in example 4.2.1 with the following parameters:

$$\mathbf{B}^{\mathrm{T}} = \begin{bmatrix} 1 & 0 & 0 & 0 & 0 \\ 0 & 0 & 1 & 0 & 0 \end{bmatrix}, \qquad \mathbf{R}^{\mathrm{T}} = \begin{bmatrix} 0 & 1 & 0 & 0 & 0 \\ 0 & 0 & 0 & 1 & 0 \end{bmatrix}, \qquad \mathbf{T} = \mathbf{0}$$

The input and output matrices suggest that there are two individual actuators at the first and the third coordinates and two displacement sensors at the second and the forth coordinates. The mode shapes are normalized and plotted in Fig 4.13. By examining the mode shapes, it can be seen that a mode is obviously uncontrollable when the actuator is placed at the nodal point. Likewise, a mode cannot be observed when the displacement sensor is placed at the nodal point. Although the mode shapes can provide an intuitive sense of the modal controllability and observability, it fails to give quantitative information and becomes harder to interpret when more actuators/sensors are implemented. The corresponding modal controllability measures for this example are listed in Table 4.2 whilst the modal observability measures are listed in Table 4.3. Those measures allows quantitative assessments of the inputs and outputs, and it can be found that the measures are in good agreement with the observation from the mode

shapes. For instance, the fourth mode is controllable from the first input and almost uncontrollable from the second input as the location of the second input is close to a nodal point. This also applies to the observability of the fourth mode in which it is almost unobservable from the second sensor at the fourth coordinate.

Table 4. 2. Modal controllability measures.

		Mode				
		1	2	3	4	5
Input	1	0.2627	0.5374	0.0664	0.9731	0.0023
	2	0.7348	0.3043	0.1529	0.0245	0.0289

Table 4. 3. Modal observability measures.

		Mode				
		1	2	3	4	5
Output	1	0.4947	0.7293	0.0421	0.2283	0.0036
	2	0.338	0.246	0.7026	0.0078	0.4342

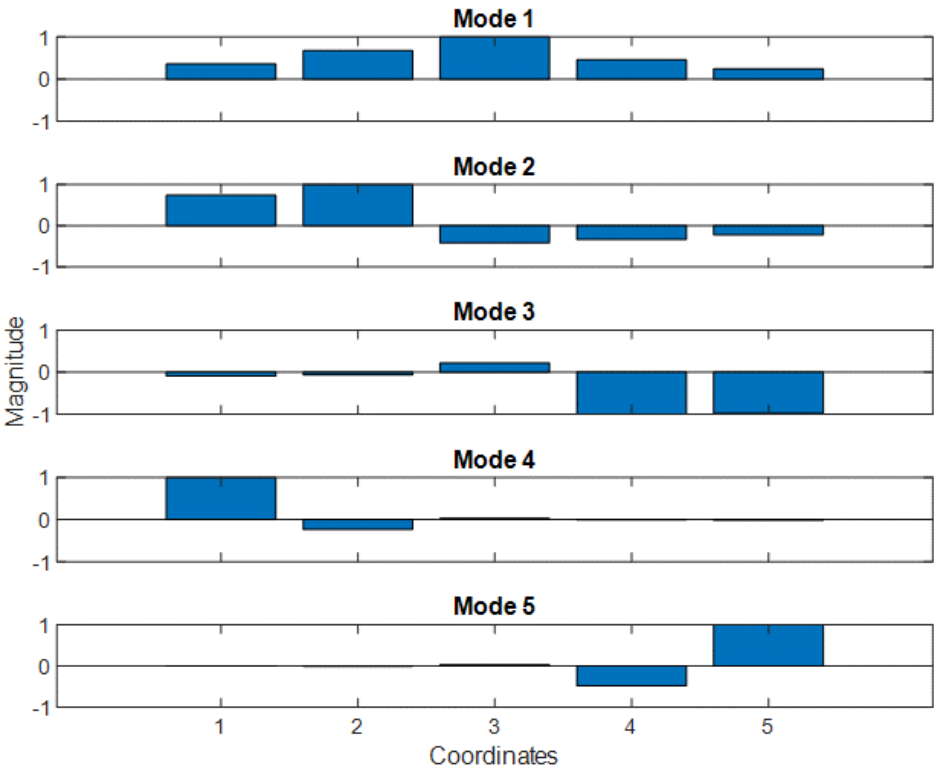

Figure 4. 13. Mode shapes of the 5-DoFs system.

4.3.1. Partial pole assignment

In the previous section, it has been shown that one or multiple poles can be assigned using receptance-based active control. However, this does not guarantee that all the other unassigned poles would remain stable or that they would not be shifted to unwanted frequencies. To overcome this issue, it is preferable to only assign the problematic poles and let the others remain unchanged. A receptance-based method for partial pole assignment was proposed by Ram and Mottershead [110] in 2013. This was a new formulation that extended the single-input control described above and was also applicable to Multiple-Input-Multiple-Output (MIMO) control. The theory is presented as follows.

Single-input control

The quadratic eigenvalue problems associated with the open loop and closed loop *n*-DoFs system are

$$\left(\lambda_k{}^2\mathbf{M} + \lambda_k\mathbf{C} + \mathbf{K}\right)\mathbf{v}_k = 0, \qquad k = 1, 2, \dots, 2n \tag{4.61}$$

and

$$\begin{gathered}(\mu_k{}^2\mathbf{M} + \mu_k\mathbf{C} + \mathbf{K})\mathbf{w}_k = \mathbf{b}(\mathbf{g}^{\mathrm{T}} + \mu_k\mathbf{p}^{\mathrm{T}})\mathbf{w}_k, \\ k = 1, 2, \dots, 2n\end{gathered} \tag{4.62}$$

Assuming that each eigenvalues in $\{\mu_k\}_{k=1}^{l}$ is distinct from eigenvalues $\{\lambda_k\}_{k=1}^{2n}$ of the open loop system and that $\mu_k = \lambda_k$ for $k = l+1, l+2, \dots, 2n$. Applying the assumption to Eq. (4.61) gives

$$\begin{gathered}\left(\lambda_k{}^2\mathbf{M} + \lambda_k\mathbf{C} + \mathbf{K}\right)\mathbf{w}_k = \mathbf{b}(\mathbf{g}^{\mathrm{T}} + \lambda_k\mathbf{p}^{\mathrm{T}})\mathbf{w}_k, \\ k = l+1, l+2, \dots, 2n\end{gathered} \tag{4.63}$$

From Eq. (4.61), a non-trivial solution to Eq. (4.63) is $\mathbf{w}_k = \mathbf{v}_k$ and thus

$$\mathbf{b}(\mathbf{g}^{\mathrm{T}} + \lambda_k\mathbf{p}^{\mathrm{T}})\mathbf{v}_k = 0, \qquad k = l+1, l+2, \dots, 2n \tag{4.64}$$

Since $\mathbf{b} \neq 0$, transposing Eq. (4.64) gives

$$\mathbf{v}_k{}^{\mathrm{T}}(\mathbf{g}+\lambda_k\mathbf{p})=0, \qquad k=l+1,l+2,\dots,2n \tag{4.65}$$

which is the equation for the closed loop system to have the original eigenvalue λ_k for $k=l+1,l+2,\dots,2n$.

On the other hand, by inverting the dynamic stiffness matrix, the first *l* equations of Eq. (4.62) are

$$\mathbf{w}_k=\mathbf{H}(\mu_k)\mathbf{b}(\mathbf{g}^{\mathrm{T}}+\mu_k\mathbf{p}^{\mathrm{T}})\mathbf{w}_k, \qquad k=1,2,\dots,l \tag{4.66}$$

Denoting $\mathbf{H}(\mu_k)\mathbf{b}=\mathbf{r}_k$ and rearranging Eq. (4.66) give

$$\mathbf{r}_k{}^{\mathrm{T}}(\mathbf{g}+\mu_k\mathbf{p})=1, \qquad k=1,2,\dots,l \tag{4.67}$$

which is the characteristic equation for the closed loop system to have the desired eigenvalue μ_k for $k=1,2,\dots,l$. Combining Eqs. (4.65) and (4.67) leads to

$$\begin{bmatrix} \mu_1\mathbf{r}_1{}^{\mathrm{T}} & \mathbf{r}_1{}^{\mathrm{T}} \\ \vdots & \vdots \\ \mu_l\mathbf{r}_l{}^{\mathrm{T}} & \mathbf{r}_l{}^{\mathrm{T}} \\ \lambda_{l+1}\mathbf{v}_{l+1}{}^{\mathrm{T}} & \mathbf{v}_{l+1}{}^{\mathrm{T}} \\ \vdots & \vdots \\ \lambda_{2n}\mathbf{v}_{2n}{}^{\mathrm{T}} & \mathbf{v}_{2n}{}^{\mathrm{T}} \end{bmatrix} \begin{Bmatrix} \mathbf{p} \\ \mathbf{g} \end{Bmatrix} = \begin{Bmatrix} 1 \\ \vdots \\ 1 \\ \mathbf{0} \end{Bmatrix} \tag{4.68}$$

This equation allows determination of the gains required for partial pole assignment using single input control. It can be noted that Eq. (4.68) requires not only receptances but also eigenvectors $\{\mathbf{v}_k\}_{k=l+1}^{2n}$. It could be argued that Eq. (4.68) may not be a receptance-based method as it also requires eigenvectors; however, in theory, the eigenvectors can be derived from the receptances. As a result, in this case there is still no need to know the systems matrices **M**, **C**, and **K**.

MIMO control

The quadratic eigenvalue problem of a closed-loop system subject to *m* multiple inputs can be written as

$$(\mu_k{}^2\mathbf{M}+\mu_k\mathbf{C}+\mathbf{K})\mathbf{w}_k=\mathbf{B}(\mathbf{G}^{\mathrm{T}}+\mu_k\mathbf{P}^{\mathrm{T}})\mathbf{w}_k \tag{4.69}$$

where

$$\mathbf{B} = [\mathbf{b}_1 \quad \mathbf{b}_2 \quad \dots \quad \mathbf{b}_m], \qquad \mathbf{G} = [\mathbf{g}_1 \quad \mathbf{g}_2 \quad \cdots \quad \mathbf{g}_m], \\ \mathbf{P} = [\mathbf{p}_1 \quad \mathbf{p}_2 \quad \cdots \quad \mathbf{p}_m] \tag{4.70}$$

Eq. (4.69) can be rewritten as

$$\mathbf{w}_k = \mathbf{H}(\mu_k)\Big(\mathbf{b}_1(\mathbf{g}_1{}^{\mathrm{T}} + \mu_k \mathbf{p}_1{}^{\mathrm{T}}) + \mathbf{b}_2(\mathbf{g}_2{}^{\mathrm{T}} + \mu_k \mathbf{p}_2{}^{\mathrm{T}}) + \cdots \\ + \mathbf{b}_m(\mathbf{g}_m{}^{\mathrm{T}} + \mu_k \mathbf{p}_m{}^{\mathrm{T}})\Big)\mathbf{w}_k \tag{4.71}$$

Let $\mathbf{r}_{\mu_k,j} = \mathbf{H}(\mu_k)\mathbf{b}_j$ and $\alpha_{\mu_k,j} = \left(\mathbf{g}_j{}^{\mathrm{T}} + \mu_k \mathbf{p}_j{}^{\mathrm{T}}\right)\mathbf{w}_k$, then Eq. (4.71) could be expressed in the form

$$\mathbf{w}_k = \sum_{j=1}^{m} \mathbf{r}_{\mu_k,j}\alpha_{\mu_k,j}\ , \qquad k = 1,2,\dots,l \tag{4.72}$$

which suggests that the eigenvector $\mathbf{w}_k$ of the closed loop system is a linear combination of $\mathbf{r}_{\mu_k,j}$ with coefficients $\alpha_{\mu_k,j}$ for $j = 1,2,\dots,m$. The denotation $\alpha_{\mu_k,j} = \left(\mathbf{g}_j{}^{\mathrm{T}} + \mu_k \mathbf{p}_j{}^{\mathrm{T}}\right)\mathbf{w}_k$ could be written in a matrix form as

$$\begin{bmatrix} \mu_k\mathbf{w}_k{}^{\mathrm{T}} & \mathbf{0} & \dots & \mathbf{0} & \mathbf{w}_k{}^{\mathrm{T}} & \mathbf{0} & \dots & \mathbf{0} \\ \mathbf{0} & \mu_k\mathbf{w}_k{}^{\mathrm{T}} & \dots & \mathbf{0} & \mathbf{0} & \mathbf{w}_k{}^{\mathrm{T}} & \dots & \mathbf{0} \\ \vdots & \vdots & \ddots & \vdots & \vdots & \vdots & \ddots & \vdots \\ \mathbf{0} & \mathbf{0} & \dots & \mu_k\mathbf{w}_k{}^{\mathrm{T}} & \mathbf{0} & \mathbf{0} & \dots & \mathbf{w}_k{}^{\mathrm{T}} \end{bmatrix} \begin{Bmatrix} \mathbf{p}_1 \\ \vdots \\ \mathbf{p}_m \\ \mathbf{g}_1 \\ \vdots \\ \mathbf{g}_m \end{Bmatrix}_{2mn\times 1} \\ = \begin{Bmatrix} \alpha_{\mu_k,1} \\ \alpha_{\mu_k,2} \\ \vdots \\ \alpha_{\mu_k,m} \end{Bmatrix}_{m\times 1} \tag{4.73}$$

or

$$\mathbf{U}_k\mathbf{y} = \boldsymbol{\alpha}_k,\ k = 1,2,\dots,l \tag{4.74}$$

with the obvious definition of $\mathbf{U}_k$, $\mathbf{y}$ and $\boldsymbol{\alpha}_k$. From Eq. (4.69), considering the unaltered poles results in

$$\begin{aligned}\Big(\mathbf{b}_1(\mathbf{g}_1{}^{\mathrm{T}}+\lambda_k\mathbf{p}_1{}^{\mathrm{T}})+\mathbf{b}_2(\mathbf{g}_2{}^{\mathrm{T}}+\lambda_k\mathbf{p}_2{}^{\mathrm{T}})+\cdots\\ +\mathbf{b}_m(\mathbf{g}_m{}^{\mathrm{T}}+\lambda_k\mathbf{p}_m{}^{\mathrm{T}})\Big)\mathbf{v}_k=\mathbf{0},\\ k=l+1,l+2,\ldots,2n\end{aligned} \tag{4.75}$$

As $\mathbf{b}_m \neq 0$, Eq. (4.75) is satisfied when

$$\begin{bmatrix}\lambda_k\mathbf{v}_k{}^{\mathrm{T}} & \mathbf{0} & \ldots & \mathbf{0} & \mathbf{v}_k{}^{\mathrm{T}} & \mathbf{0} & \ldots & \mathbf{0}\\ \mathbf{0} & \lambda_k\mathbf{v}_k{}^{\mathrm{T}} & \ldots & \mathbf{0} & \mathbf{0} & \mathbf{v}_k{}^{\mathrm{T}} & \ldots & \mathbf{0}\\ \vdots & \vdots & \ddots & \vdots & \vdots & \vdots & \ddots & \vdots\\ \mathbf{0} & \mathbf{0} & \ldots & \lambda_k\mathbf{v}_k{}^{\mathrm{T}} & \mathbf{0} & \mathbf{0} & \ldots & \mathbf{v}_k{}^{\mathrm{T}}\end{bmatrix}\begin{Bmatrix}\mathbf{p}_1\\ \vdots\\ \mathbf{p}_m\\ \mathbf{g}_1\\ \vdots\\ \mathbf{g}_m\end{Bmatrix}_{2mn\times 1} = \begin{Bmatrix}0\\0\\ \vdots\\0\end{Bmatrix}_{m\times 1} \tag{4.76}$$

or

$$\mathbf{Q}_k\mathbf{y}=\mathbf{0}, \qquad k=l+1,l+2,\ldots,2n \tag{4.77}$$

Combining Eqs. (4.74) and (4.77) gives

$$\begin{bmatrix}\mathbf{U}_1\\ \vdots\\ \mathbf{U}_l\\ \mathbf{Q}_{l+1}\\ \vdots\\ \mathbf{Q}_{2n}\end{bmatrix}_{2mn\times 2mn}\begin{Bmatrix}\mathbf{p}_1\\ \vdots\\ \mathbf{p}_m\\ \mathbf{g}_1\\ \vdots\\ \mathbf{g}_m\end{Bmatrix}_{2mn\times 1} = \begin{Bmatrix}\boldsymbol{\alpha}_1\\ \vdots\\ \boldsymbol{\alpha}_l\\ \mathbf{0}\\ \vdots\\ \mathbf{0}\end{Bmatrix}_{2nm\times 1} \tag{4.78}$$

The partial pole assignment problem for MIMO control may be addressed through the procedure:

(1) Determine the desired poles, $\{\mu_k\}_{k=1}^{l}$ and $\{\lambda_k\}_{k=l+1}^{2n}$, number of input *m*, and the input matrix B for the system.

(2) Design arbitrary $\alpha_{\mu_k,j}$ and obtain $\mathbf{w}_k$ ($k=1,2,\ldots,l$ and $j=1,2,\ldots,m$) using Eq. (4.72). It can be seen that the poles of the system are closed under conjugation if **P** and **G** are real, so one must choose $\alpha_{\mu_k,j}=\bar{\alpha}_{\overline{\mu_k},j}$.

(3) Solve Eq. (4.78) for control gains $\mathbf{p}_j$ and $\mathbf{g}_j$. When $m > 1$, the solution is not unique and depends on the choice of $\alpha_{\mu_k,j}$.

It should be noted that although in the aforementioned procedure the constants $\alpha_{\mu_k,j}$ are designed arbitrarily, $\alpha_{\mu_k,j}$ may be carefully selected to also assign the eigenvectors of the system.

Example 4.3.1

Consider the 5-DoFs system in example 4.2.1 with $\mathbf{C} = (5 \times 10^{-5} \times \mathbf{K}$. Determine the required **G** and **P** so that the first two pairs of eigenvalues are $\mu_{1,2} = -1 \pm (27 \times 2\pi)\mathrm{j}$ and $\mu_{3,4} = -1.2 \pm (37 \times 2\pi)\mathrm{j}$ and the remaining eigenstructure are unchanged.

Assuming that

$$m = 3, \mathbf{B} = \begin{bmatrix} 0 & 1 & 1 \\ 1 & 1 & 0 \\ 1 & 0 & 1 \\ 0 & 0 & 0 \\ 1 & 1 & 1 \end{bmatrix}, \text{and } \begin{Bmatrix} \alpha_{\mu_k,1} \\ \alpha_{\mu_k,2} \\ \alpha_{\mu_k,3} \end{Bmatrix} = \begin{Bmatrix} 0.5 \\ 1 \\ 2 \end{Bmatrix} \text{ for } k = 1,2,3,4$$

The control gains **G** and **P** can be obtained by following the above-mentioned procedure, which can be shown explicitly as

$$\mathbf{P} = \begin{bmatrix} -0.04 & -0.08 & -0.16 \\ -0.29 & -0.58 & -1.16 \\ -1.21 & -2.41 & -4.82 \\ -0.19 & -0.38 & -0.76 \\ -0.05 & -0.11 & -0.21 \end{bmatrix} \text{ and } \mathbf{G} = (10^4) \times \begin{bmatrix} -0.32 & -0.64 & -1.28 \\ -1.41 & -2.82 & -5.64 \\ -0.42 & -0.85 & -1.69 \\ 0.01 & 0.02 & 0.04 \\ 0.01 & 0.03 & 0.05 \end{bmatrix}$$

Note that the numbers are rounded to 2 decimal places for better representation. Substituting the gains into the closed-loop equation of motion leads to asymmetric damping and stiffness matrices. The resulting poles are listed in Table 4.4. It is clear that the desired poles are exactly achieved whilst the other poles and their eigenvectors remain the same. However, it can be seen that the control effort involved in **G** may be too large for practical implementation, and thus the *cost issue* of the controller design is of great importance. Moreover, the issue of *time delay* between the measurements

of state and the actuation of control also plays an important factor in the performance in real applications. For instance, Bai *et al.* [154] proposed an optimization algorithm for simultaneous minimization of the feedback norms and the condition number of the closed-loop system without casting the second-order system into the state-space form. The influence of time delay was also discussed and covered for a MIMO system.

Table 4. 4. The original and achieved poles.

Original poles	Original ω_n (Hz)	Achieved poles	Achieved ω_n (Hz)
-0.49 ± 140j	22.28	-1.00 ± 169.7j	27.0
-1.05 ± 204.9j	32.61	-1.20 ± 232.5j	37.0
-1.82 ± 269.7j	42.92	-1.82 ± 269.7j	42.92
-2.74 ± 331.2j	52.71	-2.74 ± 331.2j	52.71
-4.12 ± 405.7j	64.57	-4.12 ± 405.7j	64.57

5. Inverse structural modifications of a geared rotor-bearing system

Parts of this chapter are based on a journal paper written by the author (DOI: 10.1016/j.ymssp.2018.03.008).

Inverse structural modifications have been mostly studied in theory but rarely implemented in practice. In this chapter, the inverse structural modification theory based on receptances is extended. The receptance function of a modified structure can be expressed in terms of the receptance functions of the original structure and the modifications to be made, which allows measured receptances to be used instead of system matrices or a modal model. The method proposed in this chapter can be applied to assignments of several different kinds of dynamical properties such as natural frequencies, antiresonant frequencies and receptances, and to make pole-zero cancellations.

Given the lack of experimental validation of inverse structural modification problems in published papers, a geared rotor-bearing system is manufactured and tested to validate the method and provide experimental insights. Experimental results show that more than one natural frequency or antiresonant frequency can be assigned within acceptable accuracy and that the sensitivity of modifications is crucial for the solutions of modifications cast as an optimization problem. An additional application for determining the optimal locations for given modifications so as to achieve the highest first natural frequency is also presented. The experimental results obtained prove the efficacy and the ease of use of this proposed method. This work should help make inverse structural modification a popular means of passive vibration control to improve the dynamical behaviour of real structures.

5.1. Theoretical development

The Laplace transform of the equation of motion of a linear vibrating viscously damped multi-degree-of-freedom system can be expressed as

$$(\mathbf{M}s^2 + \mathbf{C}s + \mathbf{K})\mathbf{u}(s) = \mathbf{f}(s) \tag{5.1}$$

if the initial conditions are zeros. **M**, **C**, **K** are $n \times n$ mass, damping, and stiffness matrices respectively and *n* is the total number of degrees of freedom of the system. $\mathbf{f}(s)$ is the vector of any type of excitation applied to the system. Assuming that the original structure is modified in terms of mass $\Delta\mathbf{M}$, damping $\Delta\mathbf{C}$, and stiffness $\Delta\mathbf{K}$ simultaneously, the equation of motion of the modified system can be given as

$$[(s^2\mathbf{M} + s\mathbf{C} + \mathbf{K}) + (s^2\Delta\mathbf{M} + s\Delta\mathbf{C} + \Delta\mathbf{K})]\mathbf{u}(s) = \mathbf{f}(s) \tag{5.2}$$

Premultiplying both sides by receptance matrix **H**(*s*) of the original structure and inverting the resulting matrix on the left side of the equation lead to

$$\mathbf{u}(s) = [\mathbf{I} + \mathbf{H}(s)\Delta\mathbf{Z}(s)]^{-1}\mathbf{H}(s)\mathbf{f}(s) \tag{5.3}$$

where $\Delta\mathbf{Z}(s) = (s^2\Delta\mathbf{M} + s\Delta\mathbf{C} + \Delta\mathbf{K})$ is called dynamic stiffness modification matrix which has real physical meaning of the modifications made, i.e. magnitudes and coordinates. Clearly, this equation shows that the modified receptance matrix only involves the receptance matrix of the original structure and the dynamic stiffness modification matrix. The modified receptance matrix can be further defined as

$$\widehat{\mathbf{H}}(s) = \frac{\mathrm{adj}\big(\mathbf{I} + \mathbf{H}(s)\Delta\mathbf{Z}(s)\big)\mathbf{H}(s)}{\det\big(\mathbf{I} + \mathbf{H}(s)\Delta\mathbf{Z}(s)\big)} \tag{5.4}$$

which reveals a new relationship between responses and excitations of the (modified) system. Based on the definition of the adjugate matrix, a certain ($i^{\mathrm{th}}, j^{\mathrm{th}}$) element of $\widehat{\mathbf{H}}(s)$ in which *i* is the response coordinate and *j* is the excitation coordinate of the modified receptance matrix can be given by the following

$$\hat{h}_{ij}(s) = (-1)^{i+j}\frac{\det\big((s^2\mathbf{M} + s\mathbf{C} + \mathbf{K})_{(ji)} + \Delta\mathbf{Z}(s)_{(ji)}\big)}{\det\big((s^2\mathbf{M} + s\mathbf{C} + \mathbf{K}) + \Delta\mathbf{Z}(s)\big)} \tag{5.5}$$

where subscripts (ji) indicate the matrix formed after deleting the j^{th} row and i^{th} column of the original matrix. This equation can be rewritten by extracting $\det\left((s^2\mathbf{M}+s\mathbf{C}+\mathbf{K})_{(ji)}\right)$ and $\det(s^2\mathbf{M}+s\mathbf{C}+\mathbf{K})$ from the numerator and the denominator, respectively, leading to

$$\hat{h}_{ij}(s) = (-1)^{i+j}\frac{\det\left((s^2\mathbf{M}+s\mathbf{C}+\mathbf{K})_{(ji)}\right)\det\left(\mathbf{I}+\left((s^2\mathbf{M}+s\mathbf{C}+\mathbf{K})_{(ji)}\right)^{-1}\Delta\mathbf{Z}(s)_{(ji)}\right)}{\det(s^2\mathbf{M}+s\mathbf{C}+\mathbf{K})\det(\mathbf{I}+\mathbf{H}(s)\Delta\mathbf{Z}(s))} \tag{5.6}$$

The identity matrix in the numerator is now a $(n-1)\times(n-1)$ matrix. Since $(s^2\mathbf{M}+s\mathbf{C}+\mathbf{K})$ is symmetric and invertible, the relation shown below holds.

$$(-1)^{i+j}\frac{\det\left((s^2\mathbf{M}+s\mathbf{C}+\mathbf{K})_{(ji)}\right)}{\det(s^2\mathbf{M}+s\mathbf{C}+\mathbf{K})} = h_{ij}(s) \tag{5.7}$$

Finally, the $(i^{\text{th}}, j^{\text{th}})$ receptance of the modified receptance matrix can be given by

$$\hat{h}_{ij}(s) = \frac{h_{ij}(s)\det\left(\mathbf{I}+\left((s^2\mathbf{M}+s\mathbf{C}+\mathbf{K})_{(ji)}\right)^{-1}\Delta\mathbf{Z}(s)_{(ji)}\right)}{\det(\mathrm{I}+\mathbf{H}(s)\Delta\mathbf{Z}(s))} \tag{5.8}$$

Matrix $\left((s^2\mathbf{M}+s\mathbf{C}+\mathbf{K})_{(ji)}\right)^{-1} = \tilde{\mathbf{H}}_{ij}(s)$, which is called subsidiary receptance matrix, is the inverse of a dynamic stiffness matrix whose j^{th} row and i^{th} column are deleted. The matrix might be obscure in physical meaning, but it has been shown by Mottershead [36] that each element of the matrix can actually be obtained from receptances of the original system. Any element $\tilde{h}_{t_1,t_2}$ in $\tilde{\mathbf{H}}_{ij}(s)$ can be given by

$$\tilde{h}_{t_1t_2} = h_{t_1t_2} - \left(h_{jt_1}h_{it_2}\right)/h_{ji} \tag{5.9}$$

which shows that one subsidiary frequency response function requires four receptances of the original system at most. It should be noted that $t_1, t_2 = 1,2,\dots,n$, but $t_1 \neq i$ and $t_2 \neq j$. Now it is clear that it is possible to obtain the exact modified receptance function solely based on receptances of the original system; that is to say,

apart from using a numerical model the modified receptance function can also be derived from modal testing data as long as the measurement is accurate enough.

In the case of an inverse structural modification problem, the desired frequency is prescribed whilst the dynamic stiffness modification matrix should be sought. From Eq. (5.8), it is clear that the functions in the numerator or denominator could approach zero near a desired frequency; therefore, they can be treated as the basic equations for natural frequency or antiresonant frequency assignments, respectively. In addition to that, the ratio between modified receptances and the corresponding original receptances could also be readily assigned through Eq. (5.8). If the form of the modification is simple, such as a rank-one modification, it is possible to find the required modification by solving the corresponding equations directly. However, directly solving the equation could be challenging especially when the number of modification is large or there are multiple desired frequencies. In fact, an approximate solution might be sufficient in some cases in which the exact solution does not exist or is hard to compute. Besides, there might be multiple solutions to an assignment problem. Casting the assignment problem as an optimization problem provides a relatively flexible way to find a solution, which can also be seen from several published papers.

Therefore, it is reasonable to construct the basic objective function as

$$\min_{\mathbf{x}} \left\{ \sum_{r=1}^{n} \alpha_r \left(\det(\mathbf{I} + \mathbf{H}(s_r)\Delta\mathbf{Z}(s_r, \mathbf{x})) \right)^2 \right\} \tag{5.10}$$

and

$$\min_{\mathbf{x}} \left\{ \sum_{r=1}^{n} \alpha_r \left(\det\left(\mathbf{I} + \widetilde{\mathbf{H}}_{ij}(s_r)\Delta\mathbf{Z}(s_r, \mathbf{x})_{(ji)}\right) \right)^2 \right\} \tag{5.11}$$

for natural frequency and antiresonant frequency assignment, respectively. In the objective functions, α_r are the positive weighting coefficients, and the modification matrix is now a function of eigenvalues and design variables **x**. Since a determinant is used, the value of the objective function might vary enormously in the design space

especially when the desired frequency is high. In order to avoid very steep gradients in the feasible domain, which can reduce the step size in the optimization process, scaling the functions to some extent is often necessary. However, there is no definitive criterion indicating which form of scaling is the most suitable. This might be a problem that is determined on a case-by-case basis. Thus scaling is not yet implemented in either equation above. As $\Delta\mathbf{Z}(s_r, \mathbf{x})$ is symmetric in passive control and often a sparse matrix, the number of receptances required for the assignment is related to the number of non-zero entities in $\Delta\mathbf{Z}(s_r, \mathbf{x})$ and the number of desired frequencies. It can be seen that the locations where the modifications are made are the same as the locations at which the receptances are measured.

In addition to the objective functions for natural frequency and antiresonant frequency assignments, the problem for the eigenstructure assignment can be formulated in the same fashion. Premultiplying the quadratic eigenvalue problem of the modified system in Eq. (5.2) by receptance matrix $\mathbf{H}(s_r)$ gives

$$\mathbf{u}_r + \mathbf{H}(s_r)\Delta\mathbf{Z}(s_r)\mathbf{u}_r = \mathbf{0} \tag{5.12}$$

Similarly, the objective function for the eigenstructure assignment can be written as

$$\min_{\mathbf{x}} \left\{ \sum_{r=1}^{n} \alpha_r \|\mathbf{u}_r + \mathbf{H}(s_r)\Delta\mathbf{Z}(s_r, \mathbf{x})\mathbf{u}_r\|^2 \right\} \tag{5.13}$$

where $(s_r, \mathbf{u}_r)$ is the desired eigenpair. To examine the equation, it is reasonable to start from the influence of the dynamic stiffness modification matrix as it is symmetric and often sparse. It can be seen from the term $\Delta\mathbf{Z}(s_r, \mathbf{x})\mathbf{u}_r$ that the modifications are required to apply at the coordinates of which the nodal displacements are of interest in order for the modifications to be included in the objective problem. A small number of modifications is always preferred and thus $\mathbf{u}_r$ is not likely to be completely defined. In this case, the elements in $\mathbf{u}_r$ cannot define a complete eigenvector to the mode but some nodal displacements. The resulting vector in the right-hand side of Eq. (5.12) would no longer be zero even given the solution of the modification. As a matter of fact, it is much more demanding to assign eigenstructures than to assign poles or zeros.

Thus, the objective function for eigenstructure assignment should consider rows in Eq. (5.13) that are related to the DoFs of the modifications, which can be shown by

$$\min_{\mathbf{x}} \left\{ \sum_{r=1}^{n} \alpha_r \| (\mathbf{u}_r + \mathbf{H}(s_r)\Delta\mathbf{Z}(s_r, \mathbf{x})\mathbf{u}_r) \odot \mathbf{e}_r \|^2 \right\} \tag{5.14}$$

where $\mathbf{e}_r$ is a vector that has the same size of $\mathbf{u}_r$ and has 1 at the entries that associate with the DoFs of the modifications, and $\odot$ denotes the Hadamard product (also known as Schur product or entrywise product), which produces element-wise multiplication of two matrices/vectors.

There are several algorithms nowadays for solving nonlinear programming problems. For example, an interior-point algorithm “fmincon” provided by MathWorks is readily available. It has been supported and shown by many published papers that barrier methods are the foundation of modern interior method. A comprehensive paper including the history, developments, and important features of the interior-point method and its relationship with barrier methods was presented by Forsgren *et al.* [155]. Alternatively, genetic algorithms can also be used to avoid guessing initial points and prevent the solution from converging to local minimums around the initial points. Since the optimization algorithm is not the objective of this research, relevant details will not be included here.

5.2. Experimental setup

The laboratory test rig is essentially a geared rotor-bearing system shown in Figs. 5.1 and 5.3. A short shaft is coupled to a one-meter-long shaft of the same diameter (17 mm) through a pair of spur gears, and there are two identical discs which can be moved freely on the long shaft or easily removed from the rig. In fact, the discs (and the additional masses of nut sets bolted to them) will be considered to be the mass modification for the test rig. Each disc which weighs 658 g has several tapped holes uniformly distributed around its circumferential direction for possible additional mass modifications as shown in Fig. 5.2. The additional mass modification is achieved by

bolting or removing nuts on the disc. In Fig. 5.2 the M20-nut set and M16-nut set weigh 61g and 38g, respectively. The material of the shafts and discs is medium carbon steel while the material of the bearing holders is aluminium. The whole structure is bolted onto two aluminium profiles that are also bolted together as the base. The total mass of the system without discs is 16.35 kg. It is worth mentioning that the base should not be considered to be rigid in this case, which will definitely bring complexity to the system and in constructing the finite element model.

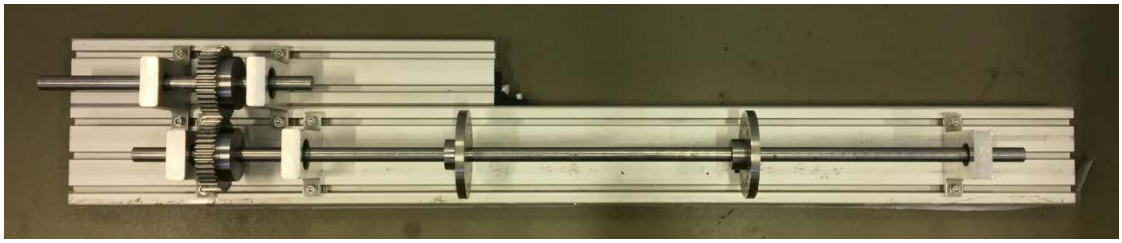

Figure 5. 1. Experimental setup.

Impact testing is utilized for the receptance measurements in this study, and there are totally 16 equally spaced measurement points with interval of 4.5 cm, denoted as p1 to p16, along the long shaft; however, not all of the measurement points may be available in practice and thus it is assumed that only five locations are available; they are p4, p5, p7, p11, and p13. Five Kistler miniature accelerometers (8728A500) that weigh 8 grams in total are used so as to minimize the mass loading effect, and the impact force is imparted through a PCB Model 086C04 impact hammer with the plastic hammer tip. Signals are sampled by LMS SCADAS III signal conditioning and data acquisition system which passes experimental data to a PC. The LMS software Test.Lab in the PC is adopted for signal processing, modal parameter estimation, and data management purposes. The experimental modal testing data can be stored and exported to the Universal File Format (.UFF), which makes processing the experimental results more convenient.

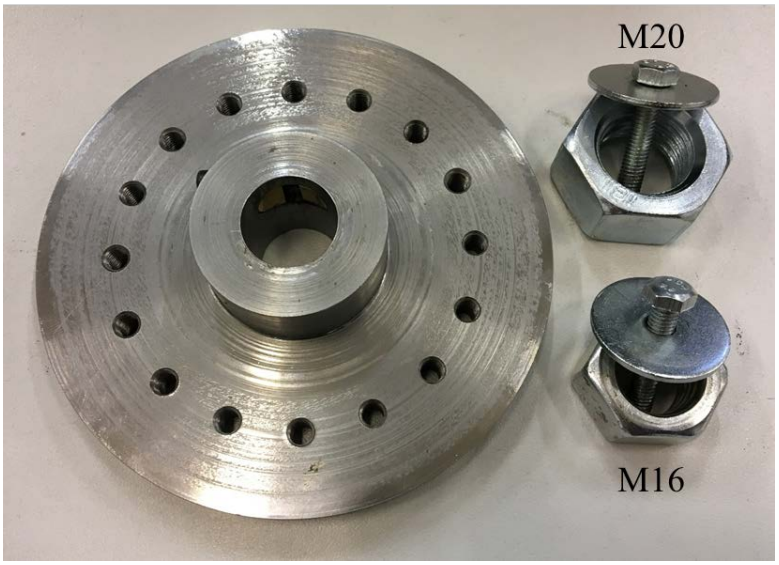

Figure 5. 2. Disc and nuts.

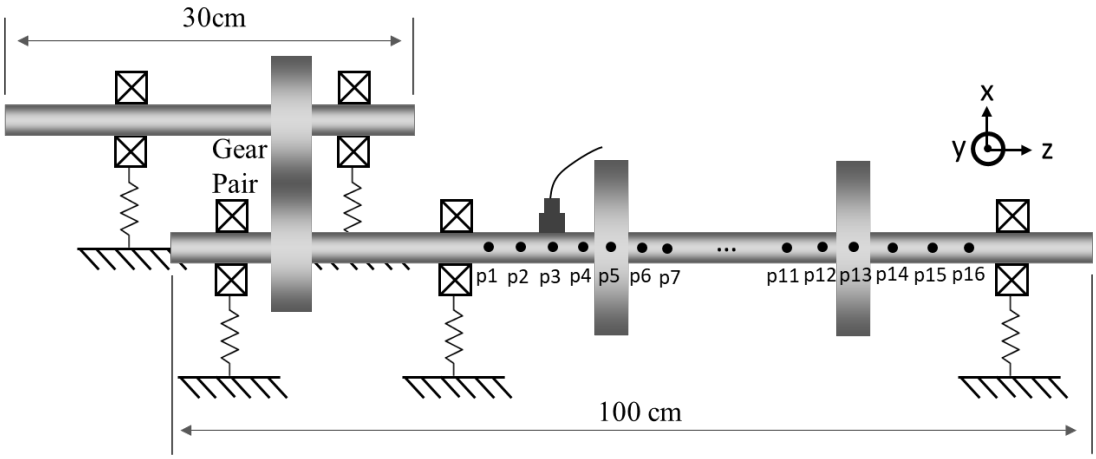

Figure 5. 3. Schematic of the geared rotor-bearing system.

5.3. Numerical simulation

The proposed technique is first applied to a numerical model (FE 1-D model) that is constructed based on the experimental setup given in the previous section. The purpose of this is to verify and evaluate the technique on such a geared rotor-bearing system. The 1-D model is first built using MATLAB, and then the model is updated based on the results from the experimental modal analysis using the inverse eigensensitivity method (see Appendix A). It should be mentioned that at this stage the discs are not included in the test rig or the model. For better discussion, a schematic of the model with the numbering of nodes is given in Fig 5.4 (Note that the lengths of the elements

in the picture are set the same for the benefit of brevity so does not reflect the true length). Each node has 5 DoFs (two in transverse directions and three in rotational directions), and thus the total number of DoFs is 150.

In the process of updating the model, the material properties (Young's modulus & Poisson ratio) of the short shaft is updated first on the component level, which are taken as the same material properties of the long shaft since the two shafts are nominally identical. Later, stiffness of the bearings (in the transverse and rotational directions) are updated on the assembly level. The first few frequencies of the updated model and the corresponding experimental results are listed and compared in Table 5.1. The experimental results are identified through modal identification technique 'PolyMAX' using LMS.Testlab from Siemens. Among the four frequencies the maximum difference is from the first frequency with just 1.34% error, and the updated parameters are given in Table 5.2. It should be pointed out that the gear contact stiffness is not updated since the torsional natural frequency is not measured and that damping is not included in the model.

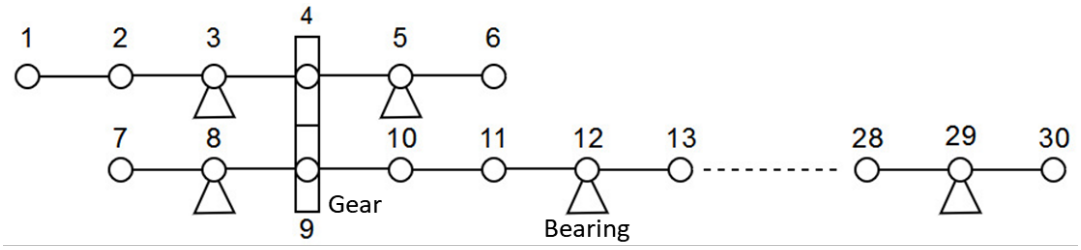

Figure 5. 4. The 1-D model with nodes indicated by circles and their numbers.

Table 5. 1. Comparison of experimentally and numerically determined natural frequencies.

	Experiment	Updated model	Difference
Bending natural frequencies (Hz)	80.59	81.78	1.48 %
	266.68	263.75	-1.10 %
	541.22	539.54	-0.31 %
	920.51	919.68	-0.09 %

Table 5. 2. Updated system parameters.

Bearing stiffness (transverse directions)	2.1753×10^7N/m	Young's modulus	203.23 GPa
Bearing stiffness (rotational directions)	28.6297 N/m	Poisson's ratio	0.3179

In this section, a number of assignment problems are studied using the updated model. For the sake of convenience, it is assumed that the form of the modification to be applied in each problem is drawn from a set of options. These options are referred to as modification set A, set B, and set C, which are: Modification set A: two point masses at node #17 and #25, Modification set B: two grounded springs at node #17 and #23 in the transverse direction, Modification set C: one spring-mass oscillator in the *y*-axis direction at whichever node. The assignment problems consisting of natural frequency assignment, antiresonant frequency assignment, eigenstructure assignment, pole-zero cancellation, and receptance assignment are presented as follows. Throughout the examples, the weighting coefficients are equal to 1 unless otherwise stated.

Natural frequency assignment

It is assumed that Modification sets A and B are available in this problem and the deign variables are arranged in **x** in sequence, which can be denoted as $\{x_1, x_2, x_3, x_4\}$. The desired natural frequency are 77 and 247 Hz. The goal is to find **x** that minimizes Eq. (5.10) in which some constraints are applied to the design variables:

$$0.1 \leq x_1 \leq 1, \qquad 0.1 \leq x_2 \leq 1, \qquad 0 \leq x_3 \leq 10^6, \qquad 0 \leq x_4 \leq 10^6$$

As this problem is an underdetermined problem, multiple solutions are possible. In order not to fall into a local minimum, particle swarm algorithm is implemented to alleviate the issue. The function "particleswarm" in Matlab is used.

A solution is found to be $\{0.1,\ 1.0,\ 7.395 \times 10^5,\ 5.929 \times 10^3\}$. The corresponding natural frequencies of the modified system are listed together with the original ones in Table 5.3. It is clear that the two desired natural frequencies are the

first two natural frequencies of the modified system and are exactly achieved. Since no constraints are imposed to the other frequencies, they are also shifted when the modifications are made. The torsional natural frequencies are not affected because no modification is made to the associated properties.

It should be mentioned that due to the nature of the particle swarm algorithm, the algorithm does not necessarily produce the same result every time it is run. For instance, another solution that achieves exactly the natural frequencies is $\{0.1318,\ 1.0,\ 8.1639 \times 10^5,\ 0.0\}$.

Table 5. 3. The original and achieved natural frequencies.

Original		Achieved	
Bending natural frequency (Hz)	Torsional natural frequency (Hz)	Bending natural frequency (Hz)	Torsional natural frequency (Hz)
(81.77, 81.77) **(263.74, 263.75)** (412.47, 412.51) (539.41, 539.43) (627.17, 627.31) (639.80, 639.95) (919.67, 919.67)	31.76 889.89	**(77.0, 77.0)** **(247.0, 247.0)** (412.47, 412.51) (491.32, 491.33) (623.40, 623.56) (639.80, 639.95) (913.47, 913.47)	31.76 889.89

Antiresonant frequency assignment

It is assumed that the receptance of interest is between node # 9 and # 20 in the *y*-axis direction and that Modification sets A and B are available for this assignment. The desired antiresonant frequency is 180 Hz. Find the design variables **x** that minimizes Eq. (5.11) in which some constraints are applied to the design variables:

$$0 \le x_1 \le 1, \qquad 0 \le x_2 \le 1, \qquad 0 \le x_3 \le 10^7, \qquad 0 \le x_4 \le 10^5$$

It is reasonable to presume that this optimization problem is quite flexible as there are four design variables to achieve one frequency assignment. In this case, interior-point algorithm is implemented to find a solution that is closest to the initial point in which

all the design variables start from zero. The algorithm would converge to a local minimum close to the initial point if a local minimum exists.

A solution is found to be $\{0.523,\ 0.1951,\ 6.8198 \times 10^4, 6.8195 \times 10^4\}$ given the initial point $\{0, 0, 0, 0\}$. An inspection on the FRFs of interest ($h_{9,20}$ in the *y*-axis direction) before and after the modifications in Fig. 5.5 can reveal that the first antiresonant frequency in the receptance function shifts from 209 to 180. The desired antiresonant frequency is exactly achieved. For better representation of the FRF in Fig. 5.5, proportional damping is added to the modified system to avoid showing deep drops/sharp peaks.

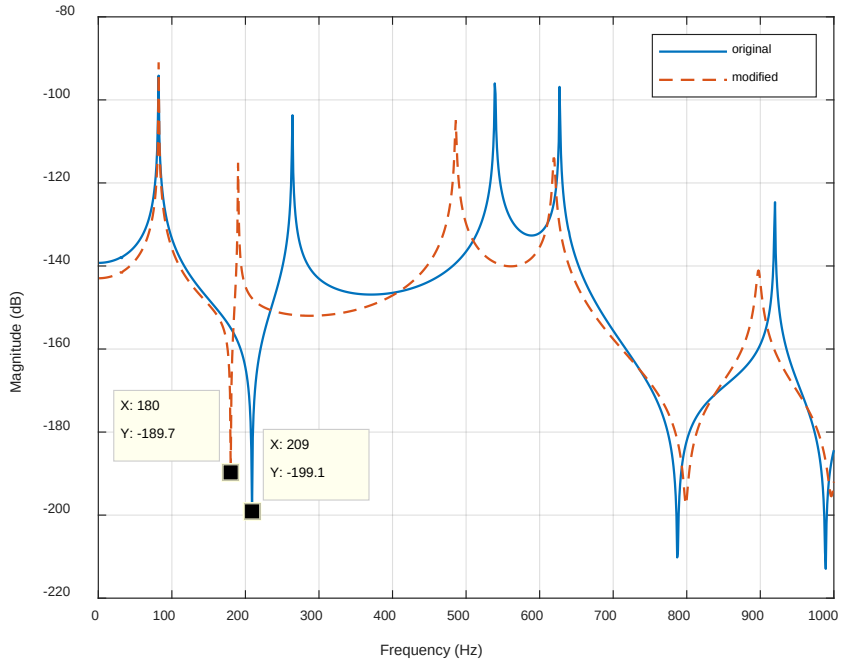

Figure 5. 5. FRFs before and after the modifications.

Natural frequency + antiresonant frequency assignment

In the previous case, it is shown that the antiresonant frequency can be perfectly assigned to 180 Hz within the feasible region. However, the second natural frequency is shifted fairly near the assigned antiresonant frequency in the modified system. The response at the DoF of concern can change significantly in only a few Hz. If one wishes to separate the two frequencies, the assignment problem requires

simultaneously assigning the natural frequency and the antiresonant frequency. Such an assignment problem is possible under the current framework where the problem is cast into an objective function. In this example, the desired antiresonant frequency is set to 180 Hz whilst two desired natural frequencies are to 82 and 250 Hz. The available Modification sets are the same as the previous examples. The resulting objective function to be minimized is simply the summation of Eqs. (5.10) and (5.11), and the constraints of the design variables are

$$0 \leq x_1 \leq 1, \qquad 0 \leq x_2 \leq 1, \qquad 0 \leq x_3 \leq 10^7, \qquad 0 \leq x_4 \leq 10^7$$

A solution is found using particle swarm algorithm, which is $\{2.9 \times 10^{-11}, 0.1227, 5.2359 \times 10^4, 0.0\}$. The resulting FRF, $h_{9,20}$ in the *y*-axis direction, is shown in Fig. 5.6 in which the achieved natural frequencies and antiresonant frequency are indicated by the cursor. It is clear that the natural frequencies are exactly achieved and that there is only a slight difference in the antiresonant frequency (roughly 1 Hz). This difference may be considered small in practice, and thus the modifications would suffice to produce the desired dynamic properties. Lastly, the value for x_1 is nearly zero, so it may be acceptable to treat it as zero in practice.

In theory, this kind of assignment can be extended to partial assignment when the number of design variables is large enough so that the objective function can be sufficiently minimized in the feasible region. However, this might be difficult to achieve in practice as the number of DoFs (poles) can be large and often relatively larger than the number of available modifications. As a compromise, this assignment problem can fix part of the unassigned frequencies while assigning some new frequencies, for instance, in this example the first desired natural frequency is intentionally assigned rather close to the original first natural frequency while the other two frequencies are two new frequencies.

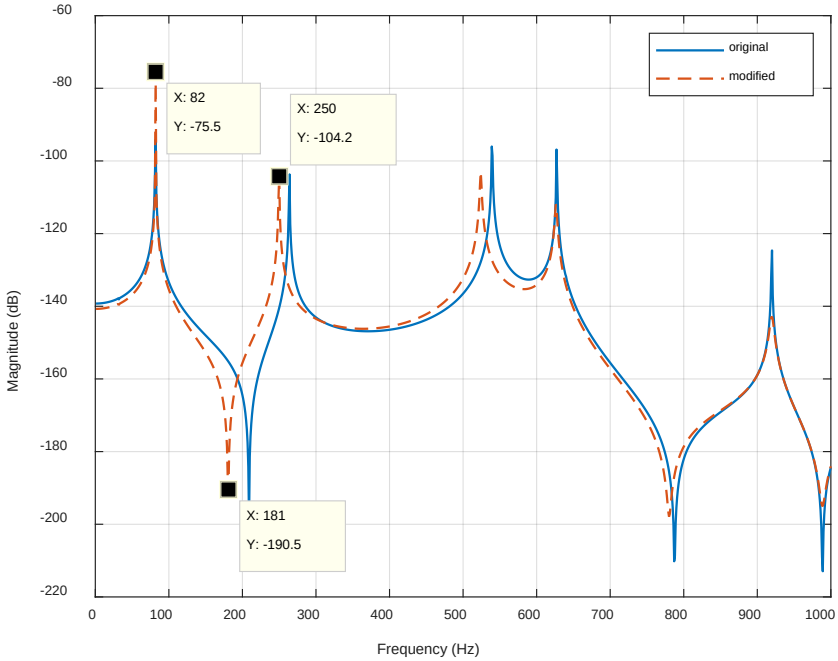

Figure 5. 6. FRFs before and after the modifications.

Eigenstructure assignment

As mentioned in Section 5.1, it is quite demanding to assign eigenstructures since it usually requires more design variables and in practice the number of receptance functions that can be measured is often limited. In the eigenstructure assignment problem, Eq. (5.14) is used to assign some nodal displacements instead of the whole mode. Assuming that one wishes to use Modification sets A and B to assign a natural frequency at 87 Hz and assign the corresponding nodal displacements at node number 17, 23, 25 to be 0.5, 1, and 0.8, respectively. Find the design variables **x** that minimizes Eq. (5.14) whilst the constraints of the design variables are

$$0 \leq x_1 \leq 2, \qquad 0 \leq x_2 \leq 2, \qquad 0 \leq x_3 \leq 10^7, \qquad 0 \leq x_4 \leq 10^7$$

A solution is found using particle swarm algorithm, which is $\{0.0173,\ 0.2509,\ 2.1261 \times 10^5,\ 0.3647\}$, and the resulting natural frequency of the first bending mode is 86.9 Hz. The mode shapes before and after the modifications are plotted together in Fig. 5.7. It can be seen that although the natural frequency is closely achieved to the desired value, there are some discrepancies between the achieved nodal displacements

and the desired ones. For a better comparison, the nodal displacements are normalized to the value at node number 23, leading to $\{0.6678,\ 1,\ 0.7854\}$ for the original nodal displacements and $\{0.5117,\ 1,\ 0.8302\}$ for the achieved ones.

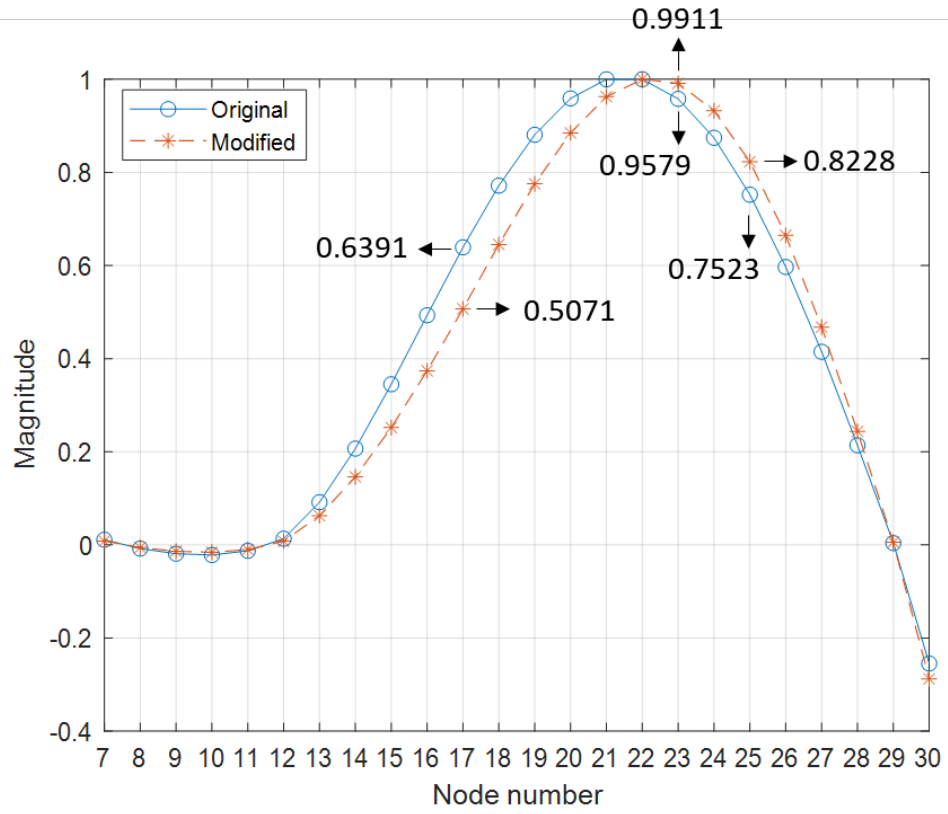

Figure 5. 7. The mode shapes on the *y*-*z* plane of the first bending mode before and after the modifications.

It should be pointed out that in the first example of natural frequency assignment, a natural frequency is assigned to a value without specifying the associated mode. For minor modifications, the original mode whose natural frequency is closest to the specified frequency would normally be the associated mode after the modifications. However, it is possible that another mode might be more sensitive to the modifications and thus be modified to become associated with the desired natural frequency. This situation could be circumvented by specifying the nodal displacements of interest. An example is given to demonstrate this idea.

For instance, for this geared rotor-bearing system, a natural frequency of 240 Hz is to be assigned to the first bending mode. As the modified mode shape of the first bending mode is expected to be similar to the original one shown in Fig. 5.7. The

desired nodal displacements are specified as $\{0.5,\ 1,\ 0.8\}$ and the desired natural frequency is set to 240 Hz. Note that 240 Hz is much closer to the original second bending mode than the first one. A solution is found using particle swarm algorithm, which is $\{1.979,\ 0,\ 5.7194 \times 10^6,\ 9.1326 \times 10^5\}$. The resulting natural frequency of the first bending mode is found to be 238.73 Hz, which is roughly 2 Hz lower than the desired one, and the associated mode shape is shown together with the original one in Fig. 5.8. The achieved nodal displacements, which are normalized to the value at node number 23, are $\{0.4898,\ 1,\ 0.8759\}$. The FRF between node 9 and 20 in the *y*-axis direction is given in Fig 5.9 to show the resulting bending natural frequencies. In this case, the first bending mode is modified towards the specified natural frequency although the desired natural frequency is much closer to the natural frequency of the second bending mode of the original structure.

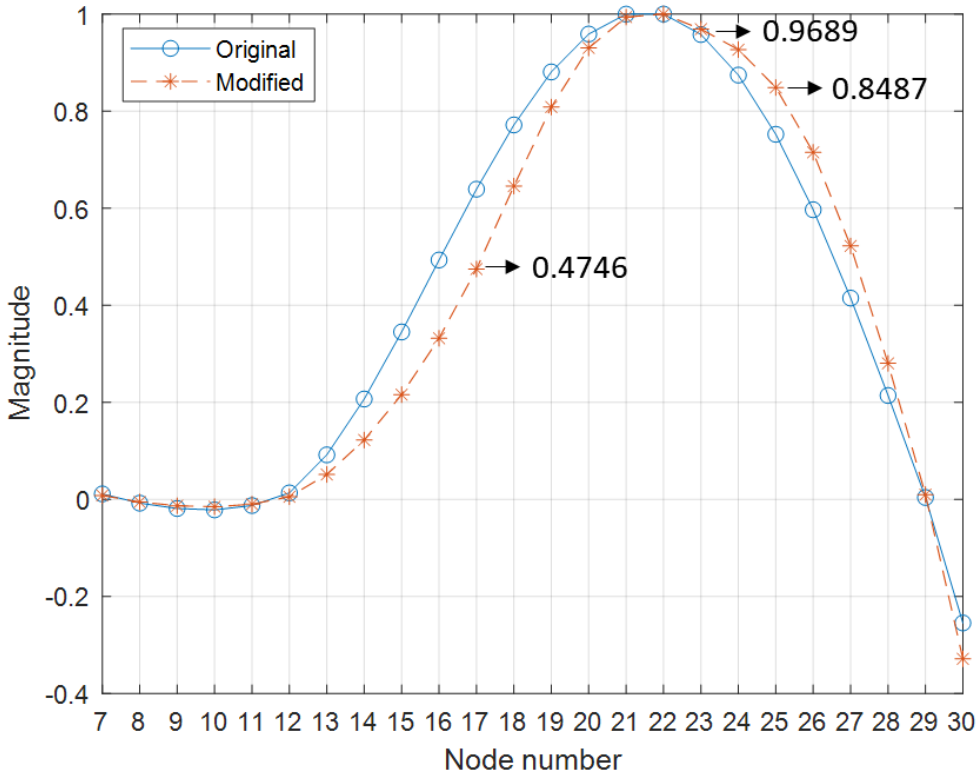

Figure 5. 8. The mode shapes on the *y*-*z* plane of the first bending mode before and after the modifications.

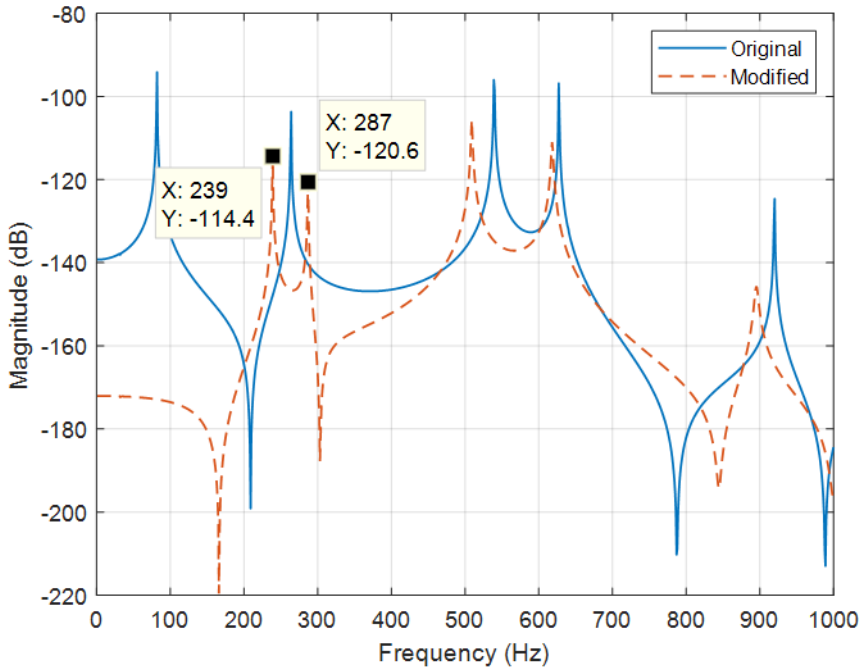

Figure 5. 9. FRFs before and after the modifications.

On the other hand, if merely Eq. (5.10) is used, it is found that the second bending mode could be modified to have 240 Hz given different initial values for the design variables. Two solutions given in Table 5.4 show the modifications that lead the first or the second bending mode to have the same desired frequency. When the interior-point algorithm is used and the initial values are set to zero, it is found that the objective function always converges to the case in which the second bending mode is shifted to the desired frequency. For the case of using Eq. (5.14) in this example, the first bending mode is shifted to the desired frequency even when the interior-point algorithm is applied and the initial points are set to zero.

Table 5. 4. Two solutions to the optimization problem.

	Solution 1	Solution 2
Design variables $\begin{Bmatrix} x_1 \\ x_2 \\ x_3 \\ x_4 \end{Bmatrix}$	$\begin{Bmatrix} 0.1109 \\ 0.0055 \\ 3.0727 \times 10^6 \\ 7.8076 \times 10^5 \end{Bmatrix}$	$\begin{Bmatrix} 1.6388 \\ 1.0488 \\ 4.115 \times 10^6 \\ 9.0589 \times 10^5 \end{Bmatrix}$
Achieved natural frequencies of the first two bending modes (Hz)	240, 400	142.86, 240

Pole-zero cancellation

In this example, the pole-zero cancellation is achieved by using the Modification set C alone, a spring-mass oscillator. It was established in Section 4.2 that the pole-zero cancellation can be achieved by assigning a pole to the frequency of the zero, and that the modification does not affect the zeros in the receptance functions related to DoFs where the modification is applied. In this case, the spring-mass oscillator is added in the *y*-axis direction of node number 24 in order to achieve a pole-zero cancellation at the point receptance. The point FRF is given in Fig. 5.10 below, and it shows that it is possible to assign a pole to the frequency of the second antiresonant frequency, which has the frequency of 530.317 Hz.

The objective function for pole assignment, Eq. (5.10), is to be minimized to find the values $\{x_1, x_2\}$ for the mass and spring of the oscillator, respectively. A solution, $\{0.7183,\ 7.9755 \times 10^6\}$, is found via particle swarm algorithm. The point FRF of the modified system is plotted together with the original one in Fig. 5.11. It can be noted that there are only three peaks in this frequency range as the third peak is cancelled with the second antiresonant frequency. The mode shape of the third bending mode shown in Fig. 5.12 confirms that a node at node number 24 is generated as a result of the pole-zero cancellation.

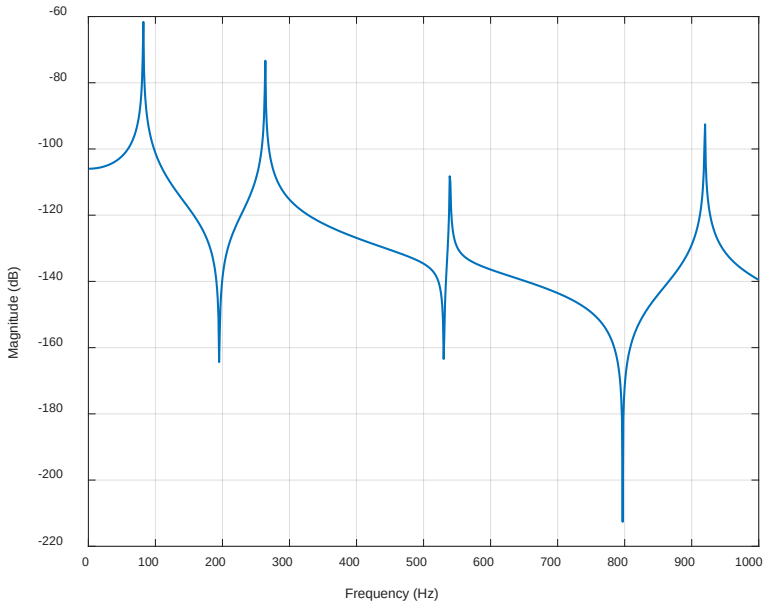

Figure 5. 10. The point FRF of node number 24 in the *y*-axis direction.

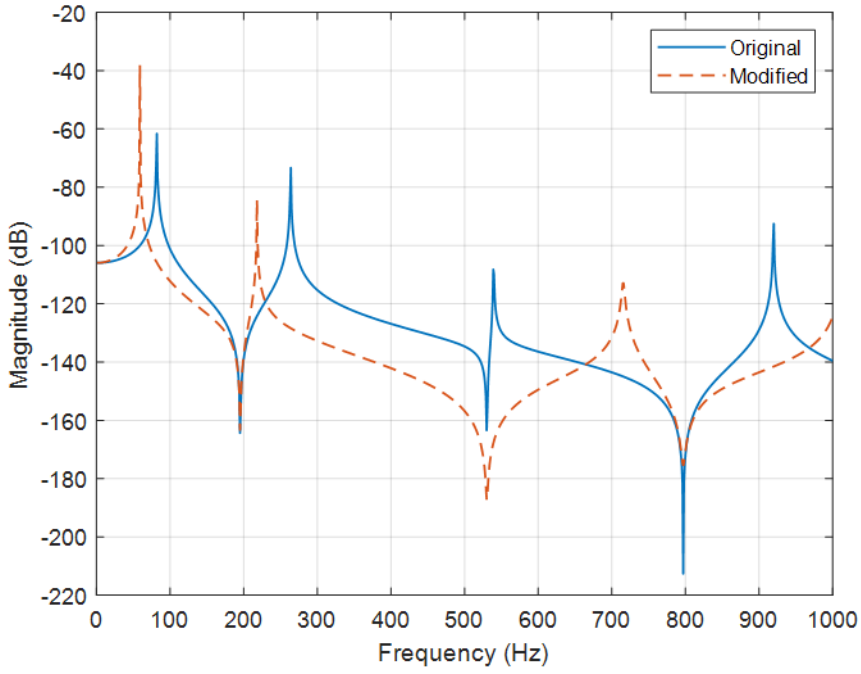

Figure 5. 11. The point FRFs before and after the modifications.

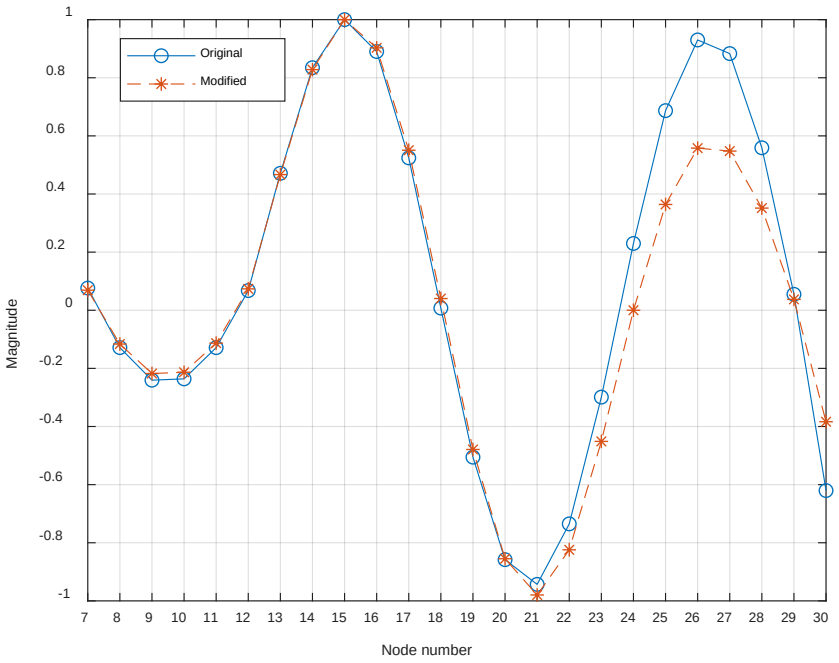

Figure 5. 12. The mode shapes before and after the modifications.

Receptance assignment

Given Eq. (5.8), the objective function for the problem of receptance assignment at frequency s_r can be designed as

$$\min_{\mathbf{x}} \left\{ \sum_{r=1}^{n} \alpha_r \left(\det\left(\mathbf{I} + \tilde{\mathbf{H}}_{ij}(s_r)\Delta\mathbf{Z}(s_r,\mathbf{x})_{(ji)}\right) - \gamma_r \times \det(\mathbf{I} + \mathbf{H}(s_r)\Delta\mathbf{Z}(s_r,\mathbf{x})) \right)^2 \right\} \tag{5.15}$$

where γ_r represents the ratio between the original receptance and the modified one at frequency s_r. In this example, Modification sets A and B are applied to make the receptances at 30 and 60 Hz 10% lower than the original values; therefore, $\{\gamma_r\}_{r=1}^{2} = 0.9$. The receptance function of concern is that between node # 9 and # 20 in the *y*-axis direction. The constraints of the design variables are

$$0 \le x_1 \le 2, \qquad 0 \le x_2 \le 2, \qquad 0 \le x_3 \le 10^7, \qquad 0 \le x_4 \le 10^7$$

A solution $\{0,\ 0.133,\ 1.6826 \times 10^4,\ 1.1426 \times 10^4\}$ is found via particle swarm algorithm. The receptance functions before and after the modifications are shown in Fig. 5.13. The ratio between the receptance at 30 Hz is roughly $1.137/1.263 = 0.9002$ and that at 60 Hz is $2.114/2.349 = 0.9$. The desired ratios are sufficiently achieved.

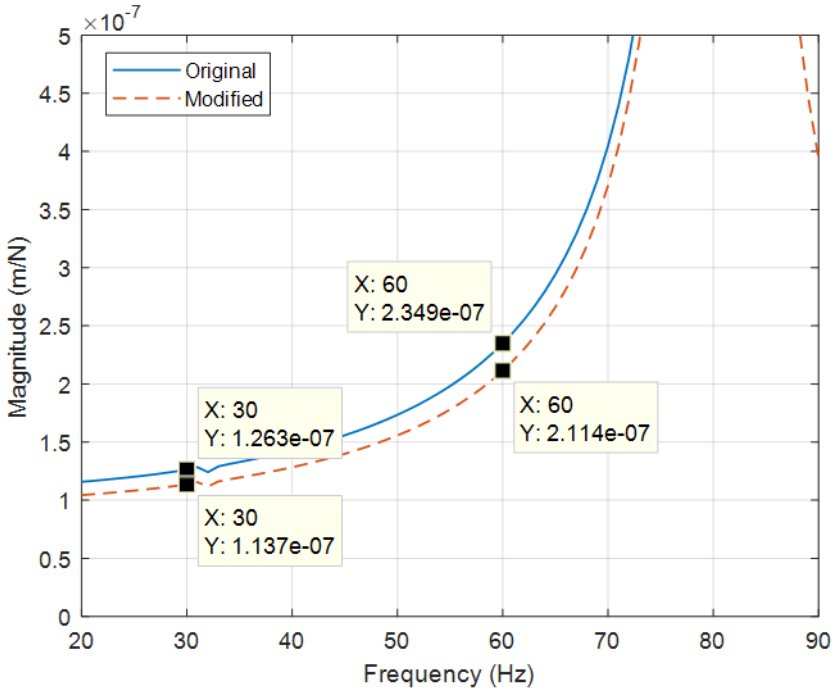

Figure 5. 13. The receptance functions before and after the modifications (linear scale).

5.4. Experimental results

The objective is to verify the proposed method through the experimental setup. For a geared rotor-bearing system, it is always more practical and easier to conduct mass modification instead of stiffness modification or damping modification; therefore, the two discs (with a few nuts bolted to them) are considered to be the only modifications for this goal. The point and cross receptances of the five accessible locations (p4, p5, p7, p11, p13 in Fig. 5.3) are measured before the modification. Then, two discs are placed at certain locations (among the accessible locations) and the corresponding modified frequencies are measured and taken as desired frequencies. Through Eqs. (5.10) and (5.11), the mass that is required to achieve the desired frequencies can be

obtained if a global/local minimum exists in the feasible domain. Since the modification is known, the difference between the predicted mass for the modification and the actual value can be used as one of the two benchmarks to reveal the effectiveness of the method. The other benchmark is the difference between the desired frequency and the frequency of the structure modified using the determined mass modification.

As can be seen from the objective function, the degrees of freedom of the modification matrix have to be defined first, and the corresponding receptances then have to be measured and included in the function. In this case only the vibration in the lateral direction, which is the out-of-plane direction *y* in Fig. 5.3, is considered since the bending vibration is dominant in the dynamic behaviour of the structure. Furthermore, the influence of the mass modification on the rotational degrees of freedom in the *y*-*z* plane are assumed to be negligible; that is to say, the discs act as point masses and the dynamic stiffness modification matrix is now a 2 by 2 matrix with the masses whose diagonal elements are the design variables. On the other hand, the receptance matrix required is also a 2 by 2 matrix which contains information of both point and cross receptances of the locations where the modifications are made.

5.4.1. Natural frequency assignment

Fig. 5.14 shows the cross FRFs of p7 to p4 in the *y* direction before and after the modification in which the two discs with additional masses of 780 g each (disc plus two M20-nut sets, i.e. 658 g + 122 g) are placed at p5 and p13. The force spectrum of the impact must be inspected first to determine the usable frequency range before any modifications, and additional care must be paid to energy distribution of the impact over the frequency range so that the noise in the FRF measurement can be minimized. The frequency range of interest is then limited to frequency below 600 Hz which covers the first four modes of the rig.

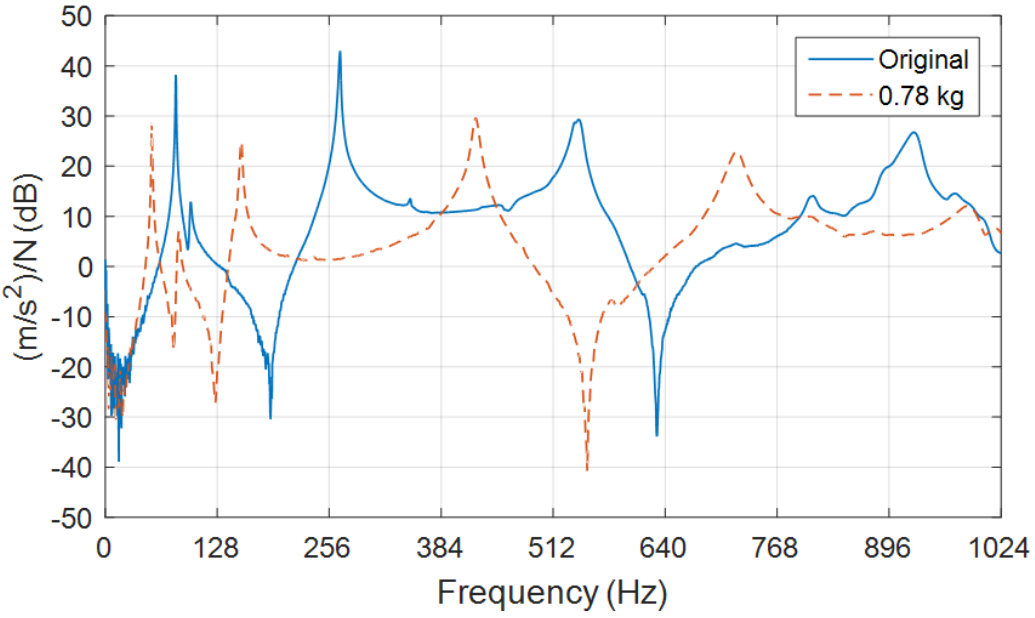

Figure 5. 14. The cross-FRF of p7-p4 before and after the modification.

The frequencies are estimated through peak picking and recorded in Table 5.5. The frequencies of the modified structure are targeted as the desired frequencies in the optimization problem. Apart from implementing Eq. (5.10) at each of the four frequencies, the objective function is subject to a linear equality constraint to ensure that two design variables have the same value. The predicted modifications are also given in Table 5.5.

First, it is clear that all of the frequencies are decreased since only mass modification is made. Second, it shows that some of the frequencies are not assignable, more precisely, the optimization finds close solutions to the first and third targeted frequencies, but fails to find the right solutions to the second and fourth targeted frequencies (the optimization procedure converges to boundary of the feasible domain); therefore, the Predicted Modifications for the second and fourth cases are left blank in table 5.5. For the first and the third frequencies, additional modifications are made in order to reflect the actual error between the desired frequency and the actually assigned frequency. Since it can be expensive or sometimes infeasible to exactly implement the determined mass modifications, some nuts are removed/added to roughly make up the difference (the fourth column of Table 5.5). A M16-nut set of 38 g is added to both discs to reflect the first case (each disc now weighs 780 + 38 g),

which leads to a first frequency that is close to the desired frequency value, and the error between them is less than 0.5 Hz. On the other hand, a M20-nut set of 61 g, which was originally bolted to the disc, is removed from both discs for the third case (each disc now weighs 780 – 61 g), which results in a third frequency at 158 Hz, a frequency difference of less than 3.5 Hz. The FRFs of the structure with the additional modifications are compared with those of modified structure in Fig. 5.15.

Table 5. 5. Results of natural frequency assignment.

Original Frequency	Modified Frequency	Predicted Modification	Difference	Remove 61g	Add 38g	Error
80.5 Hz	53 Hz	814.6 g	+34.6 g	N/A	52.5 Hz	< 0.5 Hz (0.9%)
97.5 Hz	84 Hz					
268.5 Hz	154.5 Hz	735.2 g	-44.8 g	158 Hz	N/A	< 3.5 Hz (2.3%)
542 HZ	422 Hz					

A further investigation through an FE model (shown in Fig. 5.4) has found that 422 Hz is the third bending frequency of the modified system, and both discs happen to be close to the nodes of the modified mode. The corresponding mode shape of the long shaft is shown in Fig. 5.16. In addition, the second frequency in Table 5.5 (97 Hz/ 84 Hz) is found to be the main frequency of the foundation, i.e., the stators and the aluminium profiles. These both imply that the sensitivity of the natural frequency is low to the current modifications; therefore, a local minimum might not exist in the feasible domain. Making modification on the shaft has a small effect on these frequencies, which might lead to inaccurate results. It is reasonable to expect that performing the sensitivity analysis prior to structural modifications can improve the effectiveness of the method. However, sensitivity analysis often requires a fairly accurate theoretical model (system matrices), which would take away a main advantage of the receptance method, and thus is not carried out in this section. Although experimental modal analysis itself is not sufficient to produce a complete and accurate sensitivity analysis, it can still reveal some useful insights.

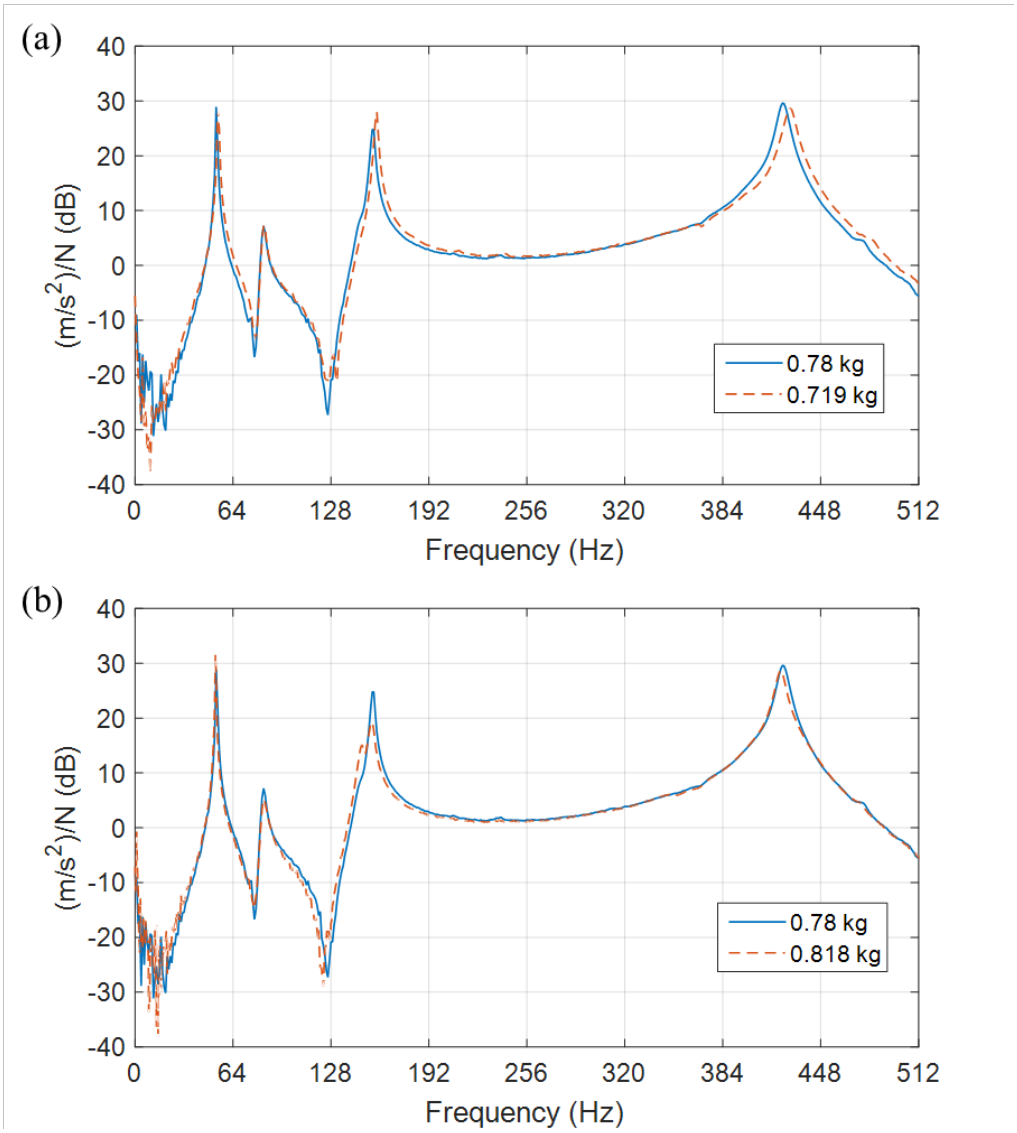

Figure 5. 15. Cross-FRFs of p7 to p4 with different modifications. (a) and (b) reflect the additional modification for the third case and the first case in Table 5.5.

Besides single natural frequency assignment, it is possible to assign multiple frequencies simultaneously through Eq. (5.10). For the sake of convenience, the first and the third modified frequencies in Table 5.5 are taken as desired frequencies, thereby resulting in $n = 2$ in Eq. (5.10). The weighting coefficients are both set to be 1. Results are shown in Table 5.6. It is clear that the predicted modification lies between those modifications of the two individual cases in Table5.5, which represents the trade-offs between the two objective functions. By examining Fig. 5.15(a), the differences between the desired and assigned frequencies in this case can be roughly estimated, which are definitely less than 1 and 3.5 Hz, respectively.

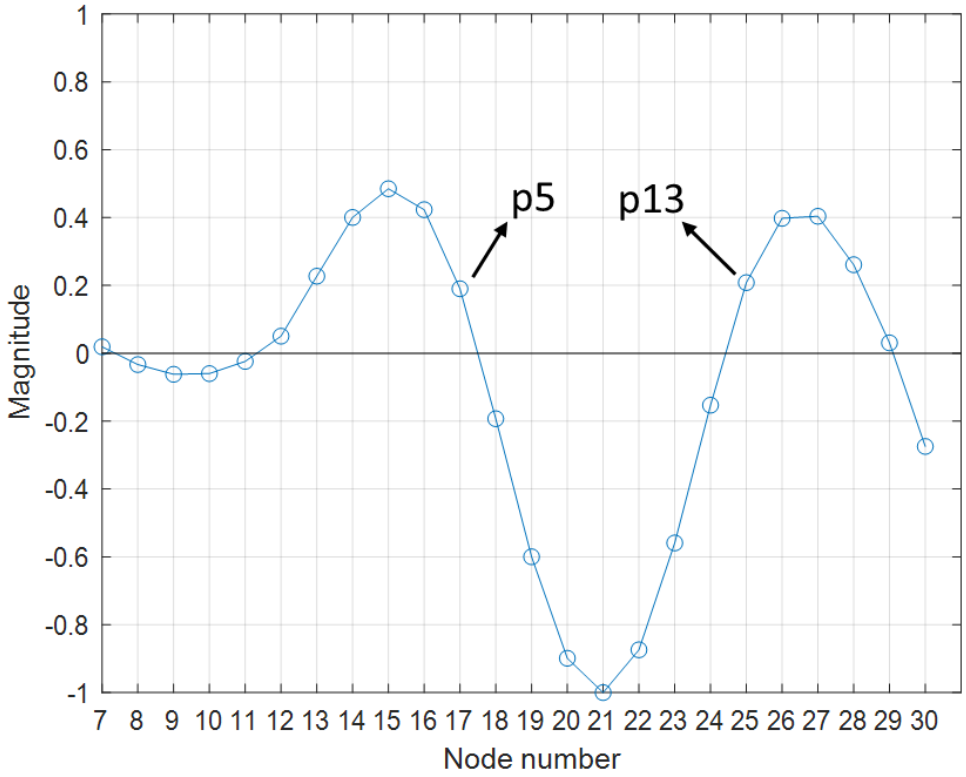

Figure 5. 16. The mode shape of the 422 Hz mode obtained from a simulated FE model.

Table 5. 6. Assignment of two natural frequencies.

Original Frequency	Modified Frequency	Predicted Modification	Difference	Remove 61g	Error
80.5 Hz 268.5 Hz	53 Hz 154.5 Hz	0.7421 kg	-37.9 g	54 Hz 158 Hz	< 1 Hz (1.9%) < 3.5 Hz (2.3%)

5.4.2. Antiresonant frequency assignment

The first two pronounced antiresonant frequencies from the cross-FRF in Fig. 5.14 are studied. Eq. (5.11) is used for assigning the identified antiresonant frequency, and the results are shown in Table 5.7. From the table, the difference in mass for the second antiresonant frequency is fairly small whilst the predicted mass for the first antiresonant frequency is only 20g heavier. After the additional modifications, it can be shown that the difference in antiresonant frequency for the first case should be less

than 0.5 Hz. The corresponding FRF is given in Fig. 5.15 (b). In the case in which two antiresonant frequencies are assigned simultaneously, the prediction is almost the same as the actual value with only a 6.6g difference.

Table 5. 7. Results of antiresonant frequency assignment.

Original Frequency	Modified Frequency	Predicted Modification	Difference	Add 38g	Error
94.5 Hz	78 Hz	0.8 kg	+20 g	78 Hz	< 0.5 Hz (0.6%)
189 Hz	126 Hz	0.7742 kg	-5.8 g		
94.5 Hz & 189 Hz	78 & 126 Hz	0.7866 kg	+6.6 g		

Another example of antiresonant frequency assignment under the same modification scenario is given below. In this case the assignment of the first pronounced antiresonant frequency of the cross-FRF of p11 to p4 is studied. As can be seen from Fig. 5.17, neither antiresonant frequencies are clear enough to be identified because of noise present in the measurement. A noise elimination technique for FRFs based on singular value decomposition (SVD) was applied to the measurements [156], in which the measured FRFs were first transformed to impulse response functions (IRF), and then Hankel matrices could be formed from the time domain data. SVD was utilized to estimate the rank of the Hankel matrices, and the rank could be used to separate uncontaminated data from noise matrices. Therefore, the rank has to be chosen appropriately. The same method to determine the rank in [156] is also adopted in this study. Once the rank is determined, the filtered data is then transformed back to FRFs to produce less noisy data. Fig. 5.18 shows the result and compares the measured FRF with the filtered FRF.

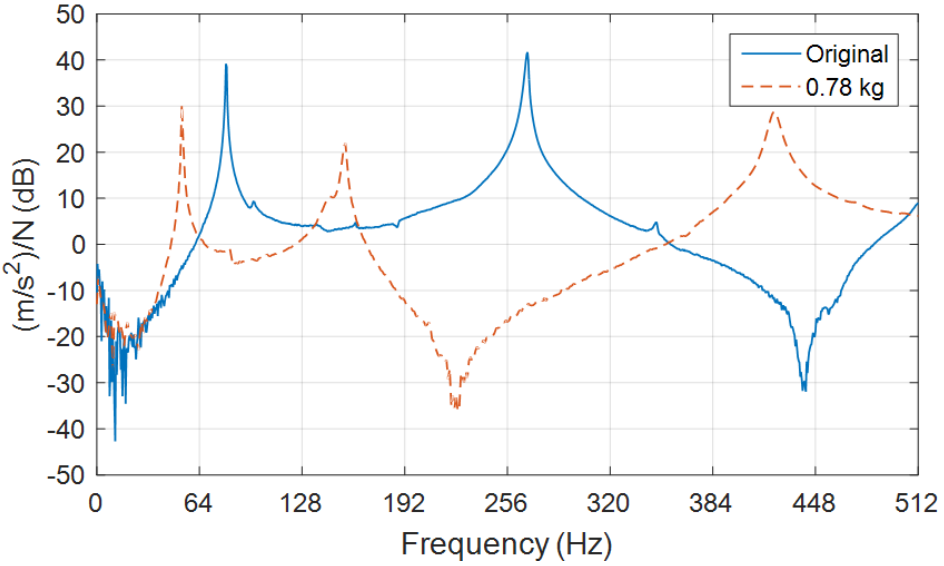

Figure 5. 17. The cross-FRF of p11-p4 before and after the modifications.

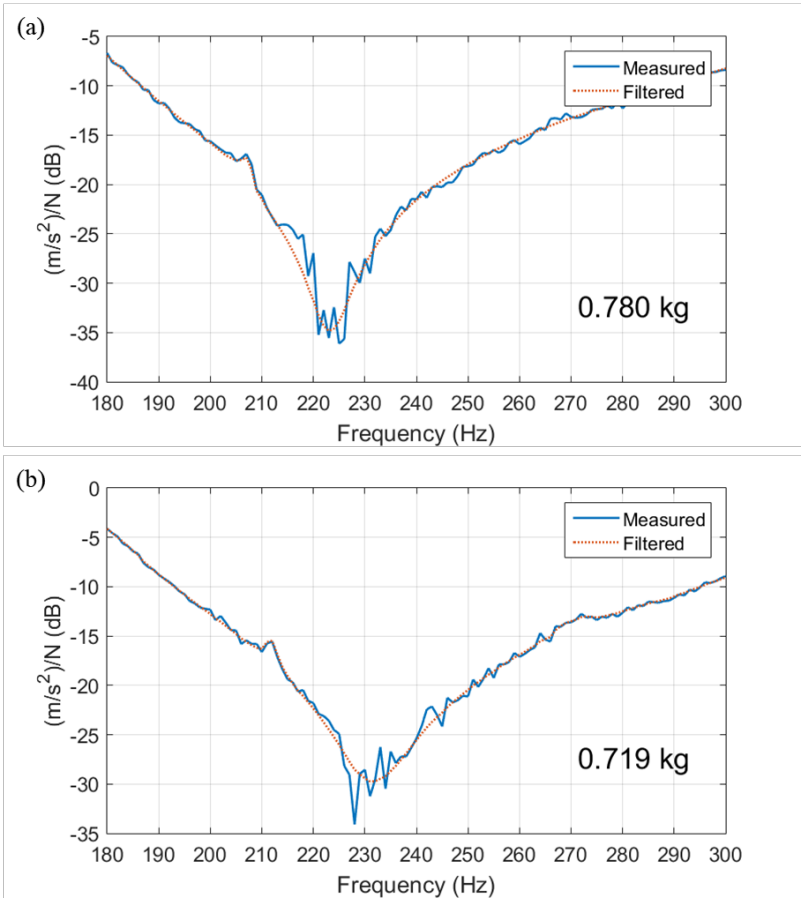

Figure 5. 18. Comparison of the measured FRFs and the filtered FRFs.

Valley picking, which is similar to peak picking, now can be used to estimate the antiresonant frequencies. The results of this assignment are given in Table 5.8. The

predicted mass is 27.6 g lighter than the actual mass. Due to the constraints of the modification available, a M20-nut set of 61g is removed from both discs (the disc now weights 719g) and an interpolation is applied to estimate the difference in antiresonant frequencies. This finds the difference in frequency to be smaller than 4 Hz, which is less than 1.8% of the desired antiresonant frequency.

Table 5. 8. Antiresonant frequency assignment for cross FRF of p11 to p4.

Original Frequency	Modified Frequency	Predicted Modification	Difference	Remove 61g	Error (interpolated)
440.5 Hz	223 Hz	752.4 g	-27.6 g	231 Hz	$<$ 4 Hz (1.8%)

5.4.3. Determination of the highest first bending natural frequency

In section 5.4.1, the required modification for assigning a frequency is determined as an inverse dynamic problem. In this section, the goal is to search for the optimal location for the given modifications among all the possible locations that results in the highest first bending natural frequency. This method is essentially a forward structural modification application, but it is included in this study since the operating speeds of some rotating machines are below the first critical speed; therefore, increasing the first natural frequency can increase the range of operating speed or possibly avoid/reduce response at resonance. In addition, the computational load to determine the optimal location would not be an issue because the number of measurements in practice is usually not large, and this application does not require an FE model of the structure.

The application can be described as follows:

1. Quantify the modifications made to the system and list the accessible locations for the modifications. Arrange the possible combinations of the modification

locations into vector $\boldsymbol{\theta}$ and create a vector $\boldsymbol{\omega} = \left\{\omega_1, \omega_2, \cdots, \omega_{n_f}\right\}^{\mathrm{T}}$ of n_f evenly spaced points in an estimated frequency range for the first natural frequency. ω_1 is the upper bound while ω_{n_f} is the lower bound.

2. Measure the point and cross receptances at the accessible DoFs before any modifications are applied. Some DoFs of lower sensitivity to the frequency of interest could be left out. This should be carefully determined.
3. Specify a threshold ζ which should be a sufficiently small number. Set $i = 0$.
4. **While** $i \leq n_f$ **do**
5. Set $i = i + 1$
6. Calculate the denominator of Eq. (5.8), which is repeated here for convenience, for all possible combinations in $\boldsymbol{\theta}$ at frequency ω_i:

$$\boldsymbol{z} = \det(\mathrm{I} + \mathbf{H}(\omega_i, \boldsymbol{\theta})\Delta\mathbf{Z}(\omega_i))$$

7. Keep records of the combination that has the smallest value in **z** and check if any of the values in **z** is equal to or smaller than ζ. If yes, exit the **While** loop. If not, then move to the next loop until the criterion is satisfied.

In this study, the two identical discs of 780 g each can be placed at any two of the five accessible locations: p4, p5, p7, p11, p13, that is to say, there are 10 possible combinations of modification in total. It is assumed that $\boldsymbol{\omega}$ ranges from 50 Hz to 70 Hz with resolution of 1 Hz and ζ is set to 0.01. Since rotational degrees of freedom are neglected and acceleration are measured at the accessible locations, only five impact tests are required to produce the receptance matrix. In this case the process is carried out throughout $\boldsymbol{\omega}$ to provide more insights into the dynamic characteristics of the structure.

The outcomes are summarized as follows: Table 5.9 lists some of the cases in which the determinant values satisfy the criterion while Table 5.10 lists those that do not; Table 5.11 shows the experimental results of the modifications on all the possible locations in descending order of the first natural frequency. It can first be seen from Table 5.10 that the smallest determinant value is decreasing as ω_i drops, and the corresponding combination of modification locations is either (p4, p5) or (p4, p13). This implies that these two combinations bring the objective function close to its global or local minimum as ω_i decreases. It is reasonable to assume that one or both

of the combinations might lead to the highest first natural frequency. The assumption can be quickly verified by Table 5.9, which indicates that the (p4, p5) combination is the first one satisfying the criterion at 58 Hz while (p4, p13) results in the lowest determinant values for the next two frequencies at 57 Hz and 56 Hz. The observation above suggests that (p4, p5) and (p4, p13) could result in similar first natural frequencies, but the one produced by (p4, p5) combination is slightly higher.

The above findings can be confirmed by experimental results given in Table 5.11. It shows that (p4, p5) combination does lead to the highest natural frequency at 57 Hz while (p4, p13) results in the second highest natural frequency at 56 Hz. It should be noted that the true error in frequency between the results in Table 5.9 and Table 5.11 is unavailable as noise is always present in the experimental results and the resolution of the spectrum from modal testing is confined by the acquisition hardware. However, the order of the objective function values from the other combinations in Table 5.9, i.e. (p5, p13), (p4, p7), (p4, p11), and (p5, p7), matches their order in Table 5.11 (from 53 Hz to 50 Hz), which suggests that the estimated optimal locations agree well with the trend in the experimental results.

Table 5. 9. Optimal locations for each frequency in $\boldsymbol{\omega}$.

ω_i in Hz	Combination	Determinant Value
58	(p4, p5)	2.03×10^{-3}
57	(p4, p13)	2.12×10^{-4}
56	(p4, p13)	5.53×10^{-4}
55	(p5, p13)	3.76×10^{-3}
54	(p5, p13)	5.71×10^{-4}
53	(p5, p13)	1.29×10^{-3}
52	(p4, p7)	5.83×10^{-6}
51	(p4, p11)	2.77×10^{-4}
50	(p5, p7)	2.43×10^{-4}

Table 5. 10. Results that do not satisfy the criterion.

f_i in Hz	Combination	Determinant Value
67	(p4, p13)	1.14
66	(p4, p13)	0.82

65	(p4, p5)	0.55
64	(p4, p5)	0.32
63	(p4, p5)	0.26
62	(p4, p13)	0.16
61	(p4, p5)	0.066
60	(p4, p5)	0.041
59	(p4, p5)	0.015

Table 5. 11. Experimental results.

Combination	First natural frequency (Hz)
(p4, p5)	57
(p4, p13)	56
(p5, p13)	53
(p4, p7)	52
(p4, p11)	51
(p5, p7)	50
(p5, p11)	50
(p7, p13)	49
(p11, p13)	47
(p7, p11)	46

5.5. Conclusions

In this chapter the theory of inverse structural modification based on the receptance method is further extended. The receptance of a modified linear structure is expressed in terms of the receptances of the original structure and the modifications to be made. The method proposed can be applied to assignments of several different kinds of dynamical properties such as natural frequencies, antiresonant frequencies, receptances, and pole-zero cancellation. Only a small number of measured receptances are needed for the assignments; therefore, a theoretical model is not necessarily required. By casting the problem into an optimization problem, the resulting equation can cover several forms of modifications previously reported in the literature, for instance, unit-rank modifications or single-DoF spring-mass absorbers (as reduced

cases). A number of numerical simulations are given to demonstrate various assignment problems and applicability of the proposed technique.

A geared rotor-bearing system is used to implement and validate the inverse method in practice. The experimental results clearly show that the method can produce a fairly accurate prediction even if the structure is complicated and that more than one frequency can be assigned simultaneously. Sensitivity of frequency of concern to the modifications is found to affect convergence in the optimisation process of searching for the solution of the modification, and thus conducting sensitivity analysis prior to structural modification is recommended when a fairly accurate theoretical model is available. Finally, the optimal locations of given modifications to achieve the highest first bending natural frequency are determined, which are found to be correctly predicted through validation with experimental results. This approach can also predict the value of the first natural frequency under given modifications at other locations.

6. Identification of Torsional Receptance

Parts of this chapter are based on a journal paper written by the author (DOI: 10.1016/j.ymssp.2019.01.050).

As a shafting system often has to transmit power through rotation, the dynamics in the torsional direction is therefore required to be carefully evaluated and considered. However, the identification of torsional receptances of shaft structures has been a challenge. This chapter deals with the problem of obtaining high-quality torsional receptances in its measurements using two different methods based on the Receptance Decoupling Technique. In both methods, a T-block needs to be attached to facilitate the generation of torsion, and only the numerical receptance data of the T-block cast in a simple theoretical model and a few measured receptance data of the assembled system are required. Both methods are studied and assessed in numerical simulation, and the more robust method is further validated in experiments.

The usage of a rotational accelerometer is shown to significantly improve the quality of the estimation when the noise level is high. It is demonstrated that high-quality torsional receptances can be indirectly measured with high repeatability using the proposed method and thus can be used subsequently to identify torsional modal parameters, update finite element models, make structural modifications, or implement active torsional vibration control. Due to ubiquitous use of rotating machines, this novel method has significant applicability.

6.1. Theoretical development

Two receptance-based approaches for the estimation of torsional receptance are developed in this section. Receptance decoupling technique is briefly introduced first and then followed by derivations of the two different techniques. As shown in Fig. 6.1(a), a coupled system AB is composed of subsystem A and subsystem B, which are

rigidly connected through a few connection coordinates denoted as “c” that is shared by both subsystems. The coordinates of subsystem A and subsystem B that are not “c” are denoted as “a” and “b”, respectively. The displacement-force relationship of the coupled system and the subsystems in the frequency domain can be defined as:

$$\begin{Bmatrix} \mathbf{u}_c^{AB} \\ \mathbf{u}_b^{AB} \end{Bmatrix} = \begin{bmatrix} \mathbf{H}_{cc}^{AB} & \mathbf{H}_{cb}^{AB} \\ \mathbf{H}_{bc}^{AB} & \mathbf{H}_{bb}^{AB} \end{bmatrix} \begin{Bmatrix} \mathbf{f}_c^{AB} \\ \mathbf{f}_b^{AB} \end{Bmatrix} \tag{6.1}$$

$$\begin{Bmatrix} \mathbf{u}_c^{B} \\ \mathbf{u}_b^{B} \end{Bmatrix} = \begin{bmatrix} \mathbf{H}_{cc}^{B} & \mathbf{H}_{cb}^{B} \\ \mathbf{H}_{bc}^{B} & \mathbf{H}_{bb}^{B} \end{bmatrix} \begin{Bmatrix} \mathbf{f}_c^{B} \\ \mathbf{f}_b^{B} \end{Bmatrix} \tag{6.2}$$

and

$$\mathbf{u}_c^{A} = \mathbf{H}_{cc}^{A} \mathbf{f}_c^{A} \tag{6.3}$$

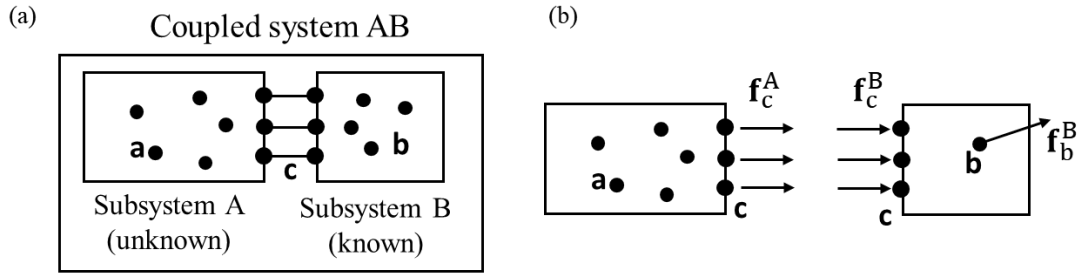

Figure 6. 1. Coupling of substructures: (a) the coupled system and (b) the free body diagram of each subsystem.

Suppose that one is only interested in the receptances of the unknown subsystem A at the connection coordinates, governed by Eq. (6.3), while some of the receptance data of the coupled system, governed by Eq. (6.1), and the receptances of subsystem B, governed by Eq. (6.2), are known. Furthermore, it is assumed that the coupled system is excited by external force $\mathbf{f}_b^{AB}$ on the coordinates associated with subsystem B. For this purpose, the influence from subsystem B has to be removed from the coupled system in order to find $\mathbf{H}_{cc}^{A}$. It is worth mentioning that Eqs. (6.2) and (6.3) do not represent the “stand alone” subsystems but pertain to the coordinates of subsystem A and B in the coupled system as illustrated in Fig. 6.1(b). Therefore, the force equilibrium and displacement compatibility conditions applied at coordinates c can be defined as:

$$\mathbf{u}_c^{AB} = \mathbf{u}_c^{B} = \mathbf{u}_c^{A}, \quad \mathbf{f}_c^{AB} = \mathbf{f}_c^{A} + \mathbf{f}_c^{B} \tag{6.4}$$

Additionally, the internal coordinates of and the external forces on subsystem B can be expressed as:

$$\mathbf{u}_b^{AB} = \mathbf{u}_b^{B}, \quad \mathbf{f}_b^{AB} = \mathbf{f}_b^{B} \tag{6.5}$$

According to Eq. (6.4) and Eq. (6.5), subtracting Eq. (6.1) by Eq. (6.2) leads to

$$\begin{Bmatrix} \mathbf{0} \\ \mathbf{0} \end{Bmatrix} = \begin{bmatrix} \mathbf{H}_{cc}^{AB} & \mathbf{H}_{cb}^{AB} \\ \mathbf{H}_{bc}^{AB} & \mathbf{H}_{bb}^{AB} \end{bmatrix} \begin{Bmatrix} \mathbf{f}_c^{AB} \\ \mathbf{f}_b^{AB} \end{Bmatrix} - \begin{bmatrix} \mathbf{H}_{cc}^{B} & \mathbf{H}_{cb}^{B} \\ \mathbf{H}_{bc}^{B} & \mathbf{H}_{bb}^{B} \end{bmatrix} \begin{Bmatrix} \mathbf{f}_c^{B} \\ \mathbf{f}_b^{B} \end{Bmatrix} \tag{6.6}$$

Extracting the first row of equations in Eq. (6.6) and applying Eq. (6.5) give

$$\begin{bmatrix} \mathbf{H}_{cc}^{B} \\ \mathbf{H}_{bc}^{B} \end{bmatrix} \mathbf{f}_c^{B} = \begin{bmatrix} \mathbf{H}_{cc}^{AB} \\ \mathbf{H}_{bc}^{AB} \end{bmatrix} \mathbf{f}_c^{AB} + \begin{bmatrix} \mathbf{H}_{cb}^{AB} - \mathbf{H}_{cb}^{B} \\ \mathbf{H}_{bb}^{AB} - \mathbf{H}_{bb}^{B} \end{bmatrix} \mathbf{f}_b^{B} \tag{6.7}$$

The internal forces at the connection coordinates of subsystem B can be expressed as:

$$\mathbf{f}_c^{B} = \begin{bmatrix} \mathbf{H}_{cc}^{B} \\ \mathbf{H}_{bc}^{B} \end{bmatrix}^{+} \left(\begin{bmatrix} \mathbf{H}_{cc}^{AB} \\ \mathbf{H}_{bc}^{AB} \end{bmatrix} \mathbf{f}_c^{AB} + \begin{bmatrix} \mathbf{H}_{cb}^{AB} - \mathbf{H}_{cb}^{B} \\ \mathbf{H}_{bb}^{AB} - \mathbf{H}_{bb}^{B} \end{bmatrix} \mathbf{f}_b^{B} \right) \tag{6.8}$$

where $[\,]^{+}$ denotes the generalized inverse matrix operation. If there is no external force applied to the connection coordinates of the coupled system, i.e. $\mathbf{f}_c^{AB} = 0$, $\mathbf{f}_c^{A}$ can then be obtained through Eq. (6.4), which is

$$\mathbf{f}_c^{A} = \begin{bmatrix} \mathbf{H}_{cc}^{B} \\ \mathbf{H}_{bc}^{B} \end{bmatrix}^{+} \begin{bmatrix} \mathbf{H}_{cb}^{AB} - \mathbf{H}_{cb}^{B} \\ \mathbf{H}_{bb}^{AB} - \mathbf{H}_{bb}^{B} \end{bmatrix} \mathbf{f}_b^{B} \tag{6.9}$$

Similarly, $\mathbf{u}_c^{A}$ can be found through Eqs. (6.2) and (6.4)

$$\mathbf{u}_c^{A} = \left(\mathbf{H}_{cc}^{B} \begin{bmatrix} \mathbf{H}_{cc}^{B} \\ \mathbf{H}_{bc}^{B} \end{bmatrix}^{+} \begin{bmatrix} \mathbf{H}_{cb}^{AB} - \mathbf{H}_{cb}^{B} \\ \mathbf{H}_{bb}^{AB} - \mathbf{H}_{bb}^{B} \end{bmatrix} + \mathbf{H}_{cb}^{B} \right) \mathbf{f}_b^{B} \tag{6.10}$$

From Eqs. (6.9) and (6.10), it can be seen that if the receptance submatrices of subsystem B and system AB are known, $\mathbf{H}_{cc}^{A}$ can be determined through Eq. (6.3). The receptance submatrices of subsystem B that is an attached simple structure will be obtained from an accurate theoretical model, while the receptance submatrices of system AB will be obtained through a few measurements. It is important to mention

that in the formulation above, the process from Eqs. (6.6) to (6.8), follows the work proposed by D'Ambrogio and Fregolent [157]. Next, Eqs. (6.9) and (6.10) are extended and explicitly applied to the estimation of torsional receptance of a subsystem for Method 1.

Method 1:

The schematic of the problem considered in this chapter is shown in Fig. 6.2 in which a T-block (subsystem B) is attached to a shafting system (subsystem A). The aim is to estimate the torsional receptance at the connection coordinate of the shafting system.

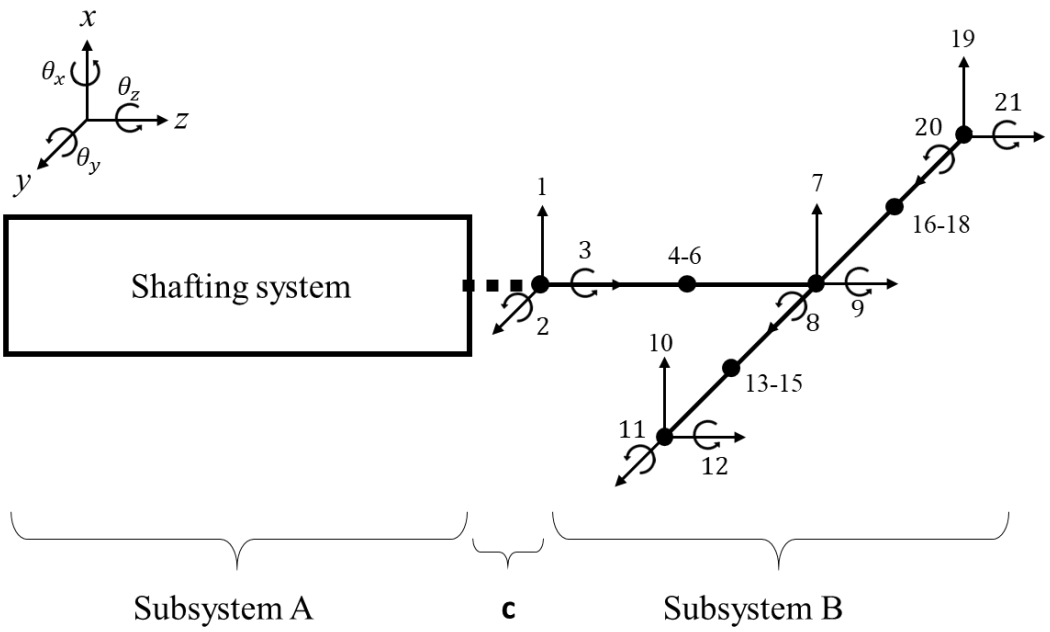

Figure 6. 2. The schematic of the assembly of a shafting system and a T-block.

For the purpose of demonstration, the T-block is represented by 6 beam elements in which each node has DoFs, which are lateral deflection, rotation for bending, and angle of twist, all in the local coordinate system, and are numbered sequentially from the leftmost node; globally, they are denoted as x, θ_y, and θ_z, respectively. Therefore, in this case, the T-block has 21 DoFs in total. For Method 1, a force is assumed to be applied at DoF 10. Accordingly, Eq. (6.7) can be explicitly written as

$$\begin{bmatrix} h_{1,1}^{\mathrm{B}} & h_{1,2}^{\mathrm{B}} & 0 \\ h_{2,1}^{\mathrm{B}} & h_{2,2}^{\mathrm{B}} & 0 \\ 0 & 0 & h_{3,3}^{\mathrm{B}} \\ h_{10,1}^{\mathrm{B}} & h_{10,2}^{\mathrm{B}} & h_{10,3}^{\mathrm{B}} \end{bmatrix} \begin{Bmatrix} f_1^{\mathrm{B}} \\ f_2^{\mathrm{B}} \\ f_3^{\mathrm{B}} \end{Bmatrix} = \begin{Bmatrix} h_{1,10}^{\mathrm{AB}} - h_{1,10}^{\mathrm{B}} \\ h_{2,10}^{\mathrm{AB}} - h_{2,10}^{\mathrm{B}} \\ h_{3,10}^{\mathrm{AB}} - h_{3,10}^{\mathrm{B}} \\ h_{10,10}^{\mathrm{AB}} - h_{10,10}^{\mathrm{B}} \end{Bmatrix} f_{10}^{\mathrm{AB}} \tag{6.11}$$

From Eq. (6.1) and Eq. (6.4), it can be seen that $u_3^{\mathrm{A}} = h_{3,10}^{\mathrm{AB}} f_{10}^{\mathrm{AB}}$. By subtracting this relationship from the third row of Eq. (6.11), it gives $h_{3,3}^{\mathrm{B}} f_3^{\mathrm{B}} - u_3^{\mathrm{A}} = -h_{3,10}^{\mathrm{B}} f_{10}^{\mathrm{AB}}$. Then, rearranging Eq. (6.11) to include u_3^{A} , which shows that

$$\begin{bmatrix} h_{1,1}^{\mathrm{B}} & h_{1,2}^{\mathrm{B}} & 0 & 0 \\ h_{2,1}^{\mathrm{B}} & h_{2,2}^{\mathrm{B}} & 0 & 0 \\ 0 & 0 & h_{3,3}^{\mathrm{B}} & -1 \\ h_{10,1}^{\mathrm{B}} & h_{10,2}^{\mathrm{B}} & h_{10,3}^{\mathrm{B}} & 0 \end{bmatrix} \begin{Bmatrix} f_1^{\mathrm{B}} \\ f_2^{\mathrm{B}} \\ f_3^{\mathrm{B}} \\ u_3^{\mathrm{A}} \end{Bmatrix} = \begin{Bmatrix} h_{1,10}^{\mathrm{AB}} - h_{1,10}^{\mathrm{B}} \\ h_{2,10}^{\mathrm{AB}} - h_{2,10}^{\mathrm{B}} \\ -h_{3,10}^{\mathrm{B}} \\ h_{10,10}^{\mathrm{AB}} - h_{10,10}^{\mathrm{B}} \end{Bmatrix} f_{10}^{\mathrm{AB}} \tag{6.12}$$

The internal torque f_3^{B} and torsional displacement u_3^{A} can be calculated by solving Eq. (6.12), and therefore $h_{3,3}^{\mathrm{A}}$ can be calculated as $-u_3^{\mathrm{A}}/f_3^{\mathrm{B}}$. The solutions are:

$$\begin{aligned} f_3^{\mathrm{B}}/f_{10}^{\mathrm{AB}} = [&\left(h_{1,10}^{\mathrm{AB}} h_{2,1}^{\mathrm{B}} h_{10,2}^{\mathrm{B}} - h_{1,10}^{\mathrm{AB}} h_{2,2}^{\mathrm{B}} h_{10,1}^{\mathrm{B}}\right) \\ &+ \left(h_{2,10}^{\mathrm{AB}} h_{1,2}^{\mathrm{B}} h_{10,1}^{\mathrm{B}} - h_{2,10}^{\mathrm{AB}} h_{1,1}^{\mathrm{B}} h_{10,2}^{\mathrm{B}}\right) \\ &+ \left(h_{1,1}^{\mathrm{B}} h_{10,2}^{\mathrm{B}} h_{10,2}^{\mathrm{B}} - h_{1,1}^{\mathrm{B}} h_{2,2}^{\mathrm{B}} h_{10,10}^{\mathrm{B}}\right) \\ &+ \left(h_{1,2}^{\mathrm{B}} h_{2,1}^{\mathrm{B}} h_{10,10}^{\mathrm{B}} - h_{1,2}^{\mathrm{B}} h_{10,1}^{\mathrm{B}} h_{10,2}^{\mathrm{B}}\right) + \left(h_{10,1}^{\mathrm{B}} h_{2,2}^{\mathrm{B}} h_{10,1}^{\mathrm{B}}\right. \\ &\left. - h_{10,1}^{\mathrm{B}} h_{2,1}^{\mathrm{B}} h_{10,2}^{\mathrm{B}}\right)]/\det(\mathbf{A}) \end{aligned} \tag{6.13}$$

and

$$\begin{aligned} u_3^{\mathrm{A}}/f_{10}^{\mathrm{AB}} = [&\left(h_{1,10}^{\mathrm{AB}} h_{3,3}^{\mathrm{B}} \left(h_{2,1}^{\mathrm{B}} h_{10,2}^{\mathrm{B}} - h_{2,2}^{\mathrm{B}} h_{10,1}^{\mathrm{B}}\right)\right. \\ &+ h_{2,10}^{\mathrm{AB}} h_{3,3}^{\mathrm{B}} \left(h_{1,2}^{\mathrm{B}} h_{10,1}^{\mathrm{B}} - h_{1,1}^{\mathrm{B}} h_{10,2}^{\mathrm{B}}\right) \\ &+ h_{10,10}^{\mathrm{AB}} h_{3,3}^{\mathrm{B}} \left(h_{1,1}^{\mathrm{B}} h_{2,2}^{\mathrm{B}} - h_{1,2}^{\mathrm{B}} h_{2,1}^{\mathrm{B}}\right) - h_{1,1}^{\mathrm{B}} h_{2,2}^{\mathrm{B}} h_{10,10}^{\mathrm{B}} h_{3,3}^{\mathrm{B}} \\ &+ h_{1,1}^{\mathrm{B}} h_{2,2}^{\mathrm{B}} h_{10,3}^{\mathrm{B}} h_{10,3}^{\mathrm{B}} + h_{1,1}^{\mathrm{B}} h_{3,3}^{\mathrm{B}} h_{10,2}^{\mathrm{B}} h_{10,2}^{\mathrm{B}} \\ &+ h_{1,2}^{\mathrm{B}} h_{2,1}^{\mathrm{B}} h_{3,3}^{\mathrm{B}} h_{10,10}^{\mathrm{B}} - h_{1,2}^{\mathrm{B}} h_{2,1}^{\mathrm{B}} h_{10,3}^{\mathrm{B}} h_{10,3}^{\mathrm{B}} \\ &- h_{1,2}^{\mathrm{B}} h_{3,3}^{\mathrm{B}} h_{10,1}^{\mathrm{B}} h_{10,2}^{\mathrm{B}} - h_{2,1}^{\mathrm{B}} h_{3,3}^{\mathrm{B}} h_{10,1}^{\mathrm{B}} h_{10,2}^{\mathrm{B}} \\ &\left. + h_{2,2}^{\mathrm{B}} h_{3,3}^{\mathrm{B}} h_{10,1}^{\mathrm{B}} h_{10,1}^{\mathrm{B}})\right]/\det(\mathbf{A}) \end{aligned} \tag{6.14}$$

where **A** is the 4-by-4 matrix on the left-hand side of Eq. (6.12). The determinant function in each equation will be cancelled out when calculating for $h_{3,3}^{\mathrm{A}}$; however, for the sake of completeness, det(**A**) is $h_{1,1}^{\mathrm{B}} h_{2,2}^{\mathrm{B}} h_{10,3}^{\mathrm{B}} - h_{1,2}^{\mathrm{B}} h_{2,1}^{\mathrm{B}} h_{10,3}^{\mathrm{B}}$ in this example.

Method 2:

Although in Method 1 the torsional receptance of the shafting system could be quickly estimated through a single modal test (one impact hammer test), the result might be prone to noise since the contaminated measured receptances are multiplied and added, as can be seen in Eqs. (6.13) and (6.14). For this reason, Method 2 is proposed, and it is later shown that Method 2 is more robust to noise and generally provides better estimations than Method 1.

First, in order to distinguish the internal DoFs that are measured by sensors from those that are subject to external forces, Eq. (6.2) is rewritten as:

$$\begin{Bmatrix} \mathbf{u}_{\mathrm{c}}^{\mathrm{B}} \\ \mathbf{u}_{\mathrm{b^m}}^{\mathrm{B}} \end{Bmatrix} = \begin{bmatrix} \mathbf{H}_{\mathrm{cc}}^{\mathrm{B}} & \mathbf{H}_{\mathrm{cb^f}}^{\mathrm{B}} \\ \mathbf{H}_{\mathrm{b^m c}}^{\mathrm{B}} & \mathbf{H}_{\mathrm{b^m b^f}}^{\mathrm{B}} \end{bmatrix} \begin{Bmatrix} \mathbf{f}_{\mathrm{c}}^{\mathrm{B}} \\ \mathbf{f}_{\mathrm{b^f}}^{\mathrm{B}} \end{Bmatrix} \tag{6.15}$$

where the subscripts $\mathrm{b^m}$ and $\mathrm{b^f}$ represent the measured internal DoFs and the internal DoFs subject to external forces, respectively. Based on Eq. (6.15), the following two equations can be established:

$$\mathbf{f}_{\mathrm{c}}^{\mathrm{B}} = \mathbf{H}_{\mathrm{b^m c}}^{\mathrm{B}}{}^{-1}\left(\mathbf{u}_{\mathrm{b^m}}^{\mathrm{B}} - \mathbf{H}_{\mathrm{b^m b^f}}^{\mathrm{B}}\mathbf{f}_{\mathrm{b^f}}^{\mathrm{B}}\right) \tag{6.16}$$

and

$$\mathbf{u}_{\mathrm{c}}^{\mathrm{B}} = \mathbf{H}_{\mathrm{cc}}^{\mathrm{B}}\mathbf{H}_{\mathrm{b^m c}}^{\mathrm{B}}{}^{-1}\left(\mathbf{u}_{\mathrm{b^m}}^{\mathrm{B}} - \mathbf{H}_{\mathrm{b^m b^f}}^{\mathrm{B}}\mathbf{f}_{\mathrm{b^f}}^{\mathrm{B}}\right) + \mathbf{H}_{\mathrm{cb^f}}^{\mathrm{B}}\mathbf{f}_{\mathrm{b^f}}^{\mathrm{B}} \tag{6.17}$$

By implementing Eq. (6.4), it can be shown that

$$\mathbf{u}_{\mathrm{c}}^{\mathrm{B}} = \mathbf{u}_{\mathrm{c}}^{\mathrm{A}} = -\mathbf{H}_{\mathrm{cc}}^{\mathrm{A}}\mathbf{f}_{\mathrm{c}}^{\mathrm{B}} \tag{6.18}$$

Substituting Eq. (6.16) and Eq. (6.17) into Eq. (6.18) leads to

$$\begin{bmatrix} \mathbf{Q} & \mathbf{R} \end{bmatrix} \begin{Bmatrix} \mathbf{u}_{\mathrm{b^m}}^{\mathrm{B}} \\ \mathbf{f}_{\mathrm{b^f}}^{\mathrm{B}} \end{Bmatrix} = -\mathbf{H}_{\mathrm{cc}}^{\mathrm{A}}\begin{bmatrix} \mathbf{H}_{\mathrm{b^m c}}^{\mathrm{B}}{}^{-1} & \mathbf{T} \end{bmatrix} \begin{Bmatrix} \mathbf{u}_{\mathrm{b^m}}^{\mathrm{B}} \\ \mathbf{f}_{\mathrm{b^f}}^{\mathrm{B}} \end{Bmatrix} \tag{6.19}$$

where

$$\mathbf{Q} = \mathbf{H}_{\mathrm{cc}}^{\mathrm{B}}\mathbf{H}_{\mathrm{b^m c}}^{\mathrm{B}}{}^{-1},\ \mathbf{R} = \mathbf{H}_{\mathrm{cb^f}}^{\mathrm{B}} - \mathbf{H}_{\mathrm{cc}}^{\mathrm{B}}\mathbf{H}_{\mathrm{b^m c}}^{\mathrm{B}}{}^{-1}\mathbf{H}_{\mathrm{b^m b^f}}^{\mathrm{B}}, \tag{6.20}$$

$$\text{and} \quad \mathbf{T} = -\mathbf{H}_{\mathrm{b^m c}}^{\mathrm{B}}{}^{-1}\mathbf{H}_{\mathrm{b^m b^f}}^{\mathrm{B}}$$

It can be shown that (see Appendix B)

$$\begin{Bmatrix}\mathbf{u}_{\mathrm{b^m}}^{\mathrm{B}} \\ \mathbf{f}_{\mathrm{b^f}}^{\mathrm{B}}\end{Bmatrix} = \begin{bmatrix}\left(\mathbf{E}\mathbf{T}_{\mathrm{b^m}}{}^{-1}\mathbf{H}_{\mathrm{b^m b^f}}^{\mathrm{AB}}\mathbf{T}_{\mathrm{b^f}}\right) + \left(\mathbf{H}_{\mathrm{b^m b^f}}^{\mathrm{B}} - \mathbf{E}\mathbf{H}_{\mathrm{b^m b^f}}^{\mathrm{B}}\right) \\ \mathbf{I}\end{bmatrix}\mathbf{f}_{\mathrm{b^f}}^{\mathrm{B}} = \mathbf{U}\mathbf{f}_{\mathrm{b^f}}^{\mathrm{B}} \tag{6.21}$$

where $\mathbf{E} = \mathbf{H}_{\mathrm{b^m c}}^{\mathrm{B}}\mathbf{H}_{\mathrm{b^m c}}^{\mathrm{B}}{}^{+}$, and $\mathbf{T}_{\mathrm{b^m}}$ and $\mathbf{T}_{\mathrm{b^f}}$ are the coordinate transformation matrixes for responses and excitations, respectively. Since $\mathbf{f}_{\mathrm{b^f}}^{\mathrm{B}} \in C^{\mathrm{b^f}}$, the resulting unmeasured receptances can be estimated by

$$\mathbf{H}_{\mathrm{cc}}^{\mathrm{A}} = -([\mathbf{Q} \quad \mathbf{R}]\mathbf{U})\left(\left[\mathbf{H}_{\mathrm{b^m c}}^{\mathrm{B}}{}^{-1} \quad \mathbf{T}\right]\mathbf{U}\right)^{+} \tag{6.22}$$

It should be mentioned that these two methods are methodologically identical but have different flexibilities in the inclusion of additional receptances and the selections of excitation and sensor coordinates. Strictly speaking, they can be referred to as two different ‘tests’.

6.2. Numerical simulation

In this section, both approaches proposed in the previous section are applied to a damped numerical model. The influence of removing the damping of the T-block and that of the presence of noise in FRFs are studied and evaluated. Later, a number of selections of the locations for excitations and measured responses are assessed. Finally, a fine FE model of the T-block is presented to provide FRFs for the estimation technique in practice.

6.2.1. Theoretical model

The theoretical model for this study is built based on a real laboratory test rig, which can be considered a rotor-bearing system. The schematic of the test rig and the T-block

is shown in Fig. 6.3. The test rig contains 3 sets of bearings, a circular shaft, a gear, and two identical discs. The shaft made of mild steel has the following properties: $E = 205$ GPa, $\rho = 7850$ kg m^{-3}, $\upsilon = 0.33$, $l = 1$ m, and $d = 17$ mm , and is modelled by Timoshenko beam elements. Each disc has mass of 0.67 kg, polar moment of inertia 7.653×10^{-4} kg m^2, and diametric moment of inertia 4.025×10^{-4} kg m^2. The gear has mass of 1.03 kg, polar moment of inertia 7.6142×10^{-4} kg m^2, and diametric moment of inertia 4.69×10^{-4} kg m^2. Bearings are treated as isotropic grounded springs, and each bearing is taken to have two transverse stiffness (2×10^7 N/m in *x*- and *y*-direction) and two rotational stiffness (26 Nm/rad in θ_x- and θ_y-direction).

In this simulation model, the T-block has the same material properties as the shaft and has a square cross-section with a width of 17 mm. For the sake of simplicity, it is modelled by 6 Timoshenko beam elements as shown in Fig. 6.2. Therefore, the detailed features, such as holes or the influence of the attached sensors, are not included in this simulation. It is worth mentioning that a multi-freedom constraint (MFC) is applied to take account of the problem of overlapping material. In this case, the node in the middle of the beam along the *y*-axis is chosen to be the master node while the node from another beam connected to the master node is the slave node. Lastly, the numerical model is assumed to be proportionally damped. As suggested by Silva [158], metal structures with joints and supports typically have damping ratios below 7%. To make the system lightly damped, the damping matrix is defined as $[\mathbf{C}] = 16.7863[\mathbf{M}] + 8.5041\times10^{-6}[\mathbf{K}]$, causing modes to have 1% to 3% of damping ratios for the frequencies below 1000 Hz. The undamped natural frequencies of the original shafting system and the assembled system below 1000 Hz are listed in Table 6.1.

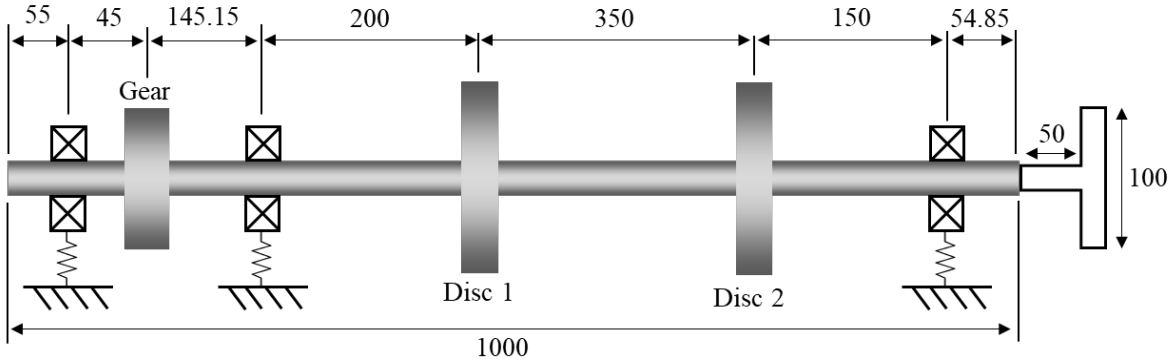

Figure 6. 3. The schematic of the numerical model (unit: mm).

Table 6. 1. The natural frequencies of the shafting system and the assembled system. (T denotes torsional natural frequency)

	Shafting system	Assembled system
Natural frequency (Hz)		63.3
	66.0	157.1
	172.6	227.4 (T)
	242.9 (T)	275.2
	421.7 (T)	411.1 (T)
	422.1	423.9
	494.9	513.6
	890.9	662.8 (T)
		905.9

The scenarios of estimating the torsional receptance through Method 1 and Method 2 are (see Fig. 6.2):

Method 1: an external excitation is applied at DoF 10 and the responses at DoFs 1, 2, and 10 are measured.

Method 2: two external excitations are applied separately at DoFs 13 and 16 and the corresponding responses to each excitation at DoFs 7 and 9 are measured.

The exact point torsional receptance at the tip of the shafting system is plotted together with the estimation results from Method 1 and Method 2 in Fig. 6.4. It is clear that both methods can yield the exact FRF when noise is not present.

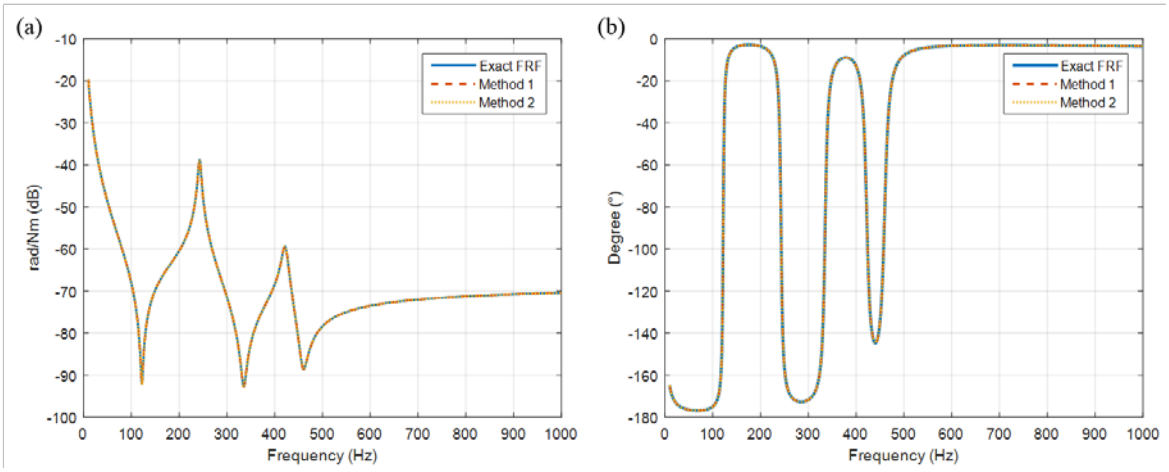

Figure 6. 4. Comparison of the exact FRF and estimated FRFs: (a) Magnitude and (b) Phase.

The removal of the damping of the T-block

In the previous case, the models and the measured FRFs are both assumed to be lightly damped, but damping could be difficult to determine when modelling the T-block. Therefore, in this example, the damping is removed from the model of the T-block while the shafting system and the assembled system are still assumed to be proportionally damped, and then the estimation results are assessed by comparing them with the exact FRFs. The results of using undamped T-block are presented in Fig. 6.5. By the observation of the magnitude and phase plots, it can be seen that the estimation results almost overlap with the exact FRFs; however, with a closer look, gaps between the estimated FRFs and the exact FRFs can be noticed, which is accounted for by the removal of damping of T-block. In this case, the mean and the variance of the magnitude differences for the two methods in dB scale from the exact FRF are both close and small, which are 0.0029 and 0.0027 for Method 2 and 0.0029 and 0.0029 for Method 1. However, it could be reasonable to surmise that the effect of removing the damping of the T-block could increase when the size of the T-block gets larger since its influence on the dynamic behaviour of the assembled system

increases when its size gets bigger. In order to confirm the speculation, the width of the T-block in Fig. 6.3 is increased from 10 cm to 30 cm, and the corresponding results (10 - 700 Hz) are shown in Fig. 6.6. It is clear that the magnitudes of the estimated FRFs are lower than the exact FRFs at the resonances, and that the estimated FRFs start to lose accuracies at high frequencies. This loss of accuracy at high frequencies could be caused by the assumption of proportional damping in this simulation model. The modal damping increases as the frequency gets higher in a proportional damping model; thus, the FRF curves can differ much from those without damping, leading to errors in the prediction of torsional FRFs. Although, in practice, the damping of the T-block itself is not expected to be large (<1%), care should be taken to avoid using a T-block that is too big or heavily damped in order to mitigate the effect as a result of the exclusion of the damping in the model of the T-block; besides, the T-block should not be too small in order to impart a sufficient moment/torsion. Generally, the size should be considered carefully and should vary on a case-by-case basis (depending on the parent structure).

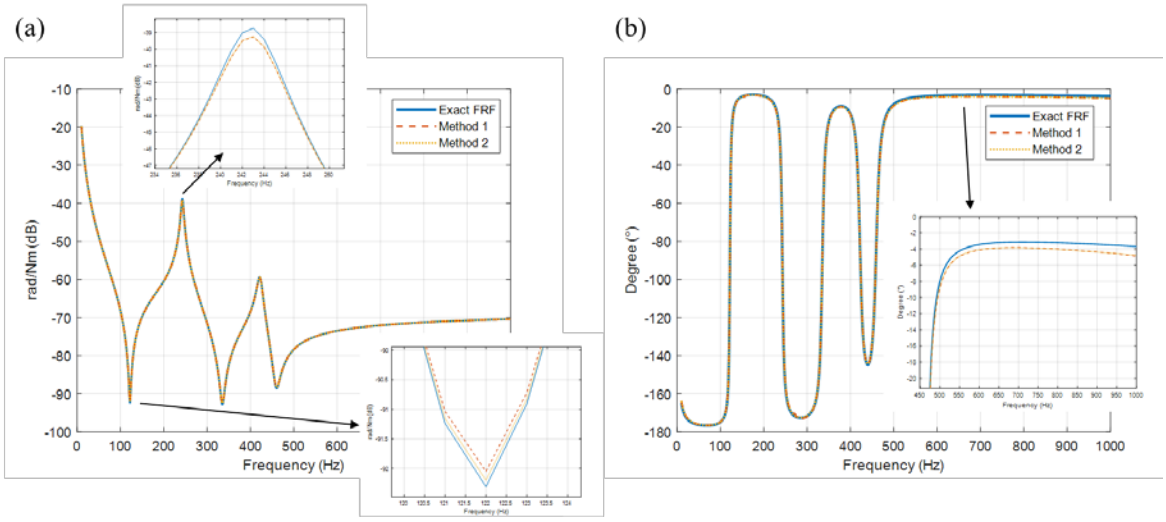

Figure 6. 5. The estimated torsional receptance when the damping of the T-block is excluded: (a) Magnitude and (b) Phase.

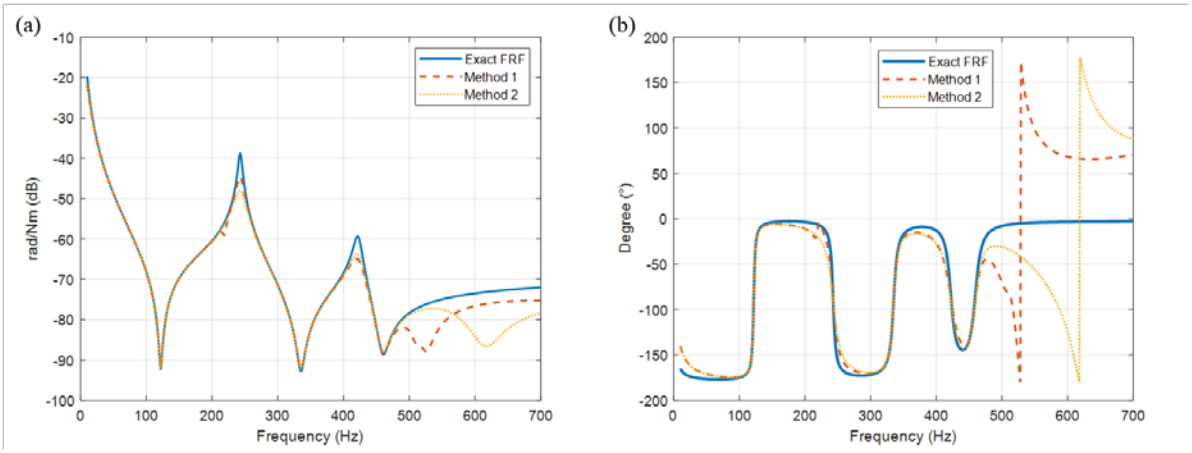

Figure 6. 6. The estimated torsional receptance when the damping of a longer T-block is excluded: (a) Magnitude and (b) Phase.

The inclusion of noise in FRFs

In order to further assess the robustness of the methods, numerical noise is then added to the FRFs of the coupled system that are to be obtained experimentally in practice (but the damping of the T-block is neglected). A magnitude-dependent contaminated FRF at frequency ω is defined as:

$$\tilde{h}(\omega) = (1 + \frac{\gamma}{100} \cdot \text{randn}) \cdot h(\omega) \tag{6.23}$$

where γ is noise level in (%) and randn is a normally distributed random number whose mean and standard deviation are 0 and 1, respectively. For instance, Fig. 6.7 shows some of the contaminated FRFs in which the noise level is set to 10%, and the resulting estimations obtained are compared with the exact FRF in Fig. 6.8. In this example, the results are the averages of 10 estimations whose FRFs are randomly contaminated through Eq. (6.23).

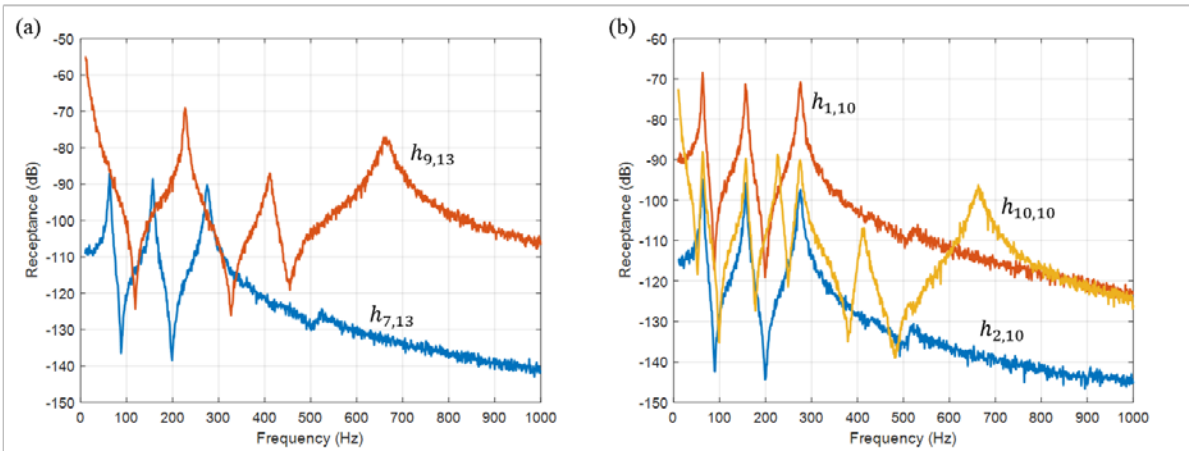

Figure 6. 7. Examples of FRFs with added numerical noise used in (a) Method 2 and (b) Method 1.

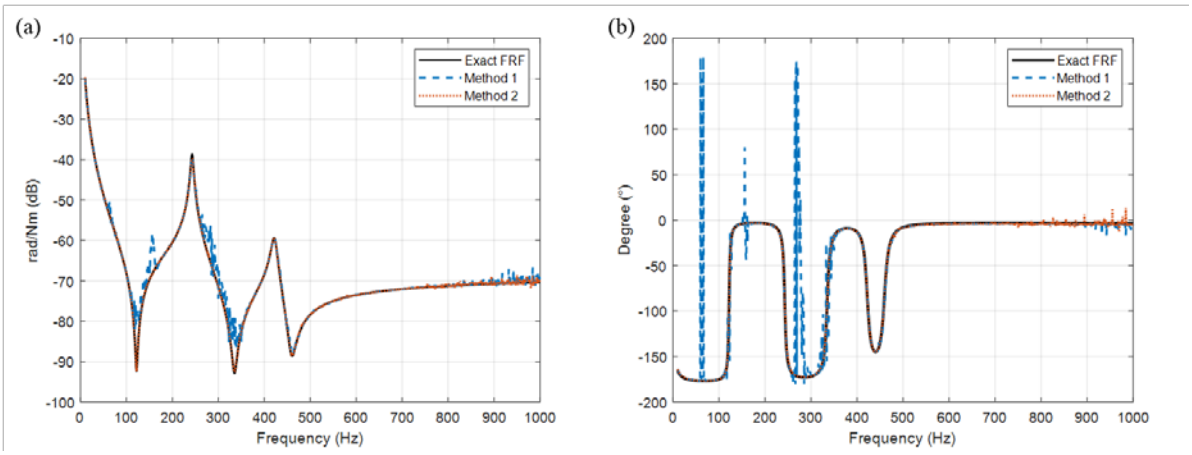

Figure 6. 8. The estimation of torsional receptance with noisy FRFs: (a) Magnitude and (b) Phase.

It can be seen that, in general, both methods can produce fairly accurate estimations especially below 800 Hz. The mean and the variance of the amplitude differences in dB scale in the frequency range of 10 – 1000 Hz, which are given in Table 6.2, are used to compare the performance of the methods. It is clear that Method 2 is better than Method 1 since those values of Method 2 are much smaller than those of Method 1 and that the estimation produced by Method 1 has several unexpected peaks other than the torsional natural frequencies. It can further be found that those unwanted peaks occur near the bending natural frequencies of the assembled system (see Fig. 6.7 and Table 6.1). In addition to this, the estimated FRFs seem to be more

sensitive to noise in the high-frequency range, which might result from the relatively smaller response in the receptances used for the estimations (see Fig. 6.7).

Table 6. 2. The mean and the variance of the magnitude difference in FRFs (10 - 1000 HZ).

	Method 1	Method 2
(Mean, Variance) of magnitude difference in dB	(0.2237, 2.3280)	(0.0383, 0.0871)

Further discussion on Method 2

Choice of responses and excitations

In the previous discussion, it has been demonstrated that both methods work well when noise is not present and that Method 2 performs better than Method 1 when noise is present. Therefore, Method 2 is chosen to be further studied. When implementing Method 2, the question of "which DoFs on the T-block should be selected for measured responses and excitations" would first arise and is of great importance to the quality of the estimated receptance.

To answer the question of the selection of measured responses, attention should be first paid to the formulation of Method 2, namely, Eqs. (6.19) to (6.22). In the formulas, it can be noticed that the inversion of $\mathbf{H}^{B}_{b^m c}$ is heavily involved, thus possibly causing numerical difficulties in the results. In order to avoid that, b^m should be selected so as not to make $\mathbf{H}^{B}_{b^m c}$ singular or close to singular; additionally, it is believed that including the rotational response (DoF 9 in Fig. 6.2) is crucial for obtaining better estimations since Eq. (6.22) is essentially solved in a least-squares sense. Considering these two points, several options for b^m are available, and different selections of measured responses can have different levels of robustness against the presence of noise in the measured FRFs.

On the other hand, regarding the excitations, there are mainly three key factors to be considered. One is the quality of the FRF measurements in practice, another is the generation of torsion, and the last one is the number of excitations required to obtain sufficiently accurate estimations. If a modal impact test is to be carried out, generating a clear impact is vital for acquiring high-quality measurements. By considering this along with the generation of torsion, excitations should be applied on the “wings” of the T-block. As double impacts are likely to happen in this test setup, locations of the excitations should not be too close to the tips of the wings (similar to the case of hitting the tip of a cantilever beam); that is to say, in Fig. 6.2, DoFs 13 and 16 could be a better choice than DoFs 10 and 19. On the other hand, if a Shaker Test is implemented in the measurement, the issue of double impacts can be circumvented. In that case, excitations on DoFs 13 and 16 could be a better choice as a greater torsional excitation can be generated.

To answer the question of the number of excitations required and the influence that different selections of measured responses can make, a number of simulations are carried out. In the simulation, a set of noisy FRFs (10% noise level) are used for different combinations of excitation DoFs and response DoFs, and the results are compared through the mean and variance of the amplitude difference from the exact FRF within the range of 10 - 700 Hz in dB scale. For the sake of clarity, only a few cases are presented so as to give a general picture. The results are presented in Fig. 6.9, and some findings are summarized below:

(1) The method is rather easy to implement since it is possible to obtain a clear estimation by a single modal impact test.
(2) Increasing the number of excitations can improve the quality of the estimation while increasing the number of measured translational responses might not necessarily have the same beneficial effect.
(3) Including the rotational response (DoF 9) can significantly improve the robustness of the estimation when the level of noise is high in the measurements and thus ought to be considered in the measurement.

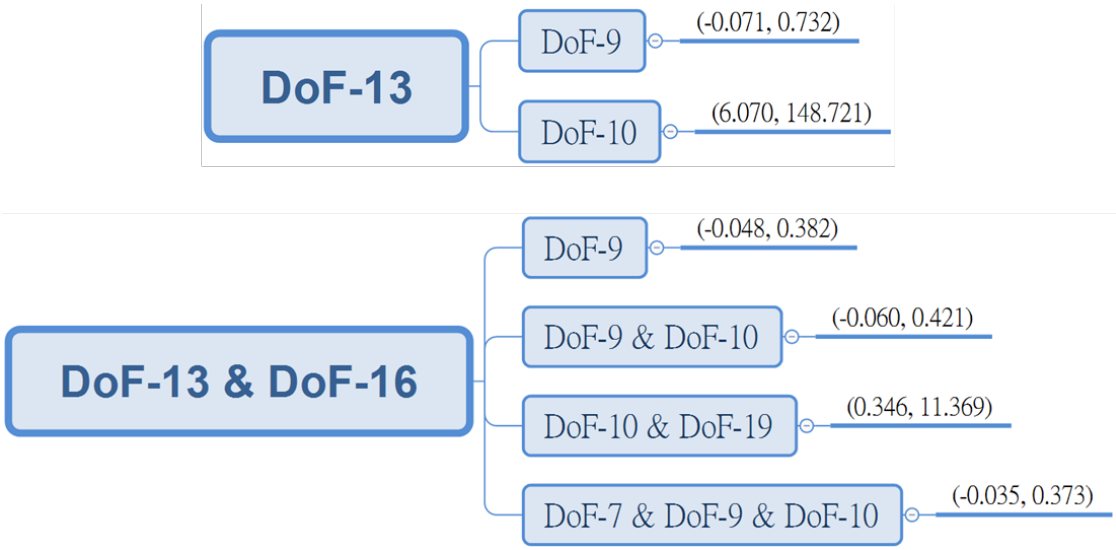

Figure 6. 9. Different combinations of excitations and responses. The blocks, from left to right, represent the DoFs for excitation, DoFs for measured responses, and the mean and variance of the corresponding result.

It is worth mentioning that, in the case of using noise-free FRFs, all the combinations listed in Fig. 6.9 produce exactly the same correct results except for the case of excitation at DoF 13 and measured response at DoF 10. The estimated torsional receptance in the last example of Fig. 6.9 is given in Fig. 6.10, and the corresponding mean and variance are -0.035 and 0.373, respectively. The exact FRF and the estimated receptance are generally in good agreement, but some fluctuations (due to noise) on the magnitude and the phase curves can also be noticed.

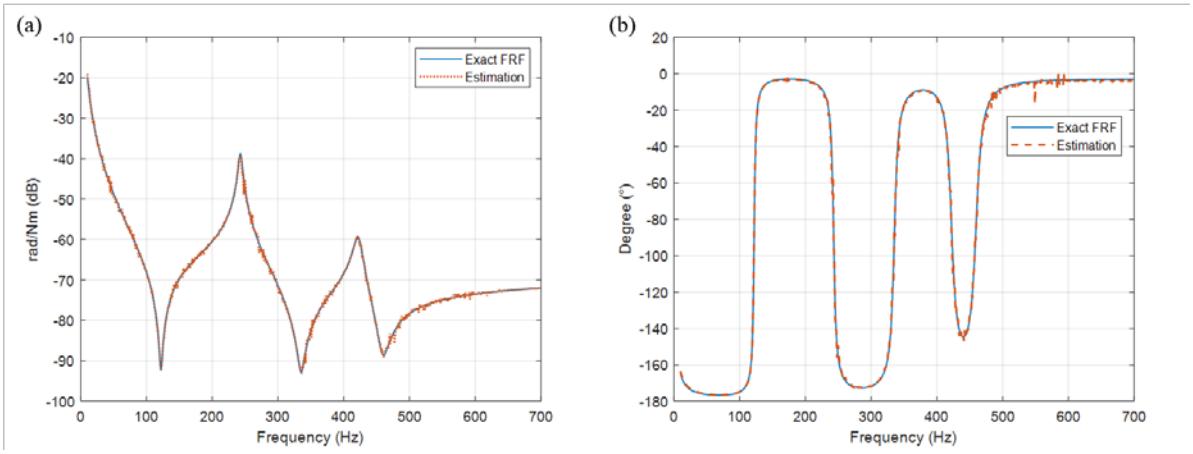

Figure 6. 10. Estimated torsional receptance: (a) Magnitude and (b) Phase.

Comparison with Lv's approach

As this work is mainly inspired by Lv's paper [97], a comparison of Method 2 proposed in this paper and their approach is presented to highlight the differences and improvements. Fig. 6.11 shows the estimated torsional FRFs using different approaches in which the noise levels of the required measured FRFs are both set to 10%. The main differences between these two approaches are (1) The choice of DoFs for responses and excitations and (2) the two-step procedure in Lv's approach in which the receptance at DoF 9 is first estimated and the torsional FRF of the parent system is then estimated based on the receptance at DoF 9 (please see [97] for more details). The DoFs for responses and excitations for Method 2 are DoFs 7, 9, 10 and DoFs 13, 16, and those for Lv's method are DoFs 10, 19 and DoFs 10, 19. From this figure, overall, it is clear that Method 2 is more robust against measurement noise. The mean and variance of magnitude difference from the exact FRF in dB scale for Method 2 are (-0.0229, 0.6221), and that for Lv's approach are (-0.0518, 4.0060). Through a closer inspection, it can be seen that the FRF from Lv's approach is prone to having extra peaks (pointed by the arrows) whose locations are close to the bending natural frequencies of the assembled system and that it fails to clearly capture the anti-resonances. These issues have been reported in Lv's paper, and the proposed Method 2 is shown to successfully resolve the issues and produce a more reliable result.

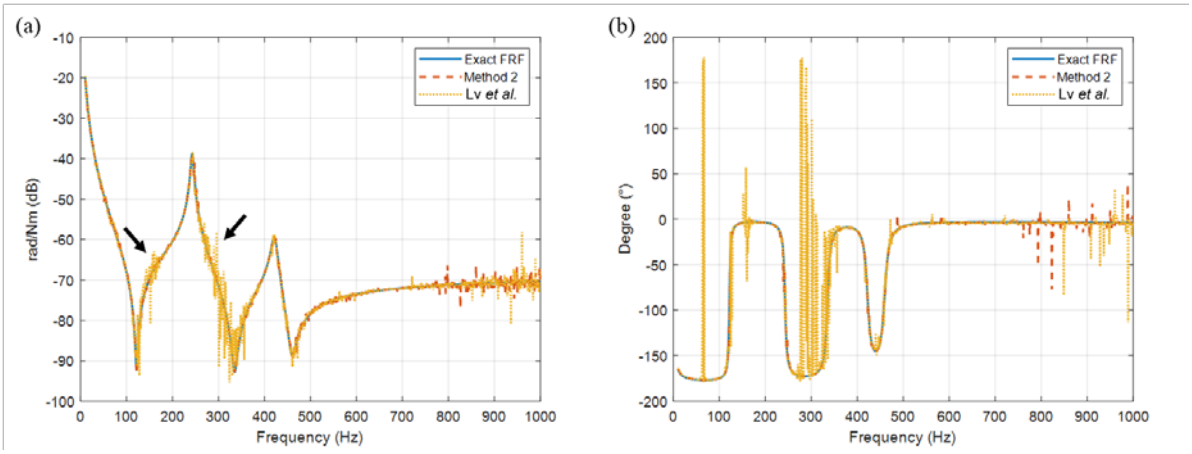

Figure 6. 11. Comparison of FRFs obtained from Method 2 and Lv's approach: (a) Magnitude and (b) Phase.

The underlying causes for the differences between Method 2 proposed in this paper and Lv's approach are further discussed and revealed through the following four targeted case studies.

- Case 1: Lv's approach is used to estimate the torsional FRF. The DoFs are the same as the original paper, which are DoFs 10, 19 for both responses and excitations.
- Case 2: Method 2 is implemented in Lv's two-step approach, but the "internal" receptances, which are estimated in the first step and passed to the second steps, include the DoFs in all three directions, x, θ_y, and θ_z. Originally, only x-axis direction is considered.
- Case 3: This is similar to Case 2, but it includes one more rotational response at DoF 9 in the first step.
- Case 4: Method 2 is directly used to estimate the torsional FRF. The DoFs for responses are DoFs 9, 10, 19 and those for excitations are 10 and 19.

As the normally-distributed artificial noise is randomly added, 50 estimations are generated for each case to evaluate their error distribution. Examples of the resulting FRFs of the four cases are plotted in Fig. 6.12. It can be seen that all the estimated FRFs are generally close to the exact FRF but show different levels of variations (robustness against noise). To evaluate the performance, the probability density function of variations for each case is estimated using kernel density estimation (KDE) with Gaussian kernel and Silverman's rule of thumb bandwidth estimator [159]. The probability density functions are plotted in Fig. 6.13.

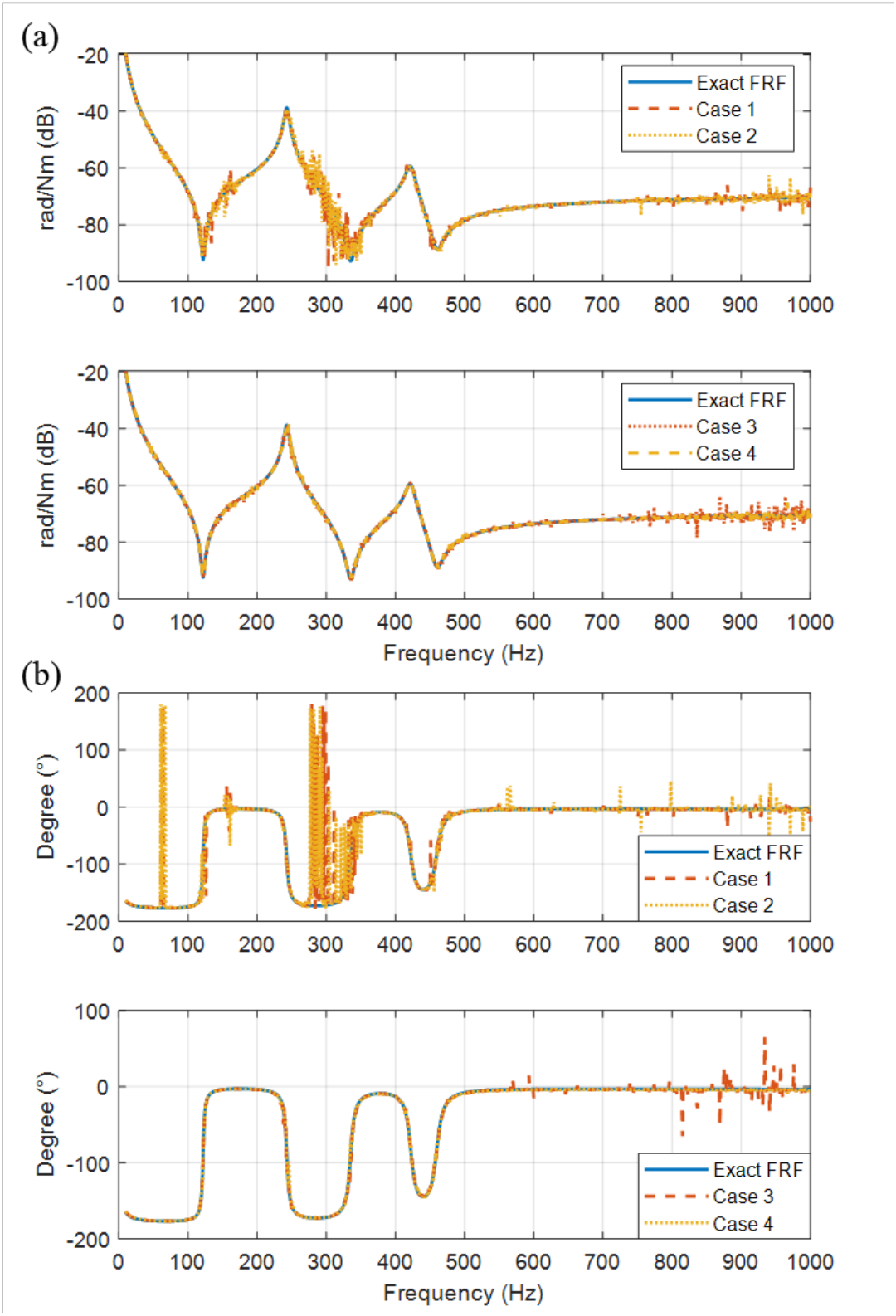

Figure 6. 12. The resulting FRFs of different cases: (a) Magnitude and (b) Phase plot.

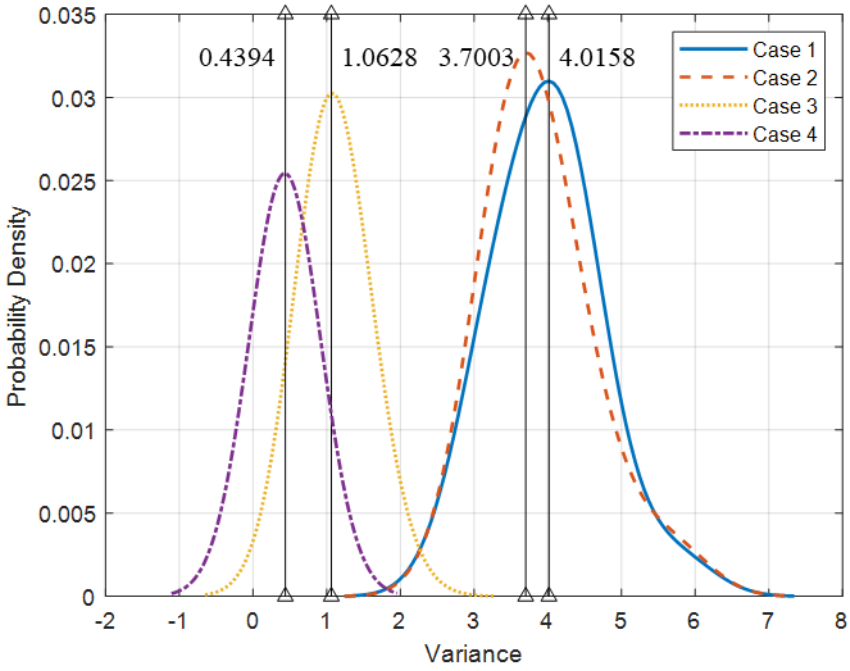

Figure 6. 13. Probability density functions for four different cases.

Case 2 is designed to answer the question whether omitting the "internal" receptances in θ_y, and θ_z directions in Lv's two-step approach would degrade the result as the excitations applied on the T-block do as well excite responses in the θ_y, and θ_z directions. Results show that Case 2 only has a slight improvement over Case 1 given that the most likely value for variance drops only slightly from 4.0158 to 3.7003; nonetheless, it is reasonable to presume that the influence of including the 'internal' receptances can become more noticeable when the T-block gets larger. Case 3 again clearly demonstrates the importance of including a measured rotational response as it reduces the most likely value for variance significantly to 1.0628. The unwanted peaks in Cases 1 and 2 have disappeared when including the rotational receptance at DoF 9 in Case 3. Lastly, Case 4 still outperforms Case 3 even though these two cases have the same selected DoFs for response and excitation. Method 2 proposed in this paper is able to produce estimations in one go and take into account receptances in all three directions, thus possibly avoiding the additional numerical errors that the two-step procedure in Lv's approach introduced; moreover, Method 2 provides the flexibility in selecting DoFs for response and excitation without difficulty. These are probably the main reasons that make Method 2 a more robust method.

6.2.2. Model updating of the T-block

In reality, the T-block might include several geometrical features or interference with the attached sensors, and thus a more detailed and accurate model has to be generated to represent the real structure. Fig. 6.14(a) shows the T-block that is used in practice for Method 2. The models of the translational accelerometer and the rotational accelerometer are Kistler 8728A500 and Kistler 8840, weighing 1.6 grams and 22 grams, respectively. The rotational accelerometer is attached to the T-block by a single socket head cap screw. It is found that the resonant frequencies and the accuracy of acceleration measurement are affected by the mounting torque of the rotational accelerometer; hence, care has to be taken to ensure the mounting torque is set to the value specified by the provider, which is 2 Nm in this case.

A finite element model of the T-block shown in Fig. 6.14(b) is built in Abaqus using quadratic hexahedral elements of type C3D20R, and the total number of nodes and elements are 12934 and 2704, respectively. The green square spots in Fig. 6.14(b) show the nodes with point masses representing translational accelerometers, and the rotational accelerometer is modelled as a point mass away from the T-block at reference point 1 (RP-1). The motion of the regions around the hole on the T-block close to the rotational accelerometer is constrained to reference point 2 (RP-2). Then, RP-1 is connected to RP-2 through springs in 4 DoFs ($x, y, \theta_x,$ and θ_y) in order to take the interaction into consideration, and the other two DoFs (z and θ_z) are assumed to be rigidly connected. The springs are assumed to be isotropic, i.e. the spring constants in *x* and *y* directions are the same.

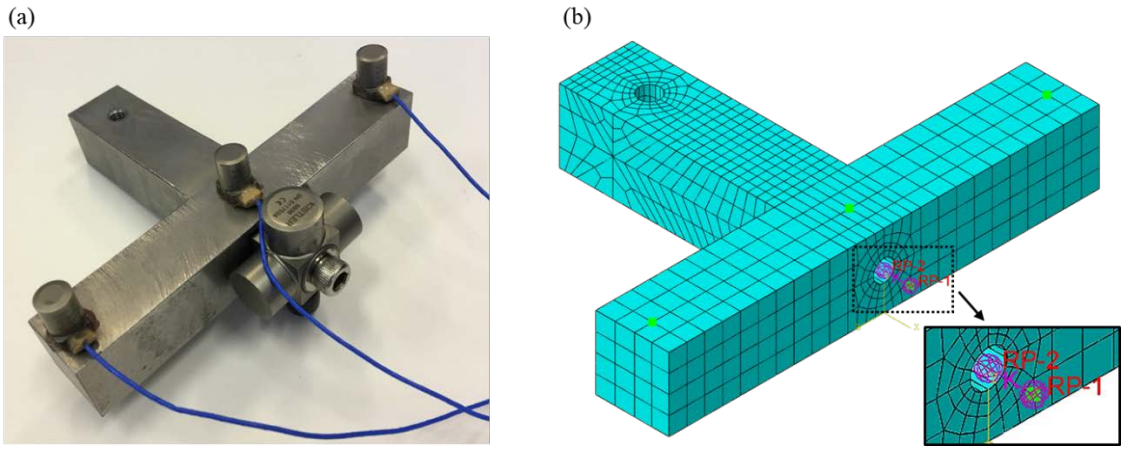

Figure 6. 14. T-block (a) the real structure (b) FE model.

Modal analysis is carried out to find the natural frequencies of the free-free T-block with those sensors attached, and the inverse eigensensitivity method is implemented to update the model parameters. The updated parameters are chosen to be Young's Modulus and the translational spring stiffness between RP-1 and RP-2 since the natural frequencies are found to be insensitive to the change of Poisson's ratio and the rotational spring stiffness. Three experimentally identified natural frequencies are used for the updating, thus leading to an over-determined problem. The updated natural frequencies and the system parameters are given in Table 6.3 and Table 6.4, respectively. Although the updated Young's modulus is on the high side, it remains within the reasonable range. From Table 6.3, it is clear that the model matches the experimental results well as all the errors are less than 0.05%.

Table 6. 3. Comparison of experimental and numerically determined natural frequencies.

	Experiment	Updated Model	Error
Natural frequency (Hz)	6193.25	6195.1	0.0299 %
	8844.27	8840.7	-0.0404 %
	13272.25	13274	0.0132 %

Table 6. 4. System parameters.

Young's Modulus (GPa)	219.63	Poisson's ratio	0.33	Density (kg/m^3)	7853.7

Rotational spring stiffness (Nm/rad)	10^5	Translational spring stiffness (N/m)	3.944×10^7

The need for updating should be justified as the natural frequencies of the T-block are much higher than the frequency range of interest of the parent structure. It is found that when the rotational accelerometer is modelled as a point mass and rigidly connected to the T-block, the simulation only shows two natural frequencies, 7112 Hz and 11546 Hz, in the frequency range calculated. The first natural frequency (6193 Hz) of the T-block identified from the experiment was due to the presence of the rotational accelerometer on the T-block and the natural frequencies of the T-block can be significantly affected by the value of the translational stiffness between RP-1 and RP-2. The translational stiffness could be associated with the mounting torque of the socket head cap screw and may vary for a different sensor by another supplier. For this particular parent structure, the identified torsional receptance changes slightly if the nominal parameter values (not updated) of the T-block are used. However, if the fundamental frequency or the frequency range of the parent structure concerned increases and is nearer the fundamental frequency of the T-block, using accurate parameter values of the T-block would become important. Thus, it is desirable to update the T-block to take account of the influence from the attached sensors.

6.3. Experimental validation

In the previous sections, Method 2 has been studied and evaluated in a numerical simulation and a detailed FE model of the T-block is built and updated; therefore, Method 2 is ready to be verified and further assessed in practice.

6.3.1. Torsional receptance estimation

The laboratory test rig for the experimental validation, on which the numerical model depicted in Fig. 6.3 is based, is shown in Fig. 6.15 below.

Figure 6. 15. The laboratory shafting structure.

For the sake of discussion, the definition of the DoFs of the experimental setup and the measured FRFs are still labelled and defined based on the schematic in Fig. 6.2. The scenario is to apply modal impact tests on the assembled structure and the selection for forces and measured responses are DoFs 13 and 16 and DoFs 7, 9, and 10, respectively. Some of the measured FRFs are shown below in Fig. 6.16 and the frequency range is set within the range of 10 to 1000 Hz. As can be seen from Fig. 6.16, there are potentially three torsional natural frequencies for the assembled structure below 1000 Hz, and there are several prominent bending natural frequencies among them. The accelerometer at the tip (DoF 10) is able to capture frequencies for both the bending (DoF 7) and torsion (DoF 9).

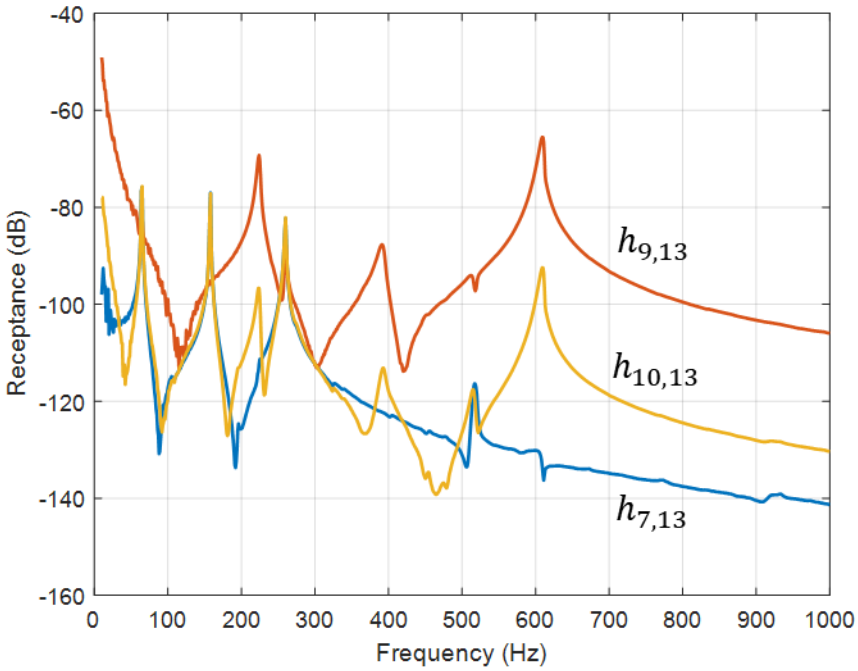

Figure 6. 16. Measured FRFs of the assembled structure.

It should be pointed out that the coordinates used in the simulation model and experiment have to be the same to ensure the estimated receptances is accurate. Moreover, it is also suggested that any near-zero singular value of $\mathbf{H}^{B}_{b^{m}{}_{c}}$ could be treated as zero when calculating the pseudoinverse of $\mathbf{H}^{B}_{b^{m}{}_{c}}$ in order to remove noise [160] in which choosing the right threshold can be a difficult task and varies on a case-by-case basis. The results of using FRFs in Fig. 6.16 are given in Fig. 6.17. Both of the magnitude and the phase of the estimated FRF are quite clear within the frequency range; the change of phase angle is clear when the frequency passes through the resonances and anti-resonances. The appearance of bending natural frequencies in torsional receptance, which is reported in Lv's paper, does not occur in this method. However, some small fluctuations and changes of phase can be noticed for frequencies below 100 Hz. A comparison of the results with Fig. 6.4 suggests that the estimated FRF matches the trend quite well and that the response level is roughly at the same order, in relation to the experimental results.

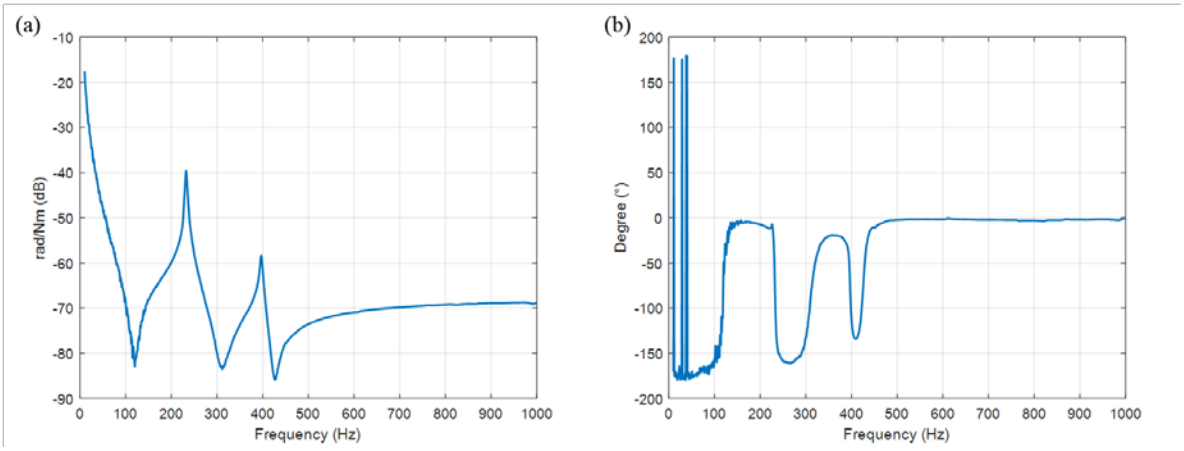

Figure 6. 17. Estimated torsional receptance: (a) Magnitude and (b) Phase.

6.3.2. Modal parameter estimation

The polyreference least-squares complex frequency-domain method (p-LSCF), which is also called “PolyMAX” in the software Test.Lab by LMS, is implemented to identify the poles of the estimated torsional receptance. p-LSCF is a multiple degree of freedom method operating on FRFs, yielding global estimations of poles and modal participation factors, and the equivalent method in time domain is the well-known least-squares complex exponential method (LSCE) [22]. Compared with other frequency-domain methods, p-LSCF has several advantages [23], for example, (1) it produces clear stabilization diagrams which allow users to select the “physical” poles, hence omitting the “mathematical” poles which are mainly caused by the presence of noise in the measurements, (2) it does not suffer from numerical instability problem as it is formulated in the z-domain, and (3) it introduces weightings in the least-squares cost function to take into account the quality or differences among measurements, hence improving the quality of estimation.

In general, it is suggested to over-specify the denominator polynomial order (model order) in the right matrix-fraction model [161] when carrying out the p-LSCF method. Therefore, in this example, the model order is set to the range of 9 to 17 although there are potentially only two natural frequencies that can be found in this frequency range (rigid body modes are excluded). In the process of constructing the stabilization diagram, the poles of an order are compared with the poles that are one-

order lower to determine whether the poles are stable or not. In this case, the tolerances for undamped natural frequency and damping ratio are set to 1% and 5%, respectively. The stabilization diagram is presented in Fig. 6.18 in which the stable frequencies and stable poles (both frequency and damping are stable) are denoted as circles and asterisks. It can be seen that the stabilization diagram is quite clear; nearly all the stable frequencies and stable poles are found to lie along the two resonant frequencies.

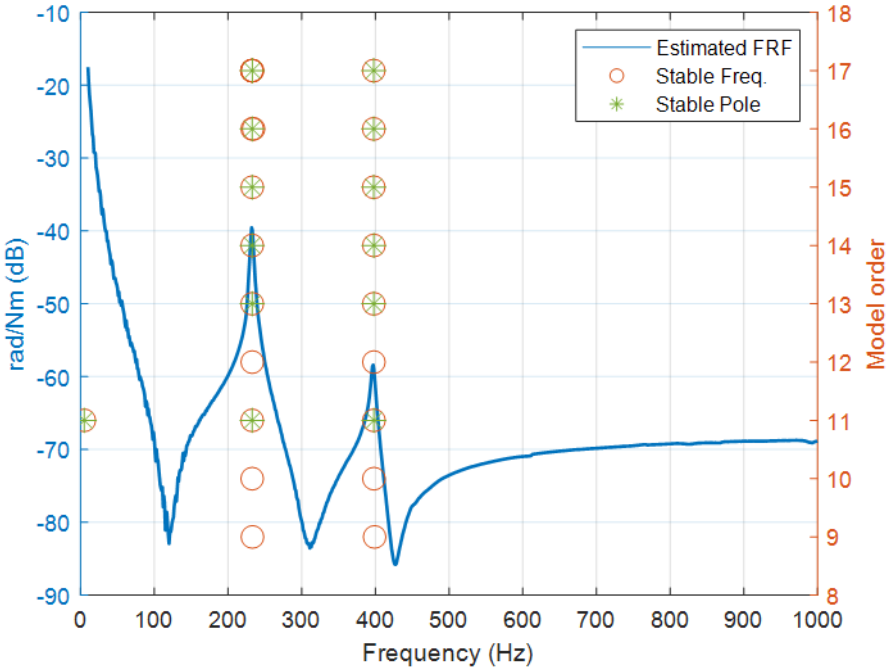

Figure 6. 18. Stabilization diagram from p-LSCF.

The natural frequencies and the damping ratios of some of the stables poles are summarized in Table 6.5. Through Fig. 6.18 and Table 6.5, it can be noticed that the frequencies are relatively stable compared with the damping ratios throughout the model orders and that the damping ratios become more stable in high model orders. For the sake of demonstration, the averaged natural frequency and damping ratio at the two resonances are: 233.15 Hz with 1.16% of damping and 397.84 Hz with 1.44% of damping.

Table 6. 5. Natural frequency and damping of stable poles.

Model order	11	13	15	17
Stable poles	232.82 Hz, 1.28%	233.87 Hz, 1.15%	232.90 Hz, 1.11%	232.99 Hz, 1.08%
	398.00 Hz, 1.59%	397.82 Hz, 1.38%	397.76 Hz, 1.39%	397.77 Hz, 1.39%

6.3.3. Repeatability of the estimated receptances

In the study of FRF estimations, the consistency of the result is of great importance. In order to examine the consistency of the torsional receptance estimation, 10 estimations are all plotted together in dotted lines in Fig. 6.19. Each estimation is derived from the average of 10 measured FRFs. In addition to this, a correlation check is implemented to assess the closeness between the estimations. The correlation check is based on the discrepancies in amplitude, and thus the amplitude correlation coefficient κ can be defined as:

$$\kappa(\omega) = \frac{2|\mathbf{h}_x(\omega)^{\mathrm{H}}\mathbf{h}_{\mathrm{a}}(\omega)|}{\mathbf{h}_x(\omega)^{\mathrm{H}}\mathbf{h}_x(\omega) + \mathbf{h}_{\mathrm{a}}(\omega)^{\mathrm{H}}\mathbf{h}_{\mathrm{a}}(\omega)} \tag{6.24}$$

where $\mathbf{h}_{\mathrm{a}}(\omega)$ is the average of the 10 torsional receptance estimations, and $\mathbf{h}_x(\omega)$ is any one of the 10 estimations. The coefficient returns a value between 0 and 1 at each frequency. There are in total 10 sets of amplitude correlation coefficients at the frequency range of 10 to 1000 Hz, and the averaged of them is plotted together with the magnitude and phase plot in Fig. 6.19. It can be noticed that, on the whole, the repeatability of the estimations is high (most coefficients are higher than 0.99) and that the estimations at resonances and anti-resonances tend to have a relatively lower repeatability. Some fluctuations can also be seen especially in the low frequency range. Moreover, there is a lack of phase consistency roughly below 100 Hz in the phase plot; the magnitudes of the phase are roughly the same, but the signs are reversed. The main

reason for these inconsistencies in low frequency is believed to be due to the use of ICP sensors in the measurement; therefore, choosing sensors having higher sensitivity at low frequencies can possibly circumvent the problem.

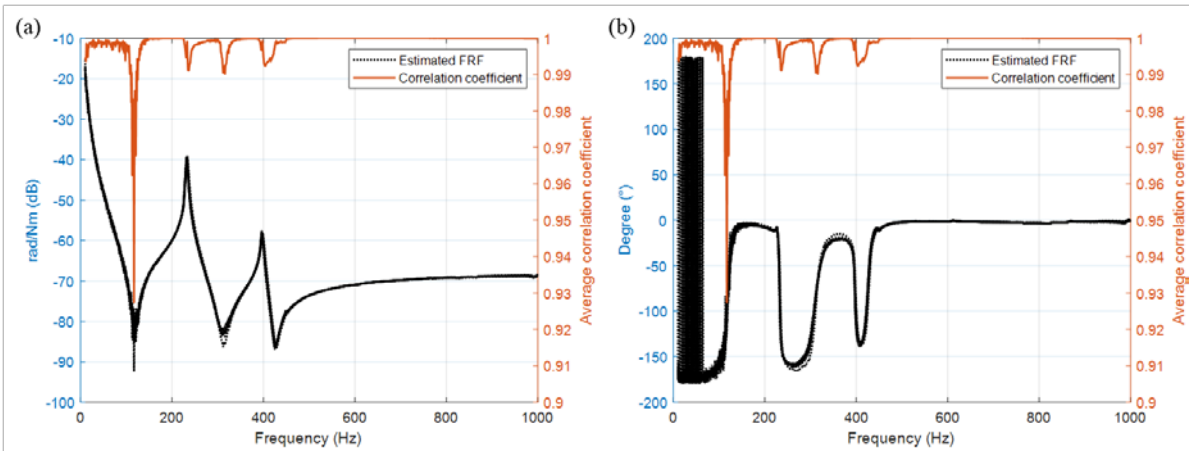

Figure 6. 19. Ten torsional receptance estimations: (a) Magnitude and (b) Phase.

The average of the 10 estimated torsional receptances in Fig. 6.19 is given in Fig. 6.20 along with its stabilization diagram. Table 6.6 summarizes the natural frequencies and damping ratios of some of the stable poles in the diagram, and the averaged values for natural frequencies and damping ratios are: 232.95 Hz with 1.15% of damping and 398.09 Hz with 1.39% of damping, which are very close to the figures previously identified using a single torsional receptance estimation.

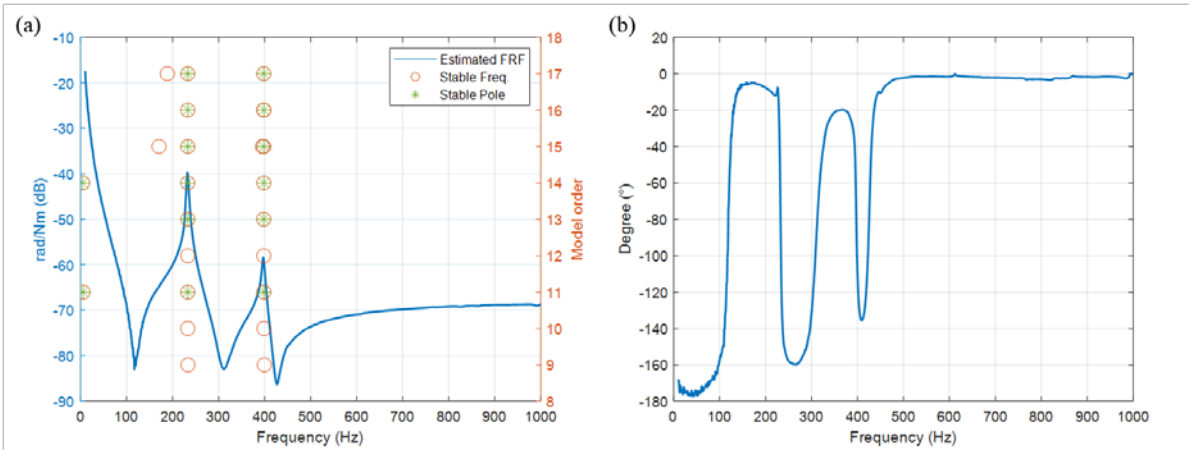

Figure 6. 20. The averaged torsional receptance: (a) Magnitude and the stabilization diagram and (b) Phase.

Table 6. 6. Natural frequency and damping of stable poles.

Model order	11	13	15	17
Stable poles	232.92 Hz, 1.27%	232.97 Hz, 1.12%	232.90 Hz, 1.10%	232.99 Hz, 1.10%
	398.21 Hz, 1.51%	397.96 Hz, 1.35%	398.11 Hz, 1.36%	398.07 Hz, 1.35%

6.3.4. Synthesis of frequency response functions

Once a stable pole is identified, a noise-free synthesized FRF can be calculated, which is produced by the so-called pole-residue model [31] evaluated along the frequency axis (jω) shown by the equation:

$$\mathbf{H}_{ij}(j\omega) = \sum_{r=1}^{n}\left(\frac{\psi_{ir}l_{rj}}{\mathrm{j}\omega - \lambda_r} + \frac{\psi_{ir}^{*}l_{rj}^{*}}{\mathrm{j}\omega - \lambda_r^{*}}\right) - \frac{LR_{ij}}{\omega^2} + UR_{ij} \qquad (6.25)$$

where *i* and *j* are locations of response and input; *n* is the number of modes involved in the curve-fitting of the FRF; λ_r are the poles that occur in complex conjugate pairs; ψ_{ir} and l_{rj} are mode shapes and modal participation factors, and LR_{ij} and UR_{ij} are the lower and upper residue terms that represent out-of-band modes. As the poles are estimated by p-LSCF and the corresponding stabilization diagram, the only unknowns are the complex conjugate pairs of ψ_{ir} and l_{rj}, and of LR_{ij} and UR_{ij}. Since the information is rich in the frequency domain, the unknowns can be solved in a weighted least-squares sense. The results are shown in Fig. 6.21 below, which shows that the synthesized FRF matches the estimated FRF well and that it removes the unwanted noise to produce clearer information.

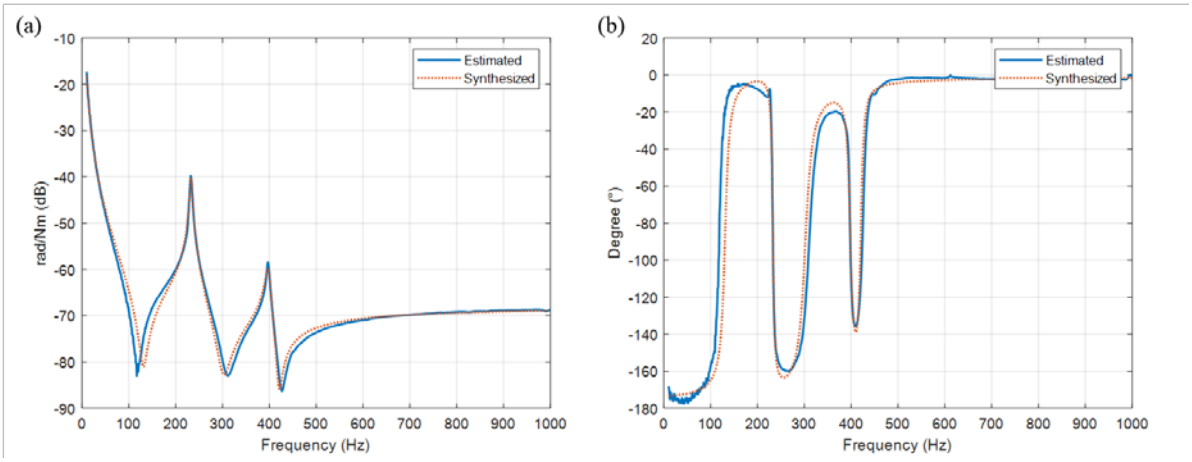

Figure 6. 21. The synthesized FRF of the averaged torsional receptance: (a) Magnitude and (b) phase.

6.3.5. Different selections of the response

As mentioned and demonstrated numerically in Section 6.2.1, different selections of measured responses can result in different qualities of estimations, and thus it is important to evaluate the real differences in practice. In this section, three more selections of responses are tested. The same set of measurement data in the previous section is used, and the measured response(s) is simply selected from the data set. Therefore, the additional cases for the selections are DoFs 9 and 10, DoF 9 only, and DoFs 7 and 10. The experimental results are presented in Fig. 6.22 and 6.23. First, it is clear that there is not much difference between the estimation of using DoFs 7, 9, and 10 and that of using DoFs 9 and 10, which implies that the inclusion of translational response of DoF 7 does not seem to improve or deteriorate the result. Second, solely using the rotational response at DoF 9 seems to be able to produce a clear estimation; however, there is an unexpected drop at around 260 Hz, which is, in fact, a bending natural frequency of the assembled system. It can be shown from the FRF in Fig. 6.16 that the rotational accelerometer also senses the bending natural frequency at about 260 Hz, which accounts for the appearance of the drop in the estimated torsional receptance. This unwanted drop can be removed by applying modal parameter identification technique and generating a synthesized torsional receptance as demonstrated in Section 6.3.2 and 6.3.4. Finally, in the last case in which

the rotational response is not included, a quite clear estimation can also be produced by only using two translational responses: DoFs 7 and 10, and the results are almost the same as the ones in the first cases. As a matter of fact, this finding does not contradict the numerical results in Section 6.2.1, and just implies that the noise level of the current measured FRFs is low; thus, in this case, adding the rotational response does not much improve the quality of the results.

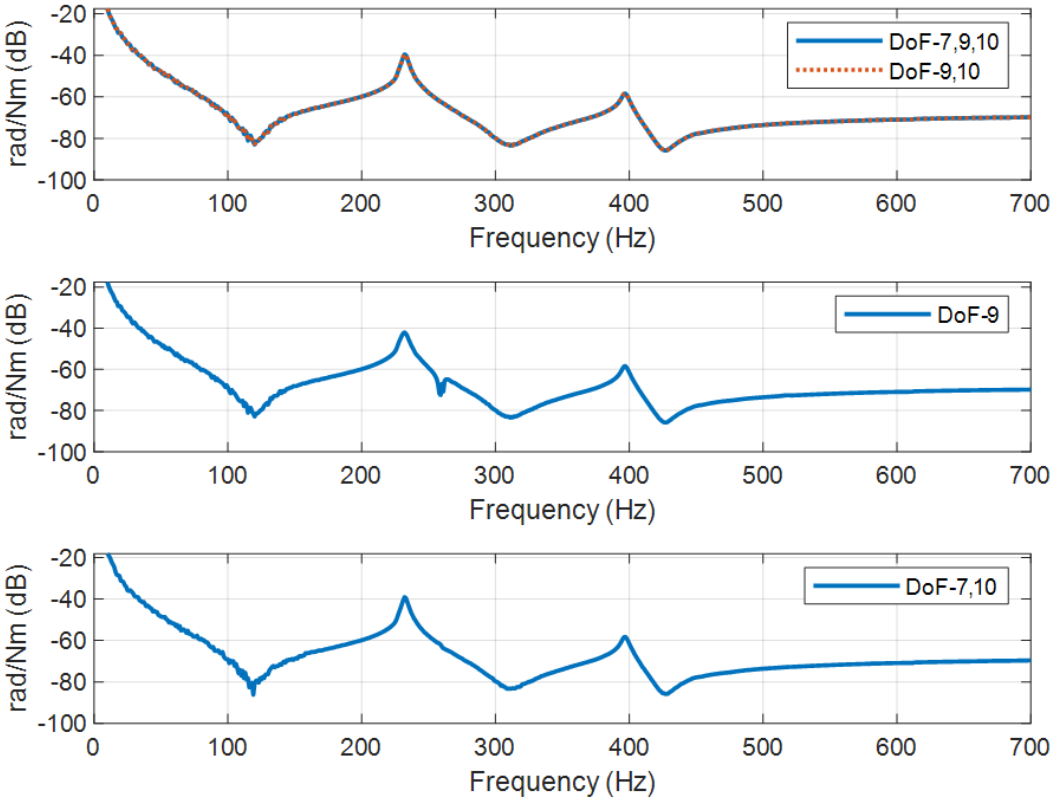

Figure 6. 22. The magnitude plot of different selections of responses.

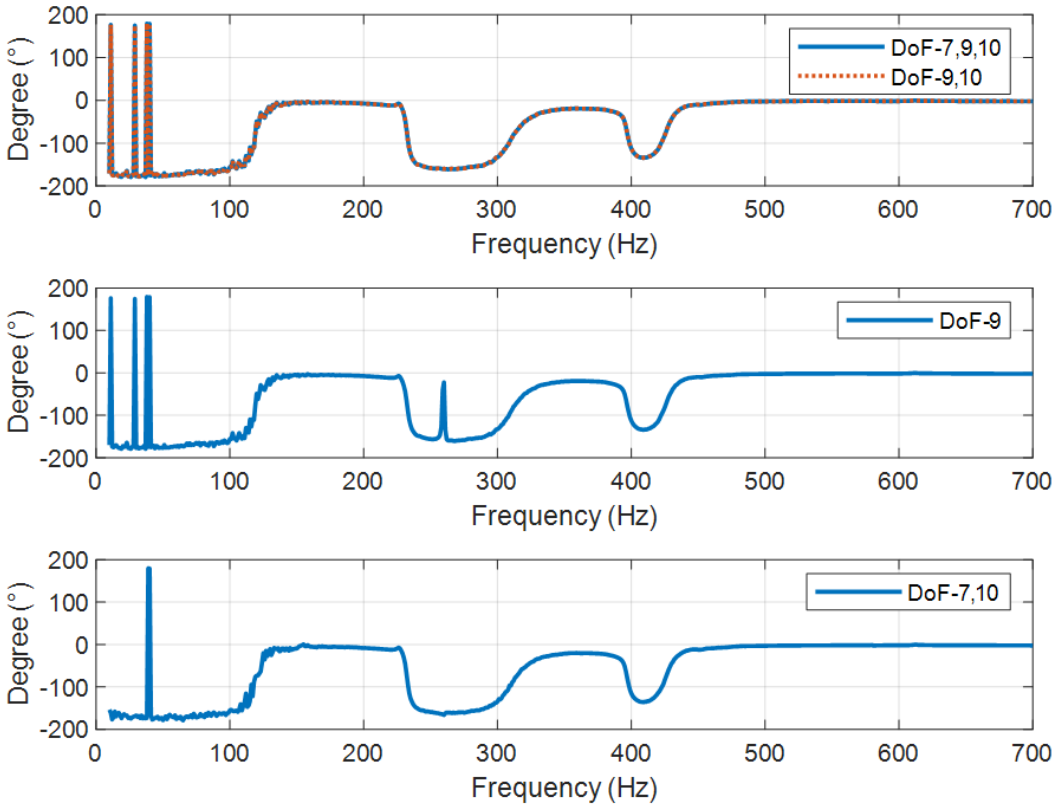

Figure 6. 23. The phase plot of different selections of responses.

6.4. Application

In this section, the proposed torsional receptance identification technique is applied to provide experimental information in order to update the geared rotor-bearing system shown in Fig 6.24. Compared with the geared rotor-bearing system given in Section 5.2, the foundation in this setup is replaced by a thick aluminum block in order to provide a stiffer boundary condition and reduce the complexity of the whole system. By replacing the foundation, it is believed that a more accurate approximation of the updating parameters can be achieved as the bearings are modelled as grounded springs in the numerical simulation.

The model updating is carried out from the component level to the assembly level; hence, the shafts are updated separately in the beginning and then the assembled system in which the shafts are engaged through a pair of gears is updated. There are 10 uncertain parameters to be updated in total, which are (#1-2) Young's modulus of

the short and the long shaft, (#3-4) bearing stiffness on the short and the long shaft, (#5-6) the locations of the discs, (#7-8) the locations of the gears, (#9) Poisson's ratio, and (#10) gear mesh stiffness. Note that the discs and the gear may not be treated as point masses, so the locations of the discs and gears are updated to improve the validity of the model by locating the locations of the point masses that can best fit the experimental results.

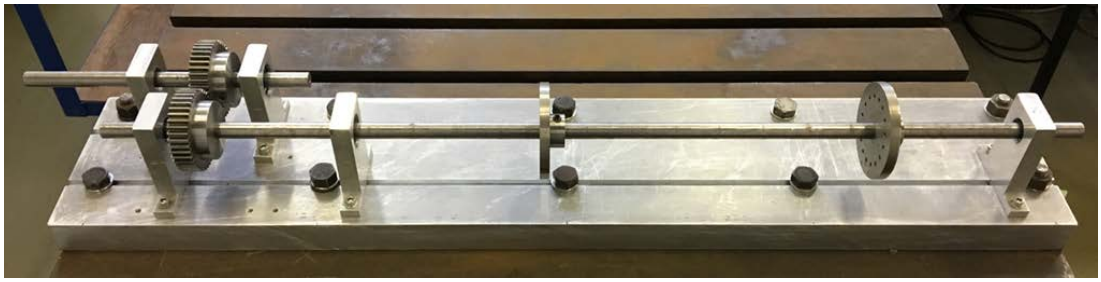

Figure 6. 24. The geared rotor-bearing system.

The updating procedure is broken down into several steps as shown in Fig. 6.25. It shows the updating process particularly for the long shaft assembly, and the short shaft assembly only requires parts of the steps. The process starts from updating the Young's modulus of the free-free long shaft and then updating the bearing stiffness when shaft and the bearing housing are assembled using measured bending natural frequencies; after that, discs are inserted and the locations of the discs and the bearing stiffness are updated together. Then, the torsional receptance identification technique is applied to estimate the torsional natural frequencies, which is used to update the Poisson's ratio. In the last step, a gear is assembled to the structure and the locations of the gear and the discs are updated. Torsional natural frequencies are then measured and used for updating the Poisson's ratio again. Eigen-sensitivity model updating approach is implemented. It can be noted that some parameters are updated more than once in the procedure. The reason is that gradient-based updating approaches tend to converge to a local minimum close to the given initial values, and setting the initial values based on the results from the component-level model updating provides a more reasonable guess.

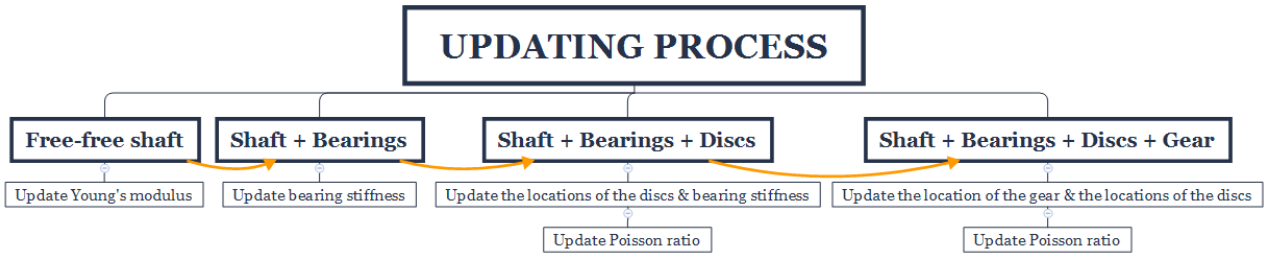

Figure 6. 25. The updating procedure for the long shaft assembly.

The measured natural frequencies in each stage of the updating process are listed in Table 6.7, and the updated parameters of the long shaft assembly are listed in Table 6.8. The locations of the discs and the gear are updated by changing the lengths of the connecting beam elements, which is 0.05m by default, and are denoted as Length 1 to 3 shown in Fig. 6.26. It can be seen that the updated parameters are close to the expected nominal values. The errors between the experimental and numerical natural frequencies below 1000 Hz are summarized in Table 6.9. The errors for the six natural frequencies are both small while the torsional natural frequencies have relatively larger errors of 1.22% and -1.34%.

Table 6. 7. Measured natural frequencies.

	Free-Free long shaft	Long Shaft + Bearings	Long Shaft + Bearings + Discs	Long Shaft + Bearings + Discs + Gear
Natural Frequency (Hz)	78.27	93.78	66.83	65.90
	215.30	302.82	177.38	174.29
	420.03	620.99	349.01 (T)	245.40 (T)
	688.33		499.62	416.01 (T)
			827.08	500.18
				885.69

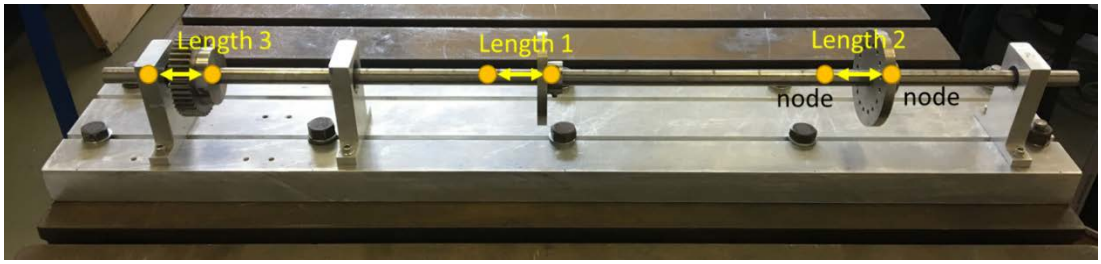

Figure 6. 26. Illustration of the locations of discs and gear.

Table 6. 8. Updated system parameters.

Density (kg/m^3)	7823.8
Young's modulus (pa)	208.09×10^9
Bearing stiffness (N/m)	1.4843×10^7
Length 1 (m) (for disc 1)	0.0646
Length 2 (m) (for disc 2)	0.0605
Poisson's Ratio	0.3089
Length 3 (m) (for gear)	0.0307

Table 6. 9. Comparison of experimental and numerically determined natural frequencies.

Experiment (Hz)	Simulation (Hz)	Error
65.90	65.87	0.05%
174.29	174.31	-0.01%
245.40 (T)	242.38 (T)	1.23%
416.01 (T)	421.59 (T)	-1.34%
500.18	499.91	0.05%
885.69	885.83	-0.01%

It is worthwhile mentioning a phenomena that is observed during the torsional receptance identification of the long shaft assembly. It is found that the poles that are identified at the two ends of the shaft assembly are slightly different, especially for the last case in Table 6.7. The torsional receptance identified at the left (near the gear) and that at the right are plotted against the updated numerical model in Fig. 6.27(a) and Fig. 6.27(b), respectively.

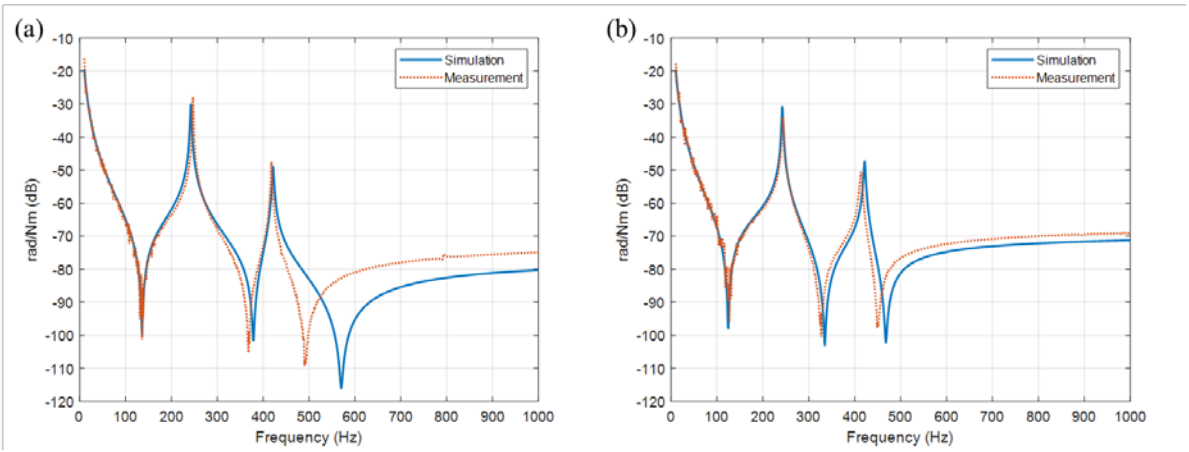

Figure 6. 27. The identified torsional receptances (a) measured at the left end near the gear (b) measured at the right end.

The corresponding poles of the measured torsional receptances are listed in Table 6.10 from which it can be seen that the identified poles at the right end tend to have lower frequencies but higher damping ratios. Since this measurement technique is essentially a SISO method, the possible cause for the variations in poles could be the due to the differences in the torque applied at the connection of the T-block and the parent structure. Different torques could lead to different levels of microslip between the structures. It is believed that the presence of microslip can affect the dynamic response, thus causing different modal properties to be identified. The averages of the two poles are used to update the model.

Table 6. 10. Poles of the measured torsional receptances.

	Frequency (Hz)	Damping Ratio
Left end	246.80	0.28%
	418.13	0.27%
Right end	244.0	0.57%
	413.9	0.54%

On the other hand, for the short shaft assembly, only two steps in the updating process are carried out. The first step is to update the Young's modulus of the short shaft under free-free boundary condition. The second is to update bearing stiffness and the location of the gear when the shaft is assembled with bearing housings and the gear. Since the assembled structure has a very high torsional natural frequency, which

is beyond the measuring range of the rotational accelerometer (1-2000 Hz), and only a few bending natural frequencies are identified in the frequency range of interest, the Poisson's ratio of the short shaft is not updated and is set to the value obtained from the updating results of the long shaft assembly.

From the experiments on the short shaft assembly, it is observed that the quality of the measured FRFs (in both transverse and torsional directions) is poor, and the response dies out very fast when an impact force is imparted; thus, the possible reasons that lead to the poor quality of the measured FRFs might be the relatively higher damping in the short shaft assembly and the influences from the bearing sets. The resulting updated parameters are listed in Table 6.11, and three identified measured bending natural frequencies are compared with the simulated ones in Table 6.12 in which the largest error is 4.68%.

Table 6. 11. Updated system parameters.

Density	7823.8
Young's modulus (Pa)	206.93×10^9
Bearing stiffness (N/m)	2.7826×10^7
Length 3 (m) (for gear)	0.0467
Poisson's Ratio	0.3089

Table 6. 12. Comparison of experimental and numerically determined natural frequencies.

Experiment (Hz)	443.44	678.78	1936.80
Updated Model (Hz)	422.69	688.66	1930.70
Error	4.68%	-1.46%	0.32%

Lastly, the assembled geared rotor-bearing system is to be updated for the aim to identify the gear mesh stiffness. Both bending and torsional natural frequencies of the assembled structure are measured. Similar to the previous case, it is found that the quality of the FRFs measured on the short shaft assembly part is still poor. Therefore, only the FRFs measured on the long shaft are used to identify the bending and torsional natural frequencies. Additionally, it is also found that there are few dents on the teeth of the gears, which happens to engage when the T-block is set in the measuring

orientation, thus affecting the backlash and deteriorating the quality of the FRFs in the torsional direction.

The identified bending natural frequencies below 1000 Hz are: 65.9, 174.7, 500.6, and 892.4 Hz, which are rather close to the ones measured from the long shaft assembly alone (see Table 6.9). The measured torsional FRFs at the left and the right end of the long shaft are plotted in Fig. 6.28(a) and 6.28(b), respectively along with their stabilization diagrams. It can be seen that the quality of the estimated FRFs are not as good as those in Section 6.3, which might be accounted for by the engagement of the gears; however, the shapes of the FRFs are similar to the torsional receptances of the long shaft assembly in Fig. 6.27, and there are also potentially two poles in the range of 10-1000 Hz. These observations suggests that the engagement of the gear and the short shaft assembly might not impose a strong effect on to the long shaft assembly. It can also be noticed that the frequencies of the stable poles identified from Figs. 6.28(a) and 6.28(b) are not identical, for instance, the stable frequencies of order 16 from Fig. 6.28(a) are 207.04 Hz and 425.06 Hz while those of the same order from Fig. 6.28(b) are 215.12 Hz and 399.02 Hz. The averaged frequencies of the first two poles are 211.08 Hz and 412.04 Hz, which are to be used to update the gear contact stiffness.

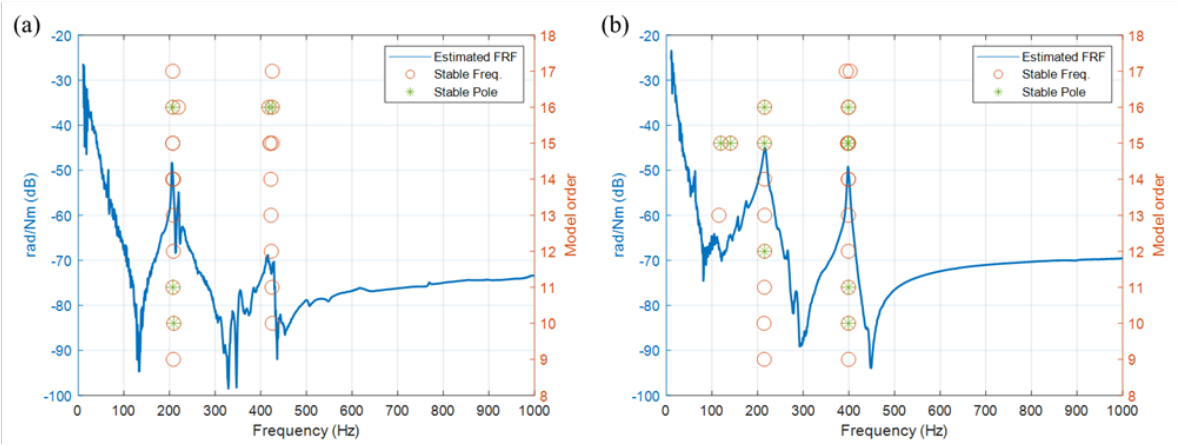

Figure 6. 28. Measured torsional receptances and the associated stabilization diagrams. (a) Receptances measured at the left end. (b) Receptances measured at the right end.

Unfortunately, it is found that the gear mesh stiffness would converge to either a negative value or a rather large value (i.e. to the order of 10^{10}) for different initial values. In order to illustrate that, the first few natural frequencies of the geared rotor-bearing system are plotted against different gear mesh stiffness in Fig. 6.29. The errors between the measured torsional natural frequencies and the closest numerical torsional natural frequencies in the two extreme cases are specifically marked out. For instance, the errors between the frequencies (in percentage) are 15.37% and 2.78% for the case in which the gear mesh stiffness is 10^3. As the torsional natural frequency would increase when the gear mesh stiffness increases. It is clear that any stiffness between the two extreme cases shown in Fig. 6.29 can result in overall larger errors. As a matter of fact, the errors are already not small in the extreme cases.

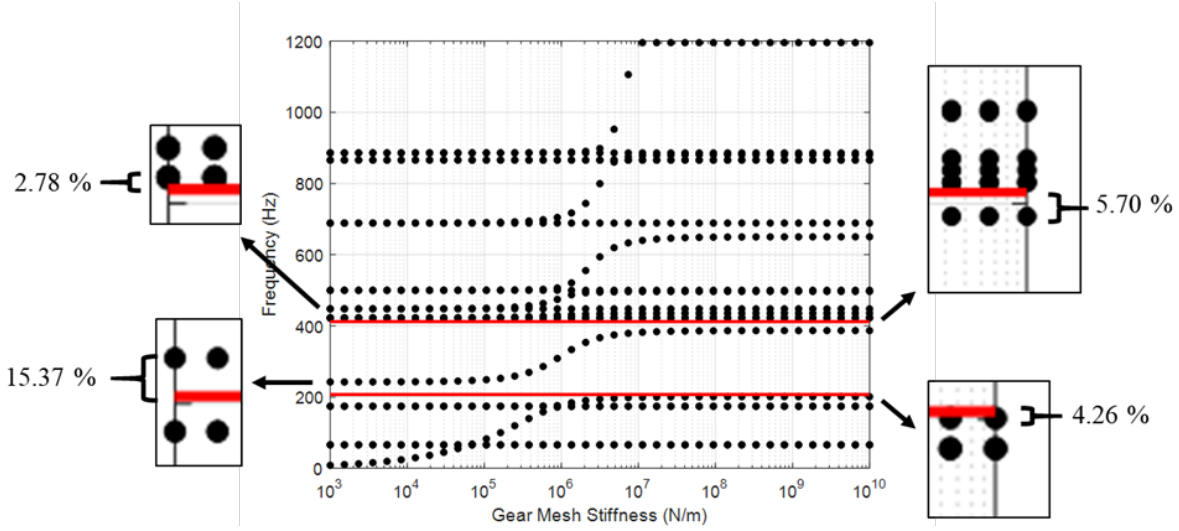

Figure 6. 29. Natural frequencies with respect to different gear mesh stiffness.

Fig. 6.30 shows the numerical torsional receptances when the gear mesh stiffness is set to 10^5 N/m and 10^7 N/m, respectively. It can be seen from Fig. 6.30(a) that there are in total three prominent torsional modes below 1000 Hz, and Fig. 6.30 (b) suggests a strong coupling between torsion and bending motions. However, the experimental results show that there are potentially only two torsional modes in the frequency range. Therefore, whether in this case this gear modelling might be the right modelling method is called into question.

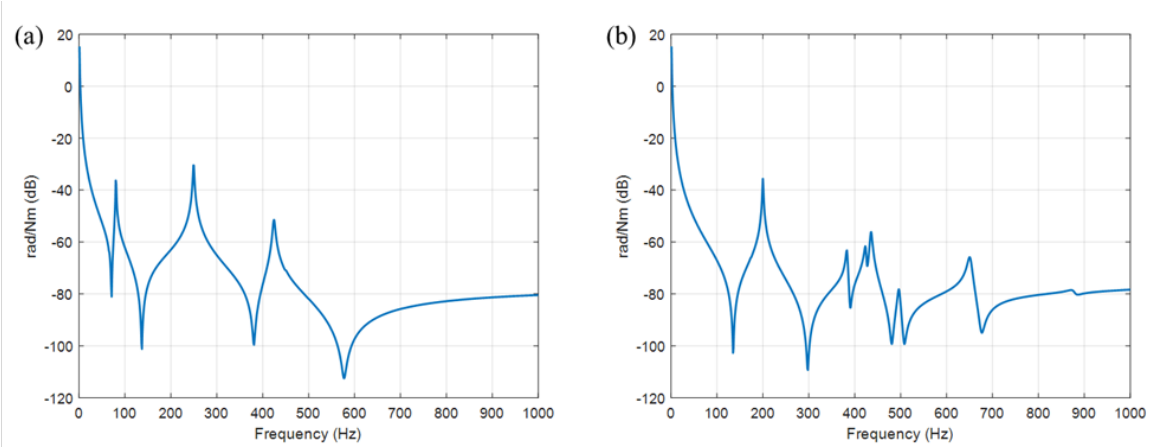

Figure 6. 30. Numerically obtained torsional receptances (a) the gear mesh stiffness is set to 10^5 N/m (b) the gear mesh stiffness is set to 10^7 N/m.

As a result, a second modelling method is sought. In light of the similarity between Fig. 6.27 and Fig. 6.28 and the identified bending natural frequencies, the short shaft assembly might be seen as a weak coupling to the long shaft assembly; hence, the short shaft assembly and the gear mesh stiffness are now treated as a single DoF spring-mass system to the long shaft system in the torsional direction at the gear location. The updated spring constant and the polar moment of inertia are 4.829×10^5 and 6.6906×10^{-4}, respectively, and the resulting natural frequencies are listed and compared with the measured ones in Table 6.13. It can be seen that the errors in bending natural frequencies are all small while the errors for torsional natural frequencies are larger but still acceptable; furthermore, they are much smaller than those in the previous modelling case in Fig. 6.29. Fig. 6.31 shows the comparison between the updated numerical torsional FRFs and the experimental results. It is clear that in general the numerical FRFs can capture the overall trend of the experimental ones.

Table 6. 13. Comparison of experimental and numerically determined natural frequencies.

Experiment (Hz)	65.91	174.65	211.08 (T)	412.04 (T)	500.59	892.36
Updated Model (Hz)	65.87	174.31	207.72	408.18	499.91	885.83
Error	0.06%	0.19%	1.59%	0.94%	0.14%	0.73%

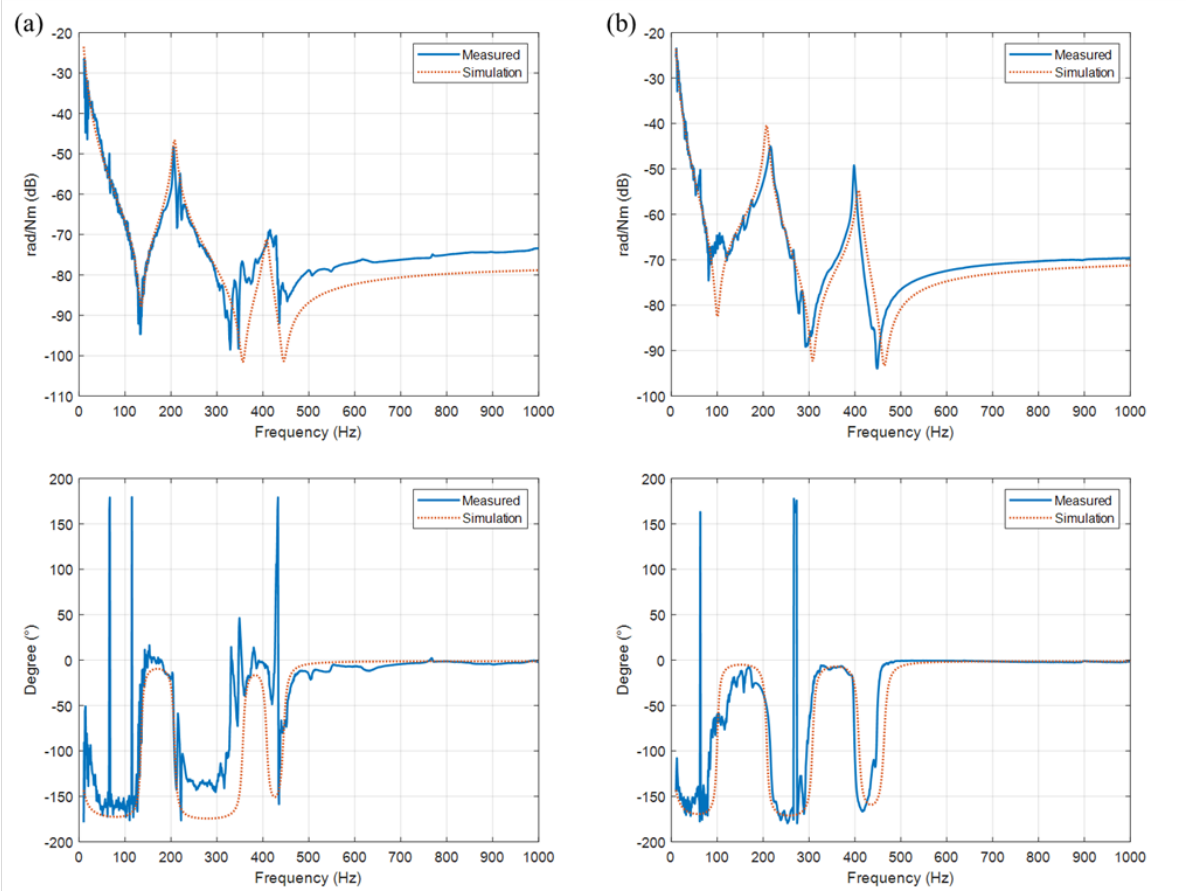

Figure 6. 31. Comparison of experimental and numerically determined torsional FRFs. (a) data obtained at the left end and (b) data obtained at the right end.

6.5. Conclusions

Two receptance-based techniques (Methods 1 and 2) for the identification of the torsional receptance of a shafting system are presented. The torsional receptance is indirectly measured through an attachment of a T-block and using both numerical and measured receptances. In the simulation, both techniques are shown to be accurate when noise is not present in the FRFs, but Method 2 is later found to be more robust against noise. For this reason, Method 2 is further assessed under different combinations of modal testing arrangements. One of the merits of Method 2 is the ability to incorporate rotational accelerometers, and it has been shown that including the rotational response in the process of estimating torsional receptance can improve the quality of the results when the noise level in the measurements is high.

Method 2 is then tested on a laboratory test rig consisting of a shaft with one gear and two discs on three sets of bearings to show its applicability in practice. The estimated torsional receptance is shown to be quite clear, and thus the torsional modal parameters then can be easily identified. Moreover, the repeatability of the torsional receptance is proven to be very high. Lastly, different selections of measured responses are evaluated, which suggests that, for Method 2, it is possible to obtain clear results using only translational responses when the noise level in the measurements is low.

For the interest of demonstration, Method 2 is applied to update the gear meshing stiffness in the numerical model of a laboratory geared rotor-bearing system. It is first found that there exists some geometric deviations from the ideal profiles in the helical gears in use, causing degeneration of the quality of the measured torsional receptances. Although the measured torsional receptances are not as clear, two torsional poles can still be identified using the stabilisation diagram generated through p-LSCF. A series of analysis results suggest that the gear modelling might not be suitable for the system of concern. Alternatively, treating the short shaft assembly as a single DoF spring-mass system to the long shaft assembly seems to produce a better fit that is close to the experimental results.

7. Frequency Assignment by Coupling of Subsystems

A rotor system can be composed of several small rotor systems and some connection components. In some situation, the available modifications on the coupled rotor system or the small rotor systems are limited and thus it is preferred to modify the connection parts without adding extra components. The chapter aims to achieve frequency assignments for the coupled system through modifying the connection part between the sub rotor systems (referred to as subsystems for short). A receptance-based technique for the purpose is developed through Receptance coupling technique. It is shown that the receptance of the coupled system can be determined from a few receptances of the connection parts and the subsystems. A concise equation can be obtained and extended to construct the objective function for the frequency assignment problem. A number of numerical simulations are given for demonstration, and the bending natural frequency or the torsional natural frequency of the coupled system can be assigned. In addition to the frequency assignment problem, the receptance estimation technique proposed in the last chapter is extended to estimate rotational receptances (in bending). The extended technique is able to produce high-quality rotational receptances and is appropriate for this frequency assignment problem of concern.

7.1. Receptance coupling technique

In this section, the classic receptance coupling technique is first briefly introduced and then extended to describe the receptance functions of a coupled system consisting of three subsystems.

7.1.1. Classical receptance coupling technique

When applying receptance coupling technique to a coupled system, the conditions of displacement compatibility and force equilibrium must be satisfied at the connection interface; moreover, it is assumed that the subsystems are rigidly connected, i.e. there is no additional degrees of freedom (DoFs) at the connection interface. As shown in Fig. 7.1, the classical receptance coupling technique considers two subsystems A and B which are connected through several DoFs. The conditions at the interface can be written as

$$\mathbf{f}_t = \mathbf{f}_t^{\mathrm{A}} + \mathbf{f}_t^{\mathrm{B}}, \qquad \mathbf{u}_t = \mathbf{u}_t^{\mathrm{A}} = \mathbf{u}_t^{\mathrm{B}} \tag{7.1}$$

which show that the force vector of the coupled system at the interface is the summation of the force vectors of the subsystems and that the resultant displacement vector equals the displacement vectors of each subsystem. If the internal DoFs of subsystems A and B are denoted as *i* and *j*, the displacement vectors on the two subsystems can be represented as

$$\begin{Bmatrix} \mathbf{u}_i^{\mathrm{A}} \\ \mathbf{u}_t^{\mathrm{A}} \end{Bmatrix} = \begin{bmatrix} \mathbf{H}_{ii}^{\mathrm{A}} & \mathbf{H}_{it}^{\mathrm{A}} \\ \mathbf{H}_{ti}^{\mathrm{A}} & \mathbf{H}_{tt}^{\mathrm{A}} \end{bmatrix} \begin{Bmatrix} \mathbf{f}_i \\ \mathbf{f}_t^{\mathrm{A}} \end{Bmatrix}, \qquad \begin{Bmatrix} \mathbf{u}_j^{\mathrm{B}} \\ \mathbf{u}_t^{\mathrm{B}} \end{Bmatrix} = \begin{bmatrix} \mathbf{H}_{jj}^{\mathrm{B}} & \mathbf{H}_{jt}^{\mathrm{B}} \\ \mathbf{H}_{tj}^{\mathrm{B}} & \mathbf{H}_{tt}^{\mathrm{B}} \end{bmatrix} \begin{Bmatrix} \mathbf{f}_j \\ \mathbf{f}_t^{\mathrm{B}} \end{Bmatrix} \tag{7.2}$$

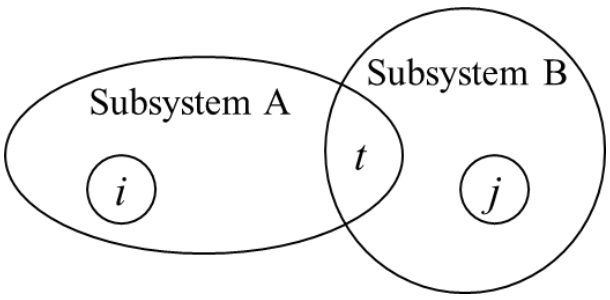

Figure 7. 1. Coupling of two subsystems.

If the goal is to find the receptance function $\mathbf{H}_{ij}$ of the coupled system, the relationship between $\mathbf{u}_i^{\mathrm{A}}$ and $\mathbf{f}_j$ or $\mathbf{u}_j^{\mathrm{B}}$ and $\mathbf{f}_i$ needs to be established. Through Eq. (7.1) and (7.2), it can be shown that

$$\mathbf{f}_t^{\mathrm{B}} = (\mathbf{H}_{tt}^{\mathrm{B}})^{-1}\mathbf{u}_t - (\mathbf{H}_{tt}^{\mathrm{B}})^{-1}\mathbf{H}_{tj}^{\mathrm{B}}\mathbf{f}_j \tag{7.3}$$

and

$$\mathbf{u}_t^{\mathrm{A}} = \mathbf{u}_t = \mathbf{H}_{ti}^{\mathrm{A}}\mathbf{f}_i + \mathbf{H}_{tt}^{\mathrm{A}}\mathbf{f}_t - \mathbf{H}_{tt}^{\mathrm{A}}\mathbf{f}_t^{\mathrm{B}} \tag{7.4}$$

Substituting Eq. (7.3) into Eq. (7.4) results in

$$\left(\mathbf{I} + (\mathbf{H}_{tt}^{\mathrm{B}})^{-1}\mathbf{H}_{tt}^{\mathrm{A}}\right)\mathbf{f}_t^{\mathrm{B}} = (\mathbf{H}_{tt}^{\mathrm{B}})^{-1}\left(\mathbf{H}_{ti}^{\mathrm{A}}\mathbf{f}_i + \mathbf{H}_{tt}^{\mathrm{A}}\mathbf{f}_t - \mathbf{H}_{tj}^{\mathrm{B}}\mathbf{f}_j\right) \tag{7.5}$$

Since $\mathbf{u}_i^{\mathrm{A}} = \mathbf{H}_{ii}^{\mathrm{A}}\mathbf{f}_i + \mathbf{H}_{it}^{\mathrm{A}}\mathbf{f}_t - \mathbf{H}_{it}^{\mathrm{A}}\mathbf{f}_t^{\mathrm{B}}$, $\mathbf{u}_i^{\mathrm{A}}$ can be expressed explicitly in terms of forces $\mathbf{f}_i, \mathbf{f}_j,$ and $\mathbf{f}_t$ by implementing Eq. (7.5), which leads to

$$\begin{aligned}\mathbf{u}_i^{\mathrm{A}} = {} & \mathbf{H}_{ii}^{\mathrm{A}}\mathbf{f}_i + \mathbf{H}_{it}^{\mathrm{A}}\mathbf{f}_t \\ & - \mathbf{H}_{it}^{\mathrm{A}}\left(\mathrm{I} + (\mathbf{H}_{tt}^{\mathrm{B}})^{-1}\mathbf{H}_{tt}^{\mathrm{A}}\right)^{-1}(\mathbf{H}_{tt}^{\mathrm{B}})^{-1}\left(\mathbf{H}_{ti}^{\mathrm{A}}\mathbf{f}_i + \mathbf{H}_{tt}^{\mathrm{A}}\mathbf{f}_t\right. \\ & \left. - \mathbf{H}_{tj}^{\mathrm{B}}\mathbf{f}_j\right)\end{aligned} \tag{7.6}$$

It is clear that $\mathbf{H}_{ij}$ can be obtained by assuming forces other than $\mathbf{f}_j$ are zero, that is

$$\mathbf{H}_{ij} = \mathbf{H}_{it}^{\mathrm{A}}\left(\mathrm{I} + (\mathbf{H}_{tt}^{\mathrm{B}})^{-1}\mathbf{H}_{tt}^{\mathrm{A}}\right)^{-1}(\mathbf{H}_{tt}^{\mathrm{B}})^{-1}\mathbf{H}_{tj}^{\mathrm{B}} \tag{7.7}$$

Eq. (7.7) can be further improved to accommodate fewer matrix inversions by matrix operations, $\left(\mathrm{I} + (\mathbf{H}_{tt}^{\mathrm{B}})^{-1}\mathbf{H}_{tt}^{\mathrm{A}}\right)^{-1} = \left((\mathbf{H}_{tt}^{\mathrm{B}})^{-1}(\mathbf{H}_{tt}^{\mathrm{B}} + \mathbf{H}_{tt}^{\mathrm{A}})\right)^{-1} = \left(\mathbf{H}_{tt}^{\mathrm{B}} + \mathbf{H}_{tt}^{\mathrm{A}}\right)^{-1}\mathbf{H}_{tt}^{\mathrm{B}}$; thus, Eq. (7.7) can be rewritten as

$$\mathbf{H}_{ij} = \mathbf{H}_{it}^{\mathrm{A}}\left(\mathbf{H}_{tt}^{\mathrm{B}} + \mathbf{H}_{tt}^{\mathrm{A}}\right)^{-1}\mathbf{H}_{tj}^{\mathrm{B}} \tag{7.8}$$

It indicates that the cross receptance of the coupled system can be estimated by the receptances functions of the subsystems. Moreover, the point receptance of the coupled system can also be obtained, for instance, substituting $\mathbf{f}_t^{\mathrm{B}}$ in Eq. (7.5) into $\mathbf{u}_j^{\mathrm{B}} = \mathbf{H}_{jj}^{\mathrm{B}}\mathbf{f}_j + \mathbf{H}_{jt}^{\mathrm{B}}\mathbf{f}_t^{\mathrm{B}}$ gives

$$\mathbf{H}_{jj} = \mathbf{H}_{jj}^{\mathrm{B}} - \mathbf{H}_{jt}^{\mathrm{B}}\left(\mathbf{H}_{tt}^{\mathrm{B}} + \mathbf{H}_{tt}^{\mathrm{A}}\right)^{-1}\mathbf{H}_{tj}^{\mathrm{B}} \tag{7.9}$$

For the purpose of completeness, the generalized formula for receptance coupling [91], which includes all the DoFs of the coupled system, is well-known as

$$[\mathbf{H}] = \begin{bmatrix} \mathbf{H}_{ii}^{\mathrm{A}} & \mathbf{H}_{it}^{\mathrm{A}} & \mathbf{0} \\ \mathbf{H}_{ti}^{\mathrm{A}} & \mathbf{H}_{tt}^{\mathrm{A}} & \mathbf{0} \\ \mathbf{0} & \mathbf{0} & \mathbf{H}_{tt}^{\mathrm{B}} \end{bmatrix} - \begin{bmatrix} \mathbf{H}_{it}^{\mathrm{A}} \\ \mathbf{H}_{tt}^{\mathrm{A}} \\ -\mathbf{H}_{jt}^{\mathrm{B}} \end{bmatrix} [\mathbf{H}_{tt}^{\mathrm{A}} + \mathbf{H}_{tt}^{\mathrm{B}}]^{-1} \begin{bmatrix} \mathbf{H}_{it}^{\mathrm{A}} & \mathbf{H}_{tt}^{\mathrm{A}} & -\mathbf{H}_{jt}^{\mathrm{B}} \end{bmatrix} \tag{7.10}$$

7.1.2. Receptance coupling of three subsystems

The classic receptance coupling technique is to be extended to a coupled system that contains three subsystems shown in Fig. 7.2. Two cases are discussed below: one is to find the receptance $\mathbf{H}_{ik}$ where *i* is on subsystem A and *k* is on subsystem C, the other is to find the receptances at the connection interface, i.e. DoFs *t* and *p*. The results show that both cases only require partial information from subsystems.

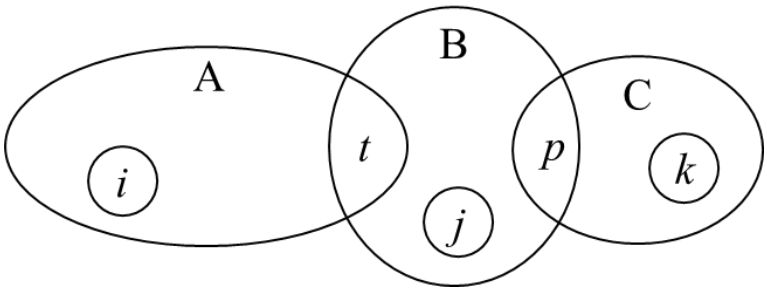

Figure 7. 2. Coupling of three subsystems.

Case 1:

First, the coupled system consisting of three subsystems can be seen as being coupled by two subsystems if a new subsystem D is form by combining subsystem A and B. If *l* denotes any DoF in subsystem D, the arrangement of DoFs in the coupled system can be illustrated by Fig. 7.3.

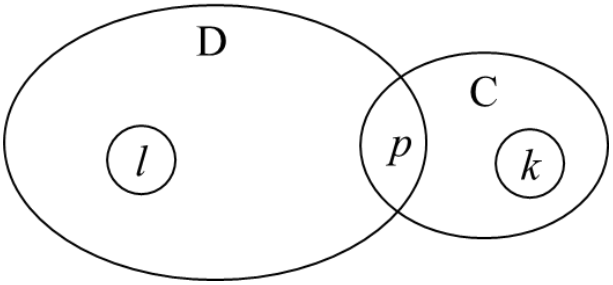

Figure 7. 3. A simplification of the coupling of three subsystems.

A cross receptance of the coupled system can be obtained from Eq. (7.8) as

$$\mathbf{H}_{lk} = \mathbf{H}_{lp}^{\mathrm{D}}\left(\mathbf{H}_{pp}^{\mathrm{D}} + \mathbf{H}_{pp}^{\mathrm{C}}\right)^{-1}\mathbf{H}_{pk}^{\mathrm{C}} \tag{7.11}$$

As the subsystem D is formed by connecting subsystems A and B, $\mathbf{H}_{lp}^{\mathrm{D}}$ and $\mathbf{H}_{pp}^{\mathrm{D}}$ in Eq. (7.11) can be expressed in terms of the receptances of subsystems A and B according to Eqs. (7.7)-(7.8). Assuming that *l* is equal to *i* in Fig. 7.2, $\mathbf{H}_{lp}^{\mathrm{D}}$ and $\mathbf{H}_{pp}^{\mathrm{D}}$ can be rewritten by the following equations

$$\mathbf{H}_{lp}^{\mathrm{D}} = \mathbf{H}_{it}^{\mathrm{A}}\left(\mathbf{H}_{tt}^{\mathrm{B}} + \mathbf{H}_{tt}^{\mathrm{A}}\right)^{-1}\mathbf{H}_{tp}^{\mathrm{B}} \tag{7.12}$$

and

$$\mathbf{H}_{pp}^{\mathrm{D}} = \mathbf{H}_{pp}^{\mathrm{B}} - \mathbf{H}_{pt}^{\mathrm{B}}\left(\mathbf{H}_{tt}^{\mathrm{B}} + \mathbf{H}_{tt}^{\mathrm{A}}\right)^{-1}\mathbf{H}_{tp}^{\mathrm{B}} \tag{7.13}$$

Substituting Eqs. (7.12) and (7.13) into Eq. (7.11) results in

$$\begin{aligned}\mathbf{H}_{ik} = \mathbf{H}_{it}^{\mathrm{A}}\left(\mathbf{H}_{tt}^{\mathrm{B}} + \mathbf{H}_{tt}^{\mathrm{A}}\right)^{-1}\mathbf{H}_{tp}^{\mathrm{B}}\Big(\mathbf{H}_{pp}^{\mathrm{B}} - \mathbf{H}_{pt}^{\mathrm{B}}\left(\mathbf{H}_{tt}^{\mathrm{B}} + \mathbf{H}_{tt}^{\mathrm{A}}\right)^{-1}\mathbf{H}_{tp}^{\mathrm{B}} \\ + \mathbf{H}_{pp}^{\mathrm{C}}\Big)^{-1}\mathbf{H}_{pk}^{\mathrm{C}}\end{aligned} \tag{7.14}$$

which gives the cross receptance of the coupled system.

Case 2:

For the case in which the receptance functions at the connections are of concern, a relatively simple expression can be obtained. For the system shown in Fig. 7.2, the displacement vectors of the subsystems and the conditions of displacement compatibility and force equilibrium are

$$\begin{aligned}\begin{Bmatrix}\mathbf{u}_i^{\mathrm{A}}\\ \mathbf{u}_t^{\mathrm{A}}\end{Bmatrix} &= \begin{bmatrix}\mathbf{H}_{ii}^{\mathrm{A}} & \mathbf{H}_{it}^{\mathrm{A}}\\ \mathbf{H}_{ti}^{\mathrm{A}} & \mathbf{H}_{tt}^{\mathrm{A}}\end{bmatrix}\begin{Bmatrix}\mathbf{f}_i\\ \mathbf{f}_t^{\mathrm{A}}\end{Bmatrix}\\ \begin{Bmatrix}\mathbf{u}_t^{\mathrm{B}}\\ \mathbf{u}_p^{\mathrm{B}}\end{Bmatrix} &= \begin{bmatrix}\mathbf{H}_{tt}^{\mathrm{B}} & \mathbf{H}_{tp}^{\mathrm{B}}\\ \mathbf{H}_{pt}^{\mathrm{B}} & \mathbf{H}_{pp}^{\mathrm{B}}\end{bmatrix}\begin{Bmatrix}\mathbf{f}_t^{\mathrm{B}}\\ \mathbf{f}_p^{\mathrm{B}}\end{Bmatrix}\\ \begin{Bmatrix}\mathbf{u}_k^{\mathrm{C}}\\ \mathbf{u}_p^{\mathrm{C}}\end{Bmatrix} &= \begin{bmatrix}\mathbf{H}_{kk}^{\mathrm{C}} & \mathbf{H}_{kp}^{\mathrm{C}}\\ \mathbf{H}_{pk}^{\mathrm{C}} & \mathbf{H}_{pp}^{\mathrm{C}}\end{bmatrix}\begin{Bmatrix}\mathbf{f}_k\\ \mathbf{f}_p^{\mathrm{C}}\end{Bmatrix}\end{aligned} \tag{7.15}$$

and

$$\mathbf{f}_t^{\mathrm{A}} + \mathbf{f}_t^{\mathrm{B}} = \mathbf{f}_t, \qquad \mathbf{f}_p^{\mathrm{C}} + \mathbf{f}_p^{\mathrm{B}} = \mathbf{f}_p \tag{7.16}$$

$$\mathbf{u}_t^{\mathrm{A}} = \mathbf{u}_t^{\mathrm{B}} = \mathbf{u}_t, \qquad \mathbf{u}_p^{\mathrm{C}} = \mathbf{u}_p^{\mathrm{B}} = \mathbf{u}_p \tag{7.17}$$

Replacing the force vector in subsystem B by Eq. (7.16) and associating $\mathbf{f}_t^{\mathrm{A}}$ and $\mathbf{f}_p^{\mathrm{C}}$ with the corresponding displacement vectors in subsystem A and subsystem C in Eq. (7.15) lead to

$$\begin{Bmatrix} \mathbf{u}_t^{\mathrm{B}} \\ \mathbf{u}_p^{\mathrm{B}} \end{Bmatrix} = \begin{bmatrix} \mathbf{H}_{tt}^{\mathrm{B}} & \mathbf{H}_{tp}^{\mathrm{B}} \\ \mathbf{H}_{pt}^{\mathrm{B}} & \mathbf{H}_{pp}^{\mathrm{B}} \end{bmatrix} \left(\begin{Bmatrix} \mathbf{f}_t \\ \mathbf{f}_p \end{Bmatrix} - \begin{Bmatrix} {\mathbf{H}_{tt}^{\mathrm{A}}}^{-1} \left(\mathbf{u}_t - \mathbf{H}_{ti}^{\mathrm{A}} \mathbf{f}_i \right) \\ {\mathbf{H}_{pp}^{\mathrm{C}}}^{-1} \left(\mathbf{u}_p - \mathbf{H}_{pk}^{\mathrm{C}} \mathbf{f}_k \right) \end{Bmatrix} \right) \tag{7.18}$$

Denoting $\mathbf{H}_{\mathrm{B}} = \begin{bmatrix} \mathbf{H}_{tt}^{\mathrm{B}} & \mathbf{H}_{tp}^{\mathrm{B}} \\ \mathbf{H}_{pt}^{\mathrm{B}} & \mathbf{H}_{pp}^{\mathrm{B}} \end{bmatrix}$ and $\mathbf{H}_{\mathrm{AC}} = \begin{bmatrix} \mathbf{H}_{tt}^{\mathrm{A}} & 0 \\ 0 & \mathbf{H}_{pp}^{\mathrm{C}} \end{bmatrix}$ and pre-multiplying both sides by the inverse of $\mathbf{H}_{\mathrm{B}}$ and rearranging the equation give

$$\begin{Bmatrix} \mathbf{u}_t \\ \mathbf{u}_p \end{Bmatrix} = \left({\mathbf{H}_{\mathrm{B}}}^{-1} + {\mathbf{H}_{\mathrm{AC}}}^{-1} \right)^{-1} \left(\begin{Bmatrix} \mathbf{f}_t \\ \mathbf{f}_p \end{Bmatrix} + {\mathbf{H}_{\mathrm{AC}}}^{-1} \begin{bmatrix} \mathbf{H}_{ti}^{\mathrm{A}} & 0 \\ 0 & \mathbf{H}_{pk}^{\mathrm{C}} \end{bmatrix} \begin{Bmatrix} \mathbf{f}_i \\ \mathbf{f}_k \end{Bmatrix} \right) \tag{7.19}$$

Note that $\begin{Bmatrix} \mathbf{u}_t^{\mathrm{B}} \\ \mathbf{u}_p^{\mathrm{B}} \end{Bmatrix}$ is equal to $\begin{Bmatrix} \mathbf{u}_t \\ \mathbf{u}_p \end{Bmatrix}$ according to Eq. (7.17). Since only the DoFs at the interface are of interests, it can be assumed that $\mathbf{f}_i = \mathbf{f}_k = 0$. The receptance relations at the interface DoFs of the coupled system can be represented as

$$\begin{Bmatrix} \mathbf{u}_t \\ \mathbf{u}_p \end{Bmatrix} = \left({\mathbf{H}_{\mathrm{B}}}^{-1} + {\mathbf{H}_{\mathrm{AC}}}^{-1} \right)^{-1} \begin{Bmatrix} \mathbf{f}_{\mathrm{T}} \\ \mathbf{f}_{\mathrm{P}} \end{Bmatrix} = \mathbf{H}_{\mathrm{AC}} (\mathbf{H}_{\mathrm{AC}} + \mathbf{H}_{\mathrm{B}})^{-1} \mathbf{H}_{\mathrm{B}} \begin{Bmatrix} \mathbf{f}_{\mathrm{T}} \\ \mathbf{f}_{\mathrm{P}} \end{Bmatrix} \tag{7.20}$$

The equation shows that the receptances at the interface of the coupled system can be determined by the receptances at the interface of the subsystems. It is also clear that the natural frequencies of the coupled system occur when $\det(\mathbf{H}_{\mathrm{AC}} + \mathbf{H}_{\mathrm{B}})$ approaches zero.

7.2. Numerical simulation

The problem of frequency assignment by coupling of subsystems is studied numerically in this section. The function that is used for the frequency assignment is mainly based on Eq. (7.20). It should be noted that not every natural frequency can be assigned to the coupled structure as the structural modifications do not modify the

whole structure but certain design parameters; also, the design parameters are usually confined by different design constraints. Therefore, the problem is treated as a multivariable optimization problem with inequality constraints, which has proven its usability in structural modification problems (see Chapter 5).

In the following discussion, the coupled system under consideration consists of only three subsystems, and it is assumed that only one of the subsystems is modifiable. In practice, this kind of assembly scenario can be easily seen and is widely applied. If the modifiable subsystem is the subsystem connected to the other two subsystems and the receptances of the two subsystems at the interface are known, the receptance of the coupled system at the connection interface can be represented as a function of design variable **x** and Laplace variable *s* shown as below

$$\mathbf{H}(\mathbf{x}, s) = \mathbf{H}_{\mathrm{AC}}(s)\left(\mathbf{H}_{\mathrm{AC}}(s) + \mathbf{H}_{\mathrm{B}}(\mathbf{x}, s)\right)^{-1}\mathbf{H}_{\mathrm{B}}(\mathbf{x}, s) \tag{7.21}$$

7.2.1. Numerical model

The numerical model of a slightly damped system shown in Fig. 7.4 is used for the study. The coupled system consists of three subsystems connected in series in which the subsystem in the middle is modelled as a beam and represent a modifiable joint. It is assumed that the length and the diameter of subsystem B are the design variables in this study. Subsystems A and C are both shafting systems containing bearings and flywheels which could reflect the main features in standard transmission systems. The material properties of the shaft and the discs and the bearing stiffness are given in Table 7.1, and the systems parameters are listed in Table 7.2. The shafts in subsystems A and C are solid circular shafts and are mostly 2cm in diameter except that a section in the middle of the shaft in subsystem C is 3cm in diameter. By default, the diameter of subsystem B is 3 cm and the total length is 5 cm. The first four undamped natural frequencies of the corresponding assembled system are listed in Table 7.3.

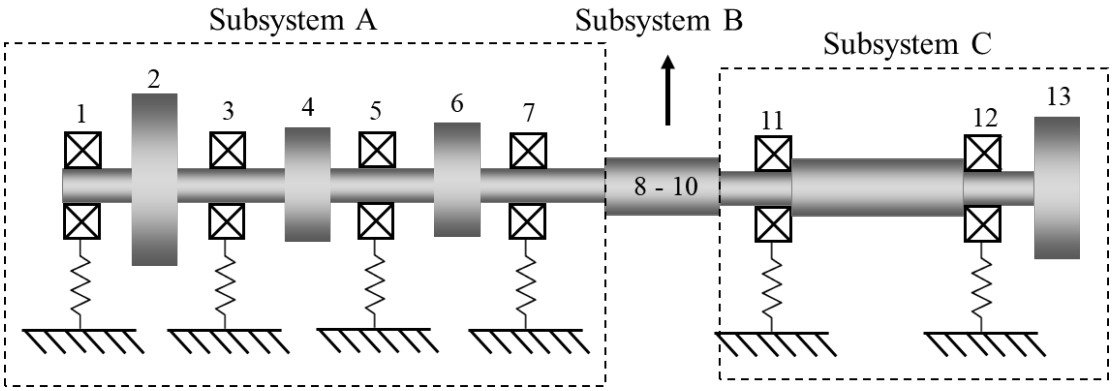

Figure 7. 4. Schematic of the numerical model.

Table 7. 1. System properties.

Young's modulus (GPa)	210	Transverse Bearing Stiffness (N/m)	10^7
Poisson Ratio	0.33	Rotational Bearing Stiffness (N/m)	10
Density (kg/m^3)	7850		

Table 7. 2. System parameters.

Parameter	Value (cm)	Parameter	Value (cm)	Disks	(OD, ID, Thickness) (cm)
$l_{1,2}$	5	$l_{7,8}$	2	node 2	(8, 2, 2)
$l_{2,3}$	5	l_{8-10}	5 (default)	node 4	(5, 2, 2)
$l_{3,4}$	5	$l_{10,11}$	2	node 6	(5, 2, 2)
$l_{4,5}$	5	$l_{11,12}$	5	node12	(6, 2, 2)
$l_{5,6}$	5	$l_{12,13}$	3		
$l_{6,7}$	5				

Table 7. 3. Undamped natural frequencies of the original assembled system.

Mode number	1	2	3 (torsional)	4
f (Hz)	587.5	617.2	701.1	774.3

Here, the importance of including rotational receptances in the estimation process is first demonstrated using an example. Fig. 7.5 shows an estimated FRF using both translational and rotational receptances from the subsystems. The FRF being estimated is the point FRF in the lateral direction at node 10 of the assembled system. It is clear

that the estimated FRF perfectly matches the true one in terms of the magnitude and the phase. Note that the system is lightly damped, and damping is taken to be proportional $[\mathbf{C}] = 27.9253[\mathbf{M}] + 2.8294 \times 10^{-6}[\mathbf{K}]$. On the other hand, Fig. 7.6 gives the results for the case in which only the receptances in the transverse direction of the subsystems are considered. It is easily seen that the estimated FRF fails to match the true FRF and that the two FRFs are fairly different. Thus, it can be seen that including both the receptances in the transverse and rotational directions in the estimation process is of vital importance to the results. That is to say, for the purpose of structural modification, rotational FRFs are necessary in addition to the translational FRFs. In the following simulations, rotational information is included unless specified otherwise.

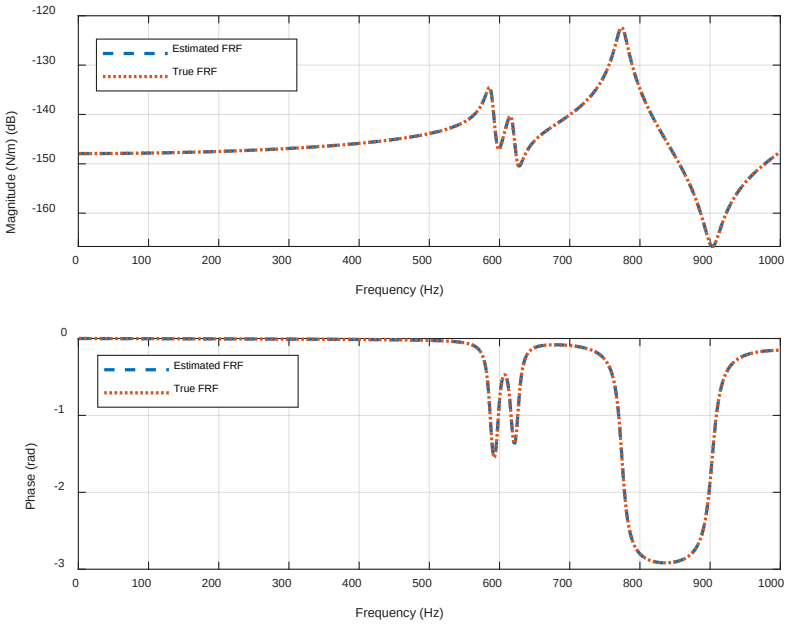

Figure 7. 5. The estimated FRF using both translational and rotational receptances.

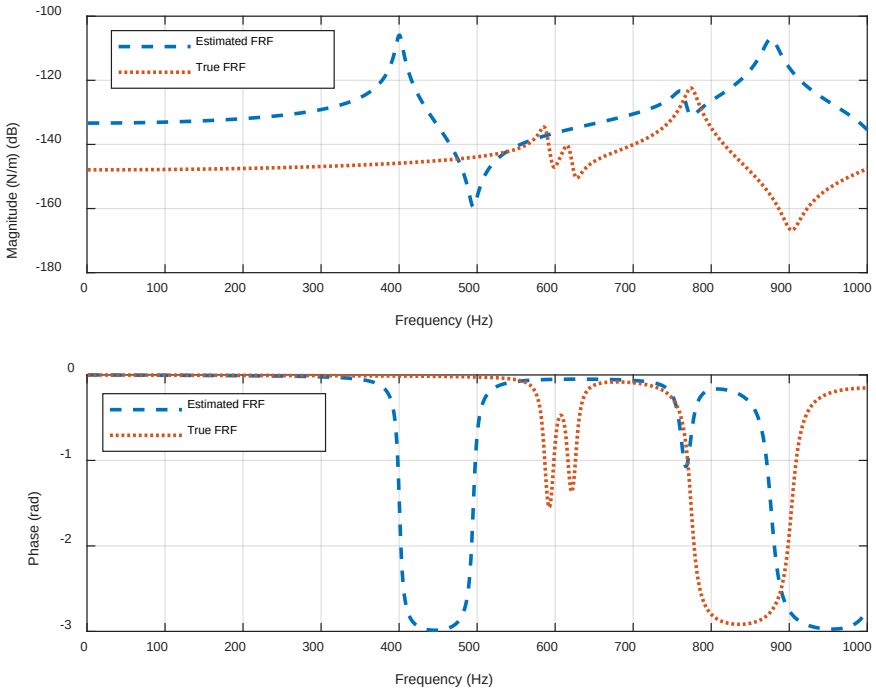

Figure 7. 6. The estimated FRF using only translational receptances.

7.2.2. Bending frequency assignment

As mentioned earlier (see Eq. (7.21)), minimizing $\det(\mathbf{H}_{\mathrm{AC}}(s) + \mathbf{H}_{\mathrm{B}}(\mathbf{x}, s))^2$ can be one possible objective function for the structural modification problem. However, it is nonlinear in nature and its value can vary drastically especially (from very small number to a big one) when the desired natural frequency is high. Few scaling parameters are required to design an objective function that is numerically more stable for optimization algorithms. It is also assumed that subsystem A and C are proportionally damped and that subsystem B is undamped. The objective function for frequency assignment under the context is designed as

$$\min_{\mathbf{x}} \left\{ \sum_{r=1}^{n} \alpha_r \log_{10}((\det(\mathbf{H}_{\mathrm{AC}}(s_r) + \mathbf{H}_{\mathrm{B}}(\mathbf{x}, s_r))/w_r)^2) + \beta g(\mathbf{x}, \mathbf{x}_0) \right\} \qquad (7.22)$$

Only the real part of $\left(\mathbf{H}_{\mathrm{AC}}(s_r) + \mathbf{H}_{\mathrm{B}}(\mathbf{x}, s_r)\right)$ is taken to calculate the determinant, but for the sake of brevity it is not written down in Eq. (7.22). The weighting w_r is defined as the product of the diagonal elements in $\mathrm{real}(\mathbf{H}_{\mathrm{AC}}(s_r))$ and $g(\mathbf{x}, \mathbf{x}_0)$ is a function

used to penalize large solutions defined as $g(\mathbf{x}, \mathbf{x}_0) = (\|\mathbf{x} - \mathbf{x}_0\|/\|\mathbf{x}_0\|)^2$ where $\mathbf{x}_0$ is a vector of the original values of the design variables. Moreover, the parameter β controls the trade-off between the cost of using large values of design variable and the cost of the assignment (the determinant function). A numerical example is given below to demonstrate the bending natural frequency assignment of a coupled system by coupling of subsystems.

It is assumed that the desired bending natural frequency of the coupled system given in Fig. 7.4 is 575 Hz. The goal is to find **x** that minimizes Eq. (7.22) given the desired frequency $\mathrm{s} = (2\pi \times 575)\mathrm{i}$. The constraints of the design variables in subsystem B are

$$0.02\ (\mathrm{m}) \leq x_1(\mathrm{diameter}) \leq 0.06\ (\mathrm{m})$$
$$0.01\ (\mathrm{m}) \leq x_2(\mathrm{length}) \leq 0.1\ (\mathrm{m})$$

Recall that the default values for them are 0.03m and 0.05m, respectively. The constant β is set to 10. To avoid falling into a local minimum, particle swarm algorithm is implemented. A solution is found to be $[x_1 \quad x_2]^{\mathrm{T}} = [0.0504 \quad 0.0815]^{\mathrm{T}}$. The first four natural frequencies of the modified coupled system are listed in Table 7.4, which shows that the achieved natural frequency is only 0.04 Hz lower than the desired one. As the number of design variables is two, the objective function surface can be visualized in a three dimensional space, which is shown by Fig. 7.7. The circle denotes the initial points whilst the cross indicates the solution found by the algorithm. It can be seen that the solution is just one of many possible solutions in the feasible domain.

Note that a natural frequency is assigned to the coupled system without specifying the associated mode, in other words, the current method is not able to assign a natural frequency to a specific mode; however, if natural frequencies of the target system are well separated, it is possible to assign a natural frequency to a particular mode by not shifting the natural frequency too much as the example suggests.

Table 7. 4. Natural frequencies of the modified coupled system.

Mode number	1 (achieved)	2 (torsional)	3	4
f (Hz)	574.96	586.48	599.83	634.39

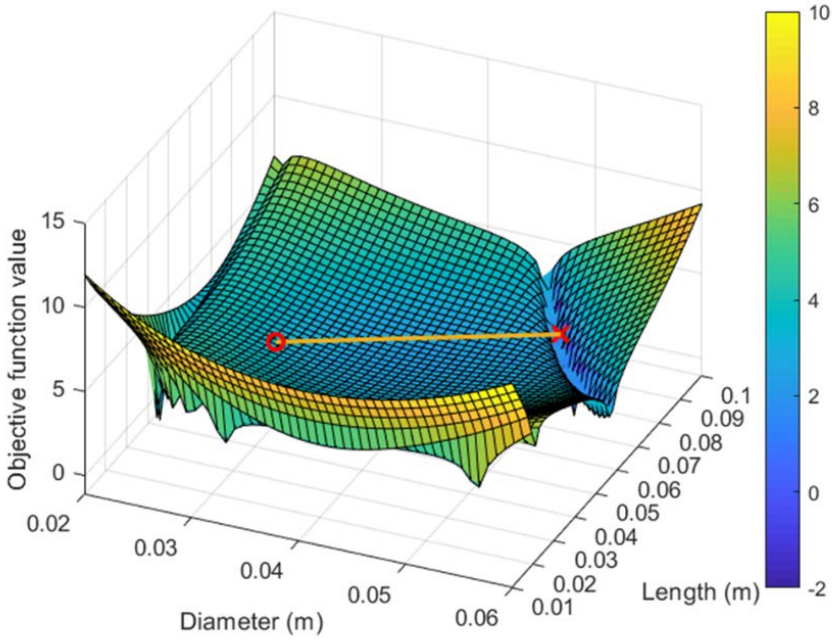

Figure 7. 7. Objective function surface.

Different solution can be found by adjusting the trade-off parameter β_r. Fig. 7.8 shows the top-view of the objective function surface of the case in which $\beta = 20$. It can be noted that the surface is different from Fig. 7.7 and that the region where the last solution is located at is not as obvious. The solution to this objective function $[0.0206 \quad 0.0534]^{\mathrm{T}}$ is closer to the initial point, which clearly demonstrates the penalization of using large values of design variables. The achieved natural frequency for the solution is almost equal to the desired one, that is 575.01 Hz. This solution could be preferable over the previous one since the effort for the modification is less and the result is closer to the desired one.

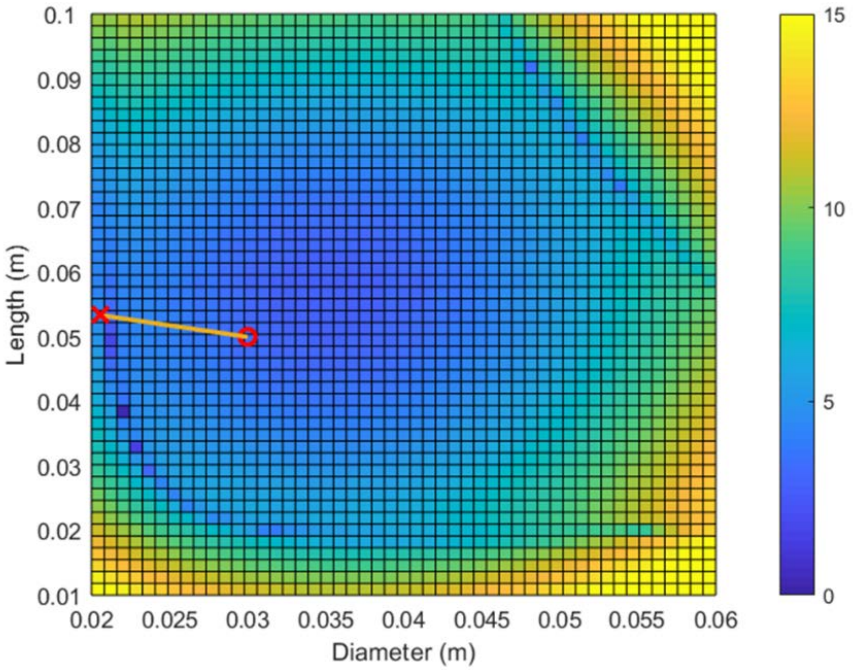

Figure 7. 8. Objective function surface when $\beta = 20$.

7.2.3. Torsional frequency assignment

If torsion is independent of bending, Eq. (7.14) can be rewritten as

$$h_{ik} = \frac{h_{it}^{\mathrm{A}} h_{tp}^{\mathrm{B}} h_{pk}^{\mathrm{C}}}{\left(h_{tt}^{\mathrm{A}} + h_{tt}^{\mathrm{B}}\right)\left(h_{pp}^{\mathrm{B}} + h_{pp}^{\mathrm{C}}\right) - h_{pt}^{\mathrm{B}} h_{tp}^{\mathrm{B}}} \tag{7.23}$$

which gives the cross receptance from DoF *i* (in subsystem A) to DoF *k* (in subsystem C) of the coupled system. The denominator can be rearranged to $\det(\mathbf{H}_{\mathrm{AC}}(s) + \mathbf{H}_{\mathrm{B}}(s))$ with the same definitions of the two matrices. Thus, the objective function presented for the bending natural frequency assignment can also be applied to the problem of torsional frequency assignment. The objective function is repeated here for convenience.

$$\min_{\mathbf{x}} \left\{ \sum_{r=1}^{n} \alpha_r \log_{10}((\mathbf{det}(\mathbf{H}_{\mathrm{AC}}(s_r) + \mathbf{H}_{\mathrm{B}}(\mathbf{x}, s_r))/w_r)^2) + \beta g(\mathbf{x}, \mathbf{x}_0) \right\}$$

In the following example, the desired torsional natural frequency is set to 715 Hz whilst β is set to 10. The constraints of the design variables and the initial values are the same as previous example:

$$0.02\ (\text{m}) \leq x_1(\text{diameter} = 0.03 \text{ by default}) \leq 0.06\ (\text{m})$$
$$0.01\ (\text{m}) \leq x_2(\text{length} = 0.05 \text{ by default}) \leq 0.1\ (\text{m})$$

A solution is found using particle swarm algorithm, which is $[x_1 \quad x_2]^{\mathrm{T}} = [0.0273 \quad 0.0231]^{\mathrm{T}}$. The achieved natural frequencies are listed in Table 7.5, and the difference from the desired torsional frequency is 0.09 Hz. The top view of the corresponding objective function surface is given in Fig. 7.9, which suggests that a solution is found in the feasible domain and that the solution is relatively closer to the initial values compared to the other solutions owing to the penalization term.

Table 7. 5. Natural frequencies of the modified coupled system.

Mode number	1	2	3 (torsional)	4
f (Hz)	575.70	617.29	714.91	809.32

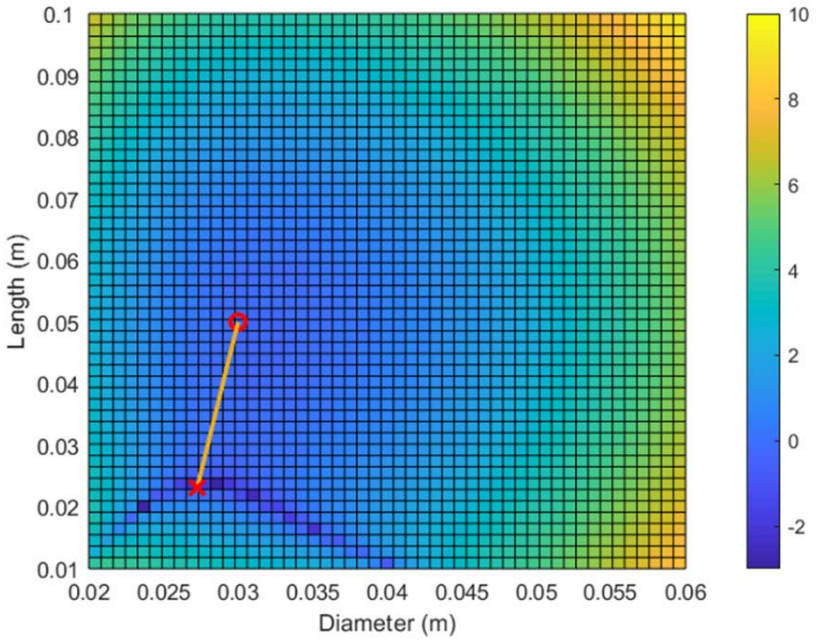

Figure 7. 9. The top view of the objective function surface.

7.2.4. Two-frequency assignment

The two-frequency assignment problem is rather demanding under the current condition as there are equally two design variables. Since it has been demonstrated that either a bending natural frequency or a torsional natural frequency can be assigned using the same objective function. An example is given here to simultaneously assign a bending natural frequency and a torsional natural frequency to the coupled system.

It can be seen from observation (see Fig. 7.8 and Fig. 7.9) that the solutions in the feasible domain are continuous in a sense that connecting their locations in the feasible domain could result in lines of troughs. That is to say, finding a solution for a multiple frequency assignment is equivalent to searching for the intersection of the objective function for each frequency assignment. For this example, the deaired frequencies for bending and torsion are 600 and 670 Hz, respectively. The constants $\{\alpha_r\}_{r=1}^{2}$ are both set to 1 and β is set to 10. A solution is found within the feasible domain using particle swarm algorithm, which is $[x_1 \quad x_2]^{\mathrm{T}} = [0.0348 \quad 0.0875]^{\mathrm{T}}$. The achieved natural frequencies, listed in Table 7.6, show that the assignment is successful. The errors towards the desired frequencies are 1.17 Hz for the bending and 0.07 for the torsion. The top-view of the objective function surface, given by Fig. 7.10, shows that the solution is found at the intersection of two lines of troughs as expected. The number of solutions to this problem are lower than that in the previous examples, which is expected since the number of desired frequencies increases.

Table 7. 6. Natural frequencies of the modified coupled system.

Mode number	1	2	3 (torsional)	4
f (Hz)	598.83	616.61	669.93	659.94

The cross FRFs in the lateral direction between node number 2 and number 13 before and after the modifications are plotted in Fig. 7.11. In this case, the vibration response of the couple system operating under the first critical speed can then be reduced and the operating frequency range is increased. It can also be noticed that the

second bending mode has lower sensitivity to the modifications made as the frequency after the modifications is rather close to the original one.

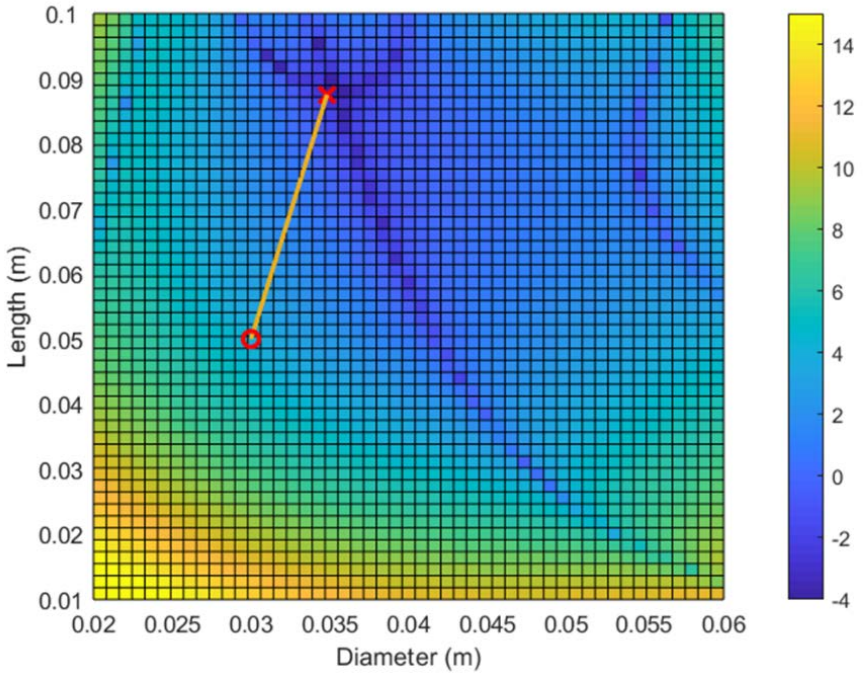

Figure 7. 10. Objective function surface.

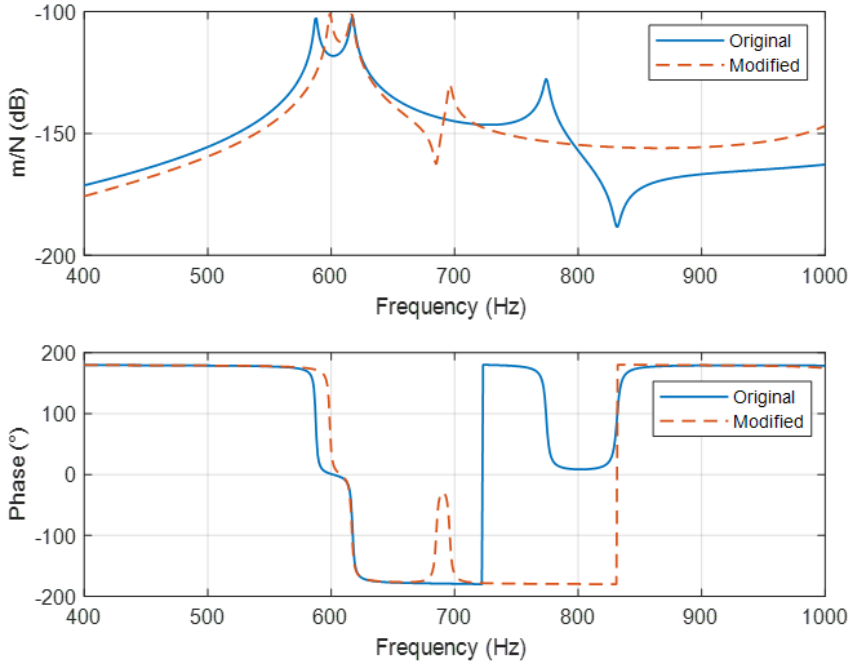

Figure 7. 11. Cross FRFs before and after the modifications.

7.3. Estimation of rotational receptances

The importance of including rotational receptances has been demonstrated by Fig. 7.6. However, currently it is not possible to directly measure high-quality rotational receptances in practice due to the lack of instruments for moment excitation and measurement. As a result, indirect measurement techniques have been proposed to replace the use of such an instrument with traditional excitation and measurement. Recall that in Chapter 6 a new method (Method 2) for estimating torsional receptances is proposed and has shown that the proposed measuring method produces better results than the method proposed in the literature. Commonly speaking, torsional receptance is a rotational receptance but in the axial direction; thus, Method 2 in theory can be applied to measurements of rotational receptances in other directions by changing the T-block's orientation, which is demonstrated in Fig. 7.12, so that the imparted force in the transverse direction can yield a moment excitation to the parent structure at the rotational DoF of interest. Moreover, note that only receptances at the connection DoFs of the subsystems are required in the frequency assignment for the coupled system, and thus Method 2 in theory can produce enough information for the assignment problem.

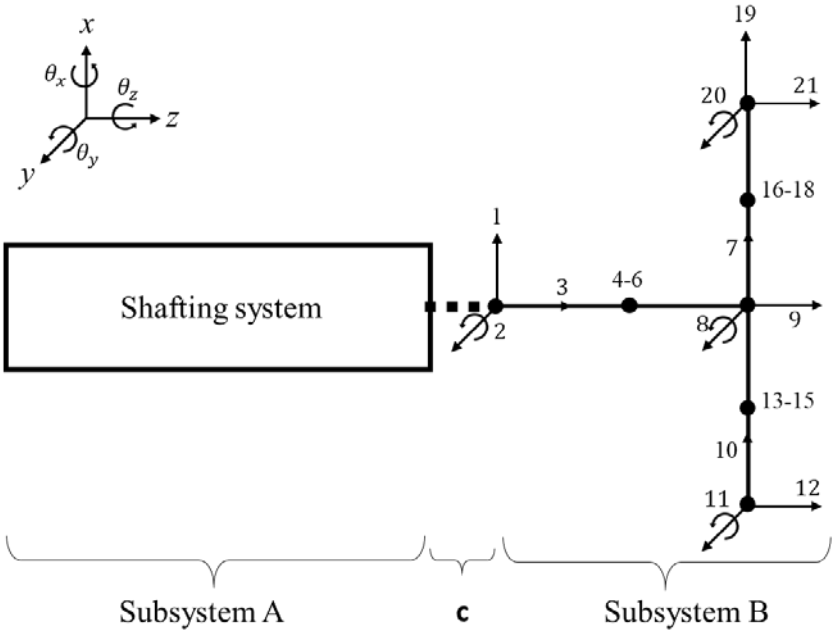

Figure 7. 12. The orientation for rotational receptance estimation.

Fig. 7.12 shows the orientation for measuring rotational receptances in the *x*-*z* plane. The receptances in the *x*-*z* plane pertaining to the rotational DoF θ_y that may not be directly measured are h_{x,θ_y}, $h_{\theta_y,x}$, and h_{θ_y,θ_y}. In fact, $h_{\theta_y,x}$ can be directly measured using rotational accelerometers and impact hammer, but the rotational accelerometers require a flat mounting surface for optimal measurement performance. This suggests that the structure of interest might have to be machined or altered. For a shaft or a rotor, this kind of alteration might not be favourable as it could introduce asymmetricity and increase costs; for that reason, $h_{\theta_y,x}$ is treated unmeasurable and will be indirectly measured through Method 2.

As an example, the receptances of Subsystem A shown in Fig. 7.4 are to be measured using the setup in Fig. 7.12. Similar to Chapter 6, the Subsystem A and the assembled structure are assumed to be lightly proportionally damped, and the damping of the T-block is excluded in the estimation process. The selections of DoFs for response are DoFs 4, 8, and 21, and that for excitation are DoFs 4, 18, and 19 (see Fig. 7.12). The receptances h_{θ_y,θ_y} and h_{x,θ_y} of Subsystem A at the connection end are estimated. Fig. 7.13 gives the corresponding estimation results using Eq. (6.22) with noise level equal to 0% and 2.5%, respectively. It can be seen that the estimated FRFs agree well with the exact ones when noise is not present. However, Fig. 7.13(b) suggests that the estimation is quite sensitive to noise, and the results are not satisfactory even when the rotational information (DoF 8) is included in the estimation process. It is also found that the noticeable fluctuation around 500 Hz is associated with a bending natural frequency of the assembled system (Subsystem A + T-block, 496.84 Hz to be exact).

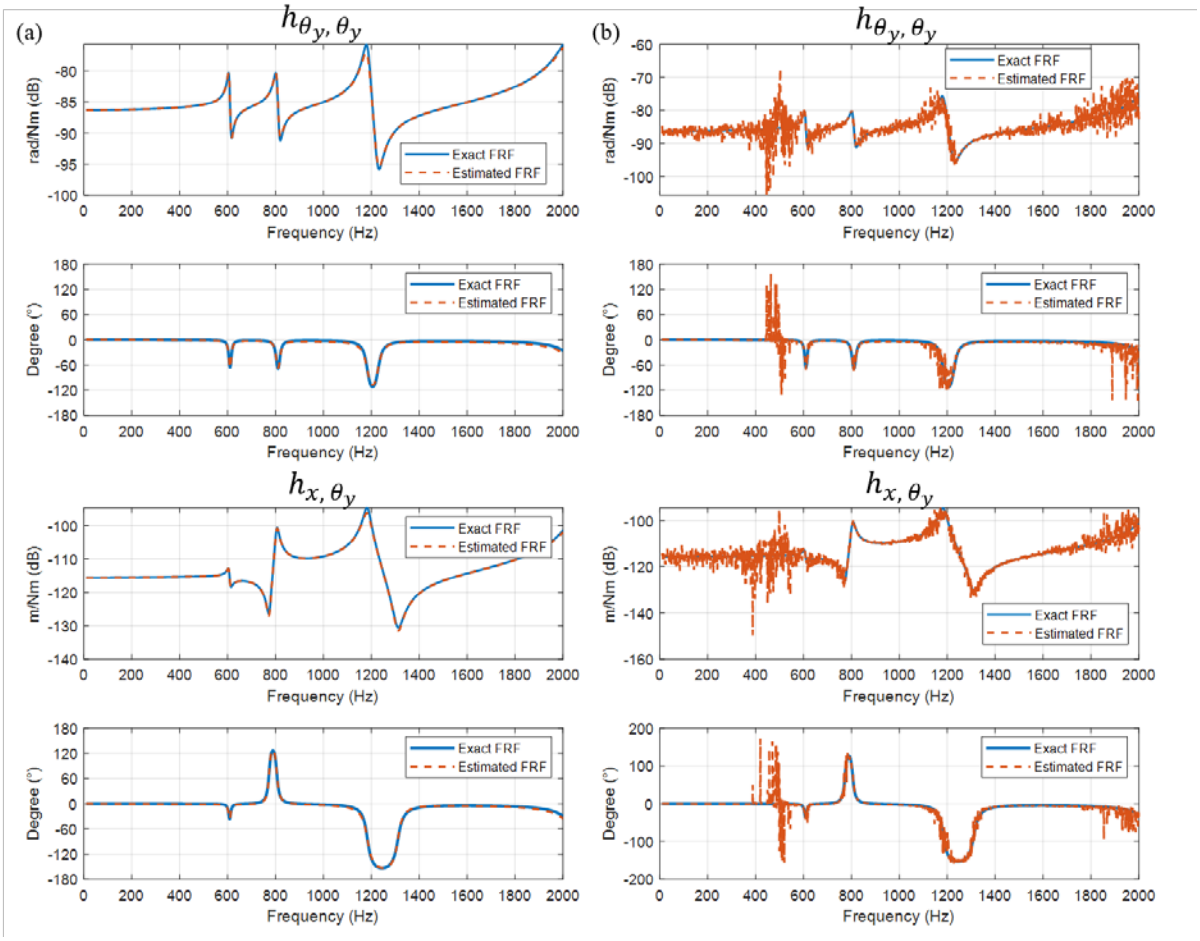

Figure 7. 13. Comparison of the estimated FRFs and the true FRFs. (a) The noise level is 0%. (b) The noise level is 2.5%.

The results can be improved by considering $h_{x,x}$ and modifying the estimation equation. For the connection end, assuming that the motion in the *z*-axis direction is not coupled with the motion in the other directions, $\mathbf{H}_{cc}^{A}$ in Eq. (6.19) can be written explicitly and Eq. (6.19) can be rewritten as

$$\mathbf{L} = \begin{bmatrix} h_{x,x} & h_{x,\theta_y} & 0 \\ h_{\theta_y,x} & h_{\theta_y,\theta_y} & 0 \\ 0 & 0 & h_{z,z} \end{bmatrix} \mathbf{R} \tag{7.24}$$

with obvious definitions of matrices **L** and **R**. Since the axial receptance $h_{z,z}$ is not of interest, the last row and the last column in **L** and **R** can both be removed, leading to

$$\begin{bmatrix} \mathbf{l}_1^{\mathrm{T}} \\ \mathbf{l}_2^{\mathrm{T}} \end{bmatrix} = \begin{bmatrix} h_{x,x} & h_{x,\theta_y} \\ h_{\theta_y,x} & h_{\theta_y,\theta_y} \end{bmatrix} \begin{bmatrix} \mathbf{r}_1^{\mathrm{T}} \\ \mathbf{r}_2^{\mathrm{T}} \end{bmatrix} \tag{7.25}$$

where the remaining entries in **L** and **R** are arranged in the row vectors whose lengths are determined by the number of excitations. If $h_{x,x}$ can be measured directly, then h_{x,θ_y} and h_{θ_y,θ_y} can be estimated using the two equations in Eq. (7.25), respectively. The equations can be solved in a least-squares sense. For instance, the residual of the first equation can be written as

$$\left(\mathbf{l}_1{}^{\mathrm{T}} - h_{x,x}\mathbf{r}_1{}^{\mathrm{T}}\right) - h_{x,\theta_y}\mathbf{r}_2{}^{\mathrm{T}} = \mathbf{e}^{\mathrm{T}} \tag{7.26}$$

Note that all the terms in Eq. (7.26) are complex for damped structures; thus, the real part and the imaginary part can be solved separately. Considering the real part of each term is extracted, the residual squared can be expressed as

$$\varepsilon = \mathbf{e}^{\mathrm{T}}\boldsymbol{e} = \mathbf{p}_1{}^{\mathrm{T}}\mathbf{p}_1 - 2h_{x,\theta_y}\mathbf{p}_1{}^{\mathrm{T}}\mathbf{r}_2 + h_{x,\theta_y}{}^{2}\mathbf{r}_2{}^{\mathrm{T}}\mathbf{r}_2 \tag{7.27}$$

where $\mathbf{p}_1{}^{\mathrm{T}} = \left(\mathbf{l}_1{}^{\mathrm{T}} - h_{x,x}\mathbf{r}_1{}^{\mathrm{T}}\right)$. $\partial\varepsilon/\partial h_{x,\theta_y} = 0$ results in the following equation

$$h_{x,\theta_y} = \frac{\mathbf{p}_1{}^{\mathrm{T}}\mathbf{r}_2}{\mathbf{r}_2{}^{\mathrm{T}}\mathbf{r}_2} \tag{7.28}$$

The real part of h_{x,θ_y} can now be obtained, and the imaginary part of h_{x,θ_y} can be solved in the same procedure. Once h_{x,θ_y} is estimated, h_{θ_y,θ_y} can be estimated using the second equation in Eq. (7.25). If the principle of reciprocity holds, the equation can be written as

$$\left(\mathbf{l}_2{}^{\mathrm{T}} - h_{x,\theta_y}\mathbf{r}_1{}^{\mathrm{T}}\right) = h_{\theta_y,\theta_y}\mathbf{r}_2{}^{\mathrm{T}} \tag{7.29}$$

in which h_{θ_y,θ_y} can also be solved in the same fashion. Fig. 7.14(a) gives the results using the modified equations. It is clear that the fluctuations due to the noise are greatly reduced, compared to Fig. 7.13(b). The noticeable fluctuation around the assembled system's bending natural frequency disappears, and the variation of errors is reduced. However, the quality of the receptances is still not good enough for receptance-based structural modifications.

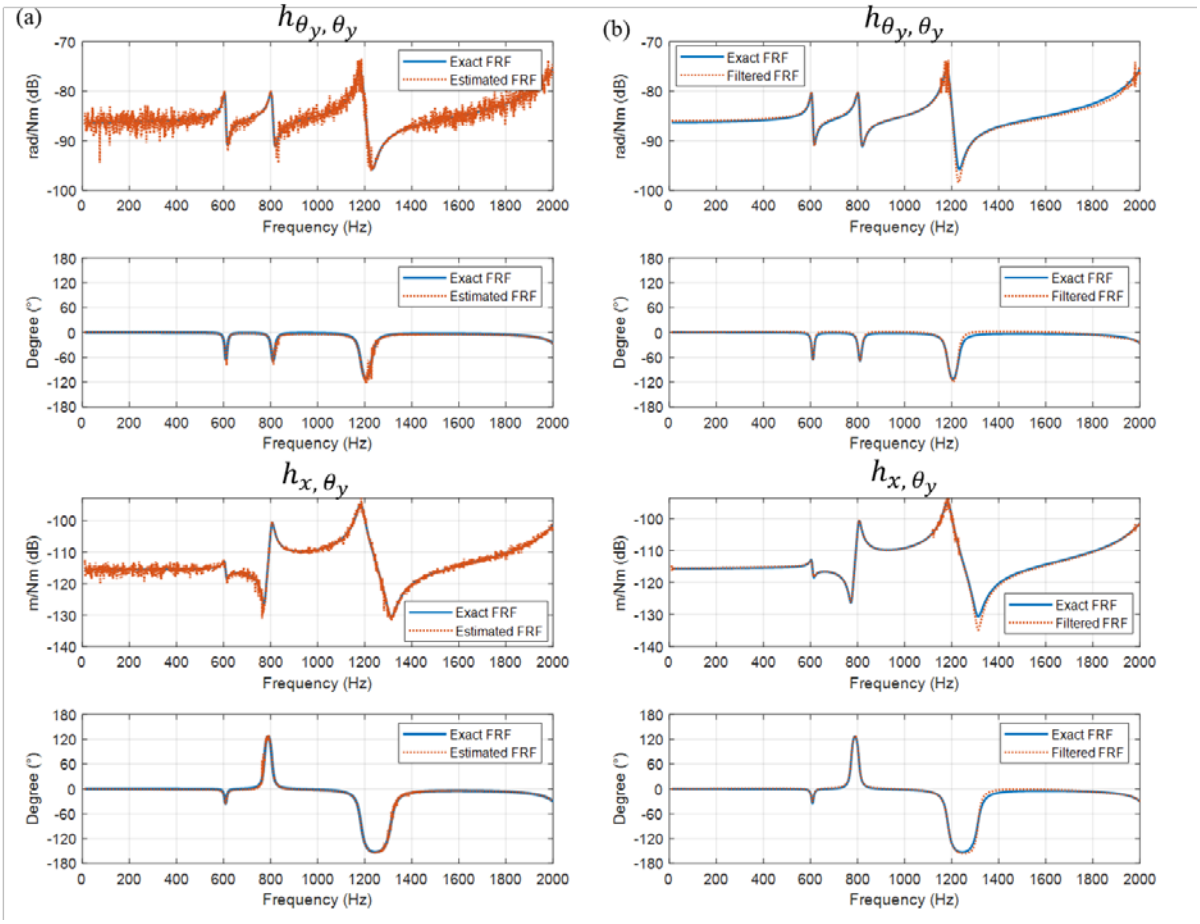

Figure 7. 14. Comparison of the estimated FRFs and the true FRFs. (a) $h_{x,x}$ is included in the estimation process. (b) FRFs are filtered to remove noise.

For this reason, the noise elimination technique proposed by Sanliturk and Cakar [156] is applied to filter out the noise in the FRFs. The number of singular values used to separate the meaningful data from noise is set to 20 for h_{θ_y,θ_y} and 40 for h_{x,θ_y}, respectively. The corresponding filtered FRFs are given in Fig. 7.14(b). It is clear that the noise is almost eliminated and that now the filtered FRFs match the exact FRFs quite well. It can be noted that noise around the peaks of the FRF still remains. This is because of the magnitude-dependent noise assumption. Fortunately, this type of noise may not be very common in reality. Therefore, it is believed that the proposed technique for rotational receptance estimation is able to produce high-quality FRFs for the structural modification problem.

7.4. Conclusion

This chapter deals with the problem of frequency assignment through the coupling of subsystems. A technique that integrates receptance coupling method, structural modification, and optimization is presented. The receptance method is first extended to a coupled system of three subsystems, and a simple representation of the receptance functions at the coupled interface of the coupled system is derived. The formulation shows that only the receptance functions of the subsystems at the connection coordinates are required to determine the receptance function of the coupled system at the same coordinates. This relationship is further used as a basic formula for structural modification.

The technique is applied to a coupled FE model to verify its applicability. The FE model consists of three subsystems that are connected in series. It is assumed that the subsystems other than the one in the middle are lightly damped and that the middle subsystem is a circular beam whose diameter and length can be modified within certain ranges. Through modifying the undamped middle beam, the coupled system can thus possess some desired natural frequencies. The simulation results show that the current technique works well with the frequency assignment problem. Bending natural frequencies or torsional natural frequencies can be assigned to the coupled system, respectively or simultaneously. None of the simulation examples exceed more than 1% of error between the desired natural frequencies and the achieved ones.

The problem of rotational receptance measurement is also dealt with as the rotational receptances are essential to the structural modification problem. A slight modification has been made to Method 2 (proposed in Chapter 6) to improve its robustness on the rotational receptance estimation. Numerical simulations show that the technique is able to produce accurate estimations and thus is appropriate for this frequency assignment problem of concern.

8. Conclusions and Outlook

This chapter summarizes the main contributions of the thesis and the outlook for the research.

8.1. Conclusions

The objectives of the research arise from the open problems identified from reviewing the literature in the area of receptance-based method for passive inverse structural modification. It can be seen that there is a gap between the growth of its theoretical study of the method and the development of the practical implementation. The main causes can be grouped into the problems in the theoretical side or the practical side. For the theoretical side, the forms of the modification are limited to only a small number of simple modifications (point mass or grounded spring for example) as, in the traditional formula, it is difficult to incorporate different types of modifications and it becomes complicated to find a solution when the number of unknown variables increases. For the practical side, it is sometimes difficult to carry out the exact modification, for instance, the stiffness modification is expensive to realise without a careful study and inspection of the material in use and the structure of concern. Moreover, it is difficult to get high-quality rotational/torsional receptances through measurements. Since the method is receptance-based, a small amount of error in the receptances can lead to an inaccurate solution that degrades the performance of the dynamical assignment. These problems have to be addressed so as to make the method more effective in real circumstances.

To deal with the theoretical side of the problem, the traditional formula for the receptance-based method is further extended so that the receptances of the modified system can be solely represented by the modifications and the receptances of the original system. The relationship between the subsidiary receptance matrix and the receptances of the original system is included. Based on the extended formula, the structural modification problem is cast into an optimization problem. By doing so, the

assignment problem can now incorporate different types of modifications and is capable of finding a solution when the number of design variables is large. It is shown numerically that various dynamic properties such as pole, zero, eigenstructure, node, and ratio of receptance can be assigned under the proposed framework. To test the applicability, it is applied to a laboratory geared rotor-bearing system for natural frequency and antiresonant frequency assignments. Only a small number of receptances are required for the problem and are all measured through traditional Impact Testing. The experimental results, which include natural frequency and antiresonant frequency assignments, are quite successful although the rotor system is comprised of many mechanical parts and also mounted on rather flexible aluminium profiles. As an additional application, the method is used to find the optimal locations for the modifications that result in the highest first bending natural frequency. It is usually preferred to have higher first bending natural frequency as it can reduce the vibration of a rotating system operating under the first critical speed.

Following the aforementioned work, the problem of obtaining rotational or torsional receptances is addressed in this thesis for the aim of estimating high-quality and accurate receptances. To achieve this goal, it is first important to note that imparting enough energy to the DoFs of interest is necessary in order for the corresponding response to be observed. By keeping this in mind, the method of exciting the structure of concern via a T-block attachment is likely to be the best strategy. Therefore, in this thesis a T-block is used to indirectly estimate the rotational and torsional receptances, and Receptance coupling technique is used to decouple the influence of the T-block attachment. Two receptance-based methods are thereby developed and one of the methods are shown to be more superior and robust. The proposed method can accommodate arbitrary locations for response and excitation and does not require any assumption about damping. As the method is receptance-based, no numerical models of the T-block or the structure of concern are required. The estimation can be all based on experimental results. However, an updated FE model of the T-block is suggested in practice since its numerical receptances would not deviate much from experimental ones and the usage of contaminated experimental data can be avoided. It is found in this thesis that the inclusion of rotational response

plays a key role in obtaining high-quality receptance in a noisy environment. The method can produce accurate receptances with appropriate selections of excitation and response and has shown to have 90% less variation in errors compared to the most recent literature. The method is as well implemented in a laboratory rotor-bearing system to estimate torsional receptances, and the results show that the estimated receptances are clear and can be used to obtain torsional modal parameters. It is also used to estimate the gear mesh stiffness of a laboratory geared rotor-bearing system (two shafts of 30 cm and 100 cm). The results suggest that the modelling method of the gear mesh adopted (skewed stiffness) may not be appropriate and that the system is dominated by the long shaft. With the proposed method, rotational and torsional receptances can now be measured with high accuracy and can be used also in the context of structural modification.

Finally, the thesis deals with the issue of utilizing modifications that are not simple in a structural modification problem. The case of interest is an assembled rotor system consisting of two rotor subsystems and a joint that is modelled as a circular beam. It is found via Receptance coupling technique that the poles of the assembled system can be determined by the receptances of the subsystems and the joint at the connection ends. The importance of including rotational receptances in this type of structural modification problem is demonstrated using simulations. Thanks to the proposed receptance estimation method, obtaining experimental rotational receptances is possible in practice. The problem of frequency assignment is addressed in the optimization fashion with an additional term penalizing large modifications. It is shown numerically that more than one frequency, bending or torsion, could be assigned to the coupled system by changing the geometric properties of the joint. For the application, a frequency band with no natural frequencies can be constructed or the bending and the torsional natural frequency can be assigned simultaneously. The operating speed of the coupled system can be adjusted and the vibration response in a frequency range can be decreased. Although in this chapter only two rotor subsystems and a joint are considered, the technique is applicable to a coupled system comprising more subsystems and joints.

8.2. Outlook

There are still issues and potential applications left unresolved in the field of receptance-based inverse structural modification method. Some of them are summarized below:

1. It would be desirable to extend the structural modification method to a “rotating” system. That is to say, one can assign desired dynamical properties to a rotating system at different spin speeds.
2. In the proposed indirect measurement method, the connection between the T-block and the parent structure is assumed to be rigid. However, this might not be true in practice. The torque required to approximate the assumption has to be studied, and this value might differ for different materials used.
3. The implementation of the torsional frequency assignment using the proposed methods in this thesis would be interesting. To the author’s knowledge, receptance-based torsional frequency assignment has not been reported in the literature.
4. In chapter 7, the joint that connects two subsystems is treated as a beam and this can be extended to a more complicated structure such as couplings.
5. There are cases in which a passive structural modification is insufficient. Simultaneously utilizing passive and active structural modification and combining their advantages can be a promising structural modification method. Semi-active control is also worth studying.
6. The uncertainty in measured FRFs and the propagation of the uncertainty onto the structural modification results are worth investigating. A source of uncertainty in the measured FRFs is the operator uncertainty, which is the uncertainty introduced as a result of human error in the measurement procedure including inconsistent force excitation and/or inconsistent excitation position.

Appendix A

The eigensensitivity model updating technique has been implemented many times throughout the study. This appendix is mainly to give the procedure of the technique and to show how the technique works. The content is mainly based on a paper by Mottershead *et al.* [21] and another one by Dorosti *et al.* [162].

It is assumed that *m* experimental eigenvalues, denoted by $\boldsymbol{\lambda}_{\mathrm{e}} \in \mathbb{C}^{m\times 1}$, are available, and that the corresponding numerical eigenvalues for the design variables $\mathbf{x} \in \mathbb{R}^{q\times 1}$ in the numerical model are $\boldsymbol{\lambda}_{\mathrm{n}}(\mathbf{x}) \in \mathbb{C}^{m\times 1}$. If the two sets of eigenvalues differ from each other, a measure that can reflect how close the numerical model reproduces the experimental results can be defined in terms of the squares of the errors as

$$\epsilon_i = [\boldsymbol{\lambda}_{\mathrm{e}} - \boldsymbol{\lambda}_{\mathrm{n}}(\mathbf{x}_i)]^{\mathrm{H}}\mathbf{W}[\boldsymbol{\lambda}_{\mathrm{e}} - \boldsymbol{\lambda}_{\mathrm{n}}(\mathbf{x}_i)] \tag{A.1}$$

The aim is thus to minimize Eq. (A1) iteratively, and *i* is the iteration number. $\mathbf{x}_i$ can be interpreted as the values of the design variables at i^{th} iteration. The weighting matrix $\mathbf{W}$ can be designed as

$$\mathbf{W} = \begin{bmatrix} \left|\lambda_{\mathrm{n},1}/\max(\boldsymbol{\lambda}_{\mathrm{n}})\right|^{-2} & 0 & 0 \\ 0 & \ddots & 0 \\ 0 & 0 & \left|\lambda_{\mathrm{n},m}/\max(\boldsymbol{\lambda}_{\mathrm{n}})\right|^{-2} \end{bmatrix} \tag{A.2}$$

in order to make each square of error to have equal contribution to ϵ_i. Linearizing $\boldsymbol{\lambda}_{\mathrm{n}}(\mathbf{x}_i)$ using the first-order Taylor series expansion gives

$$\lambda_{\mathrm{n}}(\mathbf{x}_{i+1}) \approx \lambda_{\mathrm{n}}(\mathbf{x}_i) + \frac{\partial \lambda_{\mathrm{n}}(\mathbf{x}_i)}{\partial \mathbf{x}_i}\Delta\mathbf{x}_i \tag{A.3}$$

Substituting Eq. (A3) into Eq. (A1) results in

$$\epsilon_i \approx \Delta\mathbf{r}_i^H \mathbf{W}\Delta\mathbf{r}_i \tag{A.4}$$

where

$$\Delta\mathbf{r}_i = [\boldsymbol{\lambda}_{\mathrm{e}} - \boldsymbol{\lambda}_{\mathrm{n}}(\mathbf{x}_i)] - \frac{\partial \lambda_{\mathrm{n}}(\mathbf{x}_i)}{\partial \mathbf{x}_i}\Delta\mathbf{x}_i \tag{A.5}$$

Eq. (A5) can be rewritten as

$$\Delta \mathbf{r}_i = \Delta \boldsymbol{\lambda}_i - \mathbf{S}_i \Delta \mathbf{x}_i \tag{A.6}$$

with obvious definition of $\Delta \boldsymbol{\lambda}_i$ and $\mathbf{S}_i$, and the matrix $\mathbf{S}$ is known as the sensitivity matrix. Note that Eq. (A4) is a fair approximation of Eq. (A1) in the vicinity of $\lambda_{\mathrm{n}}(\mathbf{x}_i)$. For a overdetermined problem, i.e. $q < m$, Eq. (A4) can be minimized in a least-squares sense. Calculating $\partial \epsilon_i / \partial \Delta \mathbf{x}_i = 0$ results in the following equation [162]

$$\mathrm{Re}(\mathbf{S}_i^H \mathbf{W} \mathbf{S}_i) \Delta \mathbf{x}_i = \mathrm{Re}(\mathbf{S}_i^H \mathbf{W} \Delta \boldsymbol{\lambda}_i) \tag{A.7}$$

which can be solved for $\Delta \mathbf{x}_i$. Hence, the updated parameter at the *i*+1 iteration is

$$\mathbf{x}_{i+1} = \mathbf{x}_i + \alpha \Delta \mathbf{x}_i \tag{A.8}$$

where α is a scaling factor to control the step in the iteration process. The iteration stops when ϵ_i converges. In practice, the iteration process stops until the following stopping criterion is met

$$|\epsilon_{i+1} - \epsilon_i| < \delta \tag{A.9}$$

where δ is a sufficiently small number. It is also shown in [162] that Eq. (A4) is locally convex if $\mathbf{S}_i$ is in full rank. In other words, in order for the iteration process to converge to a global minimum, it is important to have an intelligent guess on the initial design variables.

Appendix B

The following content provides the detail and the derivation for Eq. (6.21), which then constitutes the main equation for Method 2 in the torsional receptance estimation in Chapter 6.

The displacement-force relationship of a coupled system (AB) composed of subsystem A and subsystem B in the frequency domain can be defined as

$$\begin{Bmatrix} \mathbf{u}_{\mathrm{c}}^{\mathrm{AB}} \\ \mathbf{u}_{\mathrm{b^m}}^{\mathrm{AB}} \end{Bmatrix} = \begin{bmatrix} \mathbf{T}_{\mathrm{c}} & 0 \\ 0 & \mathbf{T}_{\mathrm{b^m}} \end{bmatrix} \begin{Bmatrix} \mathbf{u}_{\mathrm{c}}^{\mathrm{B}} \\ \mathbf{u}_{\mathrm{b^m}}^{\mathrm{B}} \end{Bmatrix} = \begin{bmatrix} \mathbf{H}_{\mathrm{cc}}^{\mathrm{AB}} & \mathbf{H}_{\mathrm{cb^f}}^{\mathrm{AB}} \\ \mathbf{H}_{\mathrm{b^m c}}^{\mathrm{AB}} & \mathbf{H}_{\mathrm{b^m b^f}}^{\mathrm{AB}} \end{bmatrix} \begin{Bmatrix} \mathbf{f}_{\mathrm{c}}^{\mathrm{AB}} \\ \mathbf{f}_{\mathrm{b^f}}^{\mathrm{AB}} \end{Bmatrix} \tag{B.1}$$

In this equation, the coupling conditions, Eq. (6.4) and (6.5), and the coordinate transformation matrixes of the responses, $\mathbf{T}_{\mathrm{c}}$ and $\mathbf{T}_{\mathrm{b^m}}$, are also included. Subtracting Eq. (B1) by Eq. (6.15) gives

$$\begin{aligned} \begin{Bmatrix} 0 \\ 0 \end{Bmatrix} = & \begin{bmatrix} \mathbf{T}_{\mathrm{c}}{}^{-1} & 0 \\ 0 & \mathbf{T}_{\mathrm{b^m}}{}^{-1} \end{bmatrix} \begin{bmatrix} \mathbf{H}_{\mathrm{cc}}^{\mathrm{AB}} & \mathbf{H}_{\mathrm{cb^f}}^{\mathrm{AB}} \\ \mathbf{H}_{\mathrm{b^m c}}^{\mathrm{AB}} & \mathbf{H}_{\mathrm{b^m b^f}}^{\mathrm{AB}} \end{bmatrix} \begin{Bmatrix} \mathbf{f}_{\mathrm{c}}^{\mathrm{AB}} \\ \mathbf{f}_{\mathrm{b^f}}^{\mathrm{AB}} \end{Bmatrix} \\ & - \begin{bmatrix} \mathbf{H}_{\mathrm{cc}}^{\mathrm{B}} & \mathbf{H}_{\mathrm{cb^f}}^{\mathrm{B}} \\ \mathbf{H}_{\mathrm{b^m c}}^{\mathrm{B}} & \mathbf{H}_{\mathrm{b^m b^f}}^{\mathrm{B}} \end{bmatrix} \begin{Bmatrix} \mathbf{f}_{\mathrm{c}}^{\mathrm{B}} \\ \mathbf{f}_{\mathrm{b^f}}^{\mathrm{B}} \end{Bmatrix} \end{aligned} \tag{B.2}$$

Rearranging Eq. (B2) by moving $\mathbf{f}_{\mathrm{c}}^{\mathrm{B}}$ to the right hand side of the equation and applying another coupling condition, $\mathbf{f}_{\mathrm{b^f}}^{\mathrm{AB}} = \mathbf{T}_{\mathrm{b^f}}\, \mathbf{f}_{\mathrm{b^f}}^{\mathrm{B}}$, give

$$\begin{bmatrix} \mathbf{H}_{\mathrm{cc}}^{\mathrm{B}} \\ \mathbf{H}_{\mathrm{b^m c}}^{\mathrm{B}} \end{bmatrix} \mathbf{f}_{\mathrm{c}}^{\mathrm{B}} = \begin{bmatrix} \mathbf{T}_{\mathrm{c}}{}^{-1} \mathbf{H}_{\mathrm{cc}}^{\mathrm{AB}} \\ \mathbf{T}_{\mathrm{b^m}}{}^{-1} \mathbf{H}_{\mathrm{b^m c}}^{\mathrm{AB}} \end{bmatrix} \mathbf{f}_{\mathrm{c}}^{\mathrm{AB}} + \begin{bmatrix} \mathbf{T}_{\mathrm{c}}{}^{-1} \mathbf{H}_{\mathrm{cb^f}}^{\mathrm{AB}} \mathbf{T}_{\mathrm{b^f}} - \mathbf{H}_{\mathrm{cb^f}}^{\mathrm{B}} \\ \mathbf{T}_{\mathrm{b^m}}{}^{-1} \mathbf{H}_{\mathrm{b^m b^f}}^{\mathrm{AB}} \mathbf{T}_{\mathrm{b^f}} - \mathbf{H}_{\mathrm{b^m b^f}}^{\mathrm{B}} \end{bmatrix} \mathbf{f}_{\mathrm{b^f}}^{\mathrm{B}} \tag{B.3}$$

Extracting the second row of Eq. (B3) and assuming that $\mathbf{f}_{\mathrm{c}}^{\mathrm{AB}}$ is equal to zero result in

$$\mathbf{f}_{\mathrm{c}}^{\mathrm{B}} = \mathbf{H}_{\mathrm{b^m c}}^{\mathrm{B}}{}^{+} \left(\mathbf{T}_{\mathrm{b^m}}{}^{-1} \mathbf{H}_{\mathrm{b^m b^f}}^{\mathrm{AB}} \mathbf{T}_{\mathrm{b^f}} - \mathbf{H}_{\mathrm{b^m b^f}}^{\mathrm{B}} \right) \mathbf{f}_{\mathrm{b^f}}^{\mathrm{B}} \tag{B.4}$$

where $\blacksquare^{+}$ denotes the pseudoinverse. Thus, $\mathbf{u}_{\mathrm{b^m}}^{\mathrm{B}}$ in Eq. (6.2) can be written as

$$\mathbf{u}_{\mathrm{b^m}}^{\mathrm{B}} = \mathbf{H}_{\mathrm{b^m c}}^{\mathrm{B}} \mathbf{H}_{\mathrm{b^m c}}^{\mathrm{B}}{}^{+} \left(\mathbf{T}_{\mathrm{b^m}}{}^{-1} \mathbf{H}_{\mathrm{b^m b^f}}^{\mathrm{AB}} \mathbf{T}_{\mathrm{b^f}} - \mathbf{H}_{\mathrm{b^m b^f}}^{\mathrm{B}} \right) \mathbf{f}_{\mathrm{b^f}}^{\mathrm{B}} + \mathbf{H}_{\mathrm{b^m b^f}}^{\mathrm{B}} \mathbf{f}_{\mathrm{b^f}}^{\mathrm{B}} \qquad \text{(B.5)}$$

which can be grouped into two parts for a clearer representation

$$\mathbf{u}_{\mathrm{b^m}}^{\mathrm{B}} = \left(\mathbf{E} \mathbf{T}_{\mathrm{b^m}}{}^{-1} \mathbf{H}_{\mathrm{b^m b^f}}^{\mathrm{AB}} \mathbf{T}_{\mathrm{b^f}} \right) \mathbf{f}_{\mathrm{b^f}}^{\mathrm{B}} + \left(\mathbf{H}_{\mathrm{b^m b^f}}^{\mathrm{B}} - \mathbf{E} \mathbf{H}_{\mathrm{b^m b^f}}^{\mathrm{B}} \right) \mathbf{f}_{\mathrm{b^f}}^{\mathrm{B}} \qquad \text{(B.6)}$$

where $\mathbf{E} = \mathbf{H}_{\mathrm{b^m c}}^{\mathrm{B}} \mathbf{H}_{\mathrm{b^m c}}^{\mathrm{B}}{}^{+}$.

Bibliography

1. ASME. *Boulton & Watt Rotative Steam Engine*. Available from: https://www.asme.org/about-asme/who-we-are/engineering-history/landmarks/111-boulton-watt-rotative-steam-engine.
2. E. Galloway and L. Hebert, *History and Progress of the Steam Engine: With a Practical Investigation of Its Structure and Application*. 1836: T. Kelly.
3. M. Guillaume, *Propulseur par réaction sur l'air, FR534801A*. 1922.
4. H. Bleuler, *Magnetic bearings: Theory, design, and application to rotating machinery*. 2009, Dordrecht: Springer-Verlag Berlin and Heidelberg GmbH & Co. K.
5. H.N.A. Kumar, et al., *Development of smart squeeze film dampers for small rotors.* Procedia Engineering, 2016. **144**: p. 790-800.
6. H. Ibrahim, A. Ilinca, and J. Perron, *Energy storage systems—Characteristics and comparisons.* Renewable and Sustainable Energy Reviews, 2008. **12**(5): p. 1221-1250.
7. W. Yang, et al., *Wind turbine condition monitoring: Technical and commercial challenges.* Wind Energ., 2012. **17**(5): p. 673-693.
8. V.G. Inc. *Torsional vibration analysis*. 2015; Available from: http://www.vaultgroup.ca/whatwedo/torsional.html.
9. M.S. Inc. *Failure analysis of a compressor impeller*. 2015; Available from: http://www.mechsol.com/case-study/failure-analysis-of-a-compressor-impeller/.
10. J.F. Baldwin and S.G. Hutton, *Natural modes of modified structures.* AIAA Journal, 1985. **23**(11): p. 1737-1743.
11. S. Adhikari, *Rates of change of eigenvalues and eigenvectors in damped dynamic system.* AIAA journal, 1999. **37**(11): p. 1452-1458.
12. L.C. Rogers, *Derivatives of eigenvalues and eigenvectors.* AIAA Journal, 1970. **8**(5): p. 943-944.
13. D.V. Murthy and R.T. Haftka, *Derivatives of eigenvalues and eigenvectors of a general complex matrix.* International Journal for Numerical Methods in Engineering, 1988. **26**(2): p. 293-311.
14. C.S. Rudisill, *Derivatives of eigenvalues and eigenvectors for a general matrix.* AIAA Journal, 1974. **12**(5): p. 721-722.
15. J.T. Weissenburger, *Effect of local modifications on the vibration characteristics of linear systems.* Journal of Applied Mechanics, 1968. **35**(2): p. 327-332.

16. R.J. Pomazal and V.W. Snyder, *Local modifications of damped linear systems.* AIAA Journal, 1971. **9**(11): p. 2216-2221.
17. Y.M. Ram and J.J. Blech, *The dynamic behavior of a vibratory system after modification.* Journal of Sound and Vibration, 1991. **150**(3): p. 357-370.
18. J. He, *Structural modification.* Philosophical Transactions: Mathematical, Physical and Engineering Sciences, 2001. **359**(1778): p. 187-204.
19. K. Farahani and H. Bahai, *An inverse strategy for relocation of eigenfrequencies in structural design. Part I: First order approximate solutions.* Journal of Sound and Vibration, 2004. **274**(3–5): p. 481–505.
20. H. Bahai and F. Aryana, *Design optimisation of structures vibration behaviour using first order approximation and local modification.* Computers and Structures, 2002. **80**(26): p. 1955-1964.
21. J.E. Mottershead, M. Link, and M.I. Friswell, *The sensitivity method in finite element model updating: A tutorial.* Mechanical Systems and Signal Processing, 2011. **25**(7): p. 2275-2296.
22. W. Heylen, S. Lammens, and P. Sas, *Modal analysis theory and testing*. 1998: Katholieke Universiteit Leuven.
23. B. Peeters, et al., *The PolyMAX Frequency-Domain Method: A new standard for modal parameter estimation?* Shock and Vibration, 2004. **11**(3-4).
24. Y.M. Ram and S.G. Braun, *An inverse problem associated with modification of incomplete dynamic systems.* Journal of Applied Mechanics, Transactions ASME, 1991. **58**(1): p. 233-237.
25. I. Bucher and S. Braun, *The structural modification inverse problem: An exact solution.* Mechanical Systems and Signal Processing, 1993. **7**(3): p. 217-238.
26. S.G. Braun and Y.M. Ram, *Modal modification of vibrating systems: some problems and their solutions.* Mechanical Systems and Signal Processing, 2001. **15**(1): p. 101-119.
27. I. Bucher and S.G. Braun, *Left eigenvectors: extraction from measurements and physical interpretation.* Journal of Applied Mechanics, 1997. **64**(1): p. 97-105.
28. A. Kyprianou, J.E. Mottershead, and H. Ouyang, *Structural modification. Part 2: Assignment of natural frequencies and antiresonances by an added beam.* Journal of Sound and Vibration, 2005. **284**(1-2): p. 267–281.
29. Y.G. Tsuei and E.K.L. Yee, *A Method for Modifying Dynamic Properties of Undamped Mechanical Systems.* Journal of Dynamic Systems, Measurement, and Control, 1989. **111**(3): p. 403-408.
30. E.K.L. Yee and Y.G. Tsuei, *Method for shifting natural frequencies of damped mechanical systems.* AIAA Journal, 1991. **29**(11): p. 1973-1977.

31. N.M.M. Maia and J.M. Montalvão e Silva, *Theoretical and experimental modal analysis*. Mechanical engineering research studies: Engineering dynamics series 9. 1997: Taunton, Somerset : Research Studies Press, 1997.
32. J.E. Mottershead and Y.M. Ram, *Inverse eigenvalue problems in vibration absorption: Passive modification and active control.* Mechanical Systems and Signal Processing, 2006. **20**(1): p. 5-44.
33. O. Çakar, *Mass and stiffness modifications without changing any specified natural frequency of a structure.* JVC/Journal of Vibration and Control, 2011. **17**(5): p. 769-776.
34. J.E. Mottershead and G. Lallement, *Vibration nodes, and the cancellation of poles and zeros by unit-rank modifications to structures.* Journal of Sound and Vibration, 1999. **222**(5): p. 833-851.
35. J.E. Mottershead, C. Mares, and M.I. Friswell, *An inverse method for the assignment of vibration nodes.* Mechanical Systems and Signal Processing, 2001. **15**(1): p. 100-87.
36. J.E. Mottershead, *Structural modification for the assignment of zeros using measured Receptances.* Journal of Applied Mechanics, 2001. **68**(5): p. 791-798.
37. A. Kyprianou, J.E. Mottershead, and H. Ouyang, *Assignment of natural frequencies by an added mass and one or more springs.* Mechanical Systems and Signal Processing, 2004. **18**(2): p. 263–289.
38. J. Zhu, J.E. Mottershead, and A. Kyprianou, *An inverse method to assign receptances by using classical vibration absorbers.* JVC/Journal of Vibration and Control, 2009. **15**(1): p. 53-84.
39. D. Richiedei, A. Trevisani, and G. Zanardo, *A Constrained Convex Approach to Modal Design Optimization of Vibrating Systems.* Journal of Mechanical Design, 2011. **133**(6): p. 061011-061011.
40. H. Ouyang, et al., *Eigenstructure assignment in undamped vibrating systems: A convex-constrained modification method based on receptances.* Mechanical Systems and Signal Processing, 2012. **27**: p. 397–409.
41. G.H. Golub, P.C. Hansen, and D.P. O'Leary, *Tikhonov regularization and total least squares.* SIAM Journal on Matrix Analysis and Applications, 1999. **21**(1): p. 185-194.
42. Z. Liu, et al., *Eigenstructure assignment in vibrating systems based on receptances.* Archive of Applied Mechanics, 2015. **85**(6): p. 713-724.
43. Z. Liu, W. Li, and H. Ouyang, *Structural modifications for torsional vibration control of shafting systems based on torsional receptances.* Shock and Vibration, 2016. **2016**: p. 1-8.

44. Y.M. Ram, *Dynamic structural modification.* Shock and Vibration Digest, 2000. **32**(1): p. 11-17.
45. N. Birchfield, K.V. Singh, and S. Singhal, *Dynamical structural modification for rotordynamic application*, in *International Design Engineering Technical Conferences and Computers and Information in Engineering Conference*. 2013, American Society of Mechanical Engineers.
46. S.S. Park, Y. Altintas, and M. Movahhedy, *Receptance coupling for end mills.* International Journal of Machine Tools and Manufacture, 2003. **43**(9): p. 889-896.
47. U.V. Kumar and T.L. Schmitz, *Spindle dynamics identification for receptance coupling substructure analysis.* Precision Engineering, 2012. **36**(3): p. 435-443.
48. T.L. Schmitz and R.R. Donalson, *Predicting high-speed machining dynamics by substructure analysis.* CIRP Annals - Manufacturing Technology, 2000. **49**(1): p. 303-308.
49. M.R. Movahhedy and J.M. Gerami, *Prediction of spindle dynamics in milling by sub-structure coupling.* International Journal of Machine Tools and Manufacture, 2006. **46**(3): p. 243-251.
50. M. Mehrpouya, M. Sanati, and S.S. Park, *Identification of joint dynamics in 3D structures through the inverse receptance coupling method.* International Journal of Mechanical Sciences, 2016. **105**: p. 135-145.
51. J.E. Mottershead and Y.M. Ram, *Receptance method in active vibration control.* AIAA Journal, 2007. **45**(3): p. 562-567.
52. E. Papatheou, et al. *Active control for flutter suppression: An experimental investigation*. in *IFASD 2013 - International Forum on Aeroelasticity and Structural Dynamics*. 2013.
53. J.E. Mottershead, et al., *Active vibration suppression by pole-zero placement using measured receptances.* Journal of Sound and Vibration, 2008. **311**(3–5): p. 1391-1408.
54. Y.M. Ram, A. Singh, and J.E. Mottershead, *State feedback control with time delay.* Mechanical Systems and Signal Processing, 2009. **23**(6): p. 1940-1945.
55. J.M. Araújo, *Discussion on 'State feedback control with time delay'.* Mechanical Systems and Signal Processing, 2018. **98**: p. 368-370.
56. H.K. Khalil, *Nonlinear Systems*. 2002: Prentice Hall.
57. T.L.M. Santos, J.M. Araújo, and T.S. Franklin, *Receptance-based stability criterion for second-order linear systems with time-varying delay.* Mechanical Systems and Signal Processing, 2018. **110**: p. 428-441.

58. J.E. Mottershead, M.G. Tehrani, and Y.M. Ram, *Assignment of eigenvalue sensitivities from receptance measurements.* Mechanical Systems and Signal Processing, 2009. **23**(6): p. 1931-1939.
59. M. Ghandchi Tehrani, et al., *Robust pole placement in structures by the method of receptances.* Mechanical Systems and Signal Processing, 2011. **25**(1): p. 112-122.
60. H. Ouyang, *Pole assignment of friction-induced vibration for stabilisation through state-feedback control.* Journal of Sound and Vibration, 2010. **329**(11): p. 1985-1991.
61. H. Ouyang, *A hybrid control approach for pole assignment to second-order asymmetric systems.* Mechanical Systems and Signal Processing, 2011. **25**(1): p. 123-132.
62. K.V. Singh and H. Ouyang, *Pole assignment using state feedback with time delay in friction-induced vibration problems.* Acta Mechanica, 2013. **224**(3): p. 645-656.
63. Y. Liang, H. Yamaura, and H. Ouyang, *Active assignment of eigenvalues and eigen-sensitivities for robust stabilization of friction-induced vibration.* Mechanical Systems and Signal Processing, 2017. **90**: p. 254-267.
64. M. Ghandchi Tehrani, L. Wilmshurst, and S.J. Elliott, *Receptance method for active vibration control of a nonlinear system.* Journal of Sound and Vibration, 2013. **332**(19): p. 4440-4449.
65. T.J. Gibbons, E. Öztürk, and N.D. Sims, *Rotational degree-of-freedom synthesis: An optimised finite difference method for non-exact data.* Journal of Sound and Vibration, 2018. **412**: p. 207-221.
66. J.E. Mottershead, A. Kyprianou, and H. Ouyang, *Structural modification. Part 1: rotational receptances.* Journal of Sound and Vibration, 2005. **284**(1–2): p. 249-265.
67. P.J. Tavner, *Review of condition monitoring of rotating electrical machines.* IET Electric Power Applications, 2008. **2**(4): p. 215-247.
68. K. Janssens and L. Britte. *Comparison of torsional vibration measurement techniques*. in *International Conference on Noise and Vibration Engineering 2012, ISMA 2012, including USD 2012: International Conference on Uncertainty in Structure Dynamics*. 2012.
69. Y. Li, et al., *The measurement of instantaneous angular speed.* Mechanical Systems and Signal Processing, 2005. **19**(4): p. 786-805.
70. L. Xiang, S. Yang, and C. Gan, *Torsional vibration measurements on rotating shaft system using laser doppler vibrometer.* Optics and Lasers in Engineering, 2012. **50**(11): p. 1596-1601.

71. P. Giuliani, et al., *Six degrees of freedom measurement with continuous scanning laser doppler vibrometer.* Mechanical Systems and Signal Processing, 2013. **38**(2): p. 367-383.
72. M. Dumont and N. Kinsley, *Using accelerometers for measuring rotational degrees-of-freedom.* SOUND & VIBRATION, 2016: p. 11.
73. Y. Champoux, et al., *Moment excitation of structures using two synchronized impact hammers.* Journal of Sound and Vibration, 2003. **263**(3): p. 515-533.
74. L.H. Ivarsson and M.A. Sanderson, *MIMO technique for simultaneous measurement of translational and rotational mobilities.* Applied Acoustics, 2000. **61**(3): p. 345-370.
75. M.A. Sanderson and C.R. Fredö, *Direct measurement of moment mobility: Part I: A theoretical study.* Journal of Sound and Vibration, 1995. **179**(4): p. 669-684.
76. M.A. Sanderson, *Direct measurement of moment mobility: Part II: An experimental study.* Journal of Sound and Vibration, 1995. **179**(4): p. 685-696.
77. C. Sihler, *A novel torsional exciter for modal vibration testing of large rotating machinery.* Mechanical Systems and Signal Processing, 2006. **20**(7): p. 1725-1740.
78. S.J. Drew and B.J. Stone, *Torsional (rotational) vibration: excitation of small rotating machines.* Journal of Sound and Vibration, 1997. **201**(4): p. 437-463.
79. S.H. Cho, et al., *High-frequency torsional modal testing of a long cylinder by magnetostriction.* Applied Physics Letters, 2007. **91**(7): p. 071908.
80. Y.Y. Kim and Y.E. Kwon, *Review of magnetostrictive patch transducers and applications in ultrasonic nondestructive testing of waveguides.* Ultrasonics, 2015. **62**: p. 3-19.
81. P. Avitabile. *Model reduction and model expansion and their applications Part 1 - Theory*. in *Conference Proceedings of the Society for Experimental Mechanics Series*. 2005.
82. D.J. Ewins, *On predicting point mobility plots from measurements of other mobility parameters.* Journal of Sound and Vibration, 1980. **70**(1): p. 69-75.
83. P. Avitabile and J. O'Callahan, *Frequency response function expansion for unmeasured translation and rotation DoFs for impedance modelling applications.* Mechanical Systems and Signal Processing, 2003. **17**(4): p. 723-745.
84. A. Drozg, G. Čepon, and M. Boltežar, *Full-degrees-of-freedom frequency based substructuring.* Mechanical Systems and Signal Processing, 2018. **98**: p. 570-579.

85. X. Wang, T.L. Hill, and S.A. Neild, *Frequency response expansion strategy for nonlinear structures.* Mechanical Systems and Signal Processing, 2019. **116**: p. 505-529.
86. S. Sattinger, *Method for experimentally determining rotational mobilities of structures.* Shock Vib. Bull.;(United States), 1980. **50**.
87. M.L.M. Duarte and D.J. Ewins, *Rotational degrees of freedom for structural coupling analysis via finite-difference technique with residual compensation.* Mechanical Systems and Signal Processing, 2000. **14**(2): p. 205-227.
88. O. Özşahin, et al., *A closed-form approach for identification of dynamical contact parameters in spindle–holder–tool assemblies.* International Journal of Machine Tools and Manufacture, 2009. **49**(1): p. 25-35.
89. A.S. Elliott, A.T. Moorhouse, and G. Pavić, *Moment excitation and the measurement of moment mobilities.* Journal of Sound and Vibration, 2012. **331**(11): p. 2499-2519.
90. T.L. Schmitz, *Torsional and axial frequency response prediction by RCSA.* Precision Engineering, 2010. **34**(2): p. 345-356.
91. B. Jetmundsen, R.L. Bielawa, and W.G. Flannelly, *Generalized frequency domain substructure synthesis.* Journal of the American Helicopter Society, 1988. **33**: p. 55-64.
92. Y. Yang, et al., *Generalized method for the analysis of bending, torsional and axial receptances of tool–holder–spindle assembly.* International Journal of Machine Tools and Manufacture, 2015. **99**: p. 48-67.
93. L. Cheng and Y.C. Qu, *Rotational compliance measurements of a flexible plane structure using an attached beam-like tip, part 1: analysis and numerical simulation.* Journal of Vibration and Acoustics, 1997. **119**(4): p. 596-602.
94. D. Montalvão, et al., *Estimation of the rotational terms of the dynamic response matrix.* Shock and Vibration, 2004. **11**(3-4): p. 333-350.
95. J.E. Mottershead, et al., *Structural modification of a helicopter tailcone.* Journal of Sound and Vibration, 2006. **298**(1–2): p. 366-384.
96. Y.C. Qu, L. Cheng, and D. Rancourt, *Rotational compliance measurements of a flexible plane structure using an attached beam-like tip, part 2: experimental study.* Journal of Vibration and Acoustics, 1997. **119**(4): p. 603-608.
97. B. Lv, et al., *An indirect torsional vibration receptance measurement method for shaft structures.* Journal of Sound and Vibration, 2016. **372**: p. 11–30.
98. M.V. van der Seijs, D. de Klerk, and D.J. Rixen, *General framework for transfer path analysis: History, theory and classification of techniques.* Mechanical Systems and Signal Processing, 2016. **68-69**: p. 217-244.

99. O. Zarraga, et al., *Receptance based structural modification in a simple brake-clutch model for squeal noise suppression.* Mechanical Systems and Signal Processing, 2017. **90**: p. 222-233.
100. R. Caracciolo, et al., *Designing vibratory linear feeders through an inverse dynamic structural modification approach.* International Journal of Advanced Manufacturing Technology, 2015. **80**(9-12): p. 1587-1599.
101. B.N. Datta, et al., *Partial eigenstructure assignment for the quadratic pencil.* Journal of Sound and Vibration, 2000. **230**(1): p. 101-110.
102. H. Ouyang and J. Zhang, *Passive modifications for partial assignment of natural frequencies of mass–spring systems.* Mechanical Systems and Signal Processing, 2015. **50–51**: p. 214-226.
103. R. Belotti, H. Ouyang, and D. Richiedei, *A new method of passive modifications for partial frequency assignment of general structures.* Mechanical Systems and Signal Processing, 2018. **99**(Supplement C): p. 586-599.
104. M. Gurgoze and S. Inceoglu, *Preserving the fundamental frequencies of beams despite mass attachments.* Journal of Sound and Vibration, 2000. **235**(2): p. 345-359.
105. M. Ghandchi Tehrani, R.N.R. Elliott, and J.E. Mottershead, *Partial pole placement in structures by the method of receptances: Theory and experiments.* Journal of Sound and Vibration, 2010. **329**(24): p. 5017-5035.
106. Z.J. Bai, M.X. Chen, and B.N. Datta, *Minimum norm partial quadratic eigenvalue assignment with time delay in vibrating structures using the receptance and the system matrices.* Journal of Sound and Vibration, 2013. **332**(4): p. 780-794.
107. D. Richiedei and A. Trevisani, *Simultaneous active and passive control for eigenstructure assignment in lightly damped systems.* Mechanical Systems and Signal Processing, 2017. **85**: p. 556-566.
108. J. Zhang, H. Ouyang, and J. Yang, *Partial eigenstructure assignment for undamped vibration systems using acceleration and displacement feedback.* Journal of Sound and Vibration, 2014. **333**(1): p. 1-12.
109. Y.M. Ram, J.E. Mottershead, and M.G. Tehrani, *Partial pole placement with time delay in structures using the receptance and the system matrices.* Linear Algebra and Its Applications, 2011. **434**(7): p. 1689-1696.
110. Y.M. Ram and J.E. Mottershead, *Multiple-input active vibration control by partial pole placement using the method of receptances.* Mechanical Systems and Signal Processing, 2013. **40**(2): p. 727-735.

111. Z.J. Bai and Q.Y. Wan, *Partial quadratic eigenvalue assignment in vibrating structures using receptances and system matrices.* Mechanical Systems and Signal Processing, 2017. **88**: p. 290-301.
112. K.V. Singh, R.N. Brown, and R. Kolonay, *Receptance-based active aeroelastic control with embedded control surfaces having actuator dynamics.* Journal of Aircraft, 2016. **53**(3): p. 830-845.
113. M.G. Tehrani and H. Ouyang, *Receptance-based partial pole assignment for asymmetric systems using state-feedback.* Shock and Vibration, 2012. **19**(5): p. 1135-1142.
114. R. Ariyatanapol, Y.P. Xiong, and H. Ouyang, *Partial pole assignment with time delays for asymmetric systems.* Acta Mechanica, 2018. **229**(6): p. 2619-2629.
115. F. Östman and H.T. Toivonen, *Torsional system parameter identification of internal combustion engines under normal operation.* Mechanical Systems and Signal Processing, 2011. **25**(4): p. 1146-1158.
116. S.J. Drew, et al., *The measurement of forces in grinding in the presence of vibration.* International Journal of Machine Tools and Manufacture, 2001. **41**(4): p. 509-520.
117. A. Hohl, et al. *Prediction and mitigation of torsional vibrations in drilling systems*. in *SPE/IADC Drilling Conference, Proceedings*. 2016.
118. A. Rashid and C.M. Nicolescu, *Design and implementation of tuned viscoelastic dampers for vibration control in milling.* International Journal of Machine Tools and Manufacture, 2008. **48**(9): p. 1036-1053.
119. R. Belotti and D. Richiedei, *Designing auxiliary systems for the inverse eigenstructure assignment in vibrating systems.* Archive of Applied Mechanics, 2017. **87**(2): p. 171-182.
120. L.T. Watson and R.T. Haftka, *Modern homotopy methods in optimization.* Computer Methods in Applied Mechanics and Engineering, 1989. **74**(3): p. 289-305.
121. D.M. Dunlavy and D.P. O'Leary, *Homotopy Optimization Methods for Global Optimization.* 2005.
122. V. Dua and E.N. Pistikopoulos, *An algorithm for the solution of multiparametric mixed integer linear programming problems.* Annals of Operations Research, 2000. **99**(1-4): p. 123-139.
123. H. Ouyang, et al., *Discrete mass and stiffness modifications for the inverse eigenstructure assignment in vibrating systems: Theory and experimental validation*. Vol. 64. 2012. 211 – 220.
124. P.M. Pardalos and H.E. Romeijn, *Handbook of Global Optimization*. Nonconvex Optimization and Its Applications. Vol. 2. 2002: Springer US.

125. T. Weise, *Global Optimization Algorithms -- Theory and Application*. 2008.
126. M.I. Friswell, et al., *Dynamics of rotating machines*. 2010: Cambridge University Press (CUP).
127. G. Genta, *Dynamics of Rotating Systems*. 2007: Springer New York.
128. H.D. Nelson and J.M. McVaugh, *The dynamics of rotor-bearing systems using finite elements.* Journal of Engineering for Industry, 1976. **98**(2): p. 593-600.
129. M. Geradin and N. Kill, *A new approach to finite element modelling of flexible rotors.* Engineering Computations, 1984. **1**(1): p. 52-64.
130. H. Kim and I.Y. Shen, *Ground-based vibration response of a spinning, cyclic, symmetric rotor with gyroscopic and centrifugal softening effects.* Journal of Vibration and Acoustics, Transactions of the ASME, 2009. **131**(2): p. 0210071-02100713.
131. I.Y. Shen and H. Kim, *A linearized theory on ground-based vibration response of rotating asymmetric flexible structures.* Journal of Vibration and Acoustics, 2006. **128**(3): p. 375-384.
132. H. Kim and I.Y. Shen, *Ground-based vibration response of a spinning, cyclic, symmetric rotor with gyroscopic and centrifugal softening effects.* Journal of Vibration and Acoustics, 2009. **131**(2): p. 021007-021007-13.
133. M.A. Kandil, *On rotor internal damping instability*. 2005, Imperial College London.
134. G. Genta and M. Silvagni, *On centrifugal softening in finite element method rotordynamics.* Journal of Applied Mechanics, Transactions ASME, 2014. **81**(1).
135. G. Genta and A. Tonoli, *A harmonic finite element for the analysis of flexural, torsional and axial rotordynamic behavior of discs.* Journal of Sound and Vibration, 1996. **196**(1): p. 19-43.
136. G. Genta and A. Tonoli, *A harmonic finite element for the analysis of flexural, torsional and axial rotordynamic behavior of blade arrays.* Journal of Sound and Vibration, 1997. **207**(5): p. 693-720.
137. G. Genta, C. Feng, and A. Tonoli, *Dynamics behavior of rotating bladed discs: A finite element formulation for the study of second and higher order harmonics.* Journal of Sound and Vibration, 2010. **329**(25): p. 5289-5306.
138. J.-S. Wu, *Analytical and Numerical Methods for Vibration Analyses*. 2015.
139. E.P. Gargiulo Jr, *A simple way to estimate bearing stiffness*. Vol. 52. 1980. 107-110.
140. T.C. Lim and R. Singh, *Vibration transmission through rolling element bearings, part I: Bearing stiffness formulation.* Journal of Sound and Vibration, 1990. **139**(2): p. 179-199.

141. H. Cao, et al., *Mechanical model development of rolling bearing-rotor systems: A review.* Mechanical Systems and Signal Processing, 2018. **102**: p. 37-58.
142. R. Featherstone, *Rigid Body Dynamics Algorithms*. 2014: Springer US.
143. J.S. Rao, T.N. Shiau, and J.R. Chang, *Theoretical analysis of lateral response due to torsional excitation of geared rotors.* Mechanism and Machine Theory, 1998. **33**(6): p. 761-783.
144. F. Tisseur and K. Meerbergen, *The quadratic eigenvalue problem.* SIAM Review, 2001. **43**(2): p. 235-286.
145. L. Meirovitch, *A new method of solution of the eigenvalue problem for gyroscopic systems.* AIAA Journal, 1974. **12**(10): p. 1337-1342.
146. L. Meirovitch, *A modal analysis for the response of linear gyroscopic systems.* Journal of Applied Mechanics, Transactions ASME, 1975. **42**(2): p. 446-450.
147. J.E. Mottershead, T. Li, and J. He, *Pole-zero cancellation in structures: repeated roots.* Journal of Sound and Vibration, 2000. **231**(1): p. 219-231.
148. A. Preumont, *Vibration control of active structures*, in *Solid Mechanics and its Applications*. 2011. p. 1-452.
149. B.N. Datta, S. Elhay, and Y.M. Ram, *Orthogonality and partial pole assignment for the symmetric definite quadratic pencil.* Linear Algebra and its Applications, 1997. **257**: p. 29-48.
150. B.N. Datta and D.R. Sarkissian. *Multi-input partial eigenvalue assignment for the symmetric quadratic pencil*. in *Proceedings of the 1999 American Control Conference (Cat. No. 99CH36251)*. 1999.
151. B.N. Datta and D. Sarkissian, *Theory and computations of some inverse eigenvalue problems for the quadratic pencil.* Contemporary Mathematics, 2001. **280**: p. 221-240.
152. D.J. Inman, *Vibration with Control*. 2006: John Wiley & Sons, Inc.
153. A.M.A. Hamdan and A.H. Nayfeh, *Measures of modal controllability and observability for first- and second-order linear systems.* Journal of Guidance, Control, and Dynamics, 1989. **12**(3): p. 421-428.
154. Z.J. Bai, J.K. Yang, and B.N. Datta, *Robust partial quadratic eigenvalue assignment with time delay using the receptance and the system matrices.* Journal of Sound and Vibration, 2016. **384**: p. 1-14.
155. A. Forsgren, P.E. Gill, and M.H. Wright, *Interior methods for nonlinear optimization.* SIAM Review, 2002. **44**(4): p. 525-597.
156. K.Y. Sanliturk and O. Cakar, *Noise elimination from measured frequency response functions.* Mechanical Systems and Signal Processing, 2005. **19**(3): p. 615-631.

157. W. D’Ambrogio and A. Fregolent, *Promises and pitfalls of decoupling procedures.* Proceeding of 26th IMAC. Orlando (USA), 2008.
158. C.W. de Silva, *Vibration and Shock Handbook.* 2005: CRC Press.
159. B.W. Silverman, *Density estimation: For statistics and data analysis*. Density Estimation: For Statistics and Data Analysis. 2018. 1-175.
160. G. Strang, *Introduction to Linear Algebra*. 2016: Wellesley-Cambridge Press.
161. B. Cauberghe, *Applied frequency-domain system identification in the field of experimental and operational modal analysis.* Ph.D. Thesis, Vrije Universiteit, Brussel, Belgium, 2004.
162. M. Dorosti, et al., *Iterative Pole–Zero model updating: A combined sensitivity approach.* Control Engineering Practice, 2018. **71**: p. 164-174.